

Solar Irradiance Nowcasting System to Optimize the Yield in Parabolic Trough Power Plants

Solarstrahlungs-Kürzestfrist-Vorhersagesystem für die Ertragsoptimierung eines Parabolrinnenkraftwerks

Von der Fakultät für Maschinenwesen der Rheinisch-Westfälischen Technischen Hochschule Aachen zur Erlangung des akademischen Grades eines Doktors der Ingenieurwissenschaften genehmigte Dissertation

vorgelegt von

Bijan Nouri

Berichter: Univ.-Prof. Dr.-Ing. Robert Pitz-Paal
Associate Professor Andreas Kazantzidis, PhD

Tag der mündlichen Prüfung: 05.03.2020

„Diese Dissertation ist auf den Internetseiten der Universitätsbibliothek online verfügbar.“

“It's hard to make predictions, especially about the future”
Niels Henrik David Bohr

Acknowledgement

This dissertation was prepared at the Institute of Solar Research of the German Aerospace Center (Deutsches Zentrum für Luft- und Raumfahrt e.V., DLR) within the department Qualification. The work was carried out at DLR's offices on CIEMAT's (Centro de Investigaciones Energéticas, Medioambientales y Tecnológicas) Plataforma Solar de Almería.

First of all, I would like to thank my adviser Prof. Dr. Robert Pitz-Paal, for giving me the opportunity to write my thesis. I highly appreciate his wise guidance for my work and his confidence in my research. I also want to thank Prof. Dr. Andreas Kazantzidis for his helpful advice and for acting as reviewer of this thesis.

My sincere gratitude goes to my supervisor Dr. Stefan Wilbert. He encouraged me to work on a doctoral thesis with a strong meteorology emphasis. I am grateful for the trust he placed in me and my work. His continuous professional support, the fruitful discussions and the thorough proofreading were essential for the preparation of this thesis.

I would also like to thank my doctoral colleague Pascal Kuhn. The support and preparatory work as well as the professional and personal exchange during this intensive time was of great value. Furthermore, I would like to thank my colleague Dr. Christoph Prah for his preparatory work on cloud cameras.

Special thanks are reserved to Dr. Kareem Noureldin for providing a customized version of the virtual solar field software, suitable for spatial DNI information. I thank Tim Schlichting, who identified the optimized solar field control parameters, which were utilized in this thesis.

I would like to thank Dr. Tobias Hirsch, Dr. Marion Schroedter-Homscheidt, Dr. Luis Zarzalejo, Luis Segura and Thomas Schmidt for the fruitful scientific discussions and suggestions.

Furthermore, I would like to thank Wolfgang Reinalter and Lothar Keller for their constant support in IT matters. I also appreciate the constant support of my colleagues Dr. Fabian Wolfertstetter, Dr. Nathalie Hanrieder, Sergio Gonzalez and David Muruve. Without them, the operation of many of the used meteorological stations would not have been possible. Overall, I would like to thank all of my colleagues in Almería for the great working environment they create.

My special thanks goes to my parents and my brother. They have constantly taken an important role model function in my life. Finally, I would like to thank my wife Maria del Mar. Her love, patience and tolerance made this work possible in the first place.

Contents

Nomenclature.....	7
Abstract	11
Kurzfassung.....	12
1 Introduction	13
1.1 Motivation for decarbonized electricity generation	13
1.2 Objective & approach	14
2 State of the art.....	18
2.1 Nowcasting with cameras	18
2.1.1 Nowcasting with ASIs.....	18
2.1.2 Nowcasting with shadow cameras.....	23
2.2 Virtual Solar Field simulation environment for PT power plants	25
2.2.1 Overview of virtual solar field.....	25
2.2.2 Assessing the performance of solar field controllers with VSF.....	27
3 Setup overview of used nowcasting and reference systems	29
3.1 Configuration of the considered ASI-based nowcasting system	29
3.2 Reference solar irradiance measurement stations.....	31
3.3 Reference cloud height measurement system	32
3.4 Reference cloud motion vector measurement system.....	32
3.5 Shadow camera system for reference DNI maps.....	32
4 Individual 3-D object oriented cloud modeling and tracking	33
4.1 Modeling space.....	34
4.2 ASI based modelling of cloud geometry, height and velocity	35
4.2.1 Cloud modeling and tracking with voxel carving (4Cam).....	35
4.2.2 Two camera block correlation method (2Cam).....	39
4.2.3 Four camera block correlation method (4CamH).....	42
4.3 Cloud height validation with a reference ceilometer	44
4.3.1 Understanding the deviations of the 4Cam approach.....	48
4.3.2 Understanding the deviations of the 2Cam and 4CamH approach	50
4.4 Cloud motion vector validation with a reference shadow camera.....	51
4.5 Nowcast future cloud object positions and cloud shadow projection.....	55
4.6 Conclusion cloud modeling and tracking.....	59
5 Probabilistic approach for the determination of cloud transmittance.....	61
5.1 Radiative effect of different cloud classes and cloud height layers.....	61
5.2 Determination of clear sky DNI.....	63
5.3 Analysis of the relation between cloud height and transmittance	64

5.4	Cloud transmittance estimation method for the nowcasting system	67
5.5	Creating DNI maps	69
5.6	Validation of transmittance estimation approach	70
5.7	Benchmarking of different cloud transmittance approaches	73
5.8	Discussing site dependence	74
5.9	Potential of cloud classification	75
5.10	Conclusion determination of cloud transmittance	76
6	Overall validation and uncertainty analysis of DNI maps	78
6.1	Validation of DNI nowcast	78
6.2	Weather dependent uncertainty specification	81
6.2.1	Temporal DNI variability classes	82
6.2.2	DNI variability class dependent validation	84
6.2.3	Determination of uncertainties	87
6.2.4	Real time uncertainty assessment of spatial DNI maps	89
6.2.5	Final adjustments of uncertainty and validation	94
6.3	Nowcast uncertainties at different geographical locations	97
6.4	Conclusion on validation and uncertainty analysis of DNI maps	99
7	Control optimization of PT solar fields with DNI maps	102
7.1	Spatial as well as combined temporal and spatial DNI variability classification	103
7.1.1	Spatial variability class	103
7.1.2	Combined temporal and spatial variability class	105
7.2	Introducing and benchmarking novel class dependent solar field controllers	107
7.2.1	DNI variability class dependent solar field controllers	107
7.2.2	Selection of assessment days	111
7.2.3	Comparison with a state of the art reference controller	112
7.3	Detailed performance assessment and applicability conditions	115
7.3.1	Identification of applicability conditions	115
7.3.2	Implementation of applicability for the plant control	118
7.4	Performance estimation of class dependent control strategies for whole years	122
7.5	Conclusion on control optimization of PT solar fields with DNI maps	127
8	Final conclusion and outlook	131
8.1	Final conclusion	131
8.2	Outlook	134
	Appendix A. DNI variability classification comparison	135
	Appendix B. Comparison of p68.3 values within distinct Sun elevation angle ranges	136
	Bibliography	137

Nomenclature

Acronym	
2Cam	Cloud modeling and tracking approach with two cameras (block correlation method)
4Cam	Cloud modeling and tracking approach with four cameras (models the clouds via voxel carving)
4CamH	Cloud modeling and tracking approach with four cameras (combines voxel carving and block correlation method)
Ac	Alto cumulus
AM	Air mass
ARW	Anti-reset Wind-up
As	Altostratus
ASI	All sky imager
BOP	Balance of plant
CBH	Cloud base height
Cc	Cirrocumulus
Ci	Cirrus
COT	Cloud optical thickness
Cs	Cirrostratus
CSFD	Number of changes in the sign of the first derivative
CSL	Clear sky libraries
CSP	Concentrated solar thermal power
CTH	Cloud top height
Cu	Cumulus
Dev_i	Average deviation DNI between reference stations and DNI map at time stamp i
DHI	Diffuse horizontal irradiance
DNI	Direct normal irradiance
ELM	Edge length in meter (pixel orthogonal image)
$estCRelRev_{iD}$	Overall expected relative change in revenue per day
$expCRelRev_{iC}$	Expected relative change in revenue for the corresponding class combinations
FB	Feedback
FF	Feed-Forward
GHI	Global Horizontal Irradiance
GPS	Global Positioning System
HTF	Heat transfer fluid
ISCCP	International Satellite Cloud Climatology Project
LCoE	Levelized cost of electricity
LMA	Integral Lower Minus Abscissa
MAD	Mean absolute deviation
MMCR	Millimeter-wave cloud radar
NETRA	National thermal power corporation Energy Technology Research Alliance
Ns	Nimbostratus
NWP	Numerical weather prediction models
OFR	Class dependent controller objective focus rate
OT	Class dependent controller objective temperature

PI	Proportional-integral controller
ppm	Parts per million
Pr	Average probability
PSA	Plataforma Solar de Almería
PT	Parabolic trough
PV	Photovoltaic
PV	Photovoltaic
PZA	Pixel zenith angle
REPA	Rotation and expansion performing assemblies
rev_{ref}	Revenue of the reference controller
$rev_{classDep}$	Revenue of the class dependent controller
RMSD	Root mean square deviation
RSD	Relative standard deviation
Sc	Stratocumulus
SCA	Solar collector assemblies
SPA	Sun pixel angle
St	Stratus
TES	Thermal energy storages
TL	Linke turbidity
UMC	Integral Upper Minus Clear
UML	Integral Upper Minus Lower
VSF	Virtual Solar Field
WC	Water content
WP	Water path
Latin symbols	
A_{SASF}	Shaded solar field area
A_{SF}	Complete solar field area
A_{ap}	Collector aperture area
b	Binary orthogonal relative difference images
c	Camera constant
\bar{c}_p	Integral average specific heat capacity
$c_{rel,rev}$	Change in relative revenue
$c_{rel,rev,est,iD}$	Overall estimated relative change in revenue per day
$c_{rel,rev,exp,iD}$	Expected relative change in revenue for the corresponding class combinations
d	Difference images
dx' and dy'	Distortion parameter
e_T	Temperature error of solar field controller
$f_{iD,ic}$	Daily distribution of combination of spatial and temporal DNI variability classes
f_{SP}	Solar field focus set point
G_{eff}	Effective solar irradiance falling on the collector
h	Cloud height
I_{cl}	Clear sky irradiance (DNI)
I_{sh}	Shaded irradiance (DNI)

k_{cDNI}	Clear sky index
K_p	Controller parameters process gain
m	Scaling factor
\dot{m}	Mass flow
N	Number of pixel orthogonal image (one axis)
o	Orthogonal relative difference images
p_{def}	Penalty due to defocusing
$p_{T,PB}$	Reduced power block efficiency penalty
p_{TES}	TES penalty
p_{tot}	Total economic penalty
p_δ	Differential pressure set by HTF feed pump
Q_{def}	Solar energy lost due to defocusing
$Q_{loss,oth}$	Thermal losses
$Q_{th,SF}$	Thermal solar field energy
$\dot{Q}_{th,SF}$	Solar field thermal heat flow
$\frac{Q_{OL,a}}{Q_{TES,a}}$	Annually averaged ratio of TES overload resulting in solar energy dumping
r	Radius
r	Relative difference images
R	Rotation matrix
R_{SF}	Actual revenue
R_{th}	Theoretical revenue
s	Skill score
S_A	Shadow area fraction
S_i	Shaded clear sky index
t	Time (stamp)
T	Cloud transmittance
T_0	Solar field design temperature
T_c	Controller parameters time constant T_p multiplied by a factor varying from 0.1 to 10
T_{in}	Solar field inlet temperature
T_{out}	Solar field outlet temperature
T_p	Controller parameters time constant
T_{SCA}	Temperature at the middle of the SCAs
T_{SP}	Set Point temperature for SCAs
u_{low}	Basic uncertainty lower limit
u_{up}	Basic uncertainty upper limit
v	Speed
V_{DNI}	Variability indice according to Coimbra et al. 2013
VI_{DNI}	Variability indice according to Stein et al. 2012
X, Y and Z	Reference coordinate system
x' and y'	Image pixel coordinates
x'_0 and y'_0	Image focal point
Y_i	Reference value (error metrics)
\hat{Y}_i	Estimator value (error metrics)

Greek symbols	
$\alpha_{max/min}$	Maximum or minimum camera pixel elevation angle
β	Cloud motion angle
δ	Declination
η_{PB,T_0}	Power block efficiency at the design temperature
$\eta_{PB,T}$	Power block efficiency at the current temperature
$\eta_{PB,a}$	Average annual power block conversion efficiency
η_{opt}	Optical collector efficiency
θ	Maximum zenith angle orthogonal image
θ	Incidence angle
θ_p	Controller parameters process dead time
θ_z	Solar zenith angle
κ	Tilt angles over Z Axis
φ	Tilt angles over Y Axis
φ	Camera pixel azimuth angle
Φ_d	Deviation angle of the SCA from the sun
ω	Hour angle
ω	Tilt angles over X Axis

Abstract

One of the greatest challenges facing humanity in the 21st century is the transition to a fully decarbonized society. The most abundant energy resource available to mankind is the Sun. Concentrated solar thermal power (CSP) plants with thermal energy storages (TES), such as parabolic trough (PT) power plants, could provide a renewable source of dispatchable energy capable of balancing fluctuations in electrical grids caused by intermittent sources.

Yet, whether PT power plants are going to play an important role in the future is mainly a question of cost. One of the ways to increase the competitiveness of PT power plants is the optimization of solar field controller. PT solar fields are complex spatially extended thermo-hydraulic facilities, which concentrate the direct normal irradiance (DNI) on receiver tubes. The operation of these solar fields is strongly affected by spatial and temporal variabilities of DNI, mainly caused by clouds. State of the art PT solar field controllers have only a limited awareness of the current spatial and temporal DNI variability, since these controllers have only access to irradiance measurements of one or a handful of pyrheliometers.

All sky imager (ASI) based nowcasting systems can provide spatial DNI information with an adequate temporal and spatial resolution for PT solar field controller. These ASI-based nowcasting systems consist of cameras which take hemispherical images of the sky. The common working principle of ASI-based nowcasting systems includes cloud detection, -geolocation, -tracking and assessment of the corresponding current and immediate future solar irradiance. In the past years a manifold of distinct ASI-based nowcasting systems have been developed. The potential of nowcasting systems for control optimization is often highlighted in the literature. However, to the best of the author's knowledge, there have been no investigations to date, which have analyzed the applicability of nowcasting systems with their corresponding uncertainties for the optimization of CSP power plants.

The first objective of this thesis is the development of a real time capable ASI-based nowcasting system, qualified to describe complex but frequent multi-layer cloud conditions. Therefore, a system is developed which treats each detected cloud as an individual object with attributes such as geolocation, motion vector and transmittance. The processing steps 3-D cloud modeling, -tracking and the determination of the cloud transmittance are developed, benchmarked and combined to a modular nowcasting system, which creates DNI maps for lead times up to 15 minutes ahead. These DNI maps have a spatial extension up to 64 km² with a spatial resolution ≤ 20 m as well as an intra minute temporal resolution. The entire system is validated over two complete years with three spatially distributed reference DNI measurements. Furthermore, the same dataset is used to develop a real-time capable uncertainty analysis with an average coverage factor of 68.3%, taking into consideration spatial variations within the DNI maps. An additional dataset of one year is used to validate the uncertainty analysis. Both, the system validation as well as the uncertainty analysis indicate a strong dependency of the nowcast quality with the prevailing weather conditions.

Secondly, this thesis investigates the applicability of DNI maps for the optimization of PT solar field controller, under consideration of the uncertainties. Solar field simulations are performed using the so called Virtual Solar Field (VSF), a detailed dynamic simulation tool. In a first step the DNI maps of the nowcasting system are classified in one of 7 combined spatial and temporal DNI variability classes. For each of the classes optimized control parameters are determined. Class depended control strategies with distinct objectives are benchmarked with a state of the art solar field controller. Results of detailed simulations over 22 days as well as performance estimations over two years indicate an overall significant benefit of roughly 2% in revenue for the novel class depended control strategies.

Kurzfassung

Eine der größten Herausforderungen für die Menschheit im 21. Jahrhundert ist der Übergang zu einer vollständig dekarbonisierten Gesellschaft. Die reichhaltigste Energiequelle, die der Menschheit zur Verfügung steht, ist die Sonne. Konzentrierte solarthermische Kraftwerke (CSP) mit thermischen Energiespeichern (TES), wie etwa Parabolrinnen-(PT)-Kraftwerke, könnten eine erneuerbare Energiequelle bereitstellen die in der Lage ist Fluktuationen in elektrischen Netzen auszugleichen, welche durch intermittierende Quellen verursacht werden.

Jedoch ist es vor allem eine Frage der Kosten, ob PT-Kraftwerke in Zukunft eine wichtige Rolle spielen werden. Eine der Möglichkeiten, die Wettbewerbsfähigkeit von PT-Kraftwerken zu erhöhen, ist die Optimierung von Solarfeldreglern. PT-Solarfelder sind komplexe räumlich ausgedehnte thermo-hydraulische Anlagen, die die direkte Normalstrahlung (DNI) auf Absorberrohre konzentrieren. Der Betrieb dieser Solarfelder wird stark durch räumliche und zeitliche Variabilitäten der DNI beeinflusst, die hauptsächlich durch Wolken verursacht werden. Standard PT-Solarfeldregler haben nur eine begrenzte Kenntnis hinsichtlich der aktuellen räumlichen und zeitlichen DNI-Variabilität, da diese Regler nur Zugriff auf Strahlungsmessungen von einem oder einer Handvoll Pyrheliometern haben.

All sky imager (ASI) basierende Nowcasting-Systeme können räumliche DNI-Informationen mit einer angemessenen zeitlichen und räumlichen Auflösung für den PT-Solarfeldregler bereitstellen. Diese ASI-basierten Nowcasting-Systeme bestehen aus Kameras, die hemisphärische Bilder vom Himmel aufnehmen. Das gängige Funktionsprinzip von ASI-basierten Nowcasting-Systemen umfasst die Wolkenerkennung, -geolokalisierung, -verfolgung und -bewertung der entsprechenden aktuellen und zukünftigen Sonneneinstrahlung. In den letzten Jahren wurde eine Vielzahl von verschiedenen ASI-basierten Nowcasting-Systemen entwickelt. Das Potenzial von Nowcasting-Systemen zur Regelungsoptimierung wird in der Literatur oft hervorgehoben. Nach dem derzeitigen Wissensstand des Autors gibt es jedoch keine Untersuchungen, die die Anwendbarkeit von Nowcasting-Systemen mit den entsprechenden Unsicherheiten für die Optimierung von CSP-Kraftwerken analysiert haben.

Das erste Ziel dieser Arbeit ist die Entwicklung eines echtzeitfähigen ASI-basierten Nowcasting-Systems, das komplexe aber häufig vorkommende mehrschichtige Bedingungen charakterisieren kann. Daher wird ein System entwickelt, das jede erkannte Wolke als individuelles Objekt mit Attributen wie Geolokalisation, Bewegungsvektor und Transmittanz behandelt. Die Bearbeitungsschritte 3D-Wolken-Modellierung, -Tracking und die Bestimmung der Wolkentransmission werden entwickelt, bewertet und zu einem modularen Nowcasting-System kombiniert, das DNI-Karten für Vorlaufzeiten von bis zu 15 Minuten erstellt. Diese DNI-Karten haben eine räumliche Ausdehnung von bis zu 64 km² mit einer räumlichen Auflösung ≤ 20 m sowie einer zeitlichen Auflösung von 30 Sekunden. Das gesamte System wird über zwei Jahre mit drei räumlich verteilten DNI-Referenzmessungen validiert. Darüber hinaus wird aus demselben Datensatz eine echtzeitfähige Unsicherheitsanalyse mit einem durchschnittlichen Überdeckungsgrad von 68,3% unter Berücksichtigung räumlicher Variationen innerhalb der DNI-Karten entwickelt. Ein zusätzlicher Datensatz von einem Jahr wird verwendet, um die Unsicherheitsanalyse zu validieren. Sowohl die Systemvalidierung als auch die Unsicherheitsanalyse zeigen eine starke Abhängigkeit der Vorhersagequalität von den vorherrschenden Wetterbedingungen.

Darüber hinaus wird in dieser Arbeit die Anwendbarkeit von DNI-Karten für die Optimierung von PT-Solarfeldreglern unter Berücksichtigung der Unsicherheiten untersucht. Solarfeldsimulationen werden mit dem so genannten Virtual Solar Field (VSF), einem detaillierten dynamischen Simulationstool, durchgeführt. In einem ersten Schritt werden die DNI-Karten des Nowcasting-Systems in eine von 7 kombinierten räumlichen und zeitlichen DNI-Variabilitätsklassen klassifiziert. Für jede der Klassen werden optimierte Regelparameter ermittelt. Klassenabhängige Regelstrategien mit unterschiedlichen Zielsetzungen werden mit einem Solar-Feldregler auf dem Stand der Technik verglichen. Die Ergebnisse detaillierter Simulationen über 22 Tage sowie Leistungsschätzungen über zwei Jahre hinweg zeigen einen signifikanten Umsatzzuwachs von rund 2% für die innovativen klassenabhängigen Kontrollstrategien.

1 Introduction

1.1 Motivation for decarbonized electricity generation

The increasing carbon dioxide (CO₂) concentration, is the main cause of anthropogenic climate warming (e.g. **Matthews & Caldeira 2008, Matthews et al. 2009, Gilett et al. 2011, Knutto & Rogelj 2015, MacDougall et al. 2015, Cook et al. 2016**) and reached an annual average of 406.5 ppm by 2017 with an average growth rate of 2.3ppm yr⁻¹, compared to roughly 278 ppm in pre-industrial 1750 (**Dlugokencky et al. 2018**). Some studies suggest that already 2/3 of the available CO₂ budget for a global warming below 2°C above pre-industrial levels are depleted (**Meinshausen et al. 2009, Rogelj et al. 2016**). Exactly these 2°C represent the limit on which the international community could agree on in the Paris climate agreement (**UNFCCC 2015**). This 2°C threshold is considered as a goal which can be achieved with “*comparably low economic cost*” (**Schnellhuber et al. 2016**) and should prevent any “*dangerous anthropogenic interference with the climate system*” (**UNFCCC 1992**).

To accomplish this goal, we as society have to reach a near zero or even overall negative carbon emissions, due to the long life time of CO₂ in earth’s atmosphere (**Schnellhuber et al. 2016, Rogelj et al. 2016**). Decarbonization of the human societies on a global scale has to consider three distinct tasks including (1) decarbonize electricity generation, (2) reduce energy demand (efficiency increase) and (3) electrification especially in transportation and heat generation (**Kennedy et al. 2018**). Task 1 and 3 summarize the global energy consumption of human societies. In 2016, approximately 79.5% of this energy requirement was covered by fossil fuels (**ren21 2018**). The remaining shares were covered by traditional biomass (e.g. wood burning for cooking and heating), modern renewables (hydropower, biomass, wind, solar, geothermal and ocean power) as well as nuclear energy with 7.8%, 10.4% and 2.2% respectively (**ren21 2018**). Overall, it has to be expected that the global energy demand will continue to rise for the decades to come (**Heard et al. 2017**). This increase is mainly caused by two developments. First, it is expected that the global population will continue to grow (**Bradshaw & Brook 2014**). Second, the understandable objective of developing as well as emerging countries to leave poverty behind and catch up with developed countries (**Heard et al. 2017**). Such improvements can be measured by the United Nations human development index, which has an undeniable relationship with per capita energy consumption (**Martinez & Ebenhack 2008**). The needed fast transition from fossil fuels to renewable energies has to account also for this continuously growing energy demand. If we as global society fail to make the transition in time, the consequences will be disastrous (**IPCC 2018**).

1.2 Objective & approach

The most abundant energy resource available to mankind is the Sun with $3.9 \cdot 10^9$ PJ (**Quaschnig 2008**), which reaches the Earth's surface per year. In comparison, human consumption between 2017 and 2018 was estimated at roughly $6.0 \cdot 10^5$ PJ with a growth rate of 2.3% in this period (**IEA 2019**). Solar power could play a key role both in electricity generation as well as electrification. The global installed solar power capacity reached roughly 486 GW by the end of 2018, which accounts for about 2% of the overall global electrical power capacity (**IRENA 2019**). Solar photovoltaic (PV) is with roughly 480 GW the main contributor compared to roughly 5.4 GW for CSP (**IRENA 2019**). Currently solar PV is also dominating the overall global electricity capacity increase, with additional 94 GW only in 2018 (**IRENA 2019**). **Kost et al. 2018** predicts a strong growth of solar PV with a total global capacity between 3000 GW and 9000 GW by the year 2035. More conservative estimates still range from 1180 GW to 5200 GW until 2035 (**Breyer et al. 2017**). The forecasts presented by **Kost et al. 2018** and **Breyer et al. 2017** cover a range of actual electricity generation from 4.3% to 32.7% by 2035.

However, the strong growth of intermittent electricity sources, such as solar PV, leads to new technological challenges. The magnitude of the incoming downward shortwave solar radiation depends on seasonal differences due to the Sun-Earth geometry, the day night cycle with corresponding varying angles of incidence and atmospheric extinction processes caused by aerosols and clouds. In terms of intra-hour and intra-minute solar irradiance variability clouds have the strongest impact (**Schroedter-Homscheidt et al. 2018**). Fluctuations lead to higher congestion in the grid which might cause unpredictable variations of node voltages and power within the electrical grids, or even instabilities in case of intermediate power shortages (**Woyte et al. 2006, Hart & Jacobson 2011, Bruninx et al. 2013, Chattopadhyay 2014, Perez et al. 2016**). Large grids with a low penetration of intermittent sources can compensate fluctuations. But, in a case of a PV penetration above 15% (annual energy basis), significant changes in system operation are required also for large electrical grids (**Denholm & Margolis 2016**). As consequence some electrical markets adapted in recent years their grid codes (**Braun et al. 2011**). Especially small grids are vulnerable for power ramps. Therefore, it comes as no surprise that Hawaii and Puerto Rico already introduced legal limitations for ramp rates (**Gevorgian & Booth 2013, Crăciun et al. 2017**).

The objective of a fully decarbonized society is clear. At the same time, our electrical grids need dispatchable sources to balance fluctuation caused by intermittent sources. For regions with a high annual direct normal irradiance (DNI) sum, concentrated solar thermal power (CSP) plants with thermal energy storages (TES) could provide a renewable source of dispatchable energy (**Platzer 2016**), capable in balancing fluctuations in electrical grids with a high penetration of intermittent sources (**Mehos et al. 2016**).

Yet, whether CSP is going to play an important role in the future global energy mix is mainly a question of cost. Significant reductions in levelized cost of electricity (LCoE) for CSP with storage were reached in the last couple years (**Lilliestam & Pitz-Paal 2018**), but the LCoE of solar PV without storage remains significantly lower. However, CSP plants combined with TES outcompete PV plants with battery storage of similar annual production and storage capacity, especially for storage capabilities beyond 6 hours (**Lilliestam et al. 2018**). The comparisons in cost must also take into account that CSP still offers a considerable cost reduction potential. Price reductions can be achieved by scale effects, by improving the component efficiencies or by optimizing the plant operation (**Pitz-Paal 2017**). This study contributes to the latter objective.

The operation of commercial CSP power plants is more complex compared to solar PV and offers a lot of possibilities for optimization. In the case of the most common CSP technology of parabolic troughs (PT), the collectors concentrate the DNI on receiver tubes (see Figure 1.1). A heat transfer fluid (HTF) circulates the receiver tubes and is heated up to several hundred degrees Celsius. The thermal energy is passed over heat exchangers to a conventional Rankine cycle or TES. Especially intra-hour and intra-minute solar irradiance variability caused by passing clouds pose an operational challenge for commercial PT power plants with extensive solar field sizes (**García et al. 2011; Hirsch et al. 2014**). An efficient solar field controller needs to find the best combination of field mass flow, temperature set-points and defocusing of collectors corresponding to the prevailing DNI conditions (**Wagner & Wittmann 2014**). Ideally a perfect controller would adjust the mass flow in such a way, that the design temperature is always maintained constant without any need of defocusing collectors. In order to approach this ideal, the hydraulic and thermal interactions within the solar field must be well understood, especially under transient conditions with a strong spatial and temporal variability of the DNI inside the solar field.

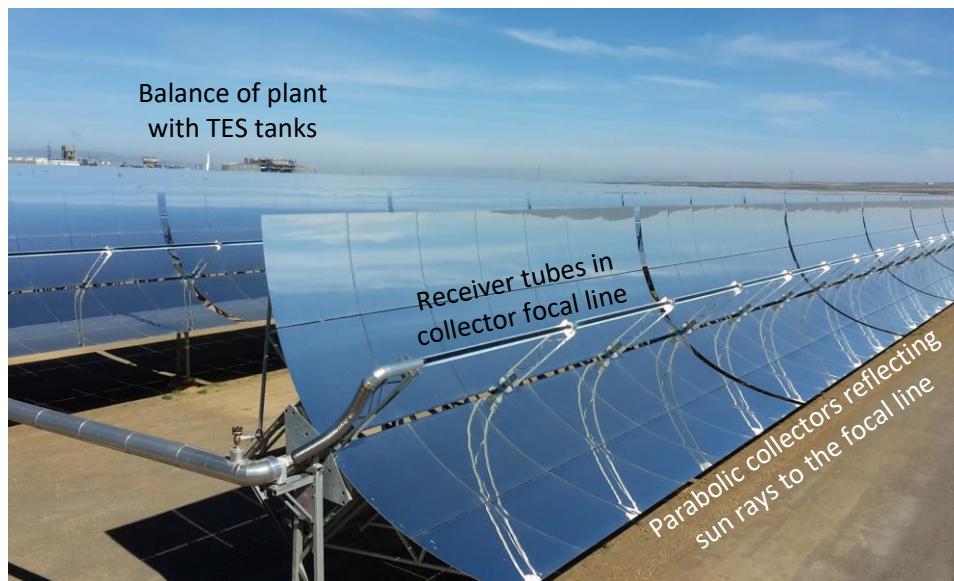


Figure 1.1: Parabolic trough collectors and balance of plant with TES tanks in the background.

Comprehensive numerical models as developed by **Hirsch & Schenk 2010, García et al. 2011, Giostri 2012, Zaversky et al. 2013, Noureldin et al. 2016** and **Noureldin et al. 2017** are useful tools to study the solar field behavior for distinct control strategies. The so called virtual solar field (VSF) as presented and validated in **Noureldin et al. 2016** and **Noureldin et al. 2017** is particularly interesting, as it models the entire solar field in a high temporal and spatial resolution under consideration of flow maldistribution due to thermal transients and inhomogeneity of the solar irradiance, as reported in **Abutayeh et al. 2014**. Furthermore, the VSF is designed to consider spatially inhomogeneous DNI information, which occur during transient conditions and have a significant impact on the solar field behavior.

The possible benefit of a PT solar field controller, with access to perfectly accurate spatial DNI information, compared to a state of the art controller, with DNI information from one or a handful of reference pyheliometers, has been studied in **Noureldin et al. 2019**. This initial study on this topic showed a significant potential with an estimated gain in revenue up to 2.5% for some days.

Spatial DNI information can be provided by satellite based systems or numerical weather models. However, due to current temporal and spatial resolution constrains, satellite based

systems and numerical weather models are not suitable (**Schroedter-Homscheidt & Gesell 2016, Lorenz et al. 2009**). All sky imager (ASI)-based nowcasting systems could provide the required temporal and spatial resolution needed for control optimization. Such systems take images of the sky, detect clouds in the sky images, geolocate them, identify their motion and analyze their radiative effect. Finally, solar irradiance information on the ground for the current conditions and immediate future are derived. The possible nowcast horizon depends on the prevailing cloud height and speed.

In the past, various ASI-based nowcasting systems have been described in the literature that are theoretically suitable for the optimization of electrical grid and power plant operation (e.g. **Chow et al. 2011, Quesada-Ruiz et al. 2014, Peng et al. 2015, Blanc et al. 2017, Kazantzidis et al. 2017**). However, the actual implementation of the nowcasts, taking into account the existing uncertainties, has not yet been sufficiently investigated.

This thesis aims to develop a real time capable, modular and cost effective ASI-based nowcasting system with a sufficient degree of accuracy for a beneficial applicability in PT power plants. A new in-house nowcasting system development is necessary, as the planned power plant control applications make a complete understanding of the nowcasting systems properties and uncertainties mandatory.

In order to cover complex but frequent multi-layer cloud conditions (**Wang et al. 2000**), the author decided from the very beginning to develop an approach which treats each detected cloud as individual object with distinct attributes (geolocation, motion vector, transmittance, etc.). As output the nowcasting system provides in real time spatial solar irradiance information with their corresponding uncertainties for the current conditions as well as nowcasts up to 15 minutes ahead. These spatial irradiance information cover field sizes corresponding to industrial size solar power plants with a spatial resolution ≤ 20 m as well as an intra minute temporal resolution.

A subsequent phase picks-up the work of **Noureldin et al. 2019** and investigates the potential benefit of the spatial solar irradiance information, with consideration of their uncertainties, for the optimization of PT solar field controller. The overall goal is to demonstrate that it is possible to improve the power plant revenue with additional spatial DNI information, despite the existing uncertainties of the nowcasting systems. Within this thesis the already significant potential benefit of spatial DNI information for lead time 0 minutes is investigated. For this purpose, novel control strategies are developed and applicability conditions are determined which take into account spatial as well as temporal variabilities of the solar irradiance. These novel control strategies are benchmarked with a state of the art solar field controller without access to spatial DNI information. Future research activities will also take into account the potential benefits of the provided nowcasts, potentially with model predictive control strategies.

The work is divided into several subtasks:

- Chapter 2: State of the art of camera based nowcasting systems & the dynamic simulation environment for PT solar fields “virtual solar field”.
- Chapter 3: Presentation of the used nowcasting setups as well as the utilized reference systems for validation purposes.
- Chapter 4: Investigation and validation of distinct cloud modeling and tracking approaches. All approaches are capable of treating each detected cloud as individual object. These individual cloud objects can be displaced according to the determined motion vectors within a 3-D modeling space for predicted cloud positions. Via raytracing binary shadow maps are created from the cloud models, under consideration of the corresponding Sun position and a topographical model.

- Chapter 5: Investigation and validation of a probabilistic approach for the determination of the cloud transmittance. The probabilistic approach analyses the current relation between cloud height and transmittance at any given moment. Shadow maps from chapter 4 are converted into DNI maps by allocating the prevailing clear sky DNI as well as the corresponding cloud transmittances. Furthermore, site dependencies of the presented approach are discussed as well as the potential to overcome these constraints by an automatic cloud classification approach.
- Chapter 6: Overall system validation as well as development of a real time uncertainty analysis. Each pixel of the DNI maps receives an upper and lower uncertainty value with a coverage factor of roughly 68.3%.
- Chapter 7: Investigation of optimized novel solar field controllers with consideration of DNI maps and their corresponding uncertainties. The controllers are tailored to a solar field design corresponding to the commercial 50 MW power plant La Africana (southern Spain). DNI maps are classified in distinct combined spatial and temporal DNI variability classes. For each class optimized control parameters are determined for two distinct objectives. The novel control strategies are benchmarked with a state of the art controller. Applicability conditions for the novel controller are identified. Finally, the impact of the new controller over a 2 year period is estimated.
- Chapter 8: An overall conclusion of this thesis as well as a short outlook is given.

2 State of the art

The state of the art of camera based nowcasting systems and the virtual sola field are summarized in this chapter. The content from this chapter has partially been published in **Nouri et al. 2019a**, **Nouri et al. 2019b**, **Nouri et al. 2019c** and **Nouri et al. 2019d**.

2.1 Nowcasting with cameras

The most common nowcasting systems consist of upward-facing ASIs. The common principle of such nowcasting systems (e.g. **Chow et al. 2011**, **Quesada-Ruiz et al. 2014**, **Peng et al. 2015**, **Blanc et al. 2017**, **Kazantzidis et al. 2017**) is to take RGB photos of the complete sky in which clouds are detected. Using several cameras, the cloud height above the ground can be detected by stereo photography or similar approaches. This information allows to compute cloud shadow maps which can be enhanced to irradiance maps with local measurements or clear sky models. The cloud movement is tracked in image series in order to predict future cloud positions and the corresponding irradiance maps. For all these evaluation steps, a variety of different methods is available from the literature.

A less common and distinct nowcasting approach uses downward-facing cameras (**Kuhn et al. 2017b**). These so-called shadow cameras are mounted on an elevated position (e.g. solar tower) and take images of the ground. Shadow maps are created by detecting the cloud shadows within the ground images. The shadow maps are converted into irradiance maps via local irradiance measurements and fully shaded as well as fully clear reference images taken from the same solar position.

2.1.1 Nowcasting with ASIs

Cloud detection/segmentation

Cloud detection/segmentation is one of the key processing steps of each ASI-based nowcasting system. The from a human perspective trivial appearing task of dividing sky images into clear and cloudy sections, is actually one of the most challenging tasks of ASI-based nowcasting systems. The difficulties of this task is described in detail by **Kuhn 2019c**. As **Kuhn 2019c** pointed out: *“This difficulty originates from color and intensity dependencies within the images regarding pixel and Sun positions, from artefacts due to saturation especially in the circumsolar region, from glare effects, from near horizon air mass related saturation within the images as well as from a multitude of physical properties of the clouds itshelves.”*

Over the years, various methods have been developed to solve this engineering challenge. Cloud detection algorithms can be based on a set of fixed thresholds applied to the images RGB values (e.g. **Heinle et al. 2010**, **Kazantzidis et al. 2012**) or other color spaces (**Dev et al., 2017**). Algorithms based on the RGB color space utilize the red to blue ratio, as a clear

atmosphere scatters more blue than red light. The share of scattered red light increases with the content of aerosols, water droplets and ice crystals within the atmosphere (**Heinle et al. 2010**). **Li et al. 2011** developed the so called hybrid thresholding algorithm (HYTA), which utilizes both fixed and dynamic thresholds. In a preceding step the images are classified in unimodal (all clear or clouded) or bimodal (mixed sky with clear and clouded parts) conditions. A fixed threshold is used during unimodal conditions. Dynamic threshold based on the minimum cross entropy (**Li & Lee 1993**) are used during bimodal conditions. **Hasenbalg et al. 2019** included a more profound image classification to the HYTA algorithm. The so called HYTA+ algorithm differentiates also whether or not the Sun is visible and improves the performance especially in the circumsolar region.

Another option to segment clouds are algorithms based on clear sky libraries (CSL) (e.g. **Chow et al. 2011**, **Wilbert et al. 2016a**). CSLs are large data bases which withhold the RGB information of clear reference images. **Wilbert et al. 2016a** uses a 4-D CSL, where the clear reference RGB values are linked to the pixel zenith angle (PZA)(see Figure 2.1), Sun pixel angle (SPA), air mass (AM) and Linke turbidity (TL). The AM describes the relative path length of the solar irradiance through the atmosphere (**Young 1994**) whereas the TL coefficient describes the extinction of the solar irradiance as multiplier of clean and dry ideal atmospheres (**Linke 1922**). Clouds are detected by comparing the deviation between the RGB information of target images with the corresponding RGB information from the CSL.

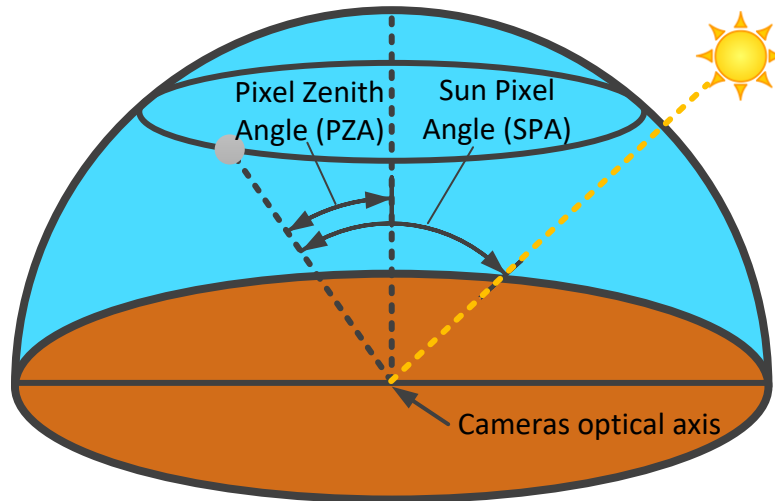


Figure 2.1: Illustration pixel zenith angle as well as sun pixel angle

In recent years, the number of machine learning based cloud segmentation approaches described in the literature is increasing (e.g. **Taravat et al. 2015**, **Xia et al. 2015**, **Ye et al. 2017**, **Hasenbalg et al. 2019**).

Cloud geolocation and tracking

Due to the strong interaction between cloud geolocation (especially cloud height) and tracking these processing steps are jointly described in the following.

The geolocation of the detected clouds is imperative for spatially resolved irradiance maps. The accurate identification of the cloud height is decisive. The error of the shadow's horizontal position on the ground is equal to the error of the cloud height in the case of a solar elevation angle of 45° . Smaller solar elevation angle increase the errors of the shadow position and vice versa. Furthermore, erroneous cloud heights lead to erroneous horizontal cloud extensions, which have an additional effect on the expected shadow position (see Figure 2.2). When nowcasting is performed, the erroneous shadow positions will also be influenced by the

tracking errors. The influence of the tracking errors on the nowcast quality rises with the lead time.

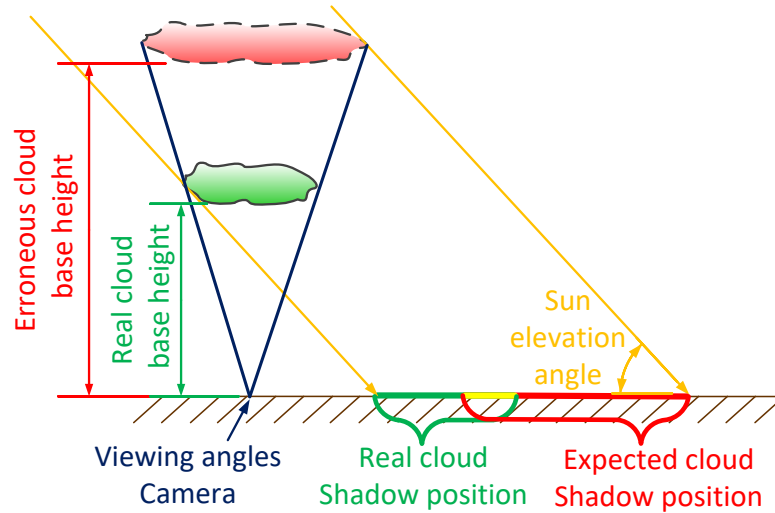


Figure 2.2: Impact of erroneous cloud base height information on the horizontal cloud extension and the shadow position. This simplified example regards a cloud directly above the camera with symmetric viewing angle.

One approach for nowcasting systems is to introduce additional accurate cloud height and tracking information from supplementary remote sensing systems. Lidars and ceilometers are commonly used to measure cloud height (**Sassen 1991**). Both instruments sample only the sky directly above the sensor. In principle, lidars are capable of measuring cloud boundaries from the cloud base height (CBH) to the cloud top height (CTH) including multiple layers. However, these capabilities are limited due to attenuation of the laser beam, especially for clouds with a high optical depth (**Venema et al. 2000**). This limits lidars often to CBH measurements of the lowest layer. Radar systems like the millimeter-wave cloud radar (MMCR) can scan the entire horizon with a range up to 30 km, measuring different cloud properties such as layer heights, thicknesses, horizontal extent and mean vertical velocity (**Moran et al. 1998**). However, MMCR measurements are less reliable in the case of clouds containing small particles, such as altocumulus and thin cirrus clouds. **Wang&Sassen 2001** combine lidar and MMCR measurements for improved cloud detection. Both lidar and radar techniques are well established systems but also costly which is problematic for their application in nowcasting systems.

Alternatively, radiosondes can be used to determine cloud boundaries and cloud amounts from vertical profiles of temperature, relative humidity and dewpoint depression (**Chernykh et al. 1995**). Cloud tracking can be done by measuring the vertical wind velocity and direction profile (**Bauer 1976**) under the common assumption that the clouds move simultaneously with the surrounding air (**Leese et al. 1971**). Temporal resolution and also cost make the radiosonde inappropriate for a real time low cost nowcasting system.

Comprehensive and continuous coverage of cloud height and motion measurements can be achieved by satellites (**Menzel et al. 1983, Nieman et al. 1993**). The advantage of satellite based systems is the large field of view. Generally, satellite based systems measure the CTH of the highest layer. Some approaches are developed to estimate CBH of the highest layer (**Noh et al. 2017**). However, the temporal and spatial resolution as of today is not suitable for shortest intra-hour nowcasts. Currently typical satellite solar nowcasting systems have a spatial resolution with a pixel edge length of 2 to 10 km and a temporal resolution of 15 minutes (**Blanc et al. 2017**). More advanced next-generation satellite systems, such as the Himawari-8

and GOES-R, reach a spatial resolution of 0.5 km² and a temporal resolution of 10 minutes for Himiwari-8 and 5 minutes for GOES-R (**Bright et al. 2018**).

Bosch & Kleissl 2013 studied the cloud motion estimation with triplets of reference cells and inverter output of a PV solar power plant. This approach might be an alternative for PV power plants, with a nowcast limitation defined by the spatial expansion of the solar field.

As we can see, there are different approaches to measure cloud height and track their motion. Nevertheless, none of the systems alone is able to describe all complex processes in the atmosphere. A study conducted by **Wang et al. 1999** compares the advantages and disadvantages of the different cloud height retrieval techniques by ceilometers, radar, radiosonde and satellites and combines them for more complete information on the vertical distribution of cloud boundaries.

Due to the financial and technical constraints of low cost nowcasting systems, a direct retrieval of cloud height and tracking information from the sky images itself is apparent. Stereoscopic approaches with two ASIs are frequently described in the literature (**Allmen et al. 1996**, **Kassianov et al. 2005**, **Seiz et al. 2007**, **Nguyen et al. 2014**, **Beekmans et al. 2016**, **Blanc et al. 2017**, **Kazantzidis et al., 2017** and **Crispel et al. 2017**). Cloud heights are determined by matching segmented clouds from images taken simultaneously by two ASIs. **Peng et al. 2015** developed a similar approach with an additional third ASI. Cloud tracking is achieved in the more recent publications with stereoscopic approaches (starting from **Nguyen et al. 2014**) by block matching with sequentially captured images using cross correlation algorithms.

Quesada-Ruiz et al. 2014 uses a so-called sector-ladder method and a single ASI. Binary images of the sky are overlaid with a Sun-centered circular grid. A cross correlation sector matching approach similar to block matching is utilized for cloud tracking. Only clouds moving towards the Sun are taken into account for the nowcast. **Bone et al. 2018** presented an enhanced sector-ladder system based on the work of **Quesada-Ruiz et al. 2014** with an additional autoregressive filtering. Due to the lack of any cloud height information, the nowcast of these approaches is limited to the vicinity around the ASI.

Cloud tracking approaches using optical flow instead of the computationally less demanding cross correlation approach are particularly suitable for nowcasting systems working with a singular ASI. **West et al. 2014** developed a system using the dense optical flow algorithm from **Farnebäck 2003**. Similar to the sector-ladder system, this approach lacks any cloud height information and can only derive angular cloud speeds. **Schmidt et al. 2016** and **Richardson et al. 2017** tackle this issue by including additional height information from nearby ceilometers. However, it has to be pointed out that current price of a ceilometer can exceed the price of an ASI by a factor greater than 30. Furthermore, as previously stated are ceilometers limited to the sky directly above the sensor.

Chow et al. 2015 and **Zaher et al. 2017** conducted comparisons of cloud tracking approaches based on optical flow and cross correlation algorithms. Both conclude that optical flow approaches outperform cross correlation approaches at the price of a greater computational effort. **Huang et al. 2012** proposed a hybrid tracking approach combining the advantages of cross correlation and optical flow approaches.

A slightly different approach presented by **Hirsch et al. 2011**, combining thermal imaging with wind profile data from radiosondes (temporal resolution 12 h). The thermal imaging enables cloud monitoring also at nighttime. A theoretical possible wind speed profile is determined by a block matching approach. The theoretical wind speed profile is compared to the wind speed profile measured by a nearby radiosonde station. The intersection of both wind speed profiles is considered as possible cloud height. The main obstacle of this system is the

need of external wind profile data from radiosondes and the corresponding temporal resolution.

Evaluating the radiative effect of clouds

The radiative effect of clouds can be analyzed by radiative transfer models. **Mejia et al. 2016** couples synthetic overcast sky images with a radiative transfer model and estimates the cloud optical thickness from the images. **Tzoumanikas et al. 2016** classifies the dominant cloud type from ASI images and studies the radiative effect by a radiative transfer model and aerosol information gathered by a Cimel Sun photometer. Another option to analyze the radiative effect, are numerous spatially distributed solar irradiance measurements on the ground (e.g. **Schmidt et al. 2016**).

Nowcasting systems with access to DNI measurements from pyrheliometers can measure directly the transmittance of clouds (T). This transmittance corresponds to the instrument specific field of view, and is measured as the ratio of shaded (I_{sh}) and clear sky irradiance (I_{cl}) according to Equation 2.1 (**Raschke & Cox 1983, Zangvil & Lamb 1997**).

$$T = I_{sh}/I_{cl}$$

Equation 2.1

For nowcasting systems which deliver spatial irradiance information, it has to be considered that various clouds detected by the ASIs might cast a shadow on the observed area within the next minutes. The angular distance of relevant clouds to the Sun as seen depends on the cloud height and speed. In the majority of cases clouds will not have their own transmittance measurement. A homogenous average transmittance, corresponding to the last measured transmittance values, for all visible clouds might be acceptable as a first approximation during single-layer conditions (see Figure 2.3). However, this approach would lead to increased uncertainties during complex but frequent multi-layer conditions (**Wang et al. 2000, Li et al 2011**). Therefore, an extended transmittance allocation approach is needed.

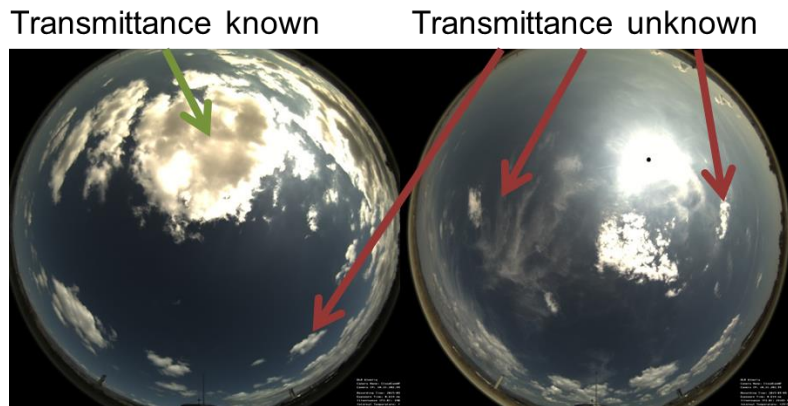


Figure 2.3: Sky images of an ASI (left) single-layer day (right) multi-layer day with different cloud types.

Validation and uncertainty

Each measurement is subject to a certain degree of uncertainty. Without an indication of measurement uncertainties, measurement results cannot be compared with each other or with reference values and are therefore incomplete. The measurement uncertainty of a measurement result is defined as an interval within which the correct value of the measurand lies with a certain probability.

The root mean square deviation (RMSD), the mean absolute deviation (MAD) and bias are often used as error metrics for nowcasting systems (e.g. **Bernecker et al. 2014, Schmidt et al. 2016, Xia et al. 2015, Fu & Cheng 2013, Kuhn et al. 2017a**). These error metrics are calculated according to Equation 2.2, Equation 2.3 and Equation 2.4

$$RMSD = \left[\frac{1}{n} \sum_{i=1}^n (Y_i - \hat{Y}_i)^2 \right]^{0.5} \quad \text{Equation 2.2}$$

$$MAD = \frac{1}{n} \sum_{i=1}^n |Y_i - \hat{Y}_i| \quad \text{Equation 2.3}$$

$$bias = \frac{1}{n} \sum_{i=1}^n Y_i - \hat{Y}_i \quad \text{Equation 2.4}$$

With Y_i as the reference value and \hat{Y}_i the value derived from the ASI system. The mentioned studies use validation periods from 15 days to six months. The validation results represent the overall accuracy of the nowcasting systems within this period for the used site. As already discussed in other studies (**Marquez & Coimbra 2013**), nowcasting validation results are strongly influenced by the chosen data set and the prevailing weather conditions. **Marquez & Coimbra 2013** proposes the well-known meteorological concept of using skill scores s (see Equation 2.5) as the main benchmarking metrics for nowcasting systems. The skill score s compares commonly the RMSD of the nowcasting system (index N) with the corresponding RMSD of a persistence nowcast (index P).

$$s = 1 - RMSD_N / RMSD_P \quad \text{Equation 2.5}$$

As most other accuracy metrics, the skill score also depends on the prevailing weather conditions during that period at the chosen geographical locations. This complicates the comparison between different nowcasting systems based on published results which refer to different observations.

2.1.2 Nowcasting with shadow cameras

ASI systems have to accurately detect the position of clouds in the sky in all three spatial dimensions. Complex but common and frequently changing atmospheric conditions, partially with multiple cloud layers, make this task challenging. A unique alternative to ASI systems are shadow camera systems, which directly detect the cloud shadows on the ground, without the detour over the clouds in the sky as in the case of the all sky imagers. This method and its validation are described in (**Kuhn et al. 2017b**), possible applications are presented in (**Kuhn et al. 2019b**). It consists of six Mobotix M24 off-the-shelf surveillance cameras, mounted on the top of an 87 m high solar tower. Figure 2.4 shows a shadow camera and an example image.



Figure 2.4: (left) Shadow camera mounted on top of a solar tower (right) image of a shadow camera

The viewing cones of the six cameras cover a 360° view around the tower. All cameras simultaneously take a new image of the ground every 15 seconds. All six images are converted to a single orthoimage (see Figure 2.5).



Figure 2.5: Orthoimage with a 360° view created from images of six shadow cameras mounted on the top of a solar tower

A difference image is calculated between the actual orthoimage and an additional reference clear sky orthoimage from a data base, corresponding to a similar Sun position with less than 3° deviation of azimuth and elevation angle. Furthermore, the reference image must be taken less than 60 days before the current image, which avoids significant differences in ground properties. Shadows on the ground are segmented, by comparing each pixel value of the difference image with empirically identified thresholds. The shadow camera system uses the DNI measurements taken by a pyrheliometer and diffuse horizontal irradiance (DHI) measurements taken by a pyranometer with a shadow ball. Unshaded sections of the orthoimage receive the clear sky DNI values identified by the most recent clear DNI measurements detected according to **Hanrieder et al. 2016**. For the identification of the DNI within the shaded sections a second reference orthoimage image is needed. This second reference image belongs to overcast conditions. The second reference image must be taken in the last 60 days and within 10° of the Sun elevation and azimuth angle for the evaluated image. The DNI in the shaded pixels is calculated according to **Kuhn et al. 2017b** from the RGB values of the three orthoimages and the DHI measurement. The sunny and the shaded reference image are used to approximate the bidirectional reflectance distribution function of each pixel in the image for the current solar position and the position of the camera. The final DNI maps have a spatial resolution of 5 m with a maximum edge length of 2 km.

2.2 Virtual Solar Field simulation environment for PT power plants

In the following section I will present the virtual solar field and the utilized performance assessment procedure. The in this work applied solar field controller are described in section 7.2.1.

2.2.1 Overview of virtual solar field

PT solar fields of commercial power plants are spatially extensive facilities with edge lengths typically above 1 km. The solar field is divided into several sections, whereas each section consists of a multitude of parallel loops. Each loop itself consists of several solar collector assemblies (SCA), which describe the smallest collector unit with an independent drive for tracking. The incoming DNI is concentrated by the parabolic shaped collectors to the receiver tube in the focal line. A heat transfer fluid circulates through the receiver tubes. All loops of the same section are connected to a cold and a hot section header pipe. In turn all the section header pipes are connected to a cold or hot main header pipe, which connects the solar field to the power block. A schematic solar field layout is illustrated in Figure 2.6. The control of such a solar field is a complex hydraulic as well as a thermal challenge. The loops of the solar field are not equipped with individual flow control valves. This means that the flow through the field is only determined by the power of the main pump supplying the whole solar field. The flow distribution over the sectors and loops is thus defined by the hydraulic resistance of each of the parallel loops in the network.

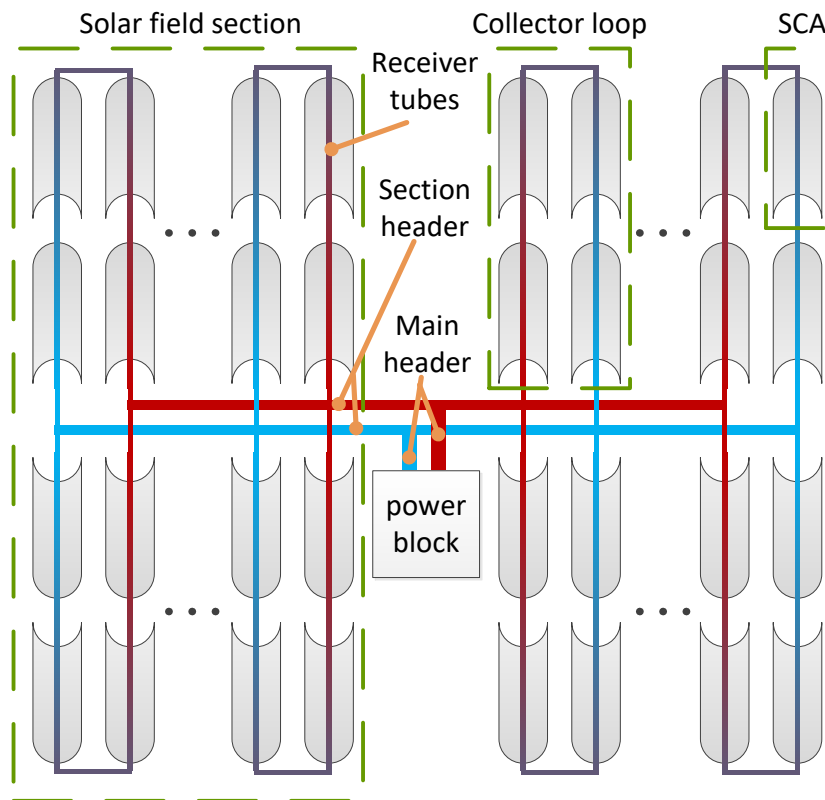


Figure 2.6: Schematic solar field layout

The VSF is a simulation environment which models the entire solar field from the power block. Common solar field designs with an arbitrary number of loops can be realized with the

VSF software. In order to accurately predict the physical behavior of the solar field, VSF couples a hydraulic network solver with a thermal solver.

The hydraulic solver computes the flow distribution within the branched piping system based on steady state assumptions. For this purpose the solar field is discretized in pipe elements of 12.5 m length within the collectors and 15 m to 50 m length within the header piping. Due to the strong variations in temperature within the solar field (also during stable conditions), the hydraulic resistance is computed for each discrete element with a temporal resolution of 2 seconds. Therefore, VSF is capable to characterize flow maldistribution due to thermal transients (e.g. triggered by variable solar irradiance conditions) or fluid distributions due to inhomogeneities in plant design or operation.

The hydraulic solver passes flow boundary conditions to the thermal solver, which in turn dynamically computes the temperatures with respect to the local thermal and operation conditions, and the thermal losses within each discrete pipe element. These calculations solve the time-dependent continuity and energy equations based on the assumption of a one dimensional flow. Previously published empirical relations are utilized for the thermal losses (e.g. **Burkholder and Kutscher 2009** for Schott PTR-70 receiver tubes). At pipe intersections the temperatures are computed by enthalpy balancing.

The coupling of the hydraulic and thermal solvers results in a computationally efficient model, which determines adequately the thermal and hydraulic conditions within the solar field. The VSF program structure is illustrated in Figure 2.7. A detailed description of VSF can be found in **Noureldin et al. 2016** and **Noureldin et al. 2017**.

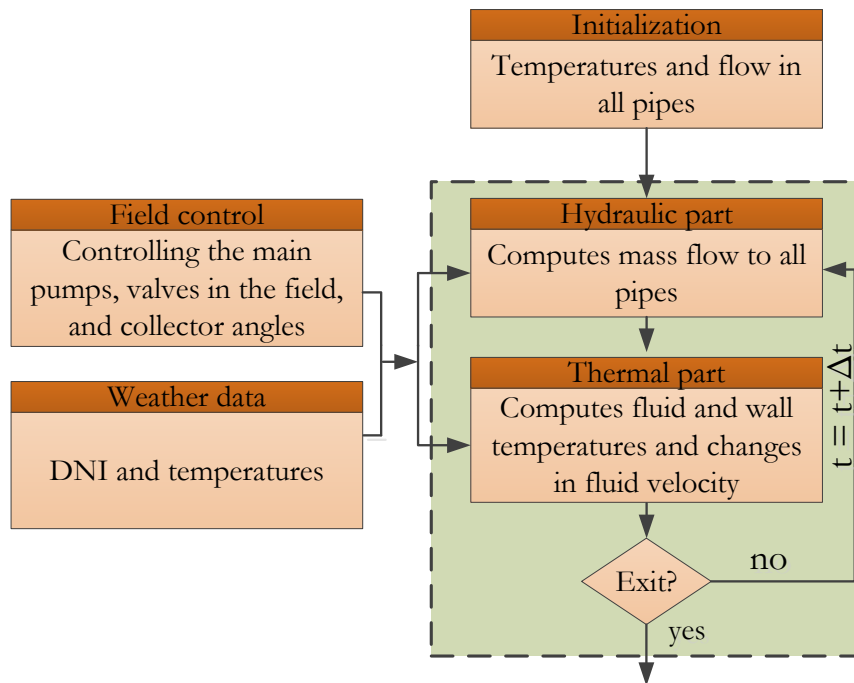


Figure 2.7: Illustration of the VSF program flow

A comprehensive validation of VSF with real plant operating data has been presented in **Noureldin et al. 2017**. For this purpose the Spanish company Marquesado Solar provided operational data from various days of the 50 MW PT power plant Andasol-3. This power plant is located in southern Spain and consists of four subfields with 38 loops each. The power plant data were supported by additionally measured values from a measurement campaign carried out simultaneously by the DLR at Andasol 3 on three test loops (**Noureldin et al. 2016**). These additional data provide flow and temperature measurements within the test loops with a

high temporal resolution. For this purpose the loops were equipped with a FLEXIM FLUXUS ADM 6725 clamp on ultrasonic flow meters with wave injectors for high temperature applications at the loop center (cross over piping) and a clamp-on temperature measuring system based on PT100s at the loop inlet and outlet (Nouri et al. 2018a). The validation was conducted over distinct cases including normal operation with predominantly clear conditions, start-up in clear mornings and conditions with strong transients due to cloud passages. For the flow distribution, deviations below 5% were observed between the simulated and measured values. During normal operation an overall RMSD in temperature of 2.75 K is observed. The RMSD rises up to 9.7 K during strong defocusing cycles. The observed VSF deviations are not significant compared to the expected uncertainties of the power plant instrumentation (Janotte 2012).

2.2.2 Assessing the performance of solar field controllers with VSF

VSF is a useful tool to comparatively assess distinct solar field controllers in terms of the yield. In Noureldin et al. 2018 and Noureldin et al. 2019 an approach is presented, which allows a monetary assessment of PT solar field controller with the results of VSF simulations. The solar field control concept is described in section 7.2. This approach is roughly summarized, for the better understanding of the results presented in chapter 7. Since the mass flow can only be altered for the whole field but not for each individual loop, inhomogeneous irradiance conditions or flow distribution may cause some loops to temporarily overheat while others do not reach the set point temperature. Each of these outcomes leads to an overall reduction of the energy yield and therefore to an economic loss. A methodology based on economic penalties has been developed to assess the solar field controller quality. The total economic penalty is composed as such:

$$p_{tot} = p_{def} + p_{T,PB} + p_{TES} \quad \text{Equation 2.6}$$

The first term p_{def} describes a loss of revenue due to defocused collectors where the amount of not usable heat Q_{def} is multiplied with the power block $\eta_{PB,a}$ efficiency and levelized cost of electricity $LCOE$,

$$p_{def} = Q_{def} \cdot \eta_{PB,a} \cdot LCOE. \quad \text{Equation 2.7}$$

The second effect is given by the fact that any reduction in solar field outlet temperature leads to a reduction of the power block efficiency. The overall heat produced by the solar field is converted to the penalty using the LCoE and the averaged power block efficiency corrected by temperature effects. The reduced power block efficiency penalty $p_{T,PB}$ is described by

$$p_{T,PB} = Q_{th,SF} \cdot \eta_{PB,a} \cdot LCOE \cdot \left(1 - \frac{\eta_{PB,T}}{\eta_{PB,T_0}} \right) \quad \text{Equation 2.8}$$

with $Q_{th,SF}$ as the thermal solar field energy, η_{PB,T_0} the power block efficiency at the design temperature and $\eta_{PB,T}$ as the power block efficiency at the current temperature. η_{PB,T_0} and $\eta_{PB,T}$ are obtained by a detailed heat flow diagram of the power block implemented in EBSILON® Professional.

Reduced solar field temperatures also have an effect on TES efficiency. This is due to an overall lower average temperature within the hot tank of the TES. This effect can be described by the TES penalty

$$p_{TES} = Q_{th,SF} \cdot \eta_{PB,a} \cdot LCoE \cdot \left(1 - \frac{T_{out} - T_{in}}{T_0 - T_{in}}\right) \cdot \frac{Q_{OL,a}}{Q_{TES,a}} \quad \text{Equation 2.9}$$

with T_{out} as the solar field outlet temperature, T_{in} as the solar field inlet temperature, T_0 as the design temperature for the solar field outlet and $\frac{Q_{OL,a}}{Q_{TES,a}}$ as the annually averaged ratio of TES overload resulting in solar energy dumping.

The quantities $\eta_{PB,a}$, $LCoE$ and $\frac{Q_{OL,a}}{Q_{TES,a}}$ are determined as average values over one year by means of annual yield simulations conducted with the Greenius simulation software (Dersch et al. 2012, Dieckmann 2017). For the La Africana power plant considered in section 7 the following values are used $\eta_{PB,a} = 0.25$, $LCoE = 192.5 \frac{\text{€}}{MWh}$ and $\frac{Q_{OL,a}}{Q_{TES,a}} = 0.33$ (Noureldin et al. 2019). The theoretical revenue R_{th} and the actual revenue R_{SF} are calculated according to the Equation 2.10 and Equation 2.11.

$$R_{th} = \eta_{PB,a} \cdot LCoE \cdot \sum_{SCA} \int [G_{eff}(t) \cdot \eta_{opt} \cdot A_{ap}]_{SCA} dt \quad \text{Equation 2.10}$$

$$R_{SF} = \eta_{PB,a} \cdot LCoE \cdot \int \dot{Q}_{th,SF} dt - (p_{TES} + p_{T,PB}) \quad \text{Equation 2.11}$$

with G_{eff} as the effective solar irradiance falling on the collector, η_{opt} as the optical collector efficiency and A_{ap} as the collector aperture area.

Thermal losses in the field are computed as

$$Q_{loss,oth} = R_{th} - p_{def} - \eta_{PB,a} \cdot LCoE \cdot \int \dot{Q}_{th,SF} dt \quad \text{Equation 2.12}$$

3 Setup overview of used nowcasting and reference systems

Various experimental set-ups are required for the development and validation of the nowcasting system as well as its application for the control optimization of PT solar fields. All set-ups used are described in this chapter. The generated data serve as basis for the chapters 4 to 7. The content from this chapter has partially been published in **Nouri et al. 2019a** and **Nouri et al. 2019b**.

3.1 Configuration of the considered ASI-based nowcasting system

Within the scope of this work, a modular nowcasting system is developed which can be operated with 2 to 4 cameras depending on the configuration. The system is developed at CIEMAT's Plataforma Solar de Almería (PSA) in southern Spain (latitude: 37.09° (north) and longitude: -2.36° (east)). At the PSA three Mobotix Q24 and one Mobotix Q25 off-the-shelf surveillance cameras are operated as ASIs (see Figure 3.1).



Figure 3.1: Mobotix Q24 camera at PSA

The Mobotix cameras are equipped with fisheye lenses, which are capable of taking hemispheric images of the sky. All sky images with a 3-mega pixel (MP) resolution are taken simultaneously by all cameras every 30 seconds with a fixed exposure time of $320 \mu\text{s}$ (Q24) or $160 \mu\text{s}$ (Q25). Subsequently the 3MP images are converted into 1 MP orthogonal image with a maximum zenith angle of 78° . In addition to the ASIs the nowcasting system requires DNI

measurements from at least one pyrliometer. The positions of the cameras and the pyrliometer are listed in Table 3.1. The shortest and longest distances between two ASIs are 494 m (ASI 1 to ASI 2) and 891 m (ASI 1 to ASI 3) respectively. Figure 3.2 illustrates the complete nowcasting system setup as well as the reference systems used for validation purposes.

Table 3.1: Positions of the ASIs and the main pyrliometer used by the nowcasting system

	Latitude	Longitude	Altitude
ASI1	37.09157° N	-2.36360° E	498 m
ASI2	37.09077° N	-2.35813° E	496 m
ASI3	37.09528° N	-2.35471° E	508 m
ASI4	37.09775° N	-2.35968° E	515 m
Main pyrliometer	37.09077° N	-2.35813° E	496 m

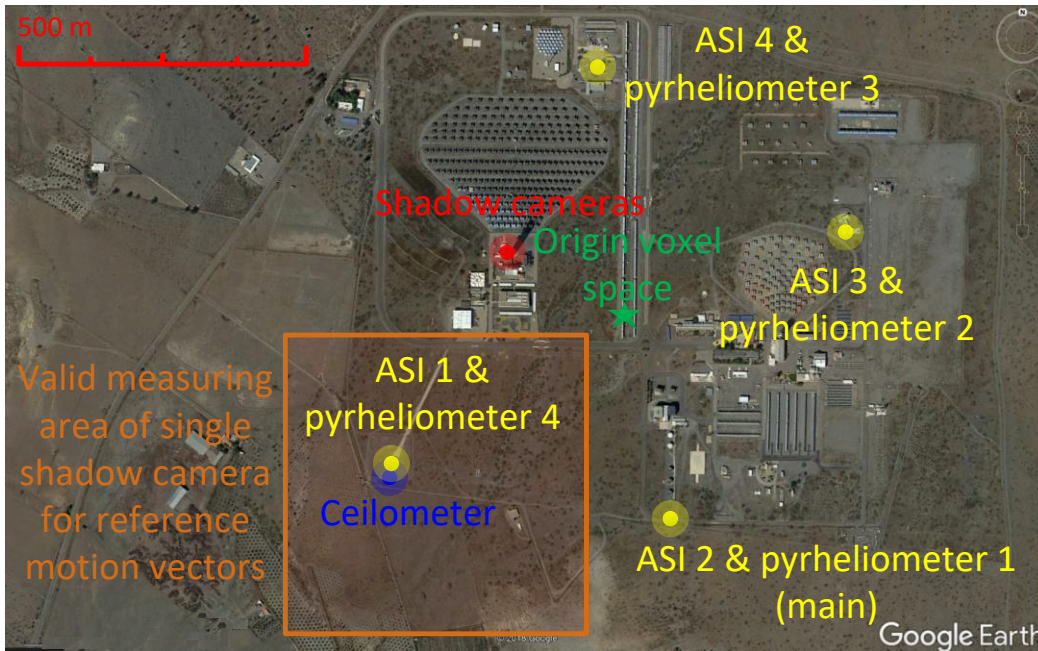


Figure 3.2: Aerial image of PSA with markers for the camera positions and reference systems as well as the point of origin of the used coordinate systems. The orange frame indicates the valid measuring area of one of the shadow cameras, in which cloud shadow speeds are determined (Source: Google Earth [Accessed: 05.05.2018]).

The unique feature of this ASI-based nowcasting system is that each detected cloud is treated as an individual cloud model with distinct attributes (geolocation, motion vector, transmittance, etc.). The image processing is divided into eight processing steps.

1. Clouds are segmented by means of 4-D CSL, accounting for different atmospheric conditions (Wilbert et al. 2016a, Kuhn et al. 2017a, Kuhn 2019c).
2. Individual cloud models are created
3. Cloud motion vectors are identified from sequential image series.

4. Future cloud positions are generated by displacing the cloud models inside a virtual modeling space.
5. Cloud transmittance properties are measured via a ground based irradiance measurement station for DNI and allocated by a probabilistic approach.
6. Cloud shadows are projected on a topographical map with ray tracing.
7. Shadow projections are combined with the ground based irradiance measurements and the optical cloud properties to spatial DNI maps, having edge lengths up to 8 km and resolution down to 5 m.
8. Real time uncertainties of the nowcasting system are determined.

Seven of the eight processing steps are developed within the framework of this work (see sections 4 to 6). The cloud segmentation procedure was developed as part of a parallel doctoral thesis (**Kuhn 2019c**) and is not the scope of this thesis. An example output of the used segmentation algorithm is illustrated in Figure 3.3.

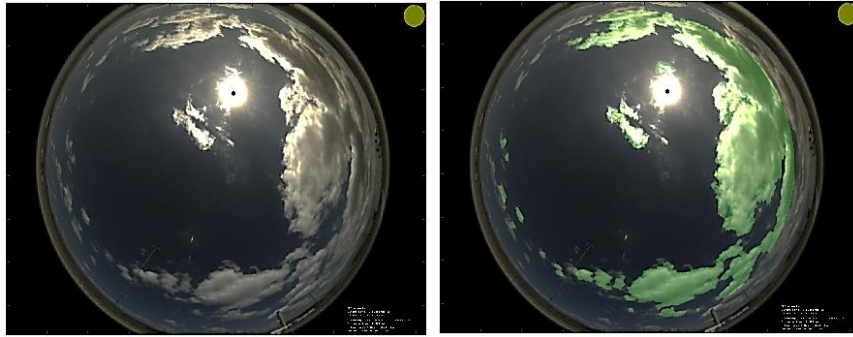


Figure 3.3: (left) Raw all sky image of Mobotix Q24 camera (right) corresponding automatically segmented image by means of a 4-D CSL

3.2 Reference solar irradiance measurement stations

A total of four reference pyrheliometers (Kipp&Zonen CHP1) are used within this experimental setup. Pyrheliometers are tracked to the sun and have an opening angle of a few degrees (5° in the case of CHP1 sensors). Inside of pyrheliometers a thermopile is exposed to the solar radiation, which generates an mV signal proportional to the incoming direct normal solar irradiance (DNI). The appropriate proportionality factor is identified by a calibration according to ISO standard 9059 (**ISO 1990**), with a reference sensor traceable to a world radiometric reference (WRR). Uncertainties due to the calibration are the most relevant contribution to the overall uncertainty of well-maintained pyrheliometers (**Nouri et al. 2016**). The 1σ calibration uncertainty of a first class CHP1 pyrheliometer amounts to roughly 1% (**Wilbert et al. 2010**).

Each of the used pyrheliometer stations is only a few meters away from one of the ASIs (see Figure 3.2). These pyrheliometers are used for the nowcast validation and uncertainty specification. However, only three stations were used simultaneously. Stations 1 to 3 are used for data sets up to the end of the year 2017. The pyrheliometer station 4 is introduced for all data sets belonging to the year 2018 as substitution for station 3, since station 3 was not operated in 2018.

The used shadow camera system (see section 3.5) needs a diffuse horizontal irradiance (DHI) signal, which is obtained at station 1 by a horizontally aligned pyranometer (Kipp&Zonen CMP21) with a 180° opening angle. This pyranometer is operated with a shading assembly, blocking at any time the DNI. Similar to the pyrhemeters the pyranometer is equipped with a thermopile. The needed proportionality factor is identified by a calibration according to ISO standard 9846 (**ISO 1993**).

The used instrumentation is cleaned each weekday and the DNI data are quality-screened, according to **Geuder et al. 2015**.

3.3 Reference cloud height measurement system

A CHM 15k Nimbus ceilometer from the G. Lufft Mess- und Regeltechnik GmbH is positioned 7 m south to the ASI 1 position in the southwest corner of the PSA (see Figure 3.2). The CHM 15k is capable of measuring multiple cloud layers simultaneously. However, the attenuation of the laser beam within clouds, limits the multi-layer capabilities to clouds with a cloud optical thickness below 3 (**Venema et al. 2000**). The global average of cloud optical thickness for low-level clouds (cumulus, stratocumulus and stratus) is around 4.7 (**Rossow & Schiffer 1999**). Therefore, in this work only the CBH measurements of the lowest cloud layer are used, as detected by the ceilometer. The ceilometer is operated at the PSA with a temporal resolution of 15 seconds.

Despite the detected average bias of 160 m between the CHM 15k and a CL31 Vaisala ceilometer by **Martucci et al. 2010**, the CHM 15k is considered sufficiently accurate as a reference system for the ASI based nowcasting systems.

3.4 Reference cloud motion vector measurement system

As reference for cloud motion a single shadow camera is used. This shadow camera is mounted at the top of an 87 m solar tower, taking ground images. Shadows on the ground are detected and tracked. **Kuhn et al. 2017b** developed this novel cloud (shadow) motion vector measurement device and used it to benchmark a Cloud Shadow Speed sensor (**Fung et al. 2013**). The benchmarking study observed a root mean square error (RMSD) of 2.69 m/s, MAD of 1.61 m/s and a bias of 0.20 m/s over a 59-days test period between the shadow camera and the shadow speed sensor. The shadow camera system observes an area in the south of the solar tower (see Figure 3.2). The measuring area has an edge length of 525 m. The geometrical size and temporal resolution of 15 s limits the shadow camera system to speeds up to 17.5 m/s. For speeds up to this limit, the shadow edge of an incoming cloud is detected in two subsequent images, even in the case of a cloud path orthogonal to the borders of the measuring area.

3.5 Shadow camera system for reference DNI maps

Both the ASI system and the shadow camera system are operated jointly at the PSA. The shadow camera system consists of six Mobotix M24 off-the-shelf surveillance cameras mounted on the top of an 87 m high solar tower (see Figure 3.2). More details of the used shadow camera system are given in section 2.1.2. The DNI maps of the shadow camera system are used in chapter 7, as actual DNI conditions acting on the solar field, but unknown by the solar field controller.

4 Individual 3-D object oriented cloud modeling and tracking

Two distinct and a hybrid cloud height and tracking approaches are developed within this thesis. The first approach utilizes four cameras and models the clouds via voxel carving (4Cam). The second approach is based on two cameras and a block correlation method (2Cam). Furthermore, a hybrid approach is developed which utilizes four cameras and combines the voxel carving and block correlation method (4CamH). An overview of the main characteristics of the three systems is given in Table 4.1.

Table 4.1: Main characteristics of the three ASI based nowcasting approaches

	4Cam	2Cam	4CamH
Number of ASIs used	4	2	4
Detection of cloud height and motion vector depends on cloud segmentation and modeling	yes	no	no
Voxel carving used for cloud modeling	yes	no	yes
Detection of cloud height and motion vector from 3-D voxel space	yes	no	no
Detection of cloud height and motion vector from differential images via a block correlation approach	no	yes	yes

These approaches have in common, that they treat each detected cloud as individual object with distinct attributes (geolocation, motion vector, transmittance, etc.), which enables these systems to describe complex multi-layer conditions.

The needed cloud modeling space, common to all investigated approaches, is described in section 4.1. Section 4.2 describes the distinct cloud modeling and tracking approaches. Validation results for the cloud height and tracking performance are presented in section 4.3 and 4.4. For the validation, the reference systems described in section 3.3 (cloud height) and 3.4 (cloud motion) are utilized. Section 4.5 describes the implemented nowcasting approach by displacing the cloud models according to the motion vectors within the modeling space. Finally, I conclude the findings of this chapter in section 4.6.

The content from this chapter has partially been published in **Nouri et al. 2018b** and **Nouri et al. 2019a**.

4.1 Modeling space

One of the main tasks of the cloud object oriented nowcasting approach is the accurate identification of the geometrical position of clouds in a reference coordinate system (X, Y and Z). This requires a transformation model that relates the image pixel coordinates (x' and y') to the reference coordinate system. Equation 4.1 describes the relationship between the reference coordinate system and the image pixel coordinates (**Luhmann 2003**).

$$\begin{bmatrix} X \\ Y \\ Z \end{bmatrix} = \begin{bmatrix} X_0 \\ Y_0 \\ Z_0 \end{bmatrix} + m \cdot R \cdot \begin{bmatrix} x' - x'_0 - dx' \\ y' - y'_0 - dy' \\ -c \end{bmatrix} \quad \text{Equation 4.1}$$

X_0 , Y_0 and Z_0 describe the location of the camera projection center in the reference coordinate system, c describes the camera constant x'_0 and y'_0 describe the image focal point and dx' and dy' the distortion parameters. The scaling factor m depends on the pixel coordinates and is unknown. Hence, only the spatial direction but not the absolute spatial position can be described for an object from a single image. The rotation matrix R is described in Equation 4.2.

$$R = \begin{bmatrix} r_{11} & r_{12} & r_{13} \\ r_{21} & r_{22} & r_{23} \\ r_{31} & r_{32} & r_{33} \end{bmatrix} = \begin{bmatrix} \cos\varphi\cos\kappa & -\cos\varphi\sin\kappa & \sin\varphi \\ \cos\omega\sin\kappa + \sin\omega\sin\varphi\cos\kappa & \cos\omega\cos\kappa - \sin\omega\sin\varphi\sin\kappa & -\sin\omega\cos\varphi \\ \sin\omega\sin\kappa - \cos\omega\sin\varphi\cos\kappa & \sin\omega\cos\kappa + \cos\omega\sin\varphi\sin\kappa & \cos\omega\cos\varphi \end{bmatrix} \quad \text{Equation 4.2}$$

With the three tilt angles ω (over X Axis), φ (over Y Axis) and κ (over Z Axis). The back projection from the reference coordinate system to the image pixel coordinates is done by the collinearity equations (see Equation 4.3) without the scaling factor m .

$$\begin{aligned} x' &= x'_0 - c \frac{r_{11}(X - X_0) + r_{21}(Y - Y_0) + r_{31}(Z - Z_0)}{r_{13}(X - X_0) + r_{23}(Y - Y_0) + r_{33}(Z - Z_0)} + dx' \\ y' &= y'_0 - c \frac{r_{12}(X - X_0) + r_{22}(Y - Y_0) + r_{32}(Z - Z_0)}{r_{13}(X - X_0) + r_{23}(Y - Y_0) + r_{33}(Z - Z_0)} + dy' \end{aligned} \quad \text{Equation 4.3}$$

Equation 4.1 and Equation 4.3 are described in total by 11 parameters, where x'_0 , y'_0 , c , dx' and dy' can be defined as inner parameters and X_0 , Y_0 , Z_0 , ω , φ and κ as outer parameters. The inner parameters are determined by a calibration method suitable for fisheye lens cameras introduced by **Scaramuzza et al. 2006**. Various images from a checkerboard pattern with known dimensions in different orientations and positions are taken. The image pixel describing corners of the pattern are extracted and the inner parameters are fitted by a least square minimization method. The GPS coordinates and altitude of the camera mounting position describe the outer parameters X_0 , Y_0 and Z_0 . The inevitable misalignment of the cameras between the optical axis and the zenith described by the parameters ω , φ and κ is determined by tracking the full moon in the camera images at nighttime. The three tilt angles are identified iteratively by minimizing the root mean square deviation between the detected moon positions and the expected moon position of an ideally mounted camera.

A virtual voxel space with a horizontal edge length >20 km, a height of 12 km and a resolution of 50 m is created with Equation 4.1. The space is created around a point of origin roughly in the center of the four cameras (see Figure 3.2). Each camera pixel can be described

as a vector through the voxel space. This space serves as a reference and modeling coordinate system for the cloud objects in all three approaches.

4.2 ASI based modelling of cloud geometry, height and velocity

4.2.1 Cloud modeling and tracking with voxel carving (4Cam)

Each camera pixel corresponds to an array of voxels, describing the line of sight from the camera lens to a voxel space border. Binary images created by the segmentation, identify the cloudy pixels. The 4Cam system takes the cloudy pixels and first marks all corresponding voxels as a cloud. Each of the segmented images would individually result in a voxel space with cone shaped clouds, starting from the cameras position. A more accurate cloud shape is achieved by voxel carving (**Kutulakos et al. 2000**), which creates the cross sections of the four generated voxel spaces (see Figure 4.1). From this point onwards the work of the author begins, which took over the voxel carving concept from **Oberländer et al. 2015**.

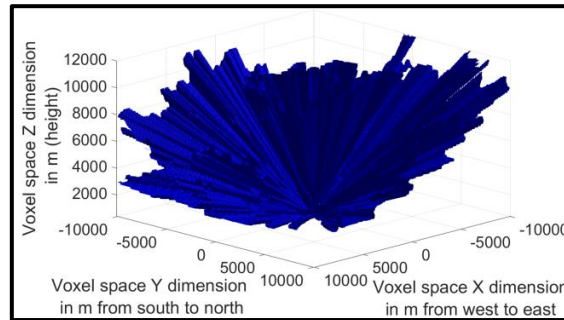


Figure 4.1: Single cloud model in voxel space

Cloud modeling with voxel carving

All cloudy voxels, connected with each other are aggregated and describe individual 3-D cloud models. Due to the size of the voxel space with an edge length >20 km (horizontal plane) and the positions of the ASI bundled around the voxel space origin (average distance ASIs to origin around 420 m), only minor deviations of the viewing angles exist between the cameras to most of the clouds. Thus, in many cases, the detected cloud models maintain their cone shape (see Figure 4.2 on the left). Subsequent cloud height detection and final modeling processing steps are needed.

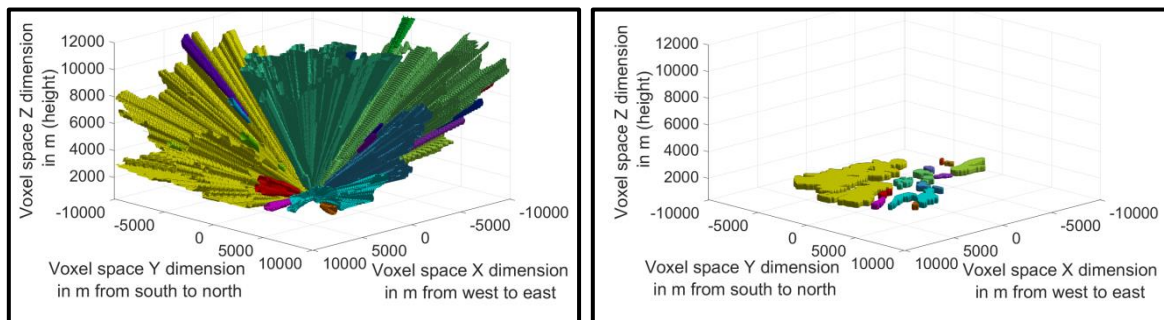


Figure 4.2: Cloud models in voxel space (each color represents an individual cloud models) (left) before height detection and final modeling (right) after height detection and final modeling

The cloud height determination is presented in Figure 4.3. The widest horizontal voxel layer approximates a position closely beneath the cloud center, for small cloud models positioned in the center of the field of view of several ASIs (Figure 4.3 (a)). For the remaining cloud models, the cloud height can be determined by the intersection of the field of views at the cloud model edges. The cloud edges are described by the corresponding minimum and maximum pixel elevation angle ($\alpha_{min/max}$) of a cloud cross section (see Figure 4.3 (b and c)). Each side of large cloud models, which is partially above the point of origin, is treated separately.

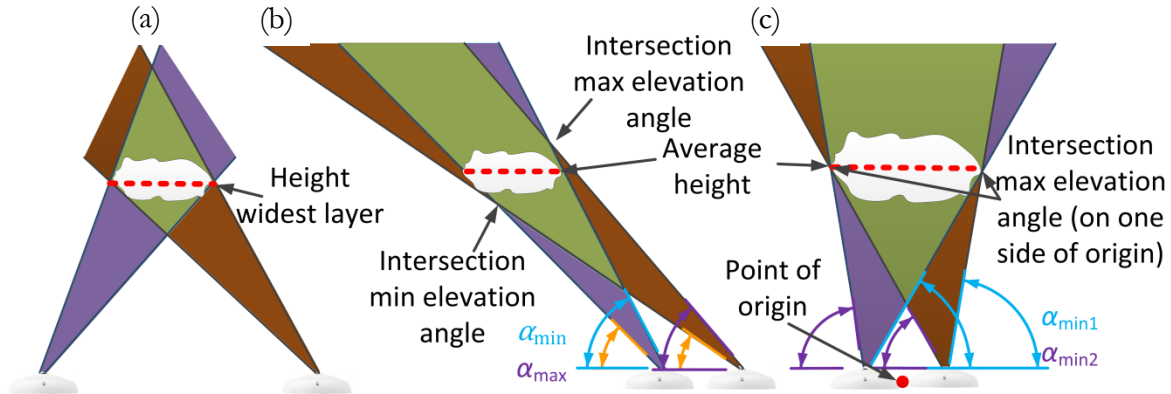


Figure 4.3: Three distinct cases for cloud height detection from the voxel space. (a) 2-D depiction of a small cloud inside the voxel space positioned between the cameras (widest voxel space layer corresponds to cloud height). (b) 2-D depiction of cloud inside the voxel space positioned at the outskirts of the field of view of several cameras (line of sight intersections of several cameras at the cloud edges correspond roughly to the cloud height). (c) 2-D depiction of large cloud inside the voxel space positioned at the center of the field of view of several cameras (intersection line of sight of several cameras at the cloud edges corresponds to cloud height)

Figure 4.4 illustrates a cloud object before the height is derived (yellow object). In order to create a cross section of this cloud object as depicted in Figure 4.3, the main direction of the cloud object has to be identified. For this purpose a 2-D projection of the cloud object in the x and y plane is created. The main direction can be described by a polynomial function of first degree between the point of origin and the average coordinates of the 2-D projection. A main plane, which cuts through the cloud object (Figure 4.4 plane in green), can be derived from the main direction. The voxels which are on the plane describe the desired cross section.

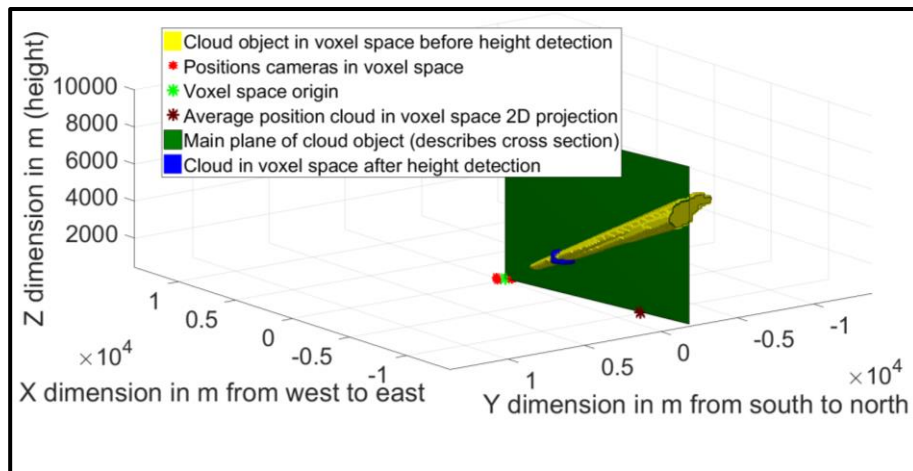


Figure 4.4: Voxel space with example cloud in yellow before height detection and in blue after height detection

The voxels which belong to the cross section can be reprojected in the four camera pixel coordinates. Thus, all corresponding camera pixel elevation and azimuth angles are known. Vector coordinates from the cameras to the cloud edges can be calculated by the functions:

$$x_{max/min} = r \cdot \sin(90 - \alpha_{max/min}) \cdot \cos(\varphi) \quad \text{Equation 4.4}$$

$$y_{max/min} = r \cdot \sin(90 - \alpha_{max/min}) \cdot \sin(\varphi) \quad \text{Equation 4.5}$$

$$z_{max/min} = r \cdot \cos(90 - \alpha_{max/min}) \quad \text{Equation 4.6}$$

with the maximum or minimum camera pixel elevation angle $\alpha_{max/min}$, the corresponding camera pixel azimuth angle φ and the radius r , which describes the distance between the camera and the vector coordinates. Radius r is increased until the intersection points between the lines of sights of the four cameras to the cloud edges are detected. With four cameras, a total of six intersection points for each cloud edge exist. The actual cloud height is calculated as the average z coordinate of all intersection points for both cloud cross section edges.

Increased uncertainties arise from clouds that are located partially or completely outside the voxel space and/or due to segmentation uncertainties. The relative standard deviation (*RSD*) between the twelve distinct cloud height values (six per cloud edge) will rise in cases with increased uncertainties. Average cloud height information with a low *RSD* ($RSD \leq 5\%$) are considered as trustworthy and saved into a short-lived database (only data from the same day). Cloud height information from modeled clouds with an *RSD* above a certain threshold value ($RSD \geq 12.5\%$) are rejected. These modeled clouds receive cloud height information from the database preprocessed by a Kalman filter (**Kalman 1960**). The *RSD* thresholds are defined based on the authors experience and first preliminary validation results. This approach will fail during fully overcast conditions. However, fully overcast conditions make cloud height information irrelevant for the creation of the DNI maps.

Some information about the cloud geometrical thickness is retrieved with multiple ASIs, but the accuracy of these readings depends strongly on the cloud position, size and height. Therefore, a simplified cloud thickness estimation is introduced. The cloud thickness is related to the cloud type (**Wang&Sassen 2001**). The occurrence of cloud types is connected to the cloud height (**Kahn et al. 2008**). Therefore, the geometrical cloud thickness is estimated as a function of the retrieved cloud center height, with a decreasing thickness while increasing cloud height. The cloud thickness estimations are chosen according to the global cloud thickness frequency distribution published by **Wang et al. 2000**. No vertical variability of the geometrical height inside a single cloud model is considered. It is clear that this estimation will struggle in the case of very thick clouds, such as nimbostratus or deep convective clouds. For such clouds, the size and distribution of the projected cloud shadows on the ground will be underestimated. However, these cloud types can be associated often with rainy overcast conditions (**Wang&Sassen 2001**), without significant shadow-free spaces on the ground. Especially, when considering the relatively small areas covered by the nowcasting system (edge lengths up to 8 km). Thus, in such conditions the irradiance nowcast quality is mainly affected by the determined cloud radiative effect and not by the determined cloud height or cloud motion. It should also be taken into account, that the cloud optical thickness of nimbostratus or deep convective clouds is above 23 (**Rossow & Schiffer 1999**), and therefore only low irradiance and no or little power generation is found in such cases.

Figure 4.2 (right) illustrates a complete voxel space with cloud objects after the height detection.

Cloud tracking

Horizontal 2-D projections of all 3-D clouds taken at the cloud center from the current image set are compared via a cross correlation algorithm to the 2-D projections of the cloud models from the previous image set (see Figure 4.5). Cloud projections with the highest correlation coefficient are allocated to each other. Matches are rejected due to significant deviations in cloud heights or unrealistically high cloud speeds. Cloud objects without a suitable allocation obtain their velocity from a look up table as explained later.

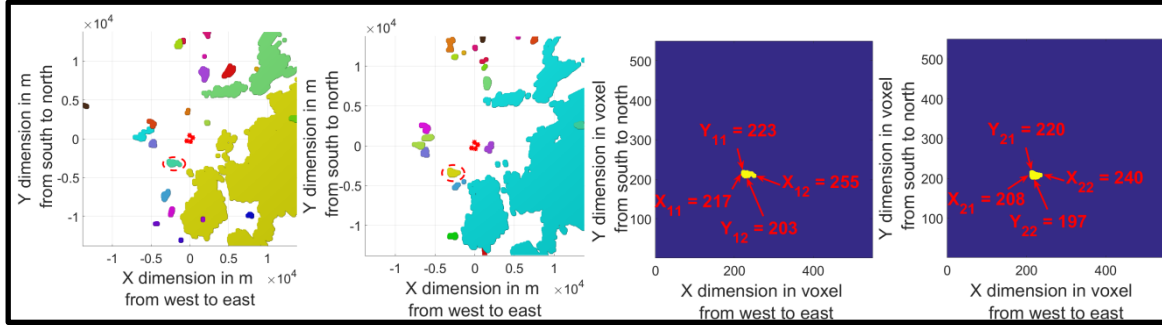


Figure 4.5: (a) Voxel space top view with cloud objects from previous image series (example cloud object marked), (b) Voxel space top view with cloud objects from current image series (example cloud object marked), (c) 2-D cross section of example cloud from previous image series with marked edges in both horizontal axes (X and Y), (d) 2-D cross section of example from current image series with marked edges in both horizontal axes (X and Y)

Motion vectors are calculated for clouds with historical information from previous images. Spatial displacements are detected by comparing the position of the 2-D cloud projection edges in both horizontal axes. Cloud segmentation errors and thus cloud 3-D modeling errors as well as cloud height detection errors increase towards the horizon. Small pixel errors can have a big impact depending on the actual height of the cloud. This complicates the cloud matching and subsequent determination of the motion vector for such clouds. Therefore, only clouds which are positioned in the inner part of the voxel space (zenith angle 35°) are considered for the determination of motion vectors (see Figure 4.6 (left)). Figure 4.6 (right) illustrates an ASI image with some exemplary highlighted clouds, which are positioned inside or outside the inner voxel space. All valid motion vectors are saved together with the corresponding cloud height into a database. Motion vectors for all cloud models without valid motion vectors are calculated from the database via a Kalman filter (**Kalman 1960**), considering only the database entries from clouds of the same day and height range.

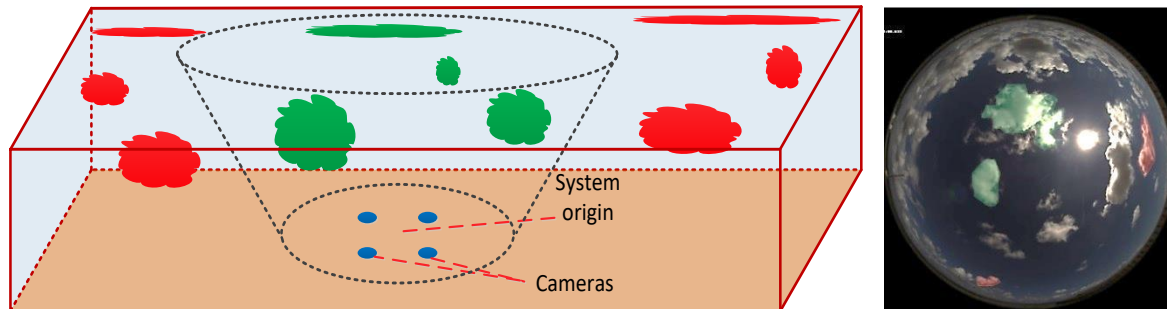


Figure 4.6: (left) Illustration of inner (dotted green line) and outer (continuous red line) voxel space. Only clouds of the inner voxel space (green clouds) are used for the determination of the motion vectors. Red clouds with higher segmentation and modeling errors get motion vectors allocated. (right) ASI sky image with exemplary clouds marked green for the inner voxel space and red for the outer voxel space

4.2.2 Two camera block correlation method (2Cam)

The accuracy of voxel carving based systems depends on the complex cloud segmentation for the cloud height detection. The tracking algorithm compares 2-D cross sections of the virtual cloud models via cross correlation. Thus, segmentation and cloud height errors have a direct impact on the tracking errors. Therefore, a cloud height detection and cloud tracking approach, which is completely independent of the previous processing steps, could improve the systems overall accuracy.

Wang G. et al. 2016 used a cloud height (h) detection method via a known cloud speed in m/s ($v_{m/s}$) measured by a phototransistor based cloud shadow speed sensor (**Fung et al. 2013**) and the angular cloud speed in pixel/s ($v_{pixel/s}$) obtained by an ASI. The cloud height is derived according to **Equation 4.7** with the maximum zenith angle θ described by N pixel (see Figure 4.7).

$$h = \frac{v_{m/s} \cdot N}{v_{pixel/s} \cdot 2 \cdot \tan(\theta)} \quad \text{Equation 4.7}$$

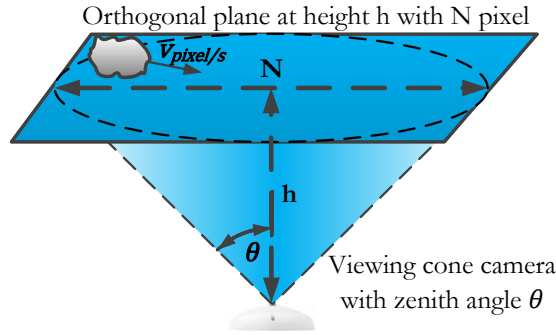


Figure 4.7: Visualization angular velocity $v_{pixel/s}$ in orthogonal plane with the maximum zenith angle θ described by N pixel at height h .

Kuhn et al. 2018 adapted this method by obtaining the velocities via two ASIs. Two subsequent orthogonal difference images are calculated from a singular ASI and converted into one binary difference image. The angular cloud speed is identified by matching subsequent binary difference images from the same ASI via a normalized 2-D cross correlation. A second ASI is needed to obtain cloud speeds in m/s. Orthogonal difference images from both ASIs are matched. Since the distance between the ASIs is known, the spatial extension per pixel can be calculated. Thus, angular speeds can be linked to absolute speeds. The method presented by **Kuhn et al. 2018** provides a cloud height and motion information completely independent from previous processing steps but it is limited to one single cloud layer at any given time derived from camera pixels located close to the Sun. In this thesis, I developed a cloud height detection approach (2Cam), based on the **Wang G. et al. 2016** concept, providing individual cloud heights and motion vectors for each pixel of the camera image.

Figure 4.8 explains the 2Cam cloud height determination and tracking approach. Both height detection and tracking are based on the same three-step strategy. Where the height determination uses two subsequent images of two distinct ASIs, the tracking uses three subsequent images of the same ASI without the third step marked in the figure. The goal of this approach is to create orthogonal height and motion maps for the cameras. Orthogonal images are created according to **Luhmann 2003**. The matching process illustrated in step 2 of Figure 4.8 is done by a block matching cross correlation algorithm. For both applications the block discretization is defined by the detected average cloud height from the previous time stamps. Higher clouds result in smaller pixel displacement at the same cloud speed. Thus, the

matching of motion via cross correlation gets more error prone with higher clouds. Larger blocks and consequently larger search areas address this challenge but reduce the height resolution and the capabilities of identifying distinct cloud layers.

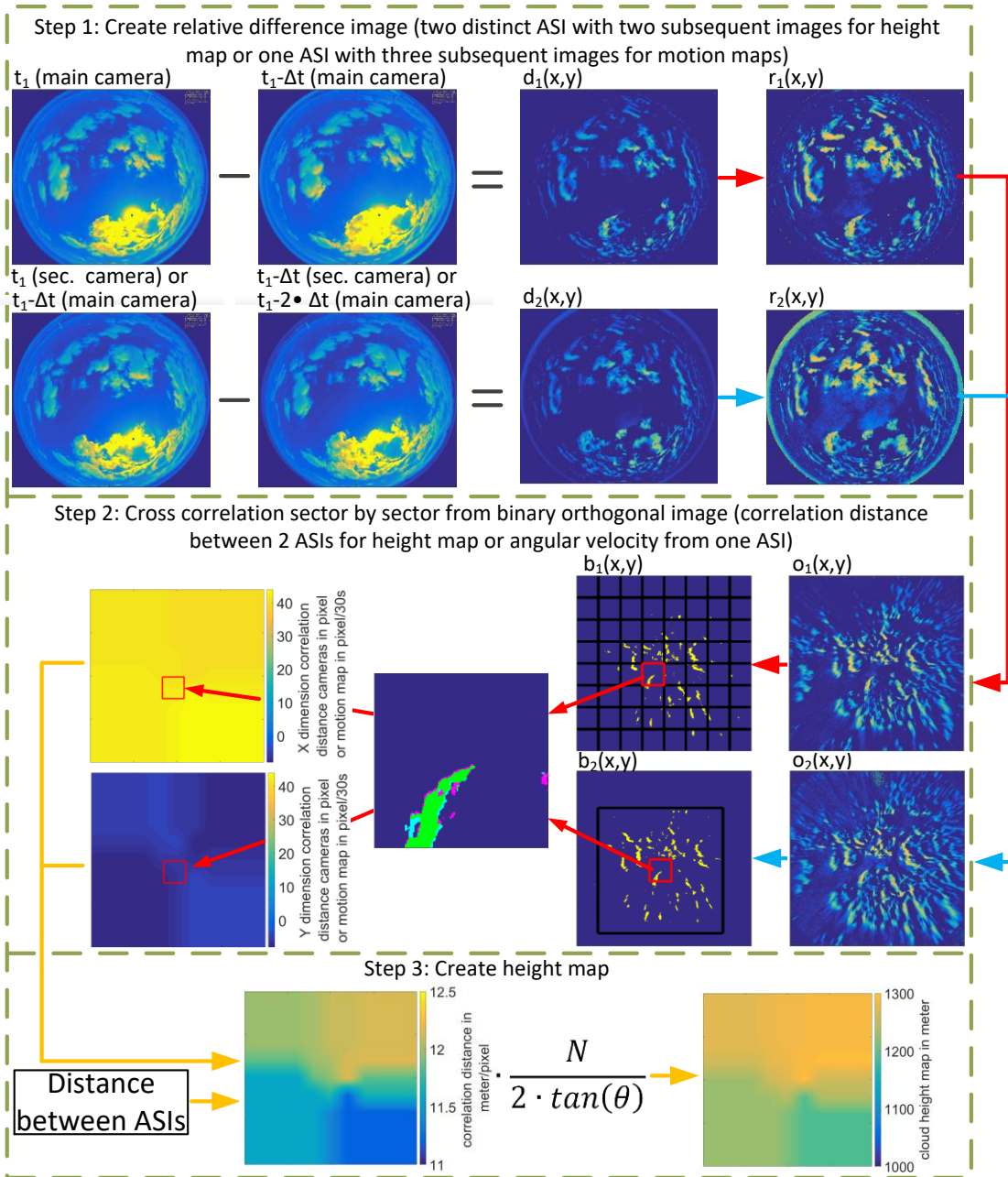


Figure 4.8: Creating motion maps (step 1 and step 2 with one ASI and three subsequent images) or create height map (step 1, step 2 and step 3 with two ASIs and two subsequent images). Step 1: Calculating difference images from the red channel of subsequent images ($d_i(x,y)$) and convert difference images into relative difference images ($r_i(x,y)$). Step 2: Create orthogonal relative difference images ($o_i(x,y)$). The orthogonal images are converted by variable thresholds into binary images ($b_i(x,y)$). Motion maps in pixel/30 s (one ASI with three subsequent images) or correlation distance maps in pixel (two ASI with two subsequent images) for both horizontal dimensions are created via cross correlation (block by block). Step 3: Under consideration of the distance between the ASIs and the correlation distance maps, the edge length in meter is known for each pixel. Finally, the cloud height map can be calculated with some geometrical informations of the orthogonal images (maximum zenith angle θ and the diameter N defined by θ in pixel).

Cloud heights are derived as long as motion is detected in the sky, which enables cloud height detections during overcast conditions. One minute average values are created for the height and motion maps. The determined cloud height corresponds to an average cloud center height and not to the CBH. The approach described in section 4.2.1 is used again to define the expected geometrical cloud thickness.

Segmentation results are not needed to derive height and motion information, but required for the creation of 3d clouds. For this purpose, the cloud height map is overlaid with an orthogonal segmented image (see Figure 4.9). Thus, the cloud height for each pixel identified as cloudy and its estimated geometrical thickness are derived. The transfer of the cloud information from the orthogonal image to the 3-D voxel space is done layer by layer. The resulting edge length in meter (*ELM*) from the corresponding pixels of the orthogonal image is calculated according to Equation 4.8.

$$ELM = \frac{\tan(\theta) \cdot h \cdot 2}{N} \quad \text{Equation 4.8}$$

The known position of the camera inside the voxel space and the pixel *ELM*, enables to match each cloudy pixel to a single voxel of the corresponding voxel space layer. The geometrical thickness of the cloud is taken into account, by marking the corresponding voxels from layers above and below. Cloud model shape and size errors induced by uncertainties of the cloud segmentation are reduced by utilizing the segmentation results of the secondary camera. A voxel remains marked as cloud, only if the corresponding pixel from the secondary camera is segmented as cloud. For high clouds, it is possible that the *ELM* surpasses the spatial resolution of the voxel space, which in turn results in a skipped voxel in both horizontal dimensions during the matching process. These systematic gaps have to be identified and filled (see Figure 4.10). Finally, each voxel marked as cloud gets a motion vector from the orthogonal motion map.

Individual 3-D cloud models are identified by grouping all connected cloudy voxels. An average motion vector is calculated from the velocities allocated to each voxel within a single 3-D cloud model. These average motion vectors and the corresponding average cloud height are saved into a database with an expiration date (12 hours). The motion vectors of the database are processed with a Kalman filter (**Kalman 1960**), treating datasets from different height layers separately. The Kalman filter weights more recent measurements stronger, and thus reacts fast when the conditions change. Older measurements only have a notable effect after longer clear sky periods. The filtered motion vectors are allocated to the 3-D cloud models according to the average cloud height.

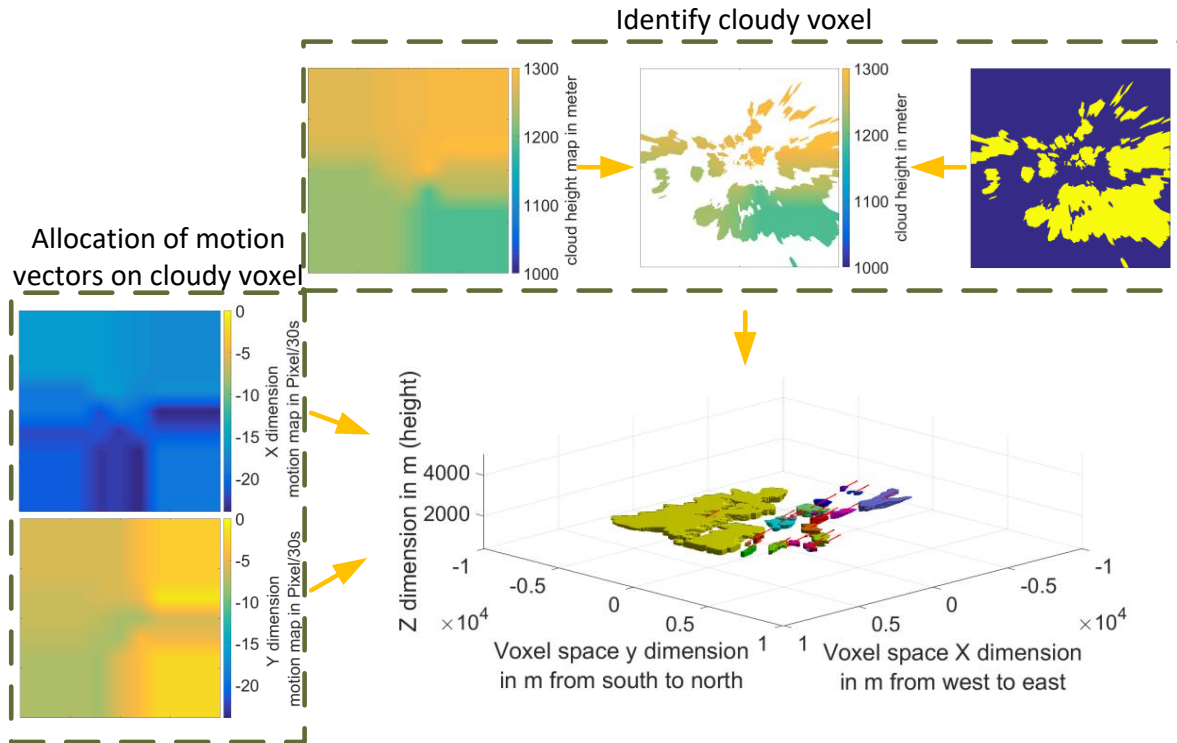


Figure 4.9: Cloud height and cloud velocity allocation for 2Cam system. Upper box: Height map overlaid with binary segmentation image. Lower right graph: Coordinate transformation from 2-D orthogonal image with height information to 3-D voxel space (each color represents an individual cloud model). Left box: Allocate cloud velocity from 2-D orthogonal motion maps to cloudy voxels. Cloud motion is shown in the lower right graph with red arrows.

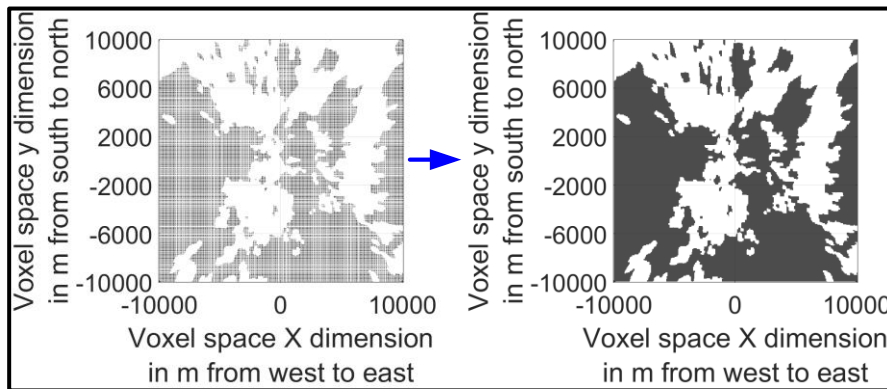


Figure 4.10: Fill gaps of voxel space in case of high clouds with ELM larger than the voxel space resolution

4.2.3 Four camera block correlation method (4CamH)

The 4CamH system is a hybridized approach, which uses the 4Cam voxel carving cloud modeling combined with the height detection and tracking approach of the 2Cam system. The cloud modeling process follows the 4Cam system as presented in section 4.2.1, up to the point before the cloud height detection and final shape correction of the cone like models. The cloud height detection and final shape correction is done differently with a height map from several camera pairs corresponding to the 2Cam approach (see 4.2.2).

Four cameras allow six distinct ASI pairs. Due to the limitations of processing time for real-time nowcasting systems, the number of used pairs is reduced to four. In this work, the following pairs are used:

- ASI 1 → ASI 2
- ASI 2 → ASI 3
- ASI 3 → ASI 4
- ASI 4 → ASI 1

Each pair generates separate cloud height maps and motion maps using the processing steps described in section 4.2.2. The four sets of motion and height maps are inspected for any strong deviations from the average (>20%). The used threshold is based on the author’s experienced and first preliminary validation results. If necessary, individual maps are rejected and the remaining maps are averaged. Increasing the amount of used ASI pairs to five or six would increase the redundancy of the cloud height and motion information. However, it is unlikely that all four currently used ASIs pairs are rejected at the same time (never experienced by the author). Thus, no significant overall improvement in cloud height and motion arise due to a further increase of the amount of used ASI pairs (without adding additional ASIs).

To obtain the final cloud shape the 3-D coordinates of each possibly cloudy voxel in the viewing cones are compared with the 2-D coordinates of the orthogonal height map (see Figure 4.11). Voxels that match the height information of the height map remain marked as cloudy, other voxels are rejected. The following processing steps concerning the geometrical cloud thickness and allocation of cloud speed information are identical to the approach of the 2Cam system presented in section 4.2.2.

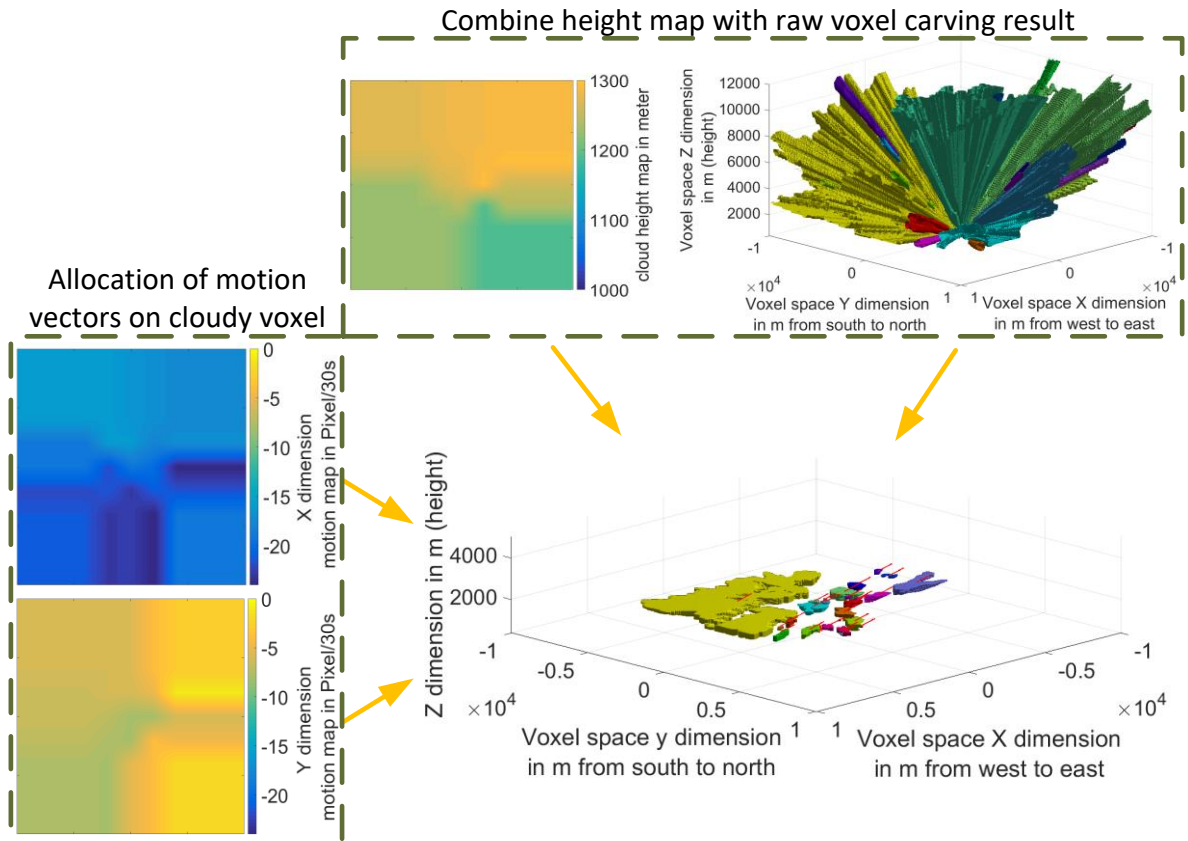


Figure 4.11: Cloud height and velocity allocation for 4CamH. Upper box: Shape correction of raw cloud viewing cones with cloud height map (each color represents an individual cloud model). Left box: Allocate speed vectors from 2-D orthogonal motion maps to cloudy voxel. Cloud motion is shown in the lower right plot with red arrows.

4.3 Cloud height validation with a reference ceilometer

Derived cloud height informations from the three ASI configurations are validated against a ceilometer. A 30 day period, distributed over the years 2015 and 2016, is used for the validation. The dataset is chosen in a way that a wide range of cloud heights, cloud motion patterns and atmospheric conditions are present.

Used error metrics include the MAD, relative MAD, RMSD and the relative RMSD. The relative error metrics are calculated from the absolute error metrics and the corresponding average reference value. For the cloud height validation, cloud models are considered if their center is within 1 km from the vertical line marked by the ceilometers field of view. Ten-minute cloud height medians are calculated of all valid cloud models and from the ceilometer cloud height measurements. Time stamps are only considered for the evaluation, if the ceilometer and all involved ASI systems provide measurements. The average cloud heights as measured by the ceilometer and the corresponding number of measurements for different cloud height ranges are given in Table 4.2.

Table 4.2: Average cloud height (h) and absolute number of measurements for reference ceilometer data

	0 m < h ≤ 3000 m	3000 m < h ≤ 6000 m	6000 m < h ≤ 9000 m	9000 m < h ≤ 12000 m	all
Average height	2001 m	3979 m	7676 m	10216 m	4089 m
Number of measurements	3752	3400	1308	566	9026

First, we have a closer look at three distinct days, one of them with simple single layer cumulus conditions and two with more complex multi-layer conditions including cumulus and cirrus clouds. Figure 4.12 illustrates the cloud height measurements for one day with predominant single layer clouds. On 19.9.2015 the ceilometer mainly measures cloud heights around 1600 m. Some clouds with a height around 2100 m appear after 16:00. The 2Cam and 4CamH systems show good alignment with the ceilometer measurements. A low relative MAD is reached for both new systems with 6.9% (2Cam) and 7.5% (4CamH) respectively. The 4Cam system shows larger fluctuations with strong outliers including deviations of various thousands of meters. The general trend of the cloud height is detected, but the relative MAD are significantly larger (16.0%).

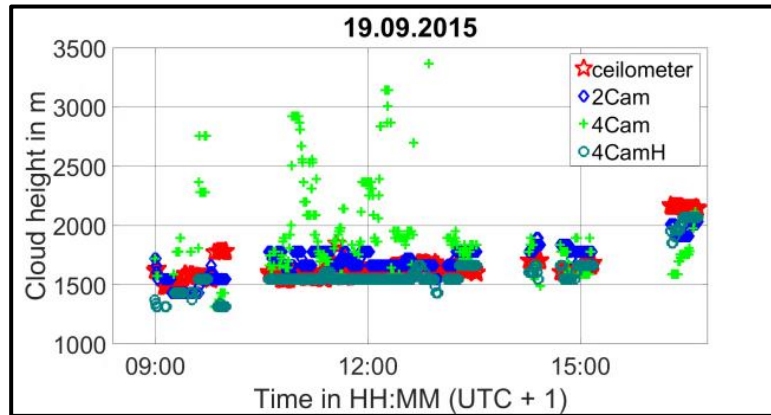


Figure 4.12: Measured cloud heights on 19.9.2015. Predominant single layer conditions are found around 1700 m.

Two days with more complex conditions are depicted in Figure 4.13. On 4.10.2015, two distinct layers are present. Often, the higher layer is blocked by the lower layer for the ceilometer as well as for the ASI systems. A short period from 10:23 to 10:30 with ceilometer

measurements around 9600 m is completely ignored by the ASI systems, which only detect the lower layer. However, during the period from 12:40 to 12:57 the 2Cam and 4CamH systems detect mainly a higher predominant layer where the ceilometer measures a few small scattered clouds at the lower layer. For this period, in particular, the 4Cam system shows a good match with the ceilometer data. In general, 2Cam and 4CamH show more stable and accurate cloud height detections and an overall good match with a relative MAD of 28.8% and 23.8% compared to 4Cam with a relative MAD of 41.2%.

On 18.10.2015 three distinct layers are visible in the data shown in Figure 4.13. The 2Cam and 4CamH systems follow the general trend of the ceilometer measurements. Higher deviations are present for the highest cloud layer, where the 2Cam and 4CamH systems often overestimate the cloud height. Especially 2Cam shows high deviations up to 3000 m, during the time period 15:23 to 15:47. 4Cam follows the general trend as well, but with higher fluctuations. The overall relative MAD for this day is around 25.7% (2Cam) and 21.6% (4CamH) and around 29.9% for 4Cam.

The larger deviations observed for 4.10.2015 and 18.10.2015 are caused by complex multi-layer cloud conditions. Often higher layers are (partially) occluded by a lower layer. During these multi-layer scenarios, with a large cloud coverage of the lower layer, small gaps in the lower layer coverage allow ceilometer height measurements of higher layers. However, due to visual obstructions, the ASI systems often see mainly the lower layer. Multiple layers can only be detected by the ASI systems at the same time, if larger gaps are present in the lower cloud layers providing an unobstructed view.

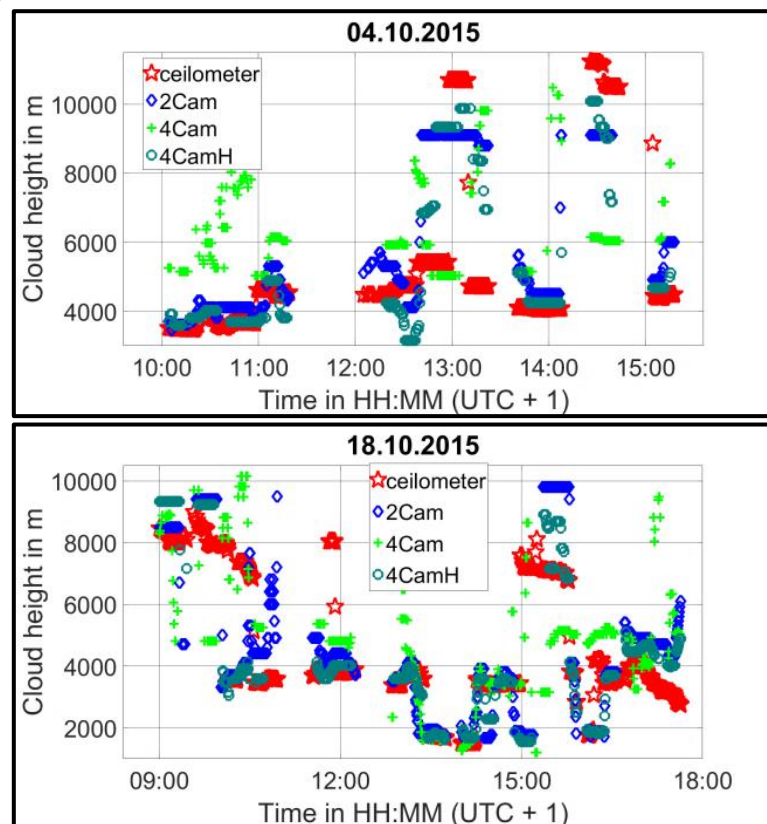


Figure 4.13: Measured cloud heights for all cloud modeling systems and reference ceilometer on 04.10.2015 and 18.10.2015. Both days show multiple cloud layers.

Figure 4.14 shows the histograms of the cloud heights obtained by the ceilometer and the three cloud modeling approaches for the complete 30-days data set. A strong mismatch can be

seen for the 4Cam system compared to the ceilometer reference in the cloud height range below 2000 m with a frequency of 9% (ASI 4Cam) compared to 25% (ceilometer). Further strong deviations are found in the range between 5000 m to 6000 m with a frequency of 22% (ASI 4Cam) compared to 4% (ceilometer). Above 6000 m the match of the distribution is acceptable. For the 2Cam system, an overall good match is achieved for cloud heights up to 9000 m. Almost no clouds are detected above 10000 m. This is related to a systematic weakness of the approach caused by the available image resolution and camera distance, which will be discussed in section 4.3.2. The overall best match is achieved by the 4CamH system. No cloud height range shows strong deviations compared to the reference distribution, with the exception of a lack of measurements above 11000 m. The systematic weaknesses of the 2Cam system are also present for the 4CamH system, but less pronounced (see section 4.3.2).

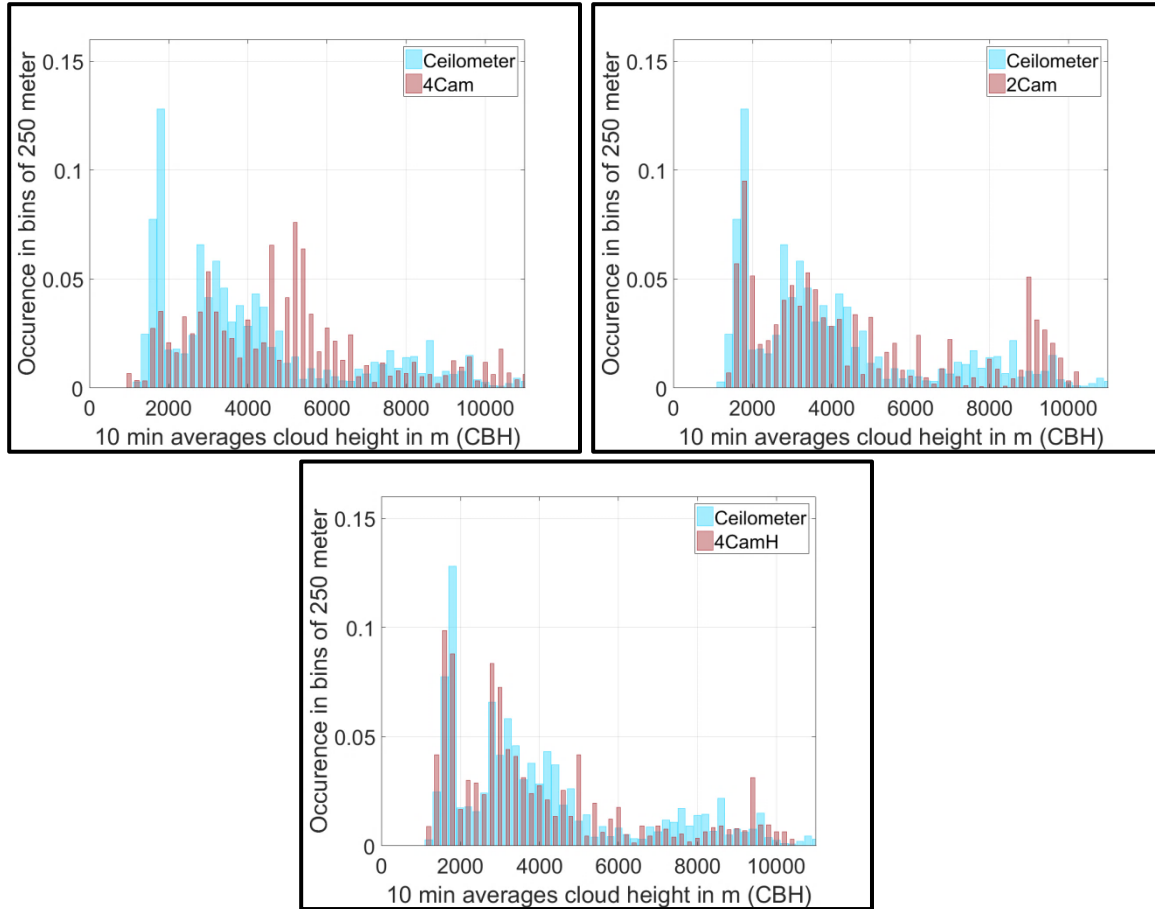


Figure 4.14: Histogram of the cloud heights obtained by the three cloud modeling approaches in comparison to the ceilometer measurements on 30-days

The comparison is also shown in scatter density plots (Figure 4.15). The reference ceilometer data are plotted on the abscissa and the ASI data on the ordinate. Each bin has a size of 250 m. The color coding represents the relative frequency for each pixel in a column of the scatter density plot. Accumulated relative frequencies of one column add up to 100%. The 4Cam system shows the largest dispersion and deviations, although up to around 5500 m the deviations are mostly below 500 m. A strong bias for higher clouds is seen in the range up to 5500 m. Dispersion and deviations further increase for higher cloud layers. A negative bias can be seen for cloud heights above 5500 m, where the ceilometer detects high clouds but the ASI system detects low clouds. The latter effect can be seen for all three systems. This is due to the previously discussed multi-layer conditions, with a strong cloud coverage of the lower layer,

which blocks the higher layers for most parts of the sky. 2Cam and 4CamH show a better matching accuracy than the 4Cam system, especially for the lower cloud heights. We can observe a positive offset for clouds higher than 4000 m. The offset increases with the cloud height. The effect is more pronounced for 2Cam and is due to the mentioned systematical issues which will be discussed in section 4.3.2.

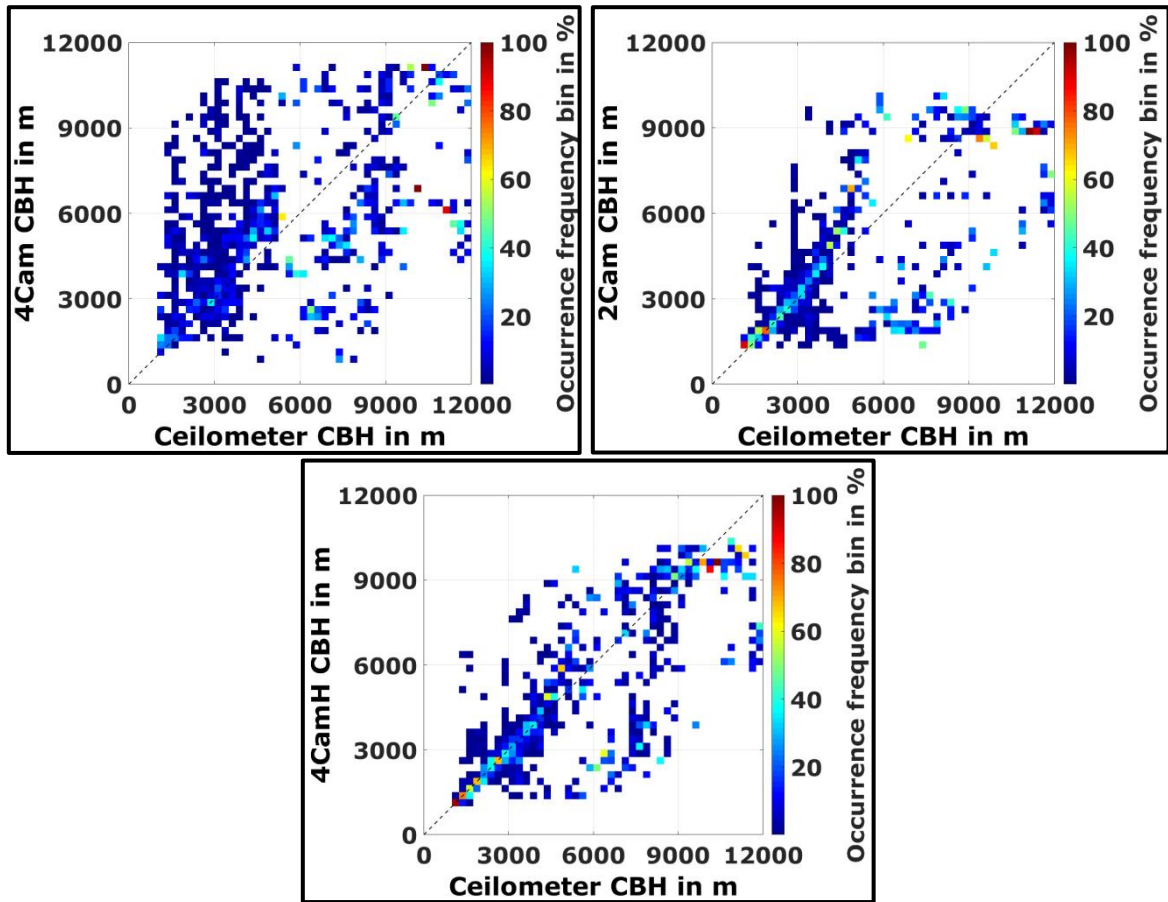


Figure 4.15: Scatter density plot of the cloud heights obtained by the three cloud modeling approaches in comparison to the ceilometer measurements on 30-days

Error metrics for distinct cloud height ranges are shown in Figure 4.16. As expected from the previous observation, the 4Cam system shows larger errors compared to 2Cam and 4CamH system. In the case of the 4Cam system, around 31% of all detected clouds received a substituted cloud height from a database, according to the procedure described in section 4.2. 4CamH has the lowest deviation of all systems. The relative MAD corresponding to the entire data set are 29% (2Cam), 17% (4CamH) and 46% (4Cam). One source for the observed deviation is that all ASI systems measure an average cloud height and derive the CBH with an estimated cloud thickness. The ceilometer on the other hand measures the CBH directly.

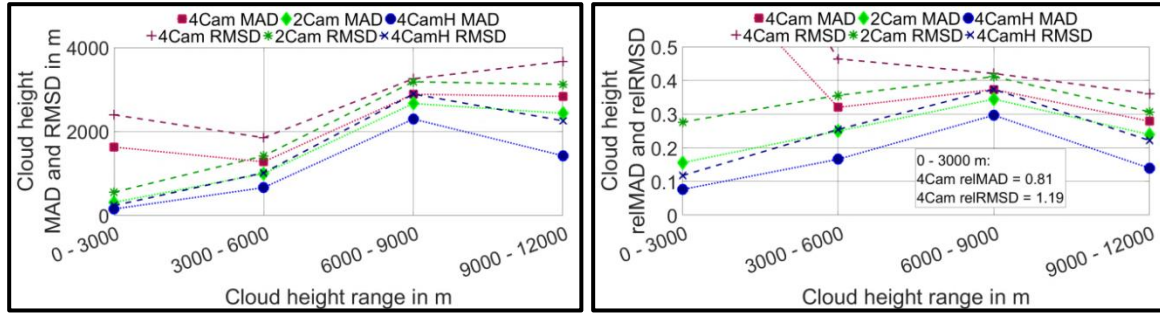


Figure 4.16: Resulting absolute (left) and relative (right) MAD and RMSD from the comparison of the ceilometer measurements discretized over cloud height ranges. The 4Cam relative MAD and RMSD for the lowest height range are given in the text field.

An intercomparison of the presented validation results and previous findings would be a very helpful exercise for the overall system assessment. A comparison between different systems is a complex task, as different systems are typically tested with different datasets from different sites. The accuracy of ASI systems depends heavily on the prevailing weather conditions. Single low layer cloud conditions with optical thick cumulus clouds represent conditions, where high accuracies are likely. High clouds pose a much tougher challenge, as we will see in section 4.3.1 and 4.3.2. This is an inherent problem of all stereoscopic approaches. High clouds are also more challenging for single ASI approaches, due to resolution constraints. Finally, complex but frequent multi-layer cloud conditions represent challenges that are even more difficult. Nevertheless, **Kuhn et al. 2018** compared cloud heights derived from a ASI system for a 59-day validation period, with an overall MAD of 872 m. In this work, the three cloud model oriented ASI systems are added to the comparison. Comparably good results are reached in the 30 day validation period with an overall MAD of 1145 m (2Cam) and 648 m (4CamH). The comparison must take into account that the procedure used by **Kuhn et al. 2018** is limited to a single cloud layer at any given time and rejects all times stamps surpassing a maximum cloud height threshold. This data filtering of high clouds obviously reduces the error metrics observed by **Kuhn et al. 2018**.

4.3.1 Understanding the deviations of the 4Cam approach

The 4Cam system identifies the cloud height of each detected cloud individually by detecting the intersection of the field of views at the cloud edges. The cloud edges are located by the corresponding minimum and maximum pixel elevation angle of a vertical cloud model cross section (see Figure 4.17). An error estimation for resulting cloud heights and position of the observed cloud edges is conducted. This study considers two cameras with a distance of 700 m to each other. Hypothetical clouds are considered, with varying cloud edge height and horizontal distance to the point of origin. The point of origin is located between the cameras. The resulting pixel elevation angles are calculated with the known relative position of the cloud edges to the cameras. In a next step, errors are added to the calculated angles (e.g. error of $+0.5^\circ$). The resulting position of the cloud edges can be calculated by the erroneous angles. Thus, the expected resulting cloud height and cloud edge position can be estimated. Real errors of the pixel elevation angle arise mainly due to not ideal ASI calibrations, ASI misalignments and segmentation errors.

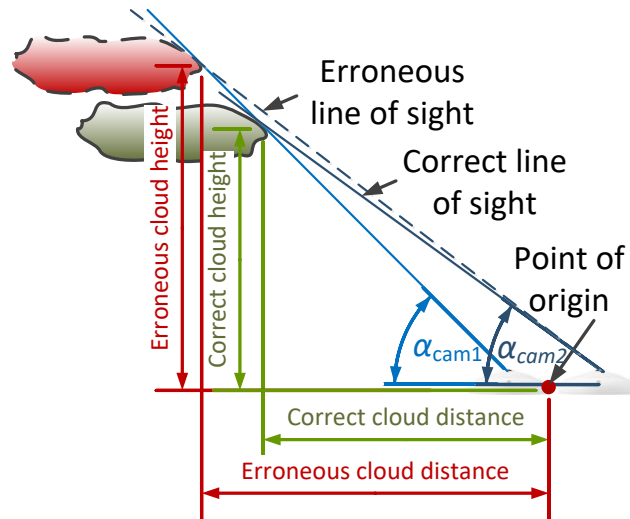


Figure 4.17: Correct and erroneous cloud edge position due to an pixel elevation angle error of $+0.5^\circ$ of cam2

Whether an erroneous lower (closer) or a higher (farther) cloud position is detected, depends on the direction of the angle error and the relative position of the corresponding camera to the second camera and the cloud. Thus, simultaneously occurring angle errors from multiple cameras can amplify or attenuate the effect.

Figure 4.18 illustrates the expected errors for cloud height (a) and cloud edge (b) positions and an erroneous pixel elevation angle of $+0.5^\circ$. 0.5° corresponds to around five pixels in the west-east or south-north axis of the image. The correct distance between the point of origin and the cloud edge is shown on the abscissa and the cloud height on the ordinate. The color bar describes the resulting error of the cloud edge in height and distance respectively. For example, the errors for a cloud with a height of 6000 m and a distance of 10000 m are $+1255$ m (height) and $+2165$ m (distance) as marked by the blue arrows. Expected errors increase for higher clouds or for clouds, which are farther away.

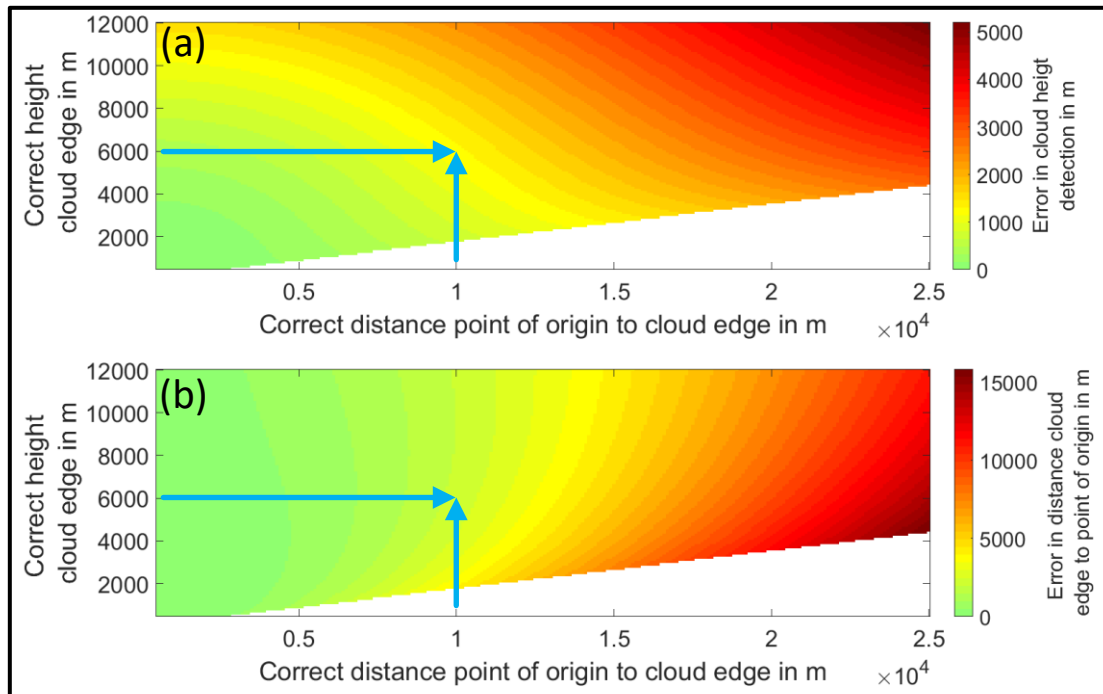


Figure 4.18: Expected errors of 4Cam in cloud height (a) and position (b) due to the erroneous pixel elevation angle of $+0.5^\circ$. Arrows mark the described example.

It has to be pointed out, that four cameras correspond to six distinct camera pairs and thus in six distinct cloud height measurements for the same cloud edge (see section 4.2). Averaging reduces the magnitude of the errors. Nevertheless, this analysis shows some weaknesses and physical limitations of the 4Cam system, especially for distant and high clouds.

4.3.2 Understanding the deviations of the 2Cam and 4CamH approach

As described in section 4.2.2 and 4.2.3, the 2Cam and 4CamH system use a cross correlation approach by matching difference images from two ASIs. The maximum resolvable height depends on the image resolution and the distance between the ASIs. A larger distance between the ASIs will allow measuring the height of higher clouds, but reduces the capability for low clouds. A cloud has to be present in the image intersection of both ASIs. For clouds at a height close to the geometrical limitations of an ASI setup (correlation distance of only a few pixels), the height resolution is defined by very large increments. Therefore, the absolute uncertainties increase for such clouds due to the limitations of the height resolution. This issue is even more pronounced if matching errors are taken into account.

As an example (see Figure 4.19), two setups of ASIs are assumed, one with a distance between the ASIs of 470 m and the second with 950 m. Both setups work with orthogonal images using a maximum zenith angle of 78° and are projected into an orthoimage of 1000×1000 pixels. Both setups observe the same cloud roughly at 10000 m above the ASIs. This corresponds to a correlation distance of 5 pixels for the first setup and 10 for the second setup. A single pixel error of -1 pixel implies a higher cloud for both setups. The first setup would detect a cloud at a height of roughly 12500 m and the second setup would detect a cloud at a height of roughly 11200 m. A pixel error of +1 pixel results at a height of 8300 m (setup 1) and 9200 m (setup 2). Figure 4.19 (a) and (b) show different pixel correlation distances for different ASI setups. The color bar of Figure 4.19 (a) describes the correct cloud height, whereas the color bar of Figure 4.19 (b) describes the expected cloud height error due to a matching error of -1 pixel. The expected errors are below 100 m for most cases. A strong increase of the expected errors can be seen for all scenarios with a matching distance below 10 pixels. These systematic errors can result in unrealistic heights (>15000 m), especially in the case of absolute matching errors larger than -1 pixel. This issue is also present for positive pixel errors, but less influential. The increment in height per pixel drops rapidly for larger correlation distances.

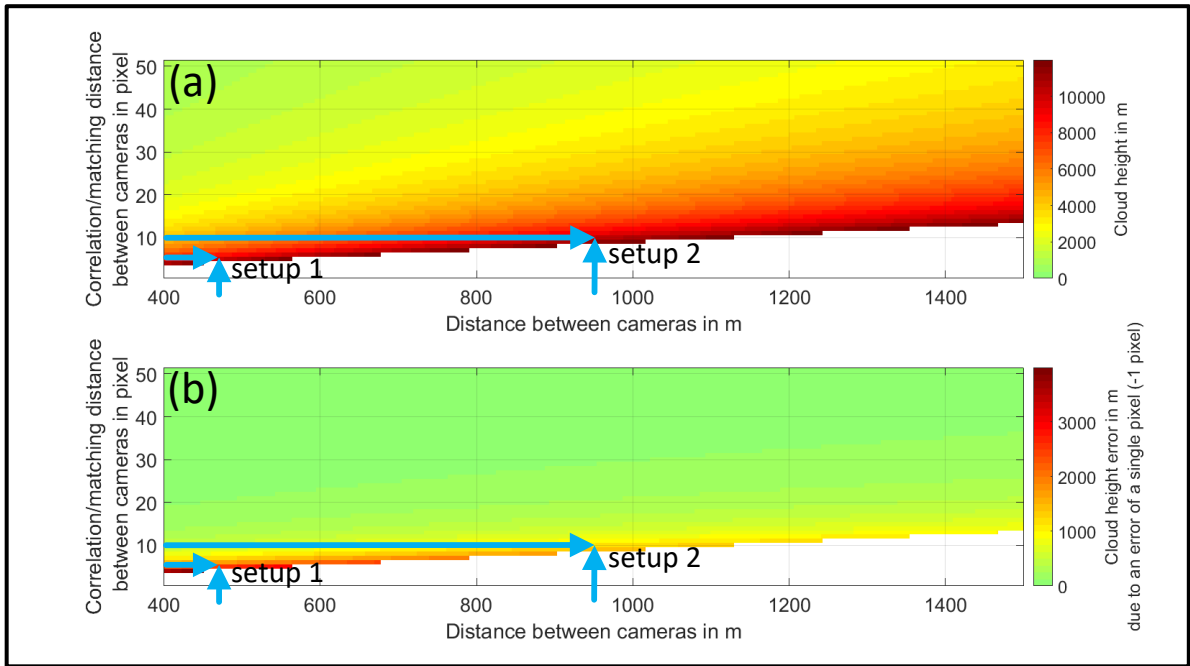


Figure 4.19: Expected errors in cloud height and position for 2Cam & 4CamH due to a matching error of -1 pixel for distinct ASI setups and corresponding matching results. Arrows mark the described example. a) Expected cloud height without errors (Cloud heights limited to 12000 m) b) Cloud height errors due to the matching errors

The 2Cam set up operated at the PSA, with a camera distance of roughly 500 m, is vulnerable to the described issue (see Figure 4.19). Cloud heights >12000 m are detected and substituted by an average cloud height from valid recent historical measurements (same day). If no valid historical cloud height information is available, the cloud height is substituted with a default value of 9000 m. This explains some of the deviations shown in Figure 4.14 and Figure 4.15 as well as the described gradually increasing offset seen in Figure 4.15.

Matching errors that lead to lower clouds are less pronounced and more difficult to detect, as realistic cloud heights are derived. This may partially explain the over-representation of lower ASI cloud heights for ceilometer readings above 6000 m (see Figure 4.15).

The 4CamH system is less prone to mismatches than 2Cam, as multiple camera pairs are used for the cloud height detection. Cloud heights >12000 m are rejected. Only in very rare cases show all used camera pairs simultaneously similar matching errors. In such cases, the described substitution process of the 2Cam system is applied.

4.4 Cloud motion vector validation with a reference shadow camera

In this section, cloud motion vectors derived from the three ASI configurations are benchmarked against a shadow camera system (see section 3.4) using 10-minute median values. Timestamps are considered, only if all involved systems provide a measurement.

The measured direction and speed of the reference system and all ASI systems is depicted in Figure 4.20. In general, all three ASI systems follow the direction as measured by the reference system. Similar results with an overall good match are reached for the cloud speed from the visual inspection in the case of 2Cam and 4CamH. 4Cam shows stronger fluctuations and some persistent deviations.

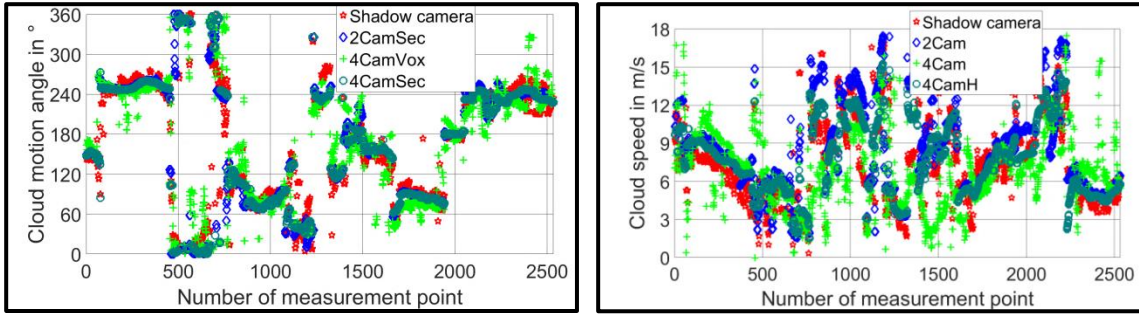
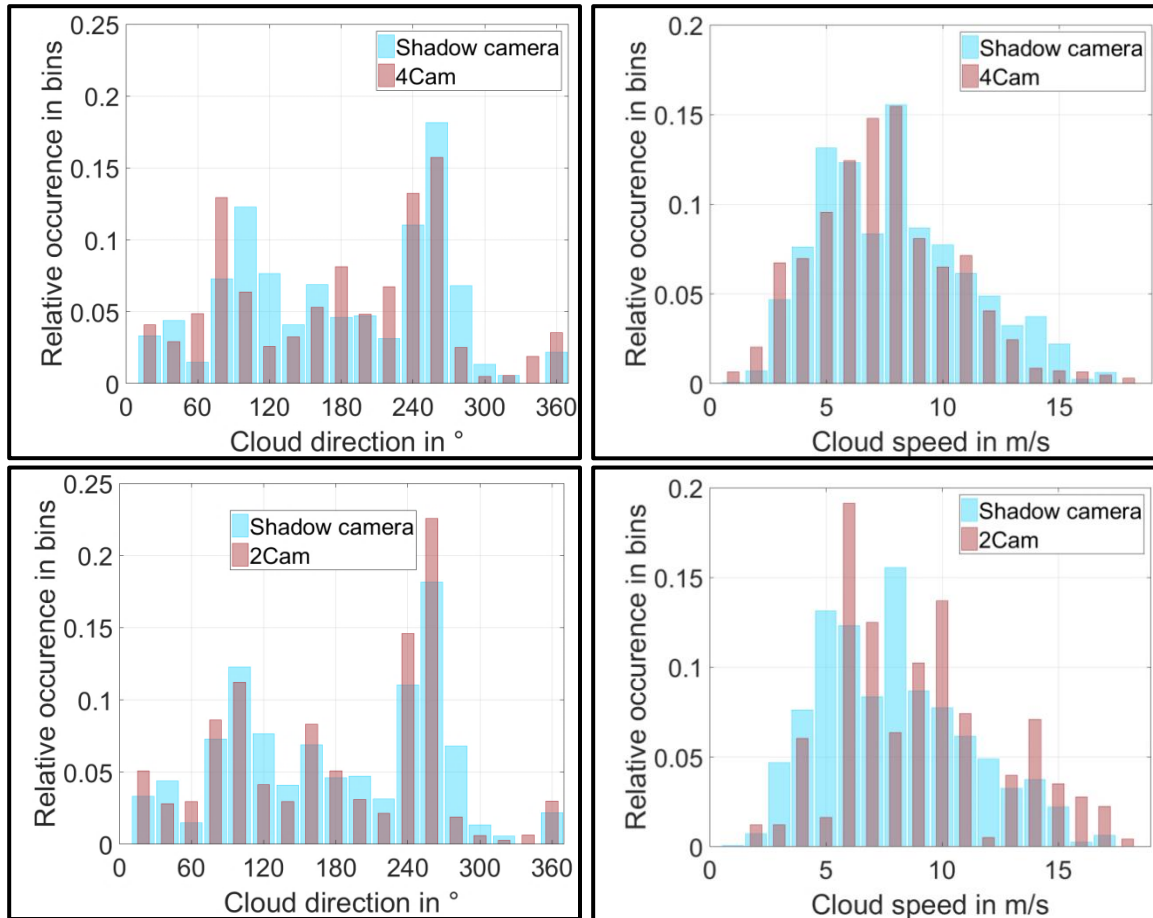


Figure 4.20: Motion direction (left) and speed (right) for the reference shadow cam and all three ASI systems over the entire data set.

The histograms illustrated in Figure 4.21, confirm the good agreement for the direction. The gap around 330° is related to the local main cloud directions at the site. Cloud movements roughly to the north are a considerable rare event above the PSA. Most clouds move in west-east direction. Interestingly, the 4Cam cloud speed distribution shows the best match with the reference system, despite the strong fluctuations (see Figure 4.20). However, this is only a statistical result, under consideration of the entire data set.

The 2Cam cloud speed distribution shows a lack of measurements in the 5 , 8 and 11 m/s bin, but this is compensated by an increased population within the neighboring bins. The 4CamH system shows an overall good agreement with the cloud speed distribution.



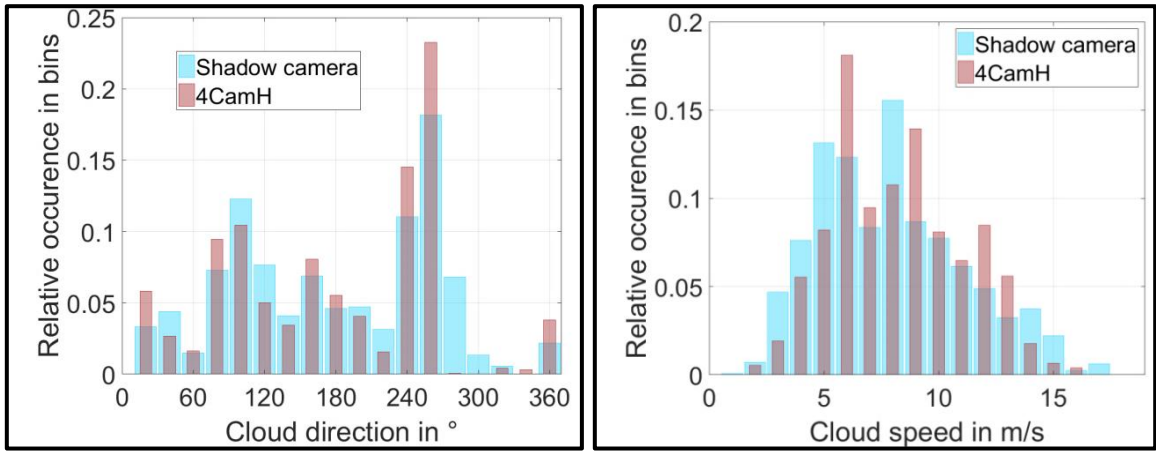
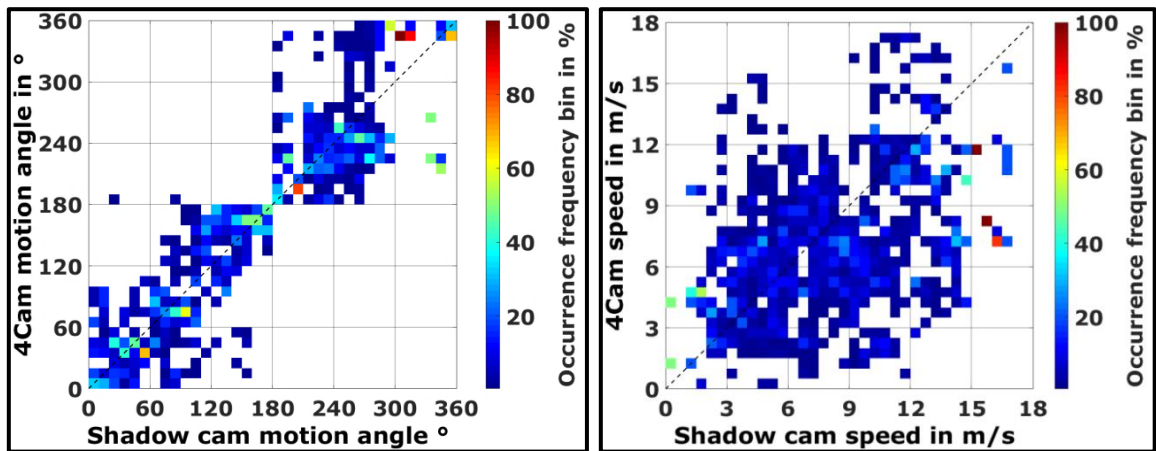


Figure 4.21: Histograms of reference and ASI systems; left: cloud motion direction (towards north: 0°, east: 90°, south: 180° and west: 270°) right: cloud speed.

Scatter density plots for the direction and speed are depicted in Figure 4.22. All frequencies in one reference bin (column) add up to 100%. As expected, the 4Cam system shows the strongest dispersion for the direction as well for the speed. Overall, the scatter density plot confirms the good agreement off all systems for the motion direction with an MAD of 22.7° (4Cam), 12.8° (2Cam) and 11.7° (4CamH) (see Table 4.3).

Despite the low deviations of the speed distribution, the scatter density plot shows a poor alignment for the 4Cam system with an overall MAD of 2.6 m/s. An improvement can be seen for the 2Cam and especially for the 4CamH system with MADs dropping to 1.8 m/s and 1.3 m/s respectively (see Table 4.3).

The 2Cam and 4CamH show a minor bias towards higher velocities that increases for higher values. This can be explained partially by difficulties in detecting altitudes of high clouds. As shown in section 4.3.2, small matching errors for high clouds have a strong impact on the detected cloud height. Clouds erroneously estimated to be too high indicate larger pixel edge lengths in m, which leads to higher cloud speeds.



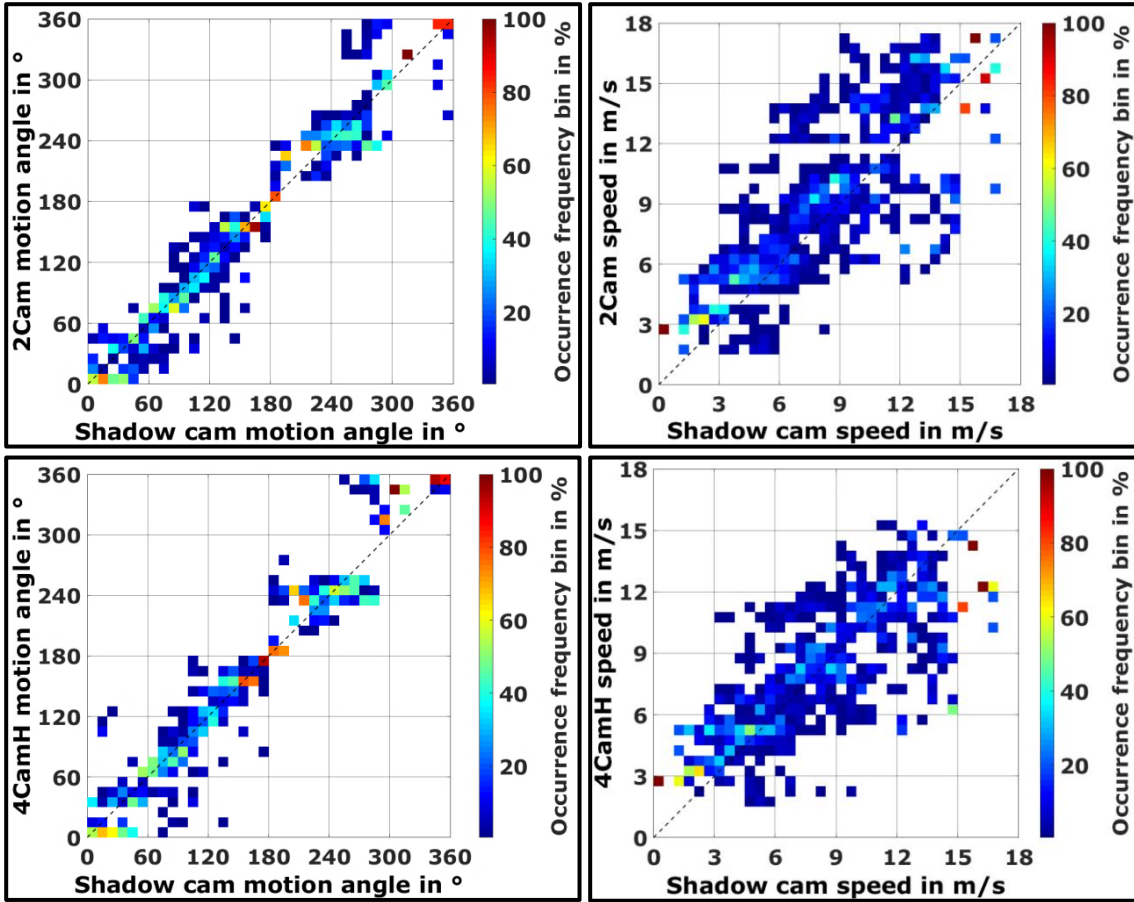


Figure 4.22: Scatter density plots of reference and ASI systems; On the left direction (towards north: 0°, east: 90°, south: 180° and west: 270°) and on the right speed

Table 4.3: Resulting MAD and RMSD from the comparison of the ASI systems to the shadow camera system over the entire range (v : cloud speed and β : cloud motion angle)

	4Cam		2Cam		4CamH	
MAD ($v \leq 18\text{m/s}$)	2.6 m/s	34%	1.8 m/s	23%	1.3 m/s	18%
MAD ($\beta \leq 360^\circ$)	22.7 °	-	12.8 °	-	11.7 °	-
RMSD ($v \leq 18\text{m/s}$)	3.3 m/s	43%	2.3 m/s	30%	1.7 m/s	23%
RMSD ($\beta \leq 360^\circ$)	29.2 °	-	17.4 °	-	16.2 °	-

MAD and RMSD over different cloud speed ranges are depicted in Figure 4.23. An absolute increase of the errors can be seen for higher velocities. 4CamH is the most accurate system in all cloud speed ranges, followed by 2Cam and finally 4Cam.

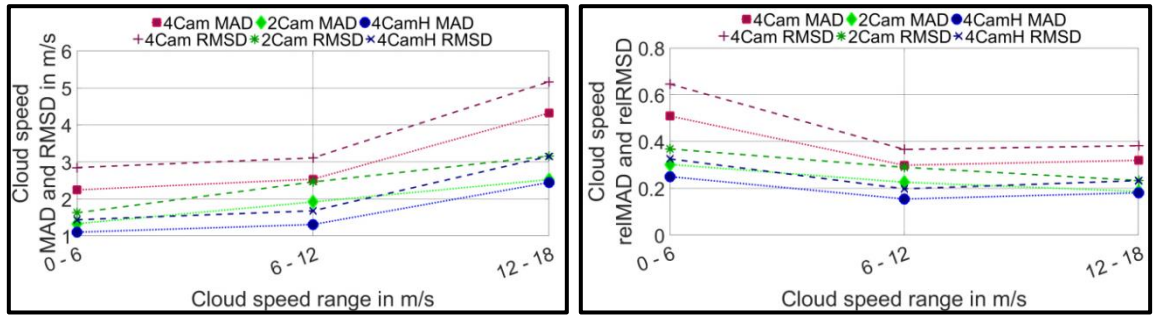


Figure 4.23: MAD and RMSD in comparison to the shadow camera system discretized over cloud speed ranges

One reason for the increased deviations of the 4Cam system, is the direct interaction with the height detection. As presented in section 4.3 the deviations for the height are the largest for the 4Cam system. Cloud height errors result in significant errors of the size and shape of modeled clouds, which increases the possibilities of mismatches (see section 4.2).

For 2Cam and 4CamH, orthogonal images of 1000x1000 pixels and zenith angles up to 78° are used. This leads to resolution constraints. In the case of a hypothetical cloud at 12000 m, the pixel edge length corresponds to roughly 113 m/pixel. Thus, small matching errors for high clouds lead to large motion deviation, which partially explains the increased deviations for high velocities.

Similar to the cloud height validation, a direct intercomparison of the presented motion vector validation results compared to previous findings would be helpful for the overall system assessment. However, due to a lack of a consistent validation procedure, is this an extremely challenging task. Most motion vector validation are done indirectly by comparing the achieved nowcast score (**Quesada-Ruiz et al. 2014 and Peng et al. 2015**) or by comparing the previously nowcasted cloud cover with the corresponding real cloud cover (**Huang et al. 2012, Chow et al. 2015 and Zaher et al. 2017**). Others estimate motion vector uncertainties (**Crispel et al. 2017 and Schmidt et al. 2016**). These mentioned results cannot be compared directly with the results presented here. The advantage of the used validation procedure is the direct validation of the motion vectors, with the reference shadow camera system. Indirect validations of the cloud motion by the nowcast score or cloud cover have the disadvantage that other uncertainty contributors are involved. A clear discretization of all involved uncertainty contributors is a difficult task.

4.5 Nowcast future cloud object positions and cloud shadow projection

For the nowcast, the derived 3D clouds are displaced individually in the modeling space according to the allocated motion vector. Predictions for the cloud positions are made for lead times up to 15 minutes ahead. However, the possible nowcast horizon of new cloud position is limited by some physical boundaries. The presented cloud tracking and modeling approaches evaluates areas of the camera images with elevation angles down to 12° . Due to the strong distortion of the fisheye lens images close to the image horizon, an accurate evaluation in areas with an elevation angles below 12° is not feasible. The effective maximum vision range for different relative cloud heights (from viewer perspective) and an elevation angle of 12° can be calculated easily with some trigonometry. Figure 4.24 illustrates the effective vision range for clouds with a relative height from 0.5 km (2.35 km vision range) to 12 km (56.46 km vision range).

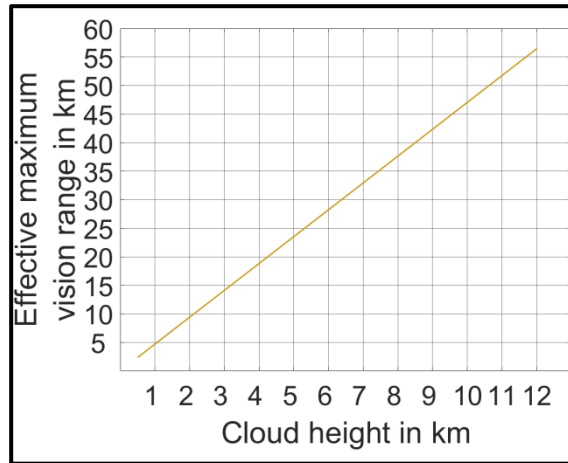


Figure 4.24: Effective maximum vision range with an elevation angle of 12° and relative cloud heights from 0.5 km to 12 km from the viewers perspective.

The theoretically possible nowcast horizon for new cloud positions depends on the cloud trajectory and cloud speed. Trajectories which lead the clouds directly over the camera zenith allow the longest nowcast horizon. Nevertheless, also in the case of a cloud trajectory directly over the camera, exist conditions where a 15 minute nowcast of future cloud positions is physically not possible. Figure 4.25 illustrates the effective possible nowcast horizon with a minimum elevation angle of 12° for clouds with a height up to 12 km and a speed up to 55 m/s. This is a simplification, as many clouds don't have a trajectory directly above the camera. In such cases the effective nowcast horizon will be smaller. The use of several cameras has also a negative effect on the nowcast horizon, as for the investigated approaches the same clouds have to be detected by several cameras. Yet, the influence of this effect is comparatively small, since the cameras are located close to each other.

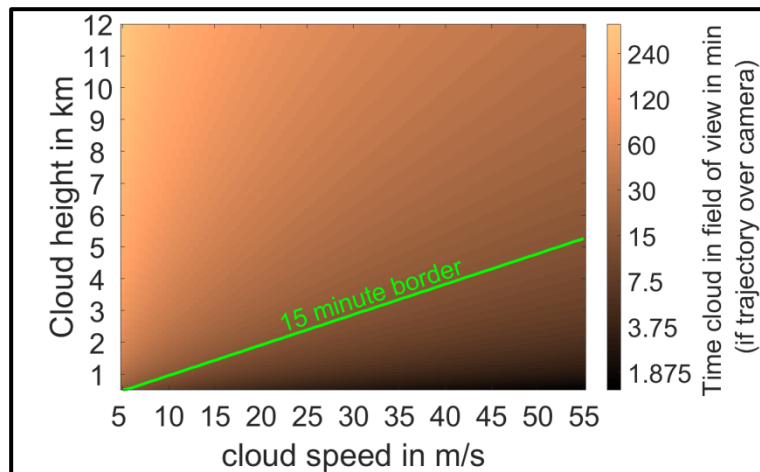


Figure 4.25: Effective time during which a cloud with a trajectory directly above the camera is within the field of view of the camera (with a min elevation angle of 12°). All conditions with an effective nowcast horizon below 15 minutes are below the green line.

Also the size of the used modeling space has an influence on the theoretically possible nowcast horizon for future cloud positions. Clouds outside the boundaries of the modeling space are not considered. For the required real-time operation of the nowcasting system, the computing time of the entire nowcasting process cannot exceed the time interval between two images of 30 s. This limits currently the modeling space to around 36 million voxels, which in turn allows an edge length of ± 20 km (from point of origin) and a height of 12 km with an

reasonable resolution (below 100 m). Depending on the height of the cloud and the elevation angle (from the center of the modeling space), clouds may already be outside the boundaries. Figure 4.26 illustrates the distance of clouds to the center of the modeling space for cloud heights up to 12 km and an elevation angle between 12° to 90° (perspective from the modeling space center). At a viewing angle of 12° clouds with a height of 4250 m are outside the 20 km boundary. For viewing angles above 30° are all clouds with a height of up to 12 km within the 20 km boundaries.

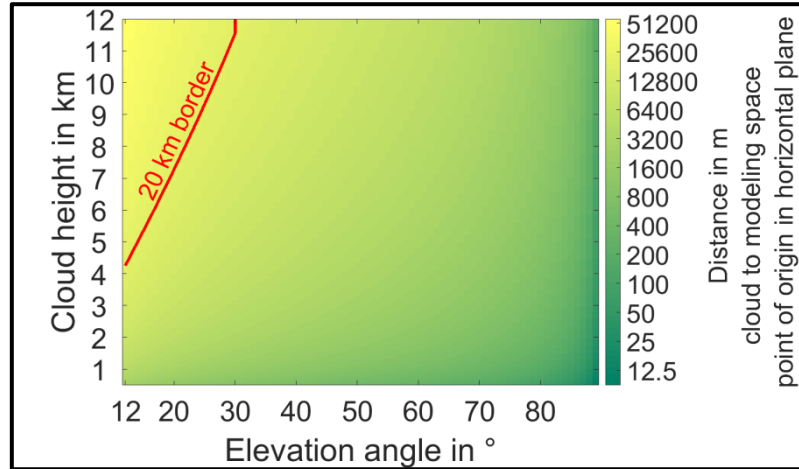


Figure 4.26: Resulting distance between clouds and the center of the modeling space for clouds up to 12 km and elevation angles between 12° and 90° . All conditions above the red border line describe clouds with a distance greater 20 km.

A continuous nowcast with lead times up to 15 minutes is requested. Figure 4.25 and Figure 4.26 presented conditions where all relevant clouds have left the modeling space, which in turn would lead to clear sky predictions regardless of the real conditions. This issue is tackled by assuming a persistent cloud pattern for the space under observation and the nowcast horizon. All cloud models with an outwards pointing trajectory which leave the modeling space at one side will reappear on the opposite side of the modeling space. Furthermore, cloud models which border the voxel space limits at lead time 0 minutes with an inwards pointing trajectory will grow into the voxel space. However, this persistence cloud pattern approach can only succeed, if the cloud models interact with the voxel space limits. In case of cloud heights below 4250 m the effective maximum vision range (min elevation angle of 12°) is smaller than the voxel space limitations of ± 20 km (see Figure 4.24). Thus, none of the modeled clouds will touch the modeling space limits. For example the effective maximum vision range for a cumulus cloud field, with an average cloud height of 1000 m, is limited to a radius of roughly 4.7 km. Therefore, the cloud persistence pattern for outwards pointing trajectories can only apply after a gap of 15.3 km has been closed, whereas the persistence pattern for inwards pointing trajectories won't apply at all. For this reason, the voxel space horizontal dimensions are dynamically adjusted (reduced from ± 20 km), if the current cloud heights won't permit a sufficiently long line of sight up to the preset voxel space limits. The used persistence cloud pattern approach is illustrated in Figure 4.27.

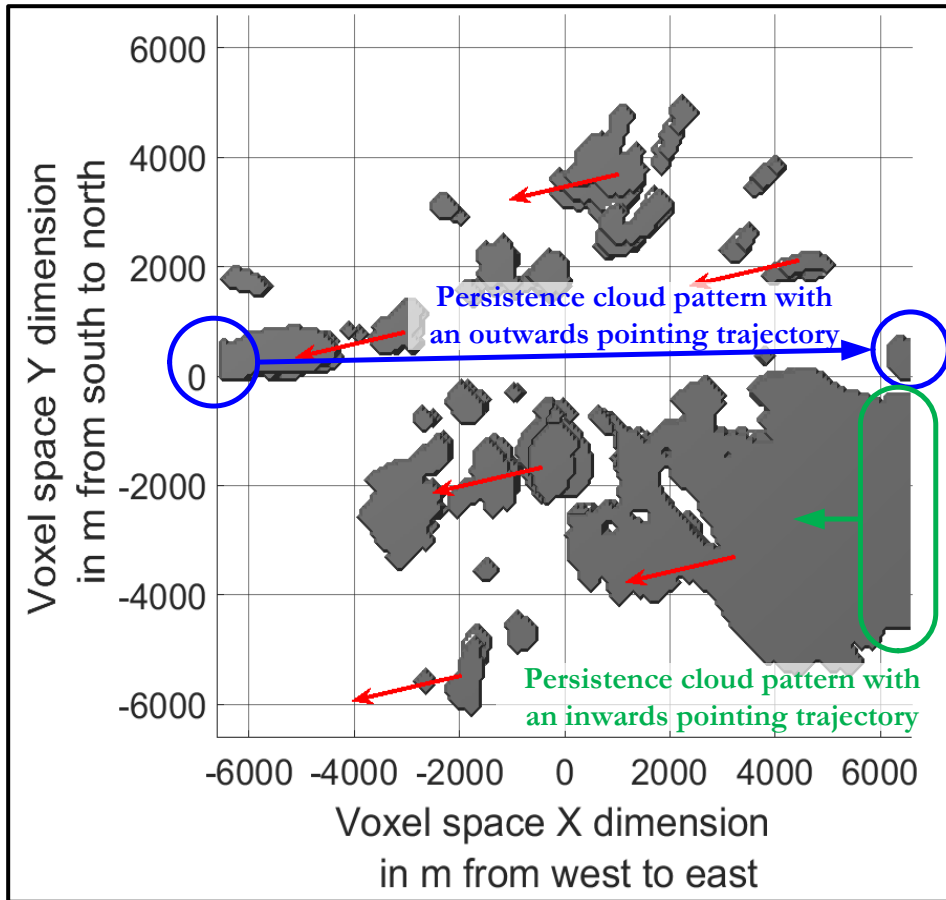


Figure 4.27: Example for persistence cloud pattern for cumulus clouds at an average height of 1.8 km and correspondingly reduced voxel space limits

For each cloud model and lead time within the modeling space an individual shadow projection is required. At first, a topographical model with an edge length up to 8 km around the point of origin is created. The topographical model is based on digital elevation measurements (90 m resolution) taken by the satellites TerraSAR-X and TanDEM-X (Martone et al. 2012). The shadow projection on the topographical model is determined via a raytracing approach (Oberländer et al. 2015). For this purpose a vector in direction of the Sun is created for each voxel identified as cloud. These vectors are turned at their base point by 180° and projected to the topographical model. All pixels of the topographical model hit by one of these vectors are considered as shaded. The shadow maps are converted with additional irradiance and cloud transmittance information to DNI maps (see Figure 4.28). A more detailed description of the conversion from shadow to DNI maps is given in section 5.5.

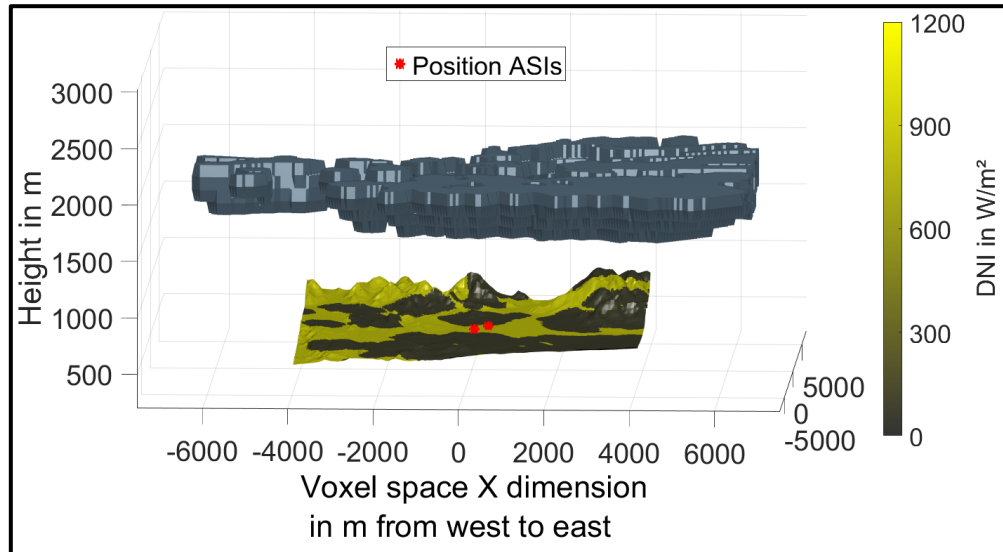


Figure 4.28: Voxel space with cumulus cloud models and topographical model around PSA with spatial DNI information

For some combinations of Sun elevation angles and cloud heights are the dimensions of the modeling space too small for a shadow projection to the topographical model. An example would be Sun elevation angle of 20° with a cloud height of 10 km. The relevant clouds are at a distance > 27 km from the point of origin and thus outside the modeling space (see Figure 4.26). Such conditions make the voxel space futile and would lead to a false clear sky interpretation at any lead time. Needed subsequent correction procedures of the final DNI maps under such conditions are presented in section 5.5.

4.6 Conclusion cloud modeling and tracking

ASI based nowcasting systems, which use individual cloud models with individual attributes such as geolocation, motion vector and transmittance were developed. 4Cam is a voxel carving based approach, utilizing sky images from four ASIs. The 2Cam system is a two ASI based cloud height detection and cloud tracking approach independent of the cloud segmentation. The 4CamH system is a hybridized approach that combines the 4Cam voxel carving approach with the 2Cam approach. In this work, the three systems were benchmarked in terms of cloud height detection with a ceilometer as reference and cloud tracking with a shadow camera system as reference.

The 30 day validation period showed the strongest deviation both for height detection and cloud tracking with the 4Cam system. The 4Cam system reached an overall MAD of 1793 m for the height, 2.6 m/s for the cloud speed and 22.7° for the motion direction. The 2Cam and 4CamH systems showed better results, with overall MAD of 1145 m (2Cam) and 648 m (4CamH) for the height, 1.8 m/s (2Cam) and 1.3 m/s (4CamH) for the speed and 12.8° (2Cam) and 11.7° (4CamH) for the direction. The comparison between the two voxel carving approaches (4Cam and 4CamH), emphasized the impact of error propagation effects of previous processing steps (e.g. cloud segmentation uncertainties). Especially the 4Cam cloud tracking was penalized by erroneous cloud heights, which lead to shape and size changes of the clouds.

4CamH outperformed 2Cam by combining the robust voxel carving approach for the cloud modeling with height and motion maps developed for 2Cam. Further reductions of the uncertainties were achieved by averaging height and motion maps from four distinct ASI pairs.

The advantages of 2Cam are lower hardware and maintenance costs and a less CPU-intensive image processing. Furthermore, the lower computing requirements of the 2Cam approach, allow a higher temporal resolution, considering the same computing capacities.

Some inherent systematical weaknesses of ASI based nowcasting systems for high altitude clouds were studied. Furthermore, strategies were presented to reduce the impact of these systematical weaknesses on the system accuracy. These strategies are limited to the 2Cam and 4CamH approach and incorporate valid recent historical cloud height measurements which substitute most likely invalid cloud height information's with cloud heights >12000 m. These weaknesses were mainly caused by the geometrical setup of the ASIs and the image resolution. A hardware upgrade consisting of cameras with a higher image resolution would reduce the impact of these effects. The drawbacks are an increased computation time.

In the following chapters the 4Cam approach will no longer be taken into account, due to the clear advantages of the approaches 2Cam and 4CamH.

5 Probabilistic approach for the determination of cloud transmittance

It is possible to determine the transmittance of individual clouds using DNI measurements (see section 2.1.1). However, with only a single pyrhelimeter for the DNI measurements, in most of the time the majority of the relevant clouds will remain without a transmittance measurement. Therefore, a transmittance allocation approach is required, especially during complex multi-layer conditions where different cloud types with distinct optical properties may occur simultaneously. For this purpose a novel probabilistic approach is developed. Clouds receive an estimated transmittance value based on (1) their height, (2) results of a probability analysis with historical cloud height and transmittance measurements as well as (3) recent transmittance measurements and their corresponding cloud height. Cloud heights are measured by the 2Cam or 4CamH cloud modeling approach (see section 4) utilizing two or four ASIs.

In section 5.1 the theoretical hypothesis of the chosen probabilistic approach is described. The probabilistic approach is based on cloud transmittance measurements, which require the knowledge of the prevailing clear sky DNI at all times. The used clear sky DNI detection approach is presented and validated in section 5.2. Section 5.3 presents the probabilistic analysis of the relation between cloud height and transmittance. The implementation of the probabilistic cloud transmittance allocation/estimation approach is presented in section 5.4. Binary shadow maps can be converted into DNI maps according to section 5.5. Validation results of the transmittance allocation/estimation approach are presented in section 5.6. In section 5.7 the probabilistic approach is benchmarked with some more simple approaches. Site dependencies and the potential of improvement by introducing an automatic cloud classification is discussed in section 5.8 and 5.9 . Finally, I conclude the findings of this chapter in section 5.10.

The content from this chapter has partially been published in **Nouri et al. 2019b**.

5.1 Radiative effect of different cloud classes and cloud height layers

A probabilistic approach is chosen which is motivated by two facts. Firstly vertical cloud profiles hold important information for distinct cloud types (**Frederick & Steele 1995, Wang & Sassen 2001, Kahn et al. 2008**). In general the troposphere is discretized into a lower, middle and high layer. Cumulus (Cu), stratus (St) and stratocumulus (Sc) clouds are associated to the lower layer, altocumulus (Ac) and altostratus (As) to the middle layer and cirrus (Ci), cirrocumulus (Cc) and cirrostratus (Cs) to the higher layer (**Rossow & Schiffer 1999**). Vertical

thick clouds like nimbostratus (Ns) and deep convective clouds can extend over all three layers. The heights of the borders between these layers are not static and dependent on latitude (**Manabe 1969, Ohring & Adler 1978, Sassen & Wang 2012**). **Sassen & Wang 2012** divide the earth in the three latitude belts, polar, mid-latitude and tropics (see Table 5.1), with corresponding borders between the three layers.

Table 5.1: Borders of troposphere low, middle and upper layer for the three latitude belts polar, mid-latitude and tropics as defined by Sassen & Wang 2012 (values in brackets describe transition zone between layers)

	Low layer	Middle layer	high layer
Polar ($> 66^{\circ}33'$ north and south)	$0 \text{ km} < h \leq 1.8 \text{ km}$ (2.4 km)	(1.8 km) $2.4 \text{ km} < h \leq 5.0 \text{ km}$ (7.0 km)	$h > (5.0 \text{ km}) 7.0 \text{ km}$
Mid-latitude ($23^{\circ}26'$ to $66^{\circ}33'$ north and south)	$0 \text{ km} < h \leq 1.8 \text{ km}$ (2.4 km)	(1.8 km) $2.4 \text{ km} < h \leq 6.0 \text{ km}$ (8.0 km)	$h > (6.0 \text{ km}) 8.0 \text{ km}$
Tropics ($< 23^{\circ}26'$ north and south)	$0 \text{ km} < h \leq 1.8 \text{ km}$ (2.4 km)	(1.8 km) $2.4 \text{ km} < h \leq 7.0 \text{ km}$ (10.0 km)	$h > (7.0 \text{ km}) 10.0 \text{ km}$

The second fact motivating the probabilistic approach is that different cloud types can be associated to different optical properties (**Chen et al. 2000**). Solar irradiance is attenuated in the atmosphere by absorption and scattering. The attenuation caused by clouds is described by the cloud optical thickness (COT). The COT of a cloud depends on micro- and macrophysical properties such as particle size distribution, shape, water path (WP), thermodynamic phase and vertical extent (**King 1987, Hess et al. 1998, Chen et al. 2000, Kokhanovsky 2004**). Especially WP, which describes the vertically integrated water content (WC), and effective particle size are proportional to COT (**Lohmann & Neubauer 2018**). The average global WP of low and middle layer clouds is significantly larger than compared to high layer clouds (**Rossow & Schiffer 1999**). Larger effective particle size leads to stronger absorptance, whereas smaller effective particle size increases the scattering (**Chang & Li 2002**).

Rossow & Schiffer 1999 used within the International Satellite Cloud Climatology Project (ISCCP) nine cloud types discretized by cloud top pressure and COT. **Hahn et al. 2001** relate ISCCP data to visual observations from the ground and reduce the ISCCP cloud type definition to four distinguishable types: all low layer clouds (Cu, Sc, St and fog), optically thin middle layer clouds (Ac and thin As), cirrus clouds (Ci, Cs and Cc) and thick high –topped clouds (cumulonimbus (Cb), Ns and thick As). The ISCCP data set states the lowest average COT with 2.2 for the cirrus clouds. Cirrus clouds consist almost exclusively of nonspherical ice crystals of various shapes (**Fu 1996**). The optical properties differ significantly between ice crystals and spherical liquid drops. The extinction coefficients of water clouds are one or two orders of magnitude greater than those of ice clouds with the same WP (**Sun & Shine 1994**). The effective particle size is at least one order of magnitude greater for ice particle compared to liquid particle with the same WC. Thus, the chance of multiple scattering is greater for water clouds (**Sun & Shine 1994**). In more recent studies with combined radar and lidar as well as CloudSat and CALIPSO measurements, the global average COT of ice clouds are found around 1 with an ice WP of 25 gm^{-2} (**Hong et al. 2016**).

The radiative properties of mixed phased clouds have to be considered too. Low layer and middle layer clouds are often considered as purely liquid clouds and high layer clouds as ice clouds. The reality is somewhat more complex. Clouds with temperatures above 0°C consist of liquid particles and clouds with temperatures below -40°C consist of ice particles. However, in between clouds may consist of supercooled liquid particles, ice particles or a mixture (**Pruppacher & Klett 1997**). Around 30% of all clouds within the temperature range of -8°C and -26°C consist of mixed phase clouds (**Sun & Shine 1994**). The related strong variation of the optical thickness can be described roughly by a linear function of the ice fraction, with

optically thicker liquid dominated clouds to optically thinner ice dominated clouds (**Sun & Shine 1994**). Especially clouds from the middle troposphere layer have temperatures associated with mixed phase clouds. Ac clouds are liquid dominated and As clouds ice dominated (**Sassen & Wang 2012**).

There is no simple relation between cloud height, type and optical thickness, due to the highly variable micro- and macrophysical nature of clouds. However, a tendency exists for mainly optically thick low layer liquid clouds, optically moderate to thick middle layer clouds and optically thin high layer ice clouds. Therefore, a probabilistic approach, including historical and current cloud height and transmittance measurements (see Figure 5.1), seems feasible to relate cloud height and transmittance for cloud transmittance estimations (if needed).

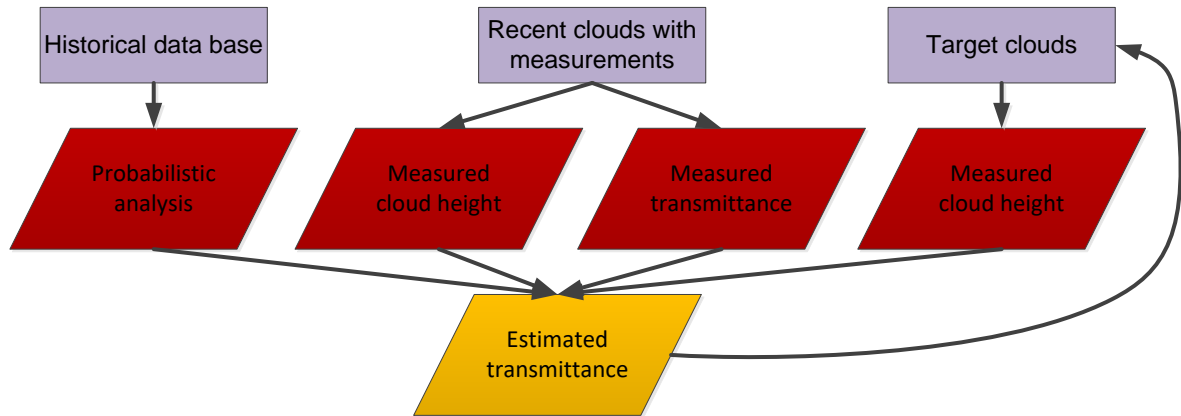


Figure 5.1: Rough structure of probabilistic cloud transmittance estimation approach. The cloud height of a target cloud is known. A corresponding transmittance value is estimated with available recent cloud height and transmittance measurements as well as the results of probability analysis with historical cloud height and transmittance measurements.

5.2 Determination of clear sky DNI

The chosen probabilistic approach utilizes cloud transmittance measurements taken by pyrheliometers as described in section 2.1.1. This requires knowledge of the clear sky DNI at all times. For the determination of the clear sky DNI, the TL is calculated from DNI measurements according to **Ineichen & Perez 2002**. Shaded DNI measurements are detected and rejected, by a so called cloud checker algorithm (**Hanrieder et al. 2016, Wilbert et al. 2016b**). The current TL is calculated by the most recent and unshaded DNI measurements, weighting more recent measurements stronger. The predicted clear sky DNI is calculated with the current TL according to **Ineichen & Perez 2002**.

Crucial for this approach is the accurate detection of the shaded DNI measurements. The so called cloud checker developed by **Hanrieder et al. 2016 & Wilbert et al. 2016b** evaluates the variability of the measured TL in 10-minute data packets. A visual inspection of the cloud checker results revealed partial failure of the algorithm during conditions with a pronounced variability of the DNI, especially with clouds corresponding to high transmittance values (e.g. cirrus). Therefore, in this work various supplementary filters are added to the existing cloud checker and tested. For the validation of the different filter strategies, a reference clear sky DNI data set is generated. This reference data set is generated by manually filtered (human cloud checker) PSA DNI data, including the complete year 2016. The tested supplementary filter are stated in Table 5.2. All needed thresholds are empirically defined.

Table 5.2: Description of supplementary cloud checker filter

Supplementary filter variation	Filter description
1	Standard deviation of pre filtered TL values over the last 2 hours
2	Floating minimal value of pre filtered TL
3	Supplementary filter 2 with subsequent time weighted average

The results of this validation period are given in Figure 5.2. Lowest error metrics are observed for the approaches supplementary filter variation 1 and 3, with a slight advantage for the variation 3. The considerably high error metrics for the purely shaded data set results partially due to long continuous periods of several hours up to 3 days without any clear conditions. Due to the less demanding computing time and the real time requirements of the nowcasting system, I selected variation 1 as final cloud checker.

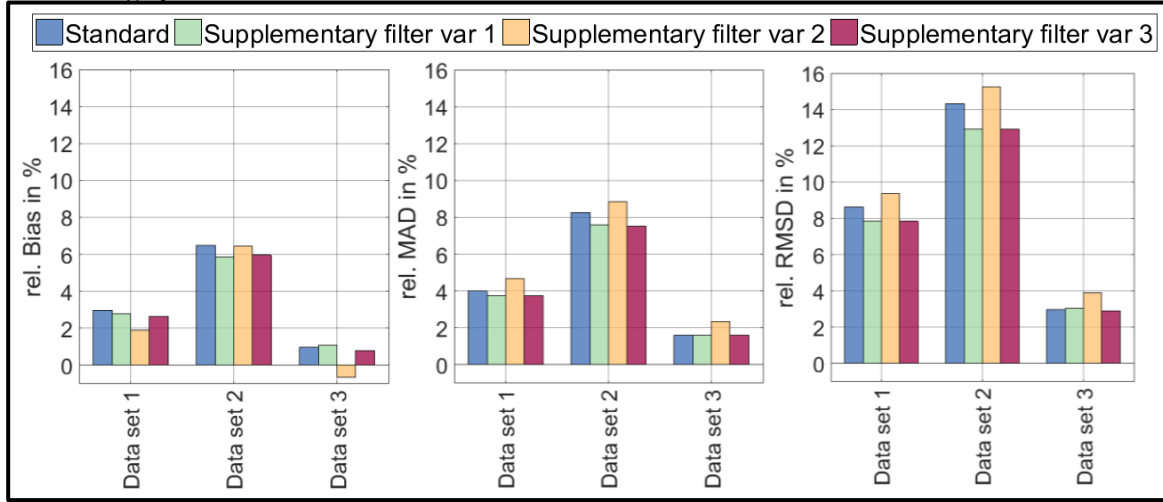


Figure 5.2: Relative bias, MAD and RMSD between reference clear sky DNI based on human cloud checker and clear sky DNI values from four distinct automatized cloud checker. Data set 1 includes all time stamps from the entire year 2016 (average reference clear sky DNI = 733W/m²), data set 2 includes only shaded time stamps from 2016 (average reference clear sky DNI = 670W/m²) and data set 3 only clear time stamps from 2016 (average reference clear sky DNI = 776W/m²)

5.3 Analysis of the relation between cloud height and transmittance

The nowcasting system treats clouds as individual objects with universal constant properties within a single cloud. However, real clouds consist of complex inhomogeneous structures with horizontal (Titov 1998, Madhavan et al. 2016) and vertical (Chang & Li 2002, Kikuchi et al. 2006) variabilities, which affect the optical properties. Moreover, cloud boundaries are not clear. Koren et al. 2007 describes a so-called twilight zone around the clouds. This twilight zone can extend tens of kilometers away from the clouds and consist of cloud fragments and hydrated aerosols. Bar-Or et al. 2010 differentiates the sky in cloud free and cloud field, where the cloud field consists of the clouds and the twilight zone with corresponding cloud properties. This spatial uncertainty of cloud boundaries is reflected by DNI measurements, making unambiguous transmittance measurements frequently challenging. However, reliable transmittance measurements are needed for the probability analysis. To study stable transmittance measurements DNI measurements with a temporal resolution of about 5 s are used. Transmittance measurements are only considered if the standard deviation is less or equal 0.05 over a time period of ± 20 s. This threshold is determined empirically.

Transmittance measurements are compared with cloud heights measured by a ceilometer. Ceilometer measurements are chosen for the probability analysis, as they are considered to be more accurate in comparison to ASI derived cloud heights (see section 4.3), which show a stronger dispersion especially for higher cloud layers. ASI derived cloud height information could be used, but for this study it is aimed to create a data base with the highest possible accuracies to test the limitations of the cloud transmittance estimation approach. Yet, the ceilometer is limited to cloud measurements directly above the sensor. Thus, the cloud height measured by the ceilometer and the cloud transmittance determined by a close by pyrliometer often do not belong to the same cloud. Therefore, the probability analysis is confined to conditions with constant lowest CBH. Conditions are defined as constant, when the standard deviation of the ceilometer measurements is less or equal to 500 m over a time period of ± 15 minutes. Furthermore, measurements are only considered if the Sun elevation angle is above 10° as for very small solar elevations the clouds shading the pyrliometers are far away from the clouds above the ceilometer.

The probability analysis is performed on 574 cloudy days between January 2014 and December 2017 at PSA. A total of 316419 valid transmittance measurements with single-layer cloud conditions are available. Figure 5.3 shows the occurrence of cloud height readings as measured by the ceilometer within this time period.

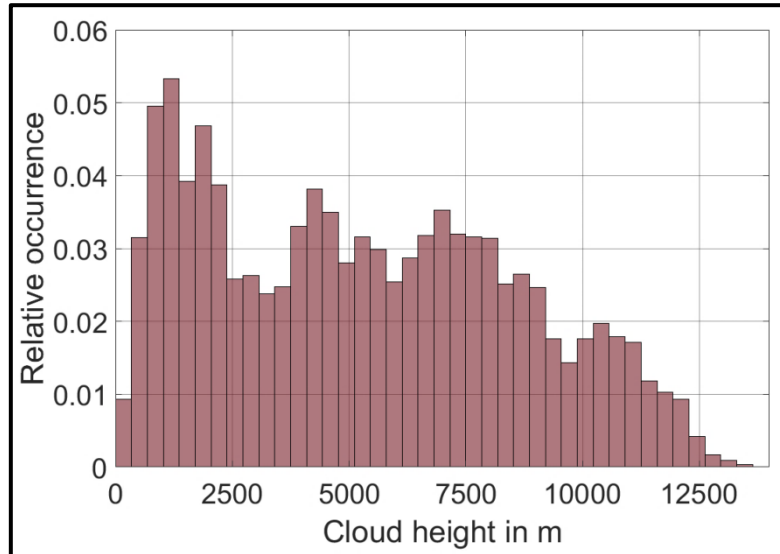


Figure 5.3: Histogram of cloud height readings as measured by the ceilometer used for the probability analysis.

Cloud heights are discretized in five height ranges from 0 to 12.5 km in 2.5 km steps. Readings above 12.5 km are not considered, due to their scarcity (see Figure 5.3). The lowest range describes all low layer clouds, whereas the second and third layer describes the middle layer clouds and the last two ranges the high layer clouds. Figure 5.4 depicts the transmittance measurement distribution over the five height ranges as box plot. The expected increase of transmittance with cloud height is clearly visible. The average transmittance measurements from the lowest to the highest cloud range are 0.06, 0.15, 0.36, 0.52 and 0.68. Especially the lowest height range shows unambiguous results. The moderate middle height range 2.5 to 5.0 km as well as the highest range 10.0 to 12.5 km show a comparatively low variability in transmittance. The 25th and 75th percentile cover a transmittance range of 0.16 and 0.29 respectively. The strongest variabilities in transmittance occur in the height ranges 5.0 to 7.5 km and 7.5 to 10.0 km, with a covered transmittance range by the 25th and 75th percentile of 0.64 and 0.54 respectively.

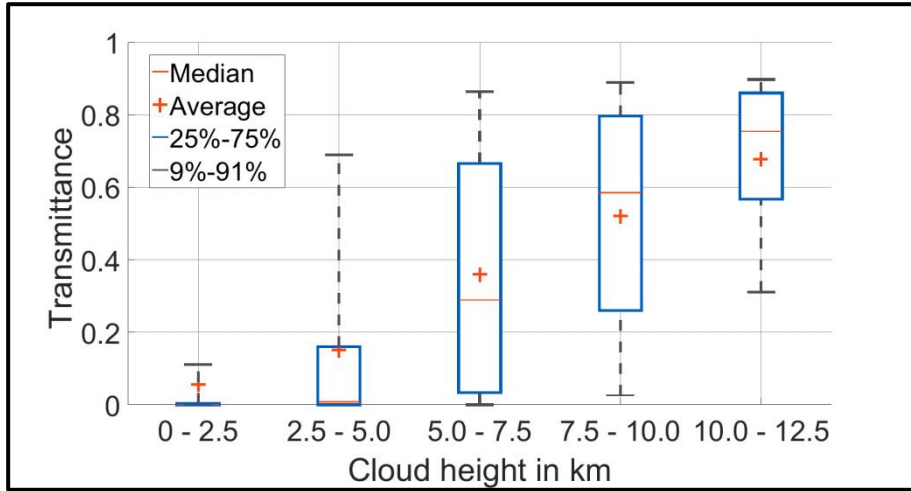


Figure 5.4: Transmittance readings discretized over cloud heights from 574 cloudy days for PSA.

For the further analysis five transmittance ranges from 0 to 0.9 in 0.18 steps are defined. Optically very thin clouds with transmittance above 0.9 are not considered by the nowcasting system. A reliable detection of these optically very thin clouds by the ASIs cannot be assured. The occurrence probability of the defined transmittance range within the height ranges is analyzed for each of the 574 days separately. The box plots in Figure 5.5 show the probability distribution of transmittance range occurrence within the five height ranges over all days. For the two lowest height ranges, the average probability for optically very thick clouds ($0 \leq T < 0.18$) are 93% ($0 \leq h < 2.5$ km) and 77% ($2.5 \leq h < 5.0$ km). The remaining transmittance ranges have an average probability below 10%. The height ranges 5.0 to 7.5 km and 7.5 to 10.0 km show the strongest dispersion in probability of transmittance. In the case of the height range 5.0 to 7.5 km the highest average probability remains with the optically very thick clouds (42%). However, the average probability for optically thin clouds ($0.72 \leq T \leq 0.9$) rises to 21%. An almost inverse situation is observed for the height range 7.5 to 10.0 km, with an average probability of 21% for the optically thick clouds and 34% for the optically thin clouds. For both height ranges the remaining transmittance ranges show a significantly high average probability above 10%. The average probability for thick clouds is quite low with 2% ($0 \leq T < 0.18$) and 6% ($0.18 \leq T < 0.36$) for the highest cloud height range. On the opposite side of the transmittance spectrum the average probabilities are 23% ($0.54 \leq T < 0.72$) and 54% ($0.72 \leq T \leq 0.9$).

The more ambiguous results in transmittance probability for the layers 5 to 10 km were expected. These middle troposphere layers covers a wide temperature range, which enables supercooled liquid, ice and mix particle clouds. Thus, the determination of optical properties is more difficult for the middle layer (Sassen & Wang 2012, Kayetha & Collins 2016).

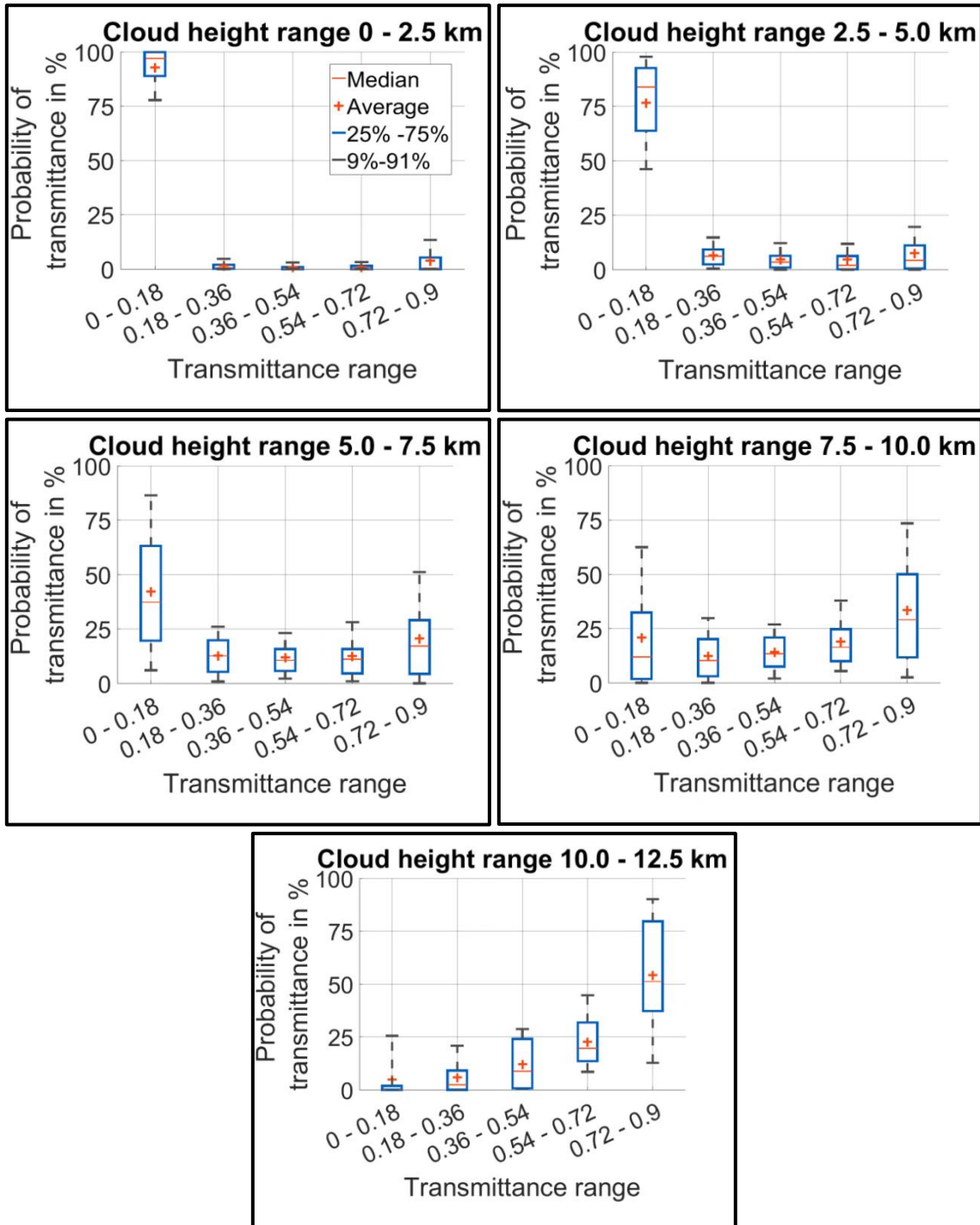


Figure 5.5: Probability of cloud transmittance occurrence for different cloud transmittance and cloud height ranges from 574 cloudy days for PSA.

5.4 Cloud transmittance estimation method for the nowcasting system

The transmittance estimation for the nowcasting system is based on the ASI derived cloud height, measured transmittances and the probability of the transmittance as shown in the previous section. Shadow projection is done individually for each cloud. Thus, the responsible

cloud for each transmittance measurement is known together with its corresponding cloud height. The nowcasting system saves the recent transmittance measurements and cloud height information in a data base. The transmittances of all detected clouds in the sky without transmittance measurement are determined based on (1) the cloud height, (2) the probability analysis results and (3) recent transmittance measurements. The flow chart for the transmittance estimation method, which explains the method in detail including examples, is shown in Figure 5.6.

The fact that ASI based cloud heights are used instead of ceilometer cloud heights could lead to additional transmittance errors. Average relative mean-absolute deviations (MAD) of $\approx 10\%$, $\approx 18\%$ and $\approx 22\%$ of the ASI cloud heights compared to the ceilometer cloud heights were observed for low layer, middle layer and high layer clouds respectively (see section 4.3). The possible deviation of ASI derived and ceilometer derived cloud heights could lead to erroneous transmittances. These errors are estimated to be acceptable for the method given the distribution of transmittances within each cloud height and the wide height bins.

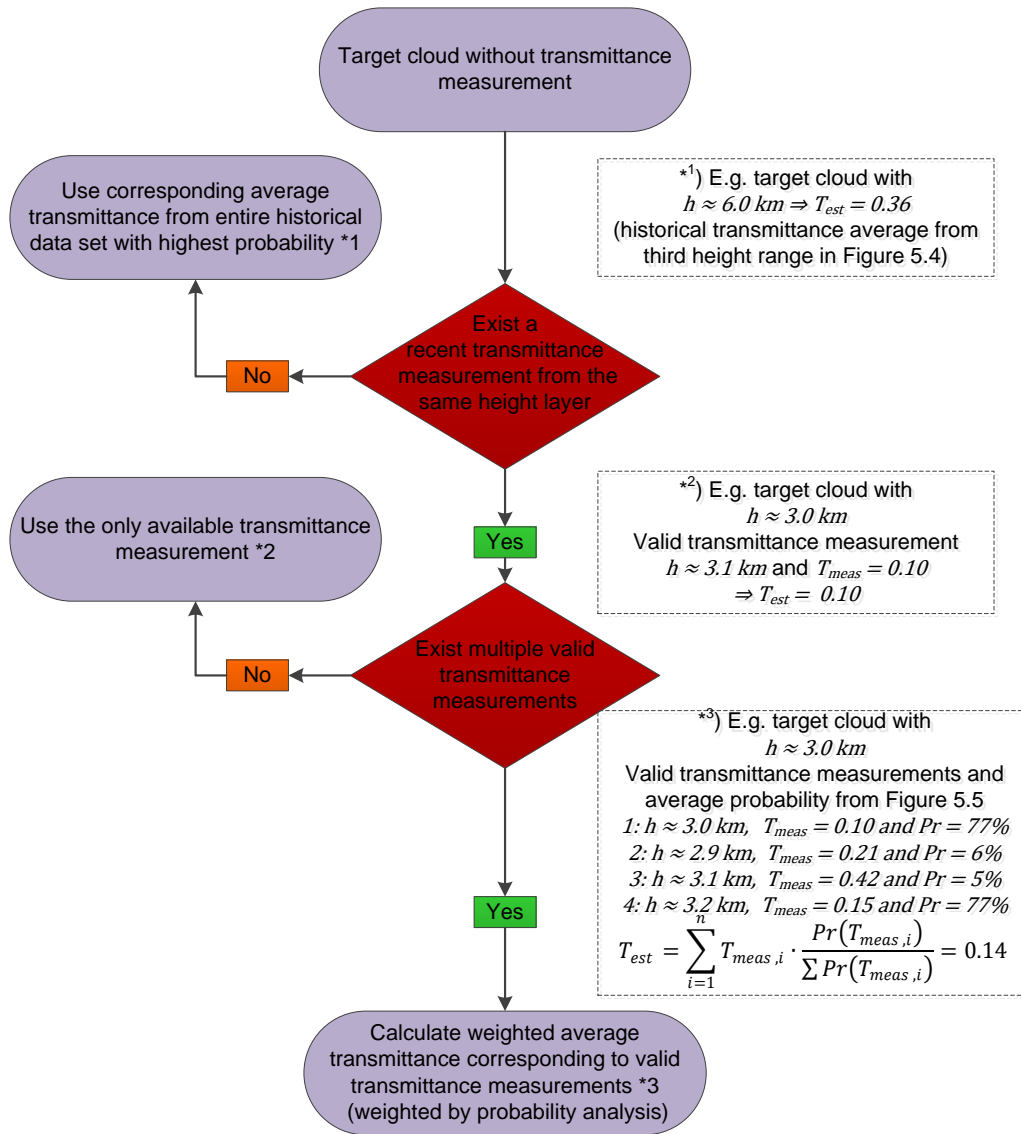


Figure 5.6: Flowchart for the transmittance estimation with historical results from the probability analysis and recent cloud transmittance and height measurements within the nowcasting system (h: cloud height, T_{meas} : measured transmittance, T_{est} : estimated transmittance and Pr: average probability corresponding to cloud transmittance and cloud height range). Examples of the three options are given marked by *.

5.5 Creating DNI maps

Now that the transmittance of the clouds is known, spatially resolved DNI maps can be created. In a first step, the clear sky DNI, determined according section 5.2 is assigned to all unshaded pixels of the topographical map. The remaining shaded pixels contain the product of the clear sky DNI and the corresponding cloud transmittances. As previously mentioned the shadow projection is done individually for each cloud model. Therefore, each shaded pixel of the topographical map can be assigned to one or multiple overlaid clouds. If multiple clouds shade the same pixel, the DNI of that pixel corresponds to the product of all involved cloud transmittance values and the clear sky DNI.

While the used approach accepts different clouds with different transmittance it does not allow any inhomogeneity within the individual clouds. Of course this is a strong simplification, which leads to additional spatial uncertainties since real clouds are complex inhomogeneous structures (see section 5.3). Such uncertainties can be corrected at least for the immediate surroundings of the needed reference pyrliometer. So-called “Sun clouds” are created inside the voxel space for this purpose. All voxels which describe the Sun disk from the viewing angle of the pyrliometers are combined to a new individual cloud. This cloud always receives the current cloud transmittance as determined by the currently measured DNI and the corresponding clear sky DNI (see Equation 2.1). A voxel space with a Sun cloud is illustrated in Figure 5.7. The Sun cloud receives a motion vector from the Kalman filter (see section 4.2.2) just as any other cloud and will be displaced accordingly for the nowcasts.

The Sun cloud also reduces uncertainties from erroneous cloud positions, if a cloud is expected between pyrliometer and solar disk although there is no cloud. In this case, the actually non-existing cloud receives a transmittance of 100%. Also, the Sun cloud method help if an existing cloud that shades the pyrliometer is missed. In such cases a new cloud is generated. This new cloud receives the most recent average cloud height as well as the current measured cloud transmittance and incorporates those voxel which are in the pyrliometer’s field of view.

A similar approach is utilized, when the voxel space dimensions are insufficient for the current Sun elevation angle and cloud height (see section 4.5). This issue occurs only for very low Sun elevation angles and comparatively high clouds. Then, the Sun cloud shades the complete topographical map. This simplification is necessary, since the available voxel space does not hold any relevant information for the topographical map.

The overall system accuracy can be increased, if more than one irradiance measurement station is available, as the above mentioned corrections can also be carried out for several stations.

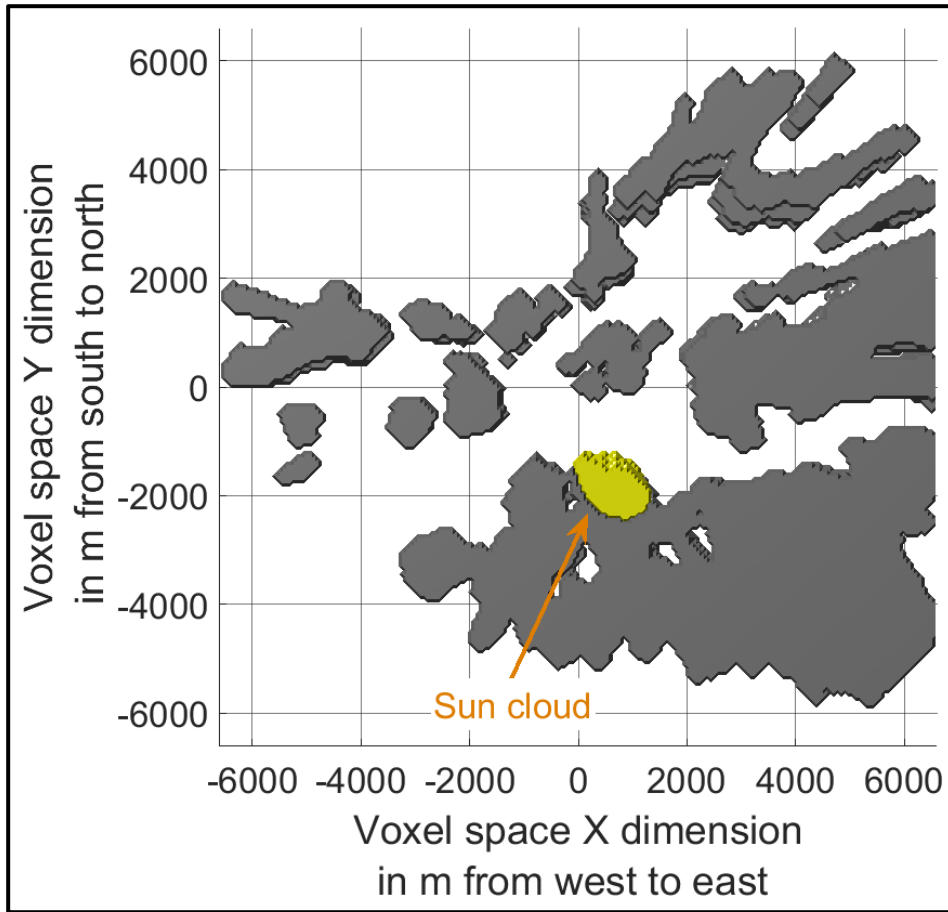


Figure 5.7: Illustration cloud model with independent Sun cloud

5.6 Validation of transmittance estimation approach

Sky images of a two years data set (2016 and 2017) taken at PSA are processed with the nowcasting system including the transmittance estimation approach described in section 5.4. DNI maps for the current situation and nowcasts up to 15 minutes ahead in 1 minute steps are created. Each valid transmittance measurement over the 2 years is saved into a database. Transmittance measurements are gathered in around 14.2% of all processed image series (considering only conditions with clouds). The validation method utilizes all corresponding DNI maps with lead time 0 and 1 minute describing the time stamps of the transmittance measurements. The actual cloud transmittance measurement is applied to the DNI map with a lead time of 0 minute. For the clouds responsible for the transmittance measurement a transmittance estimation according to the statistical approach from section 5.4 is also available. The estimation from a forecast with a lead time of 1 minute is validated with the later measurement (see Figure 5.8).

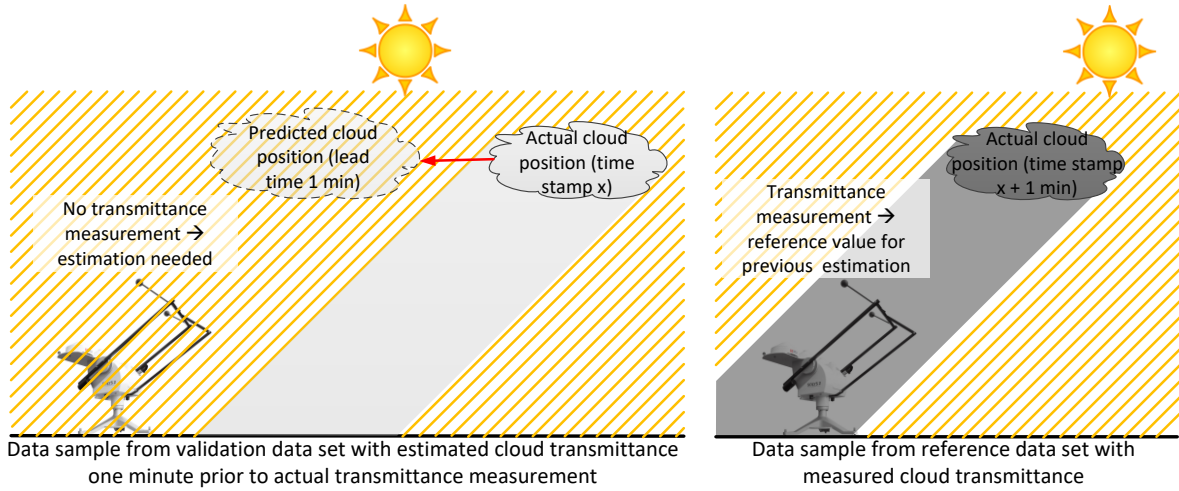


Figure 5.8: Illustration matching transmittance measurements with previously estimated transmittance values from the same cloud. (left) Cloud with estimated cloud transmittance 1 minute prior to actual transmittance measurement. (right) Cloud with transmittance measurement.

A scatter density plot of this validation is shown in Figure 5.9. Accumulated relative frequencies of each column add up to 100%. Overall a good agreement is reached with the strongest deviations for the moderate transmittance ranges. A frequent transmittance overestimation by about 5% is apparent. This is due to two causes. Firstly, the cloud height measurements for the probability analyses are obtained by a ceilometer. As mentioned before, the ceilometer measurements are limited to clouds directly above the sensor. Thus, the cloud height and cloud transmittance measurements do not belong to the same cloud in many cases. This issue is addressed by limiting the data set of the probability analysis to conditions with a constant lowest CBH, assuming quasi constant cloud heights for all visible clouds (see section 5.3). This limits the probability analysis almost entirely to single-layer conditions. Multi-layer conditions are only considered in the case of a continuous lowest layer overcast condition, which is a rare case for the PSA. But in general the occurrences of multiple cloud layers are not rare. On a global scale, multi-layer conditions occur in around 42% of all cases (**Wang et al. 2000**). The total attenuation increases with these multi-layer conditions since the direct solar rays have to pass through several cloud layers. The validation period includes such multi-layer conditions, but receives cloud transmittance estimation corresponding mainly to single-layer conditions. Secondly, the cloud height validation of the nowcasting system detected a tendency for a slight overestimation of the cloud height (see section 4.3), which also leads to transmittance overestimations.

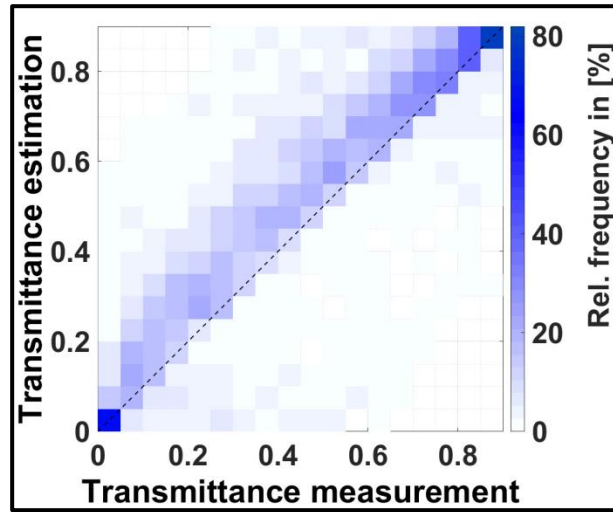


Figure 5.9: Transmittance estimation over transmittance measurement for the validation data set. The color coding represents the relative frequency for each pixel in a column of the scatter density plot. Accumulated relative frequencies of one column add up to 100%.

Figure 5.10 shows the MAD and RMSD within transmittance ranges (0.045 step size) and the corresponding data density. Nearly 25% of all transmittance measurements belong to the optically very thick clouds with $T \leq 0.045$. Each of the remaining transmittance ranges contains less than 10% of the data. The comparatively high share of optically very thick clouds is partially due to multi-layer conditions, which often attenuate the majority of direct irradiance.

The MAD amounts to 0.06 for the optically very thick clouds and rises to a maximum of 0.20 with $0.315 \leq T < 0.36$. Afterwards the MAD drops down to 0.03 for optically thin clouds with $0.855 \leq T \leq 0.9$. The higher deviations for the moderate transmittance ranges comply with the results of the probability analysis. The strongest occurrences of the moderate transmittances are found for the middle cloud layer and the lower part of the higher cloud layer up to 10 km (see Figure 5.4). These are also the layers with the strongest transmittance dispersion. As previously discussed comes this not as a surprise, since especially the middle troposphere covers a wide temperature range, which enables supercooled liquid, ice and mix particle clouds. It is this variety in the possible cloud composition, which makes the determination of optical properties more difficult (Sassen & Wang 2012, Kayetha & Collins 2016).

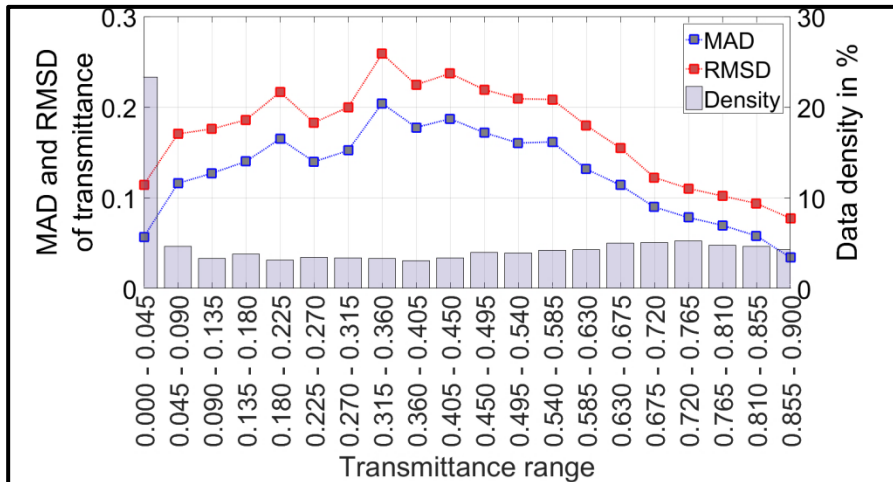


Figure 5.10: MAD, RMSD and data density over transmittance ranges for the validation data set.

The overall average MAD and RMSD over the entire data set are 0.11 and 0.16 respectively. It has to be pointed out, that these deviations are only relevant if estimates for the transmittance are required. Often consecutive transmittance measurements occur (due to horizontally large clouds/cloud fields), which makes the estimation of cloud transmittance unnecessary for many relevant clouds that shade the target area and leads to a significant reduction of the deviations. This is especially the case for the current conditions and the immediate future of a couple of minutes ahead. For nowcast looking further into the future, the clouds transmittance estimation becomes more important.

5.7 Benchmarking of different cloud transmittance approaches

In the following the probabilistic transmittance estimation approach is benchmarked with four more basic transmittance estimation approaches.

- Binary approach with a transmittance of 0 for all clouds.
- Binary approach with a transmittance of 0.32 for all clouds (average transmittance over entire data set of the probability analysis).
- Cloud transmittance estimation according to the average transmittance within the corresponding cloud height bin as given in Figure 5.4 (This is equivalent to the presented probabilistic approach if no recent transmittance measurements are available).
- A persistence approach, which allocates a transmittance corresponding to the last measured transmittance to all clouds.

The additional transmittance approaches are validated according to the procedure described in section 5.6. The overall average MAD and RMSD of all approaches are stated in Table 5.3. The lowest deviations are achieved with the probabilistic approach. The strong deviations of the binary approaches are no surprise, considering the observed distribution in cloud transmittance (see section 5.3). The advantage of the probabilistic approach compared to the remaining approaches can be explained by the combination of historical with recent information, whereas the simple approaches use only historical or recent information.

Table 5.3: Overall MAD and RMSD for different transmittance estimation approaches

	MAD	RMSD
Probabilistic approach	0.11	0.16
Binary 0	0.39	0.49
Binary 0.32	0.27	0.31
Historical average height dependent	0.24	0.30
Persistence	0.17	0.26

The deviations discretized over transmittance ranges are illustrated in Figure 5.11. The binary approaches dominate the bins they are related to, with a linear increasing deviation from these bins. The advantage of the probabilistic approach is most visible for optical very thick or very thin clouds.

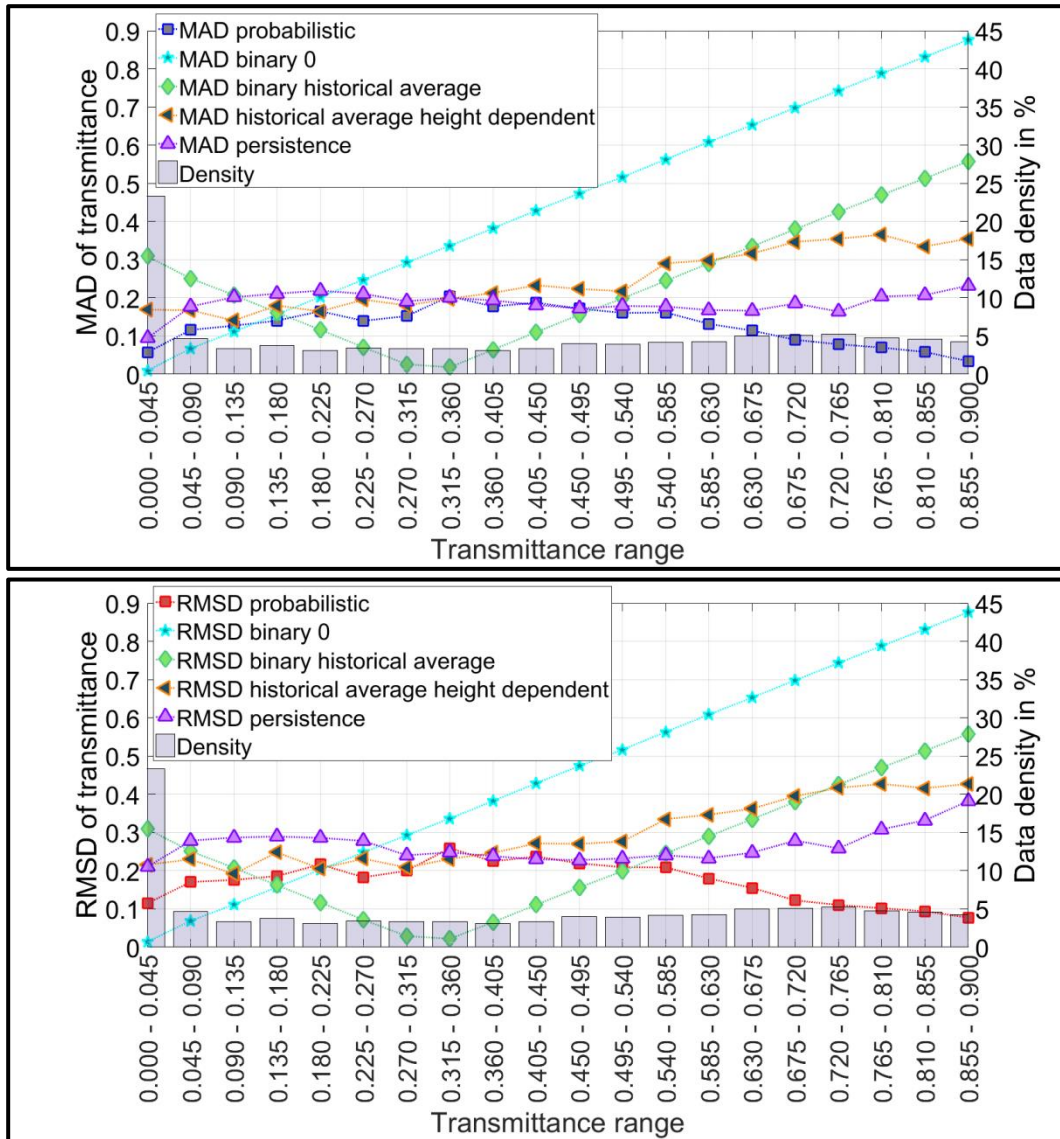


Figure 5.11: MAD, RMSD and data density over transmittance ranges for the validation data set for different transmittance estimation approaches

5.8 Discussing site dependence

The transmittance estimation approach presented here uses a probabilistic look-up table generated for and corresponding to the local conditions of PSA. Other sites might have different statistical relationships between the distribution of cloud transmittance and height. Especially latitude dependencies regarding e.g. cloud height related moisture and cloud type distributions must be taken into account (Manabe 1969, Ohring & Adler 1978, Sassen & Wang 2012). Deviations in cloud type distribution, despite equal latitude, occur due to local meteorological conditions. Furthermore, the occurrence of low layer clouds is higher in the southern hemisphere compared to the northern hemisphere, probably due to the larger proportion of ocean surfaces (Stubenrauch et al. 2006). Seasonal or diurnal dependencies of the cloud distribution (Stubenrauch et al. 2006) are currently not considered.

However, the described approach always includes recent cloud transmittance measurements belonging to the actual site. During operation the cloud transmittance

measurements and the corresponding height measurements taken by the nowcasting system are saved into a database. Thus, the PSA probability data base is gradually improved and finally replaced by measurements belonging to the new site, improving the nowcasting quality with time.

5.9 Potential of cloud classification

An accurate automatic cloud classification from the ASI images could improve the transmittance estimation approach. The site dependency issue during the initial phase at a new site could be reduced by linking transmittance measurements directly to the cloud type rather than cloud height. Furthermore, the distinction between different middle layer cloud types with liquid dominated Ac and ice dominated As clouds would be helpful, although the optical cloud properties from the same cloud class remain variable especially for middle layer clouds (Sassen & Wang 2012, Kayetha & Collins 2016).

Objective visual classification of clouds with its strong variation of micro- and macrophysical properties is a difficult task. A bias depending on the experience and preferences of the user is unavoidable. However, various groups developed cloud classification approaches from ASI images (e.g. Heinle et al. 2010, Kazantzidis e al. 2012, Wacker et al. 2015, Huertas-Tato et al. 2017). All of the mentioned groups use approaches with machine learning algorithms, such as the k-nearest neighbor’s or random forests algorithm. In most cases up to seven cloud types are considered, including clear sky, cumulus, stratus/altostratus, stratocumulus, cirrocumulus/altocumulus, cirrus/cirrostratus and cumulonimbus/nimbostratus (Heinle et al. 2010). Huertas-Tato et al. 2017 added the class multicloud, which does not distinguish between different cloud types, but indicates if more than one cloud type is present.

The cloud classification approaches from ASIs achieve high accuracies with correct hit rates around 90% for single-layer conditions (see Table 5.4). However, the accuracies drop significantly with random data sets including multi-layer conditions (Wacker et al. 2015).

Table 5.4: Some published average cloud classification accuracies

	Average hit rate	
	Single-layer conditions	Single & Multi-layer conditions
Heinle et al. 2010	87.52%	n/a
Kazantzidis e al. 2012	87.90%	n/a
Wacker et al. 2015	91.70%	Down to \approx 50%
Huertas-Tato et al. 2017	77.3%	72.60%(*)

(*) Including multicloud class without further specification of the present cloud classes

To estimate the potential improvement, 10% of the transmittance validation data set (see section 5.6) are manually classified. The data selection considers 10% of each day, within a day the data is chosen randomly. Thus, no bias is introduced due to the data selection. Only the clouds which mask the Sun from the perspective of the ASI are classified. The cloud classes cumulus, stratus/altostratus, stratocumulus, cirrocumulus/altocumulus and cirrus/cirrostratus are used according to Heinle et al. 2010. Situations with cumulonimbus/nimbostratus, which seldom occur at PSA, are rejected. The transmittance validation data set includes no clear sky conditions. Multi-layer conditions are accepted, as long as the cloud covering the Sun (ASI perspective) is clearly distinguishable/classifiable. The transmittance of each manually

classified cloud is known, thus transmittance ranges are discretized over cloud classes. The relative occurrence of transmittance ranges within cloud classes is shown in Figure 5.12. Different colors refer to different transmittance ranges. Rather unambiguous results exist for predominantly optically thick cumulus and stratocumulus as well as predominantly thin cirrus/cirrostratus clouds. A strong dispersion is visible for the cloud classes stratus/altostratus as well as cirrocumulus/altostratus. In particular the combined class, including low layer stratus and middle layer altostratus clouds, is unfavorable for the transmittance determination. A slightly different classification scheme is recommended to be combined with the cloud height base approach, distinguishing between separate stratus and altostratus as well as cirrocumulus and altostratus clouds. However, the results shown in Figure 5.12 show a good agreement with the results of the probability analysis (section 5.3) as well as the validation of the transmittance estimation (section 5.6). Such a combined method could be used to further improve the transmittance determination.

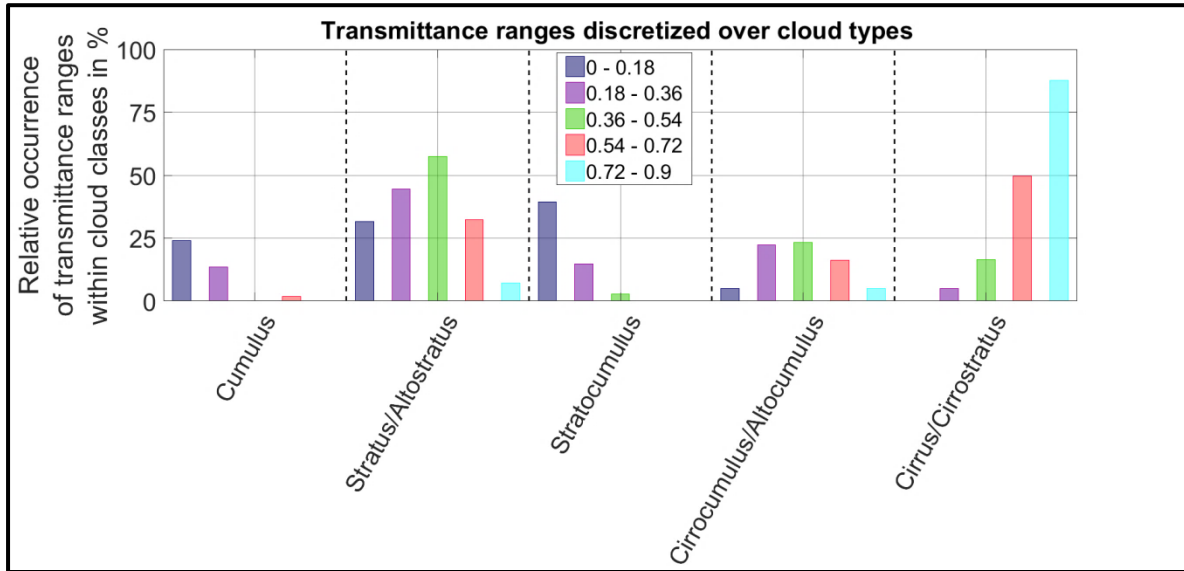


Figure 5.12: Relative occurrence of transmittance ranges within cloud classes (manually classified). Different colors refer to different transmittance ranges. All bars of the same transmittance range add up to 100%.

5.10 Conclusion determination of cloud transmittance

A novel probabilistic approach has been developed, connecting cloud transmittance measurements and cloud height measurements. A transmittance estimation approach suitable for real-time operation was developed, which calculates a weighted average transmittance from recent transmittance measurements with corresponding cloud heights. The weighting factors are defined by the average probability of transmittance values within the corresponding height range. Transmittance and accurate ceilometer cloud height measurements from 574 cloudy days distributed over the years 2014 to 2017 were analyzed. The results of the probability analysis show a clear connection between cloud height and transmittance for low layer clouds and high layer clouds which are optically thick and optically thin, respectively. Middle layer clouds are ambiguous with a strong dispersion from optically thin to optically thick clouds. This was to be expected, due to the micro- and macrophysical properties of middle layer clouds (Sassen & Wang 2012, Kayetha & Collins 2016). Nevertheless, the presented validation of the transmittance estimation procedure, over the entire years 2016 and 2017, reached an overall low MAD and RMSD of 0.11 and 0.16 respectively. The probabilistic

transmittance estimation approach was compared with two binary, a simple statistical and a persistence approach. The probabilistic approach clearly outperforms all of them.

The site dependence of the presented approach was discussed. The cloud height and transmittance distribution of the used probability analysis represents the conditions at PSA. However, new cloud transmittance and height measurements of a new site will substitute with time the PSA data and thus improve the system accuracy.

ASI based cloud classifications could improve the transmittance estimation and reduce the site dependence. However, a system improvement requires particularly high classification accuracies with middle layer clouds and multi-layer conditions. Currently the highest classification inaccuracies are found with stratus/altostratus and cirrocumulus/altocumulus (**Wacker et al. 2015**) as well as multi-layer conditions (**Wacker et al. 2015, Huertas-Tato et al. 2017**). These are precisely the conditions, in which also the probabilistic approach shows the highest deviations. Furthermore, the relationships between cloud type and transmittance for the cloud classes stratus/altostratus and cirrocumulus/altocumulus, which include the middle layer clouds, are ambiguous. A simplified classification could be conceivable, which discretizes the cloud cover in optically thin and optically thick clouds within the cloud height ranges. This would be also a first step away from clouds with homogenous optical properties to more realistic clouds with both horizontal and vertical variability.

6 Overall validation and uncertainty analysis of DNI maps

Every measurement or nowcast is subject to a certain degree of uncertainty. Without an indication of uncertainties, results cannot be used to the full extent and are therefore incomplete. Scalar error metrics, such as mean absolute deviation, root mean square deviation, and skill score are commonly used to estimate the accuracy of nowcasting systems. For the nowcasting based on the 2Cam cloud modeling approach, such overall error metrics are given in section 6.1. However, these overall error metrics represented by a single number per metric are neither suitable to determine the real time accuracy of a nowcasting system in the actual weather situation, nor suitable to describe any spatially resolved nowcast accuracy. The performance of ASI-based nowcasting systems is strongly related to the prevailing weather conditions. Depending on weather conditions, large discrepancies between the overall and current system uncertainties are conceivable. Furthermore, the nowcast accuracy varies strongly within the irradiance map as higher errors may occur at transient zones close to cloud shadow edges. Therefore, a novel approach for the spatially resolved real-time uncertainty specification of ASI-based nowcasting systems is described and validated in section 6.2. In section 6.3 it is shown how the results from section 6.2 can be utilized to estimate the expected uncertainties of the nowcasting systems at different location, solely by DNI measurements. Finally, I conclude the findings of this chapter in section 6.4.

The content from this chapter has partially been published in **Nouri et al. 2019b**, **Nouri et al. 2019c** and **Nouri et al. 2019e**.

6.1 Validation of DNI nowcast

Three reference pyrhemeters are used to validate the overall nowcast quality of the DNI maps (pyrheliometer number 1, 2 and 3 see Figure 3.2). Pixels from the DNI maps corresponding to pyrheliometer positions are compared to the reference DNI values (see Figure 6.1(left)). One minute average values are used for this validation. Relative deviation metrics of the validation period are shown in Figure 6.2 (left). These relative deviation metrics are calculated as the quotient of the absolute deviation metrics and the average reference DNI over the validation period. The used dataset for this validation consist of the years 2016 and 2017. The relative bias, MAD and RMSD for lead time 0 minutes are approximately 2%, 4% and 8%, respectively, and rise up to 5%, 16% and 26%, for a lead time of 15 minutes.

As previously mentioned, the deviations of the nowcasting system arise due to errors on the shadow position and magnitude of the DNI attenuation. The influence of the deviations due to false shadow position and DNI attenuation can be reduced by spatial filtering of the DNI maps (**Schmidt 2017**). In this thesis a 2-D Gaussian filter is used. The transition region

for the Gaussian filter is defined by a given standard deviation σ and increases with higher lead times due to the higher uncertainties. An optimization process for ideal transition regions, aiming to reduce the overall RMSD, is conducted over a 30 days validation period. The validation period is chosen to cover a wide range of ambient conditions. The results of the optimization process are depicted in Table 6.1.

Table 6.1: Optimized transition region σ for 2-D Gaussian filter

Lead time in min	0	1	2	3	4	5	6	7	8	9	10	11	12	13	14	15
σ in km	0.1	0.3	0.5	0.7	0.7	1.0	1.0	1.5	1.5	1.5	1.5	1.5	1.5	1.5	1.5	1.5

The effect of the 2-D Gaussian filter on a DNI map with a lead time of 2 minutes is depicted in Figure 6.1(right). Comparing the validation results over the entire two years, we see only a slight reduction of the error metrics for low lead times, despite the utilized Gaussian filter. However, for a lead time of 15 minutes the rel. RMSD drops by 2 percent points and the rel. MAD by 1 percent point. This corresponds to a relative improvement of roughly 7.7% for the RMSD and 6.3% for the MAD.

When considering the effect of the spatial filter, we have to take into account that the ambient conditions over an entire metrological year at the PSA consist of clear sky conditions in roughly 70% of the cases (see 6.2.3). The impact of the spatial filter on a highly variable day is depicted in Figure 6.3. At lead time 15 minutes we see a reduction in rel. RMSD from 51% to 38% and in rel. MAD from 28% to 23%, which corresponds to an relative improvement of roughly 25% (RMSD) and 18% (MAD) respectively.

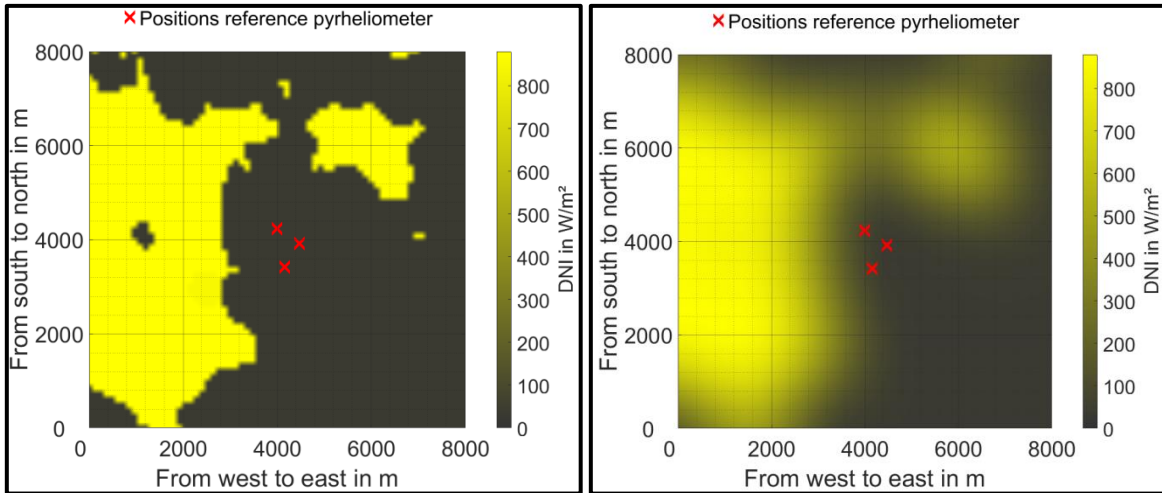


Figure 6.1: Example DNI map with marked positions of reference pyrheliometers (left) without filter (right) with filter (lead time 2 min)

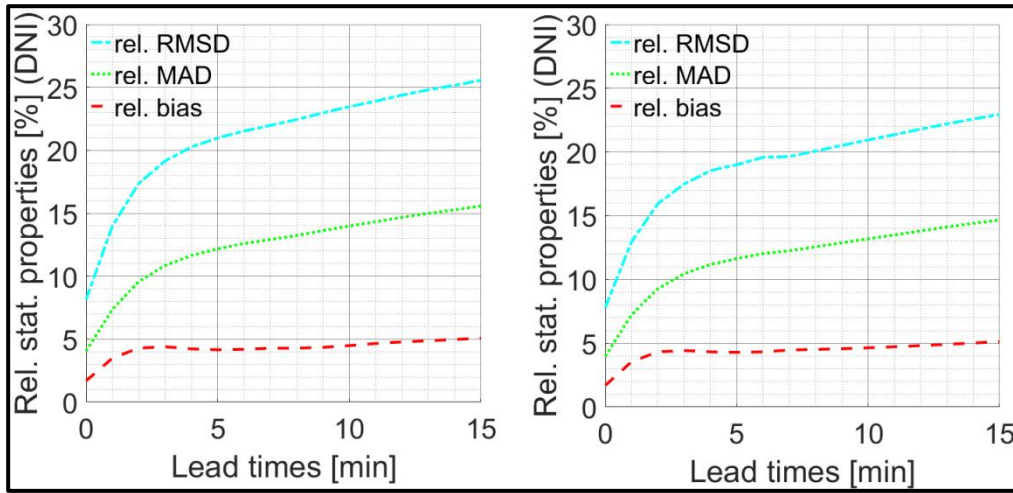


Figure 6.2: Relative statistics of DNI maps validation with three reference pyrhemliometer including the years 2016 and 2017 (left) without spatial filter (right) with spatial filter

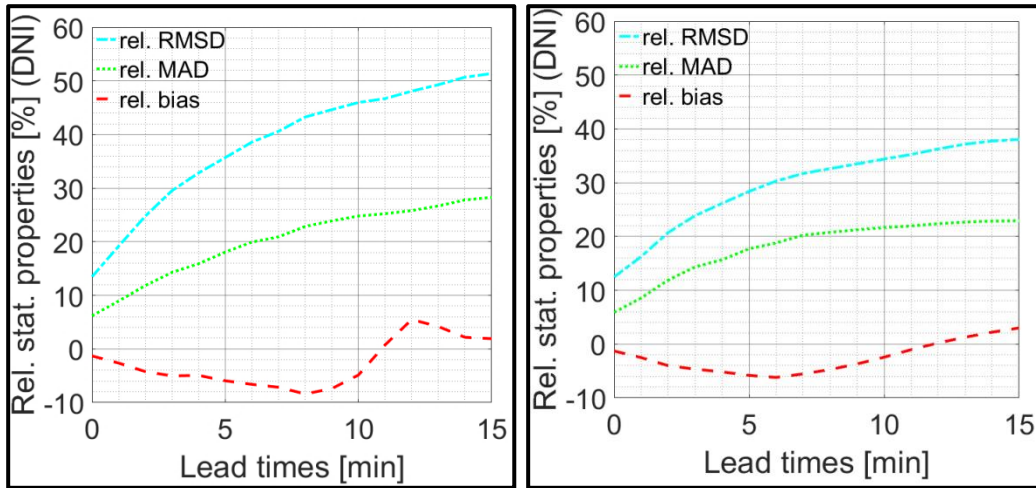


Figure 6.3: Relative statistics of DNI maps validation with three reference pyrhemliometer for a variable day (left) without spatial filter (right) with spatial filter

Nowcasting systems should be capable of outperforming simple persistence nowcasts, which assume constant ambient conditions over time. The overall system skill score (according to Equation 2.5) over the entire 2 year data set is shown in Figure 6.4 (blue line). The skill score drops from lead time 1 to lead time 15 from around 0.11 to 0.01. However, the chosen validation data set has also a strong impact on the skill score. ASI based nowcasting deviations rise in the case of multi-layer conditions including middle and high layer clouds, compared to more simple single layer conditions with low layer clouds. The orange line of Figure 6.4 shows the skill score, when 10% of the days are filtered out of the validation data set. These filtered days include multi-layer conditions with middle and high layer clouds. We can observe a skill score improvement of up to 10%. The comparison of two example days shows this even more clearly. The yellow curve of Figure 6.4 shows the skill score of a complex multi-layer day with stratus/altostratus as well as cirrus/cirrostratus clouds. The persistence nowcast outperforms the presented nowcasting system on this day. On the contrary, on a single layer day with cumulus clouds, the presented nowcasting system clearly outperforms the persistence nowcast (see purple curve of Figure 6.4). The DNI curves of both example days are illustrated in Figure 6.5.

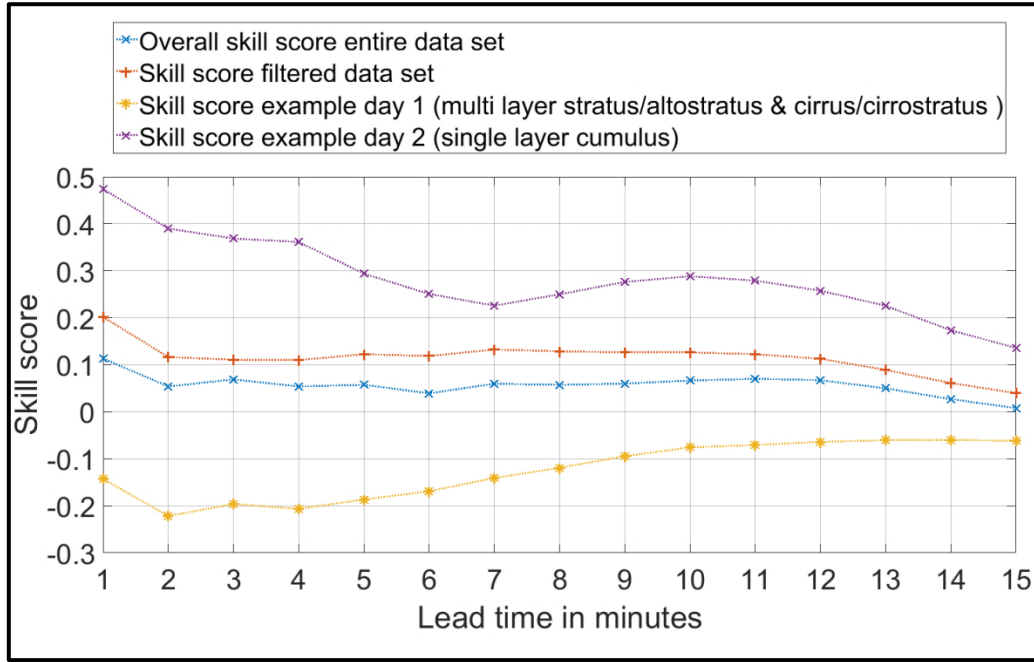


Figure 6.4: Skill score of entire data set (blue), filtered data set without 10 % of the most complex days (multi-layer including high layer clouds)(orange), complex example day with multi-layer stratus/altostratus & cirrus/cirrostratus clouds (yellow) and simple day with single layer cumulus clouds (purple)

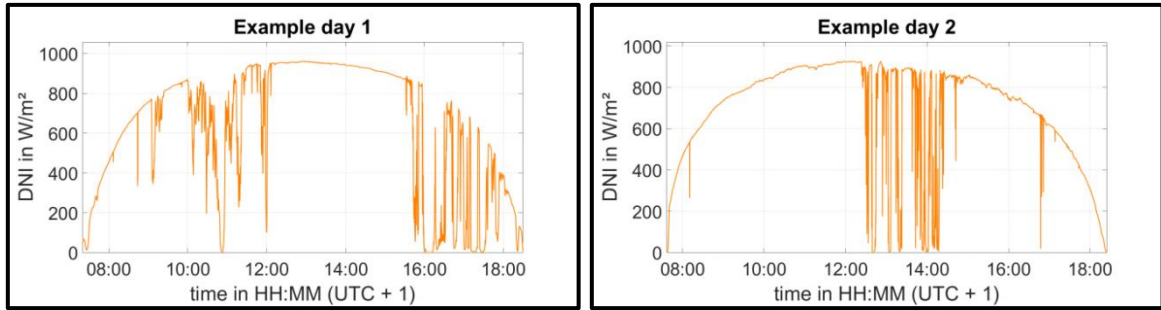


Figure 6.5: DNI curves of example days: (left) Example day 1 with complex multi-layer stratus/altostratus & cirrus/cirrostratus clouds. (right) Simple day with single layer cumulus clouds

6.2 Weather dependent uncertainty specification

As already mentioned, the performance of ASI-based nowcasting systems is strongly related to the prevailing weather conditions. Therefore, a novel validation procedure is introduced, which discretizes the data set in distinct weather conditions. This strategy is also utilized to introduce a real time capable uncertainty analysis, which takes spatial variations of the uncertainties into account. Section 6.2.1 introduces a temporal DNI variability classification which is utilized for the data discretization. The novel DNI variability class dependent validation is presented in section 6.2.2. In section 6.2.3 the system uncertainty under distinct conditions is identified. Spatial variations of the uncertainty within transient zones are introduced in section 6.2.4. Section 6.2.5 shows the validation results of the uncertainty analysis.

6.2.1 Temporal DNI variability classes

For the determination of real time uncertainties, a variability classification of the most recent irradiance conditions is used. This classification method is based on eight distinct variability classes for 1 minute resolved DNI data on an hourly basis, which can be used for systematic studies. Originally this procedure was introduced by **Schroedter-Homscheidt et al. 2018**, slight adaptations were included as explained later. The classes are as follows:

- Class 1 describes clear sky conditions.
- Classes 2 and 3 describe nearly clear sky conditions with a stronger variability and comparatively lower average DNI in the case of class 3.
- Class 4 shows a strong temporal variability but with an overall high average DNI.
- Class 5 describes less variable conditions with a lower average DNI compared to class 4.
- Class 6 resembles class 4 with a strong temporal variability, but with a significantly lower average DNI.
- Class 7 describes nearly complete overcast situations with some ramps.
- Class 8 corresponds to overcast situations.

The classification procedure described in **Schroedter-Homscheidt et al. 2018** uses 13 variability indices, which partially have been introduced in previous publications (see Table 6.2). It has to be pointed out that the definition of clear sky (class 1) must be viewed with caution, as clouds in the sky cannot be ruled out. The classification is done by comparing these 13 normalized variability indices with corresponding typical values for each variability class and determining the class with the lowest distance metric to the mean of a reference probability density distribution of all variability classes. These probability densities are derived once, using a manually classified reference data set (**Schroedter-Homscheidt et al. 2018**).

Table 6.2: Variability indices used by Schroedter-Homscheidt et al. 2018

Index	Description	Unit	Introduced by
CSFD	CSFD (number of Changes in the Sign of the First Derivative) applied for DNI	-	Kraas et al. 2013
meank _{cDNI}	$k_{cDNI} = DNI/cDNI$ as clear sky index (clear sky DNI := cDNI) Average clear sky index: $\bar{k}_{cDNI,\sigma} = \sum_{i=1}^n k_{cDNI,i}/n$	-	Perez et al. 2011
$\Delta k_{cDNI,\sigma}$	Standard deviation of deviation between consecutive clear sky index values $\Delta k_{cDNI,i} = \begin{matrix} k_{cDNI}(i) - k_{cDNI}(i-1) \\ \vdots \\ k_{cDNI}(n) - k_{cDNI}(n-1) \end{matrix}$ $\Delta k_{cDNI,\sigma} = \sqrt{\frac{1}{n-1} \sum_{i=1}^n (\Delta k_{cDNI,i} - \bar{\Delta k}_{cDNI})^2}$	-	Perez et al. 2011
Δk_{cDNI_mean}	Average of deviation between consecutive clear sky index values	-	Perez et al. 2011

The motivation for the reduction of the temporal resolution can be seen in Figure 6.6. The DNI of an example day, with highly variable and stable time windows, is depicted together with the clear sky DNI and the assigned variability class. A new assessment of the variability takes place with every new time stamp (1 min resolution), considering the prevailing DNI of the last 60 or 15 minutes. The 60-min approach is often too inert for an intra-hour consideration. This is particularly evident in the time windows from 11:54 to 12:38, 13:21 to 13:59, and 15:30 to 16:00, which show clear sky conditions. The 60-min approach reacts slower than the 15-min approach and misses the two clear windows from 13:21 to 13:59 and 15:30 to 16:00 completely. The 15-min approach reacts 2 minutes after the start of the clear windows by moving toward class 1.

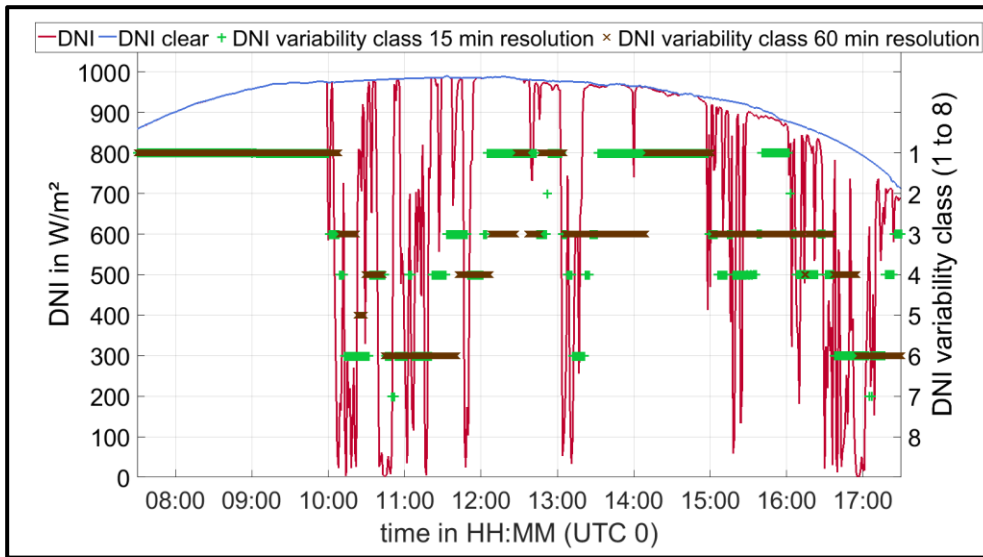


Figure 6.6: Measured DNI, clear sky DNI, and variability classification with 60-min and 15-min resolution for the 14.05.2016 at PSA.

It is analyzed whether a single point like DNI measurement (e.g., pyrheliometer) is meaningful to derive the variability class for an entire industrial size solar field of 2 km². A perfect match of the selected variability class is observed in 94.9% of all cases across a 30-day test period, comparing the classification based on a point like DNI measurement or the DNI field average derived from DNI maps. Therefore, it is concluded that a single point like measurement is suitable to identify the variability class for the whole area of a large commercial solar field. More detailed results of this analysis are given in appendix A.

6.2.2 DNI variability class dependent validation

The data set including the years 2016 and 2017 from section 6.1 is also used for the task of class dependent validation. For each time stamp the DNI variability is classified. Only the last 15 minutes of the DNI observation of one of the three reference pyrheliometer is used for the classification (sensor next to ASI 2, see Figure 3.2), according to the procedure described in section 6.2.1. As already mentioned, the point like measurement of a single pyrheliometer is sufficiently adequate to classify the area around the three reference pyrheliometers and two ASIs placed to each other at a largest distance of 891 m. The nowcasted DNI with lead times > 0 minutes could be used for the DNI variability classification. However, this would mean that the yet unknown uncertainties of the nowcasting system would affect the DNI classification, which, in turn, serves as the basis of the uncertainty analysis. The use of the more accurate measured DNI signal of the past 15 minutes might cause a poorly defined

uncertainty in the case of sudden atmospheric changes of the conditions, especially for high lead times, but this is only a short-term effect. As it is discussed in section 6.2.1, the DNI variability classification procedure on the basis of a 15-minute time window, reacts rapidly on any changes of irradiance conditions. Furthermore, additional spatial adaptations within transient zones of the DNI maps will be introduced in section 6.2.4, which reduce potential negative effects of the DNI variability classification with data from the recent past.

The temporal DNI variability classes of the data set are shown in Figure 6.7. Almost 70% of the data set belongs to the low variable clear sky conditions (class 1, 2 and 3). Around 17% of the data belong to variable and highly variable classes 4, 5 and 6. The remaining time consist of overcast conditions (class 7 and 8).

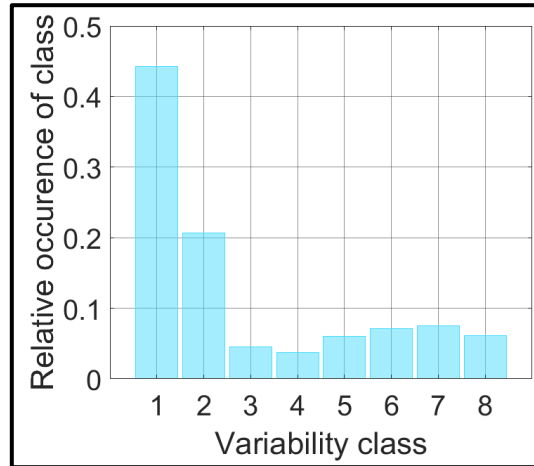


Figure 6.7: Histograms of temporal DNI variability classes at PSA for the years 2016 and 2017.

Figure 6.8 shows the MAD and RMSD distributed over DNI variability classes and lead time for the entire data set. The influence of the DNI variability classes is clear. The highest deviations are visible for the most variable classes 4, 6 and 7. These classes show also the strongest increase in deviation with lead time. For example the MAD in class 6 increases from 70 W/m² at lead time 0 minutes to 264 W/m² at lead time 15 minutes. Class 4, 6 and 7 are followed by Class 5, which shows a spread in MAD from 40W/m² to 215 W/m². Class 5 conditions are described with an intermediate variability as well as clear sky index. Class 3 and 8 are by definition very distinct. However, both classes show similar deviation over the lead times with a narrower spread compared to the previous classes. The spread in deviation over lead time is considerably lower for class 2 with an MAD of 23 W/m² to 109 W/m². The by far lowest deviations are seen in class 1. Class 1 has by definition a very low variability and a high clear sky index. Even the increase in deviations over lead times is considerably lower for class 1, with a spread in MAD of 7 W/m² to 30 W/m². The distinct behavior in deviations between class 1 and class 8 may be incomprehensible at a first glance. Both classes are defined by a very low variability. The reason for this considerable difference in these classes is that the nowcasting system does sometimes oversee clouds in a very cloudy sky. At the same time, it almost never occurs that clouds are falsely detected in an overall clear sky.

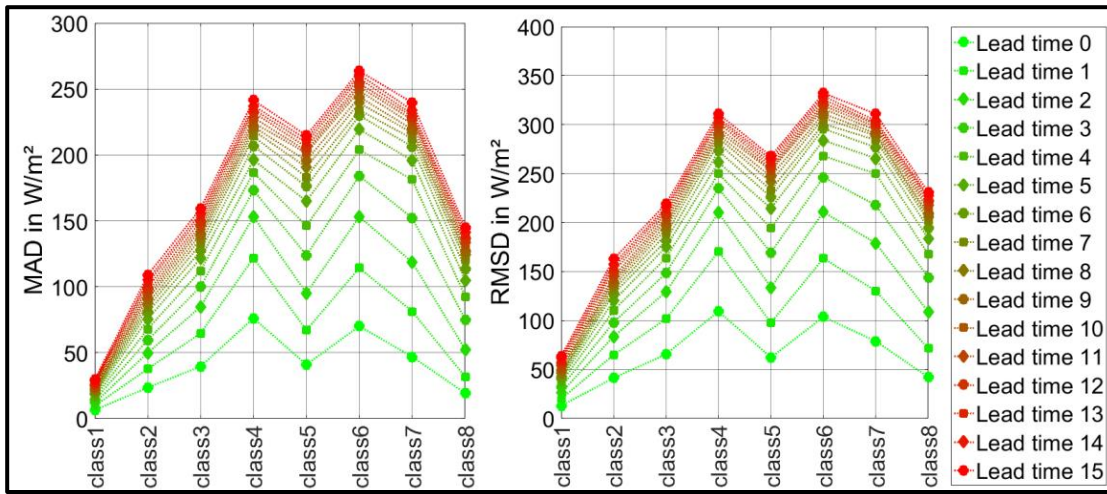


Figure 6.8: MAD & RMSD discretized over DNI variability classes and lead time in minutes at PSA for the years 2016 and 2017.

Besides the impact of the DNI variability classes on the error metrics, we can observe a significant fluctuation in the daily average error metrics per class. The daily MAD and RMSD distribution is shown as function of the lead time and DNI variability classes in Figure 6.9 and Figure 6.10. The mean over all days resembles the deviations shown in Figure 6.8. The small differences arise, since Figure 6.8 describes the average over all time stamps whereas Figure 6.9 and Figure 6.10 describe the error metrics over entire days. Each day gets the same weight for the final average.

Overall the box plots show a significant spread between the 25 and 75 percentiles in MAD and RMSD over all days. The strongest fluctuations over the days are visible within DNI variability class 8 and a lead time of 15 minutes, with a MAD spread of 42 W/m^2 (p25) to 349 W/m^2 (p75). The mean and median deviations over all days remain for class 8 lower compared to the more variable classes 4, 5, 6 and 7 with an MAD of 186 W/m^2 (mean MAD, class 8 and lead time 15 min) and 137 W/m^2 (median MAD, class 8 and lead time 15 min) respectively. These strong fluctuations over the days indicate that a discretization of the deviations in DNI variability classes by itself is not sufficient to explain the observed deviation. More factors, such as Sun elevation angle, cloud height, cloud type and cloud speed, which have no direct impact on the DNI variability classification have an influence on the nowcasting accuracy. Furthermore, complex multi-layer conditions are more error prone than single-layer conditions with low layer clouds (e.g. cumulus clouds). Worth mentioning are the conditions at the PSA. The PSA is less than 30 km away from the Mediterranean sea and surrounded by the four mountain ranges Sierra de Gádor, Sierra Nevada, Sierra de los Filabres and Sierra Alhamilla. These geographical circumstances often lead to fast changing complex conditions with a scattered cloud cover of multiple layers. Therefore, the strong fluctuations in nowcasting performance between days come as no surprise.

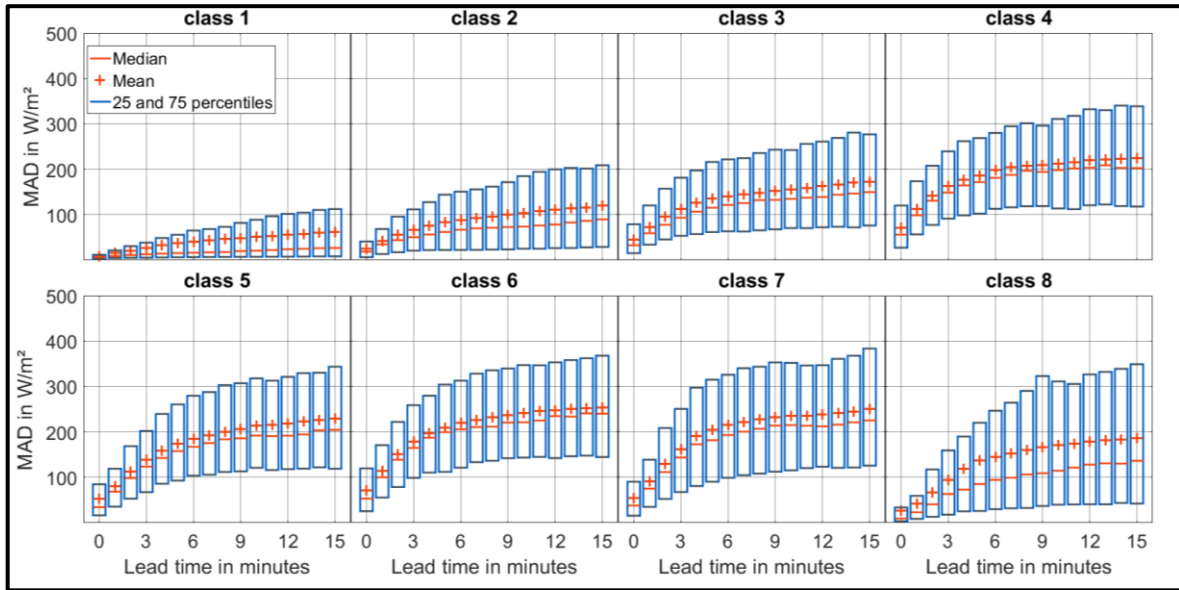


Figure 6.9: Daily distribution of MAD discretized over DNI variability classes and lead time at PSA for the years 2016 and 2017.

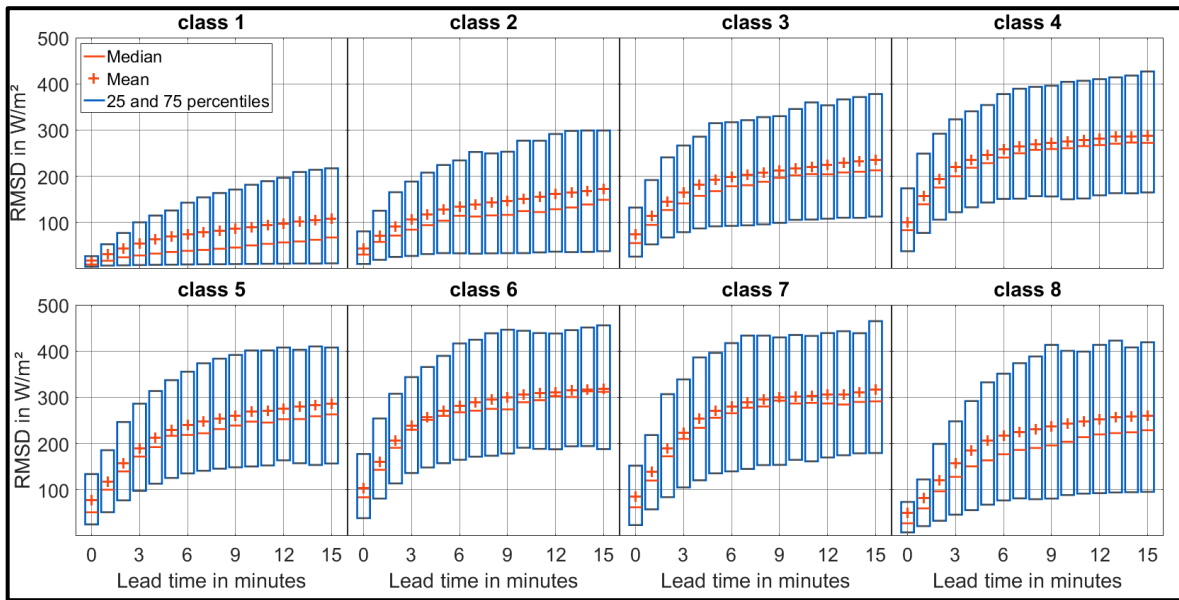


Figure 6.10: Daily distribution of RMSD discretized over DNI variability classes and lead time at PSA for the years 2016 and 2017.

6.2.3 Determination of uncertainties

In section 6.2.2 one could see a clear dependencies of the observed error metrics and the DNI variability classes. Nevertheless, it is also clear that additional effects play a significant role in the system uncertainty, as discussed in the previous section (see 6.2.2). In this section the so-called “basic uncertainty” of the nowcasting system is determined in dependence of the DNI variability classes and the Sun elevation angle. In section 6.2.4 an additional spatial component is added to the uncertainty, which accounts for increased uncertainties within transient zones close to cloud shadow edges and reduced uncertainties within stable zones of the DNI maps. These additional spatial components take into account the current cloud height, speed, Sun elevation angle and lead time.

The basic uncertainty of the nowcasting system is derived from the deviations between the reference sensors and the nowcasting system. Initially, the average deviation Dev_i between the three spatially distributed reference pyrheliometers and the corresponding nowcasting DNI from the DNI maps for each time stamp i is calculated according to Equation 6.1.

$$Dev_i = \frac{\sum_{st=1}^3 (DNI_{i,st,ref} - DNI_{i,st,nc})}{3} \quad \text{Equation 6.1}$$

The index st describes the reference station number, ref the reference DNI, and nc the corresponding nowcasted DNI. The resulting deviations for each image series are discretized over the DNI variability classes and two Sun elevation ranges (above and below 30°). The distribution of the deviations Dev_i over the entire data set is analyzed within each DNI variability class, Sun elevation range, and lead-time. Figure 6.11 shows the distribution within each DNI variability class and lead-time as a 2-D histogram with a logarithmic scale (Sun elevation angle above 30°). From the distribution within each DNI variability class, the upper (positive Dev_i values) and lower (negative Dev_i values) limits are detected, which frame a coverage probability of 68.3% (p68.3). These p68.3 values are marked as pink dashed lines in Figure 6.11, and describe always the smallest possible p68.3 interval. The discretization in two Sun elevation ranges above and below 30° is chosen due to notable deviation in p68.3 values between these Sun elevation ranges. The results of a study, which compares p68.3 values within different Sun elevation ranges, is presented in appendix B.

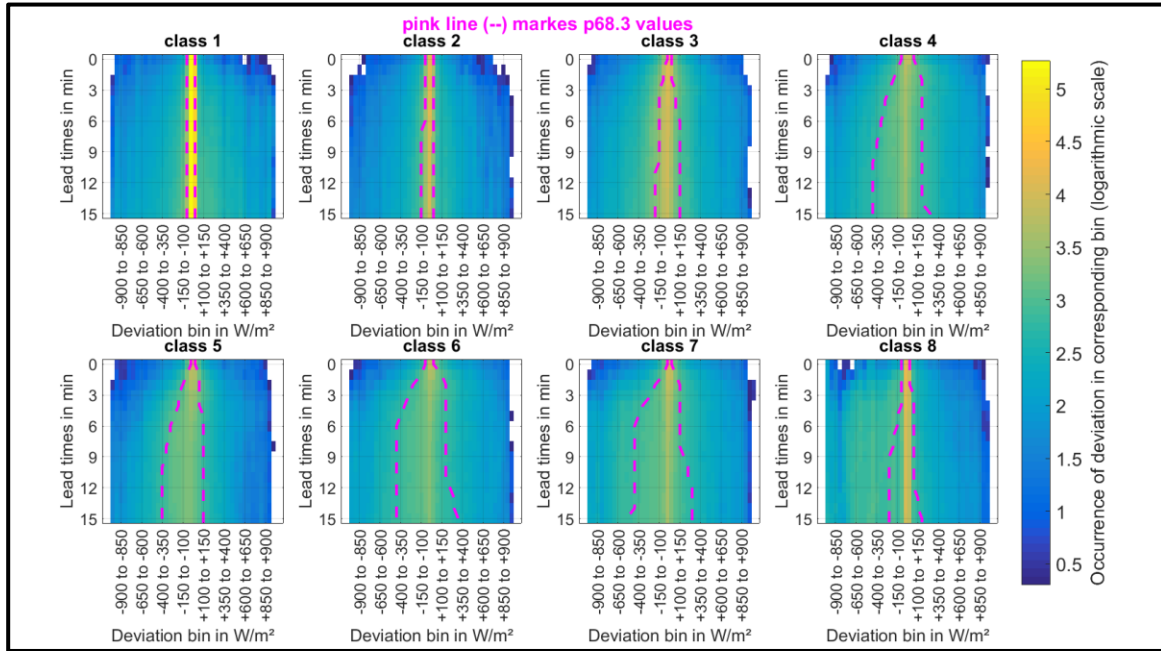


Figure 6.11: 2-D histogram of DNI deviations Dev_i for Sun elevation angles above 30° (shown as an example). A pink, dashed line marks the coverage probability of p68.3.

The p68.3 lower and upper range limits are saved in a look-up table, according to the DNI variability class, Sun elevation angle, and lead time (Figure 6.12). These values are considered as the basic uncertainty of the nowcasting system. In this thesis, I use the terms u_{up} for the positive and u_{low} for the negative part of the uncertainty. Class 1 and class 2 show the narrowest range between u_{up} and u_{low} with almost no impact on the lead-time. The remaining classes show an increasing range with an increasing lead-time. This increase of the u_{up} and u_{low} range is particularly strong within the lead times of 0 to 4 minutes, starting with a range of ± 100 W/m² or smaller for all classes. The widest u_{up} and u_{low} ranges are reached by the highly

variable classes 4 and 6 as well as class 7 and a lead-time of 15 minutes. For the Sun elevation range above 30° , class 7 shows a pronounced bias toward negative deviations. This bias exists also for the Sun elevation range below 30° , but is less pronounced. The bias indicates that the nowcasting system rather misses clouds than falsely detects a clear sky section as cloud. From the look up table, it is clear that the presented nowcasting system can deliver accurate DNI information for the current situation and immediate intra-minute nowcasts. However, the uncertainties increase rapidly in the case of variable conditions and higher lead times. During the operation of the nowcasting system, the DNI variability is classified constantly with measurements of the pyrheliometer. The expected basic uncertainty is derived from the look-up table shown in Figure 6.12 according to the current DNI variability class, Sun elevation angle, and lead-time.

For some applications, intra-minute nowcasts could be of interest as e.g., in the aim point strategy of solar tower power plants (Schwarzbözl et al. 2011). As it can be seen in Figure 6.12, the uncertainties for lead times up to 1 minute ahead and all DNI variability classes is below $\pm 150 \text{ W/m}^2$, for the presented nowcasting system.

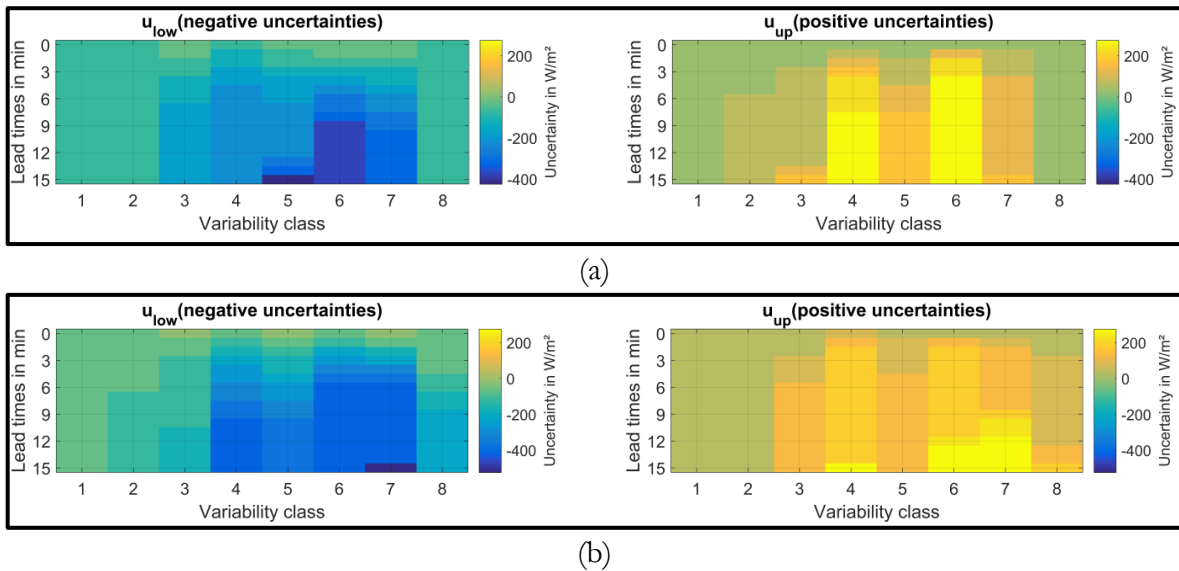


Figure 6.12: Basic uncertainty values corresponding to coverage probabilities of 68.3% discretized over lead times and variability classes. (a) Sun elevation angles up to 30° . (b) Sun elevation angles above 30° .

6.2.4 Real time uncertainty assessment of spatial DNI maps

The nowcasting system delivers three distinct DNI maps for each time stamp and lead time, including the standard DNI map without uncertainty, the DNI map with u_{up} as the upper limit, and the DNI map with u_{low} as a lower limit. A direct homogenous application of the basic uncertainty on the spatial DNI maps is not useful. Corrections are necessary for some areas of the DNI map. On the one hand, there are physical boundaries. The DNI values of the DNI map cannot drop below 0 W/m^2 or surpass the current clear sky DNI. The u_{up} and u_{low} are adjusted in regions of the DNI map, where these physical boundaries would be surpassed. DNI values of these regions are set to 0 W/m^2 or to the current clear sky DNI, respectively. On the other hand, transition zones lead to a spatially limited increase of the uncertainties. These transition zones describe areas close to cloud shadow edges on the DNI maps. Erroneous shadow edge positions lead to large, spatially confined errors of the DNI magnitude, depending on the prevailing clear sky DNI and cloud transmittance for the

corresponding DNI map pixel. Figure 6.13 illustrates the expected and possible alternative cloud edge position as well as the influence of uncertain cloud edge positions on the spatial DNI information around an arbitrary reference point.

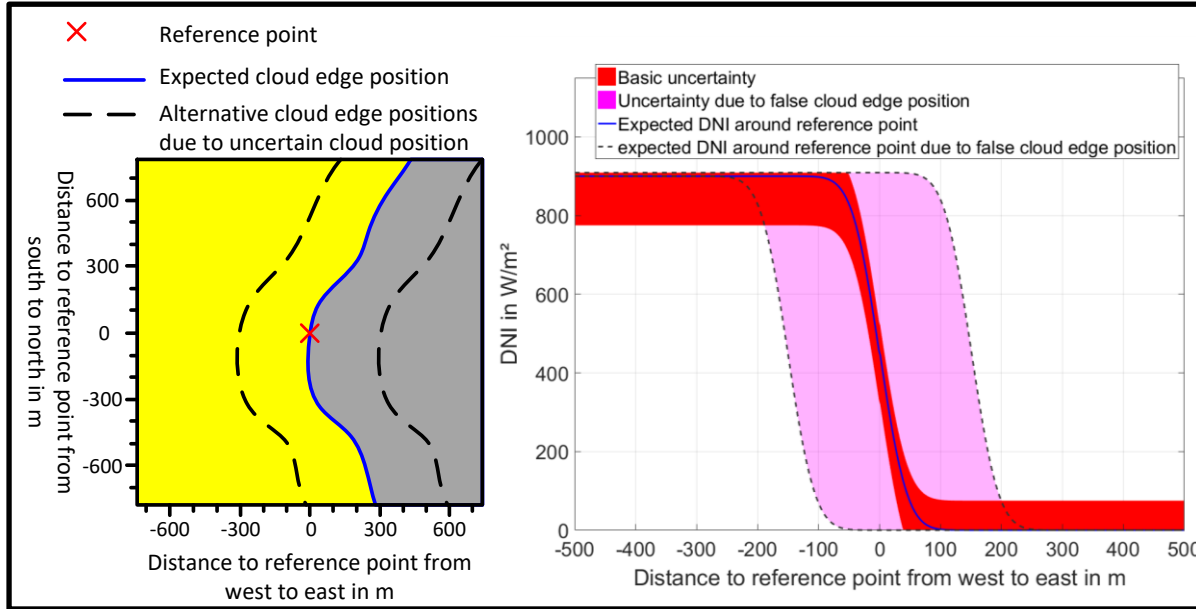


Figure 6.13: Influence of erroneous positions of cloud edges on expected uncertainties. (left) Illustration of expected and alternative cloud shadow edge positions. (right) Expected uncertainty around an arbitrary reference point. The uncertainty within the stable zone consists only of the basic uncertainty. The uncertainty in transient zone increases due to the uncertain cloud edge position.

For the nowcasting system, the main sources of errors of the shadow positions are the cloud height detection and cloud tracking. **Kuhn et al. 2019a** investigated the impact of the ideal camera distance for cloud height measurements with ASIs. The used setup with an ASI distance of roughly 494 m and orthogonal image resolution of 1MP (maximum zenith angle of 78°) is less suitable for cloud heights above 5000 m (**Kuhn et al. 2019a**). These results are in alignment with actual cloud height and tracking validation results of the used nowcasting system (see section 4.3 and 4.4). The overall results of the validation are presented in Table 6.3, discretized over cloud height and cloud speed ranges. The increase of the deviations for higher cloud height ranges and cloud speed ranges is due to the used ASI setup and the chosen resolution. For the cloud movement directions, an overall MAD of 12.8° was determined.

Table 6.3: Validation results of ASI-based cloud height and cloud tracking approach over cloud height and cloud speed ranges for the selected multi-ASI configuration

Cloud Height Range	MAD Cloud Height	Cloud Speed Range	MAD Cloud Speed
0–3000 m	312 m	0–6 m/s	1.33 m/s
3000–6000 m	996 m	6–12 m/s	1.92 m/s
6000–9000 m	2665 m	12–18 m/s	2.52 m/s
9000–12000 m	2431 m		

The impact of an uncertain cloud height on the cloud shadow position depends on the Sun elevation angle. Lower Sun elevation angles lead to more pronounced uncertainties of the cloud shadow position. This effect is illustrated in Figure 6.14.

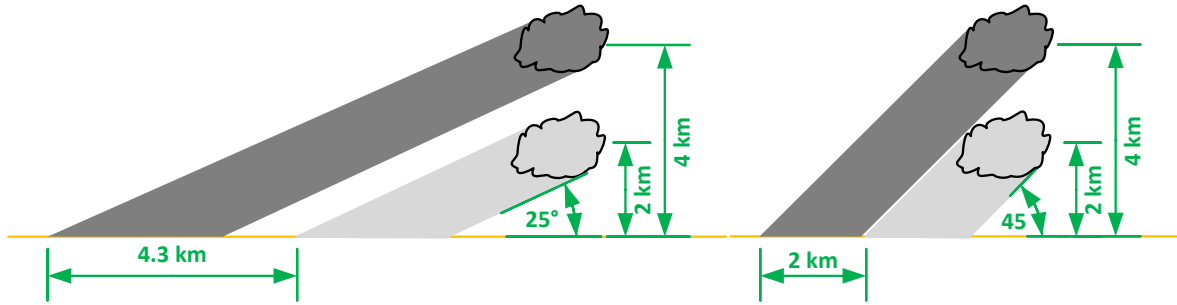


Figure 6.14: Impact of false cloud height on cloud shadow position for two distinct Sun elevation angles.

The influence of an erroneous cloud speed on a false cloud shadow position increases with lead-time. Figure 6.15 shows the expected uncertainties on the cloud shadow edge position due to the expected uncertainties in cloud height and cloud speed for some exemplary Sun elevation angles and lead times. During the operation, the uncertainty of the cloud shadow position is estimated according to the currently measured average cloud height and cloud speed as well as the Sun elevation angle and lead-time. The uncertainties due to cloud height and cloud speed are combined by means of a squared sum. Further sources of erroneous shadow positions (camera alignment, camera calibration, cloud segmentation, cloud movement direction, and shadow projection) are already included in the cloud height and speed uncertainties or have a comparably small impact, which currently cannot be quantified in real time. Therefore, they are assumed to be the same for all pixels in the uncertainty map and to be covered by the basic uncertainty, as presented in section 6.2.3. The influence of the cloud movement direction is considered by treating the uncertainty of the cloud shadow edge homogeneously around the cloud edge.

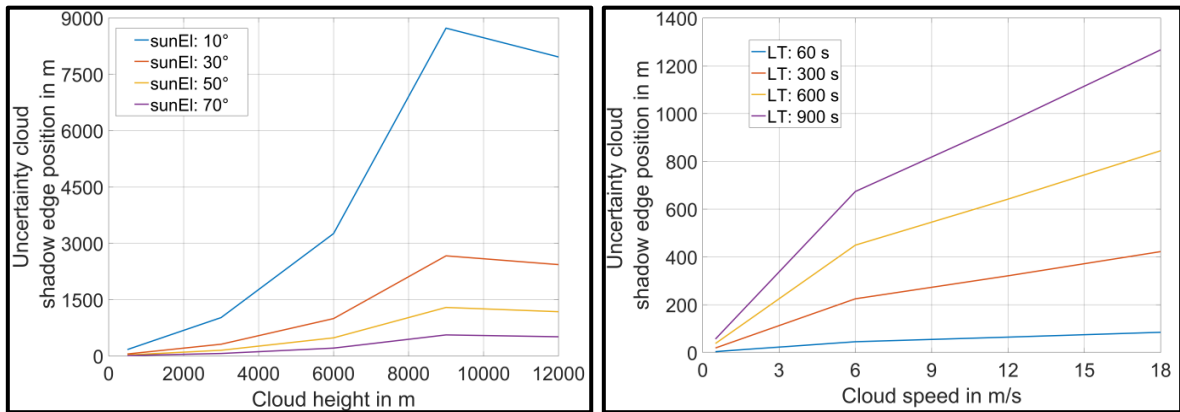


Figure 6.15: (left) Expected uncertainty of the cloud shadow edge position due to cloud height and some examples of Sun elevation angles. (right) Expected uncertainty cloud shadow edge position due to cloud speed and some exemplary lead times.

The combined uncertainty of the cloud shadow edge position describes the width of the current transient zone with expected higher uncertainties. The implementation of the uncertainties on spatial DNI maps is shown schematically in Figure 6.16. This procedure consists of four processing steps, which are described below.

- The basic uncertainties corresponding to the DNI variability class, Sun elevation angle, and lead time are added to the DNI map → taking the previously described physical boundaries into account.
- The DNI map is converted into a binary map (true = shaded). The expected uncertainty of the cloud shadow edge position is used as the width to dilate (lower

uncertainty range) and erode (upper uncertainty range) the shaded part of the binary map. The used morphological filters are based on the intrinsic MATLAB® functions `imdilate` and `imerode` according to **Van Den Boomgaard & Van Balen 1992**.

- The transient and stable zones of the DNI maps are detected by comparing the original binary map to the binary maps treated by the morphological filters. All pixels with a changed status are part of the transient zone.
- Final DNI maps with uncertainty are created by a linear 2-D interpolation between shaded and clear areas, which are only within the transient zones.

The combined binary map with stable and transient zones indicates low (stable) and high (transient) uncertainty areas. The actual final spatial upper and lower uncertainties can be calculated by the differences between the DNI map without uncertainty and the final DNI maps with uncertainties.

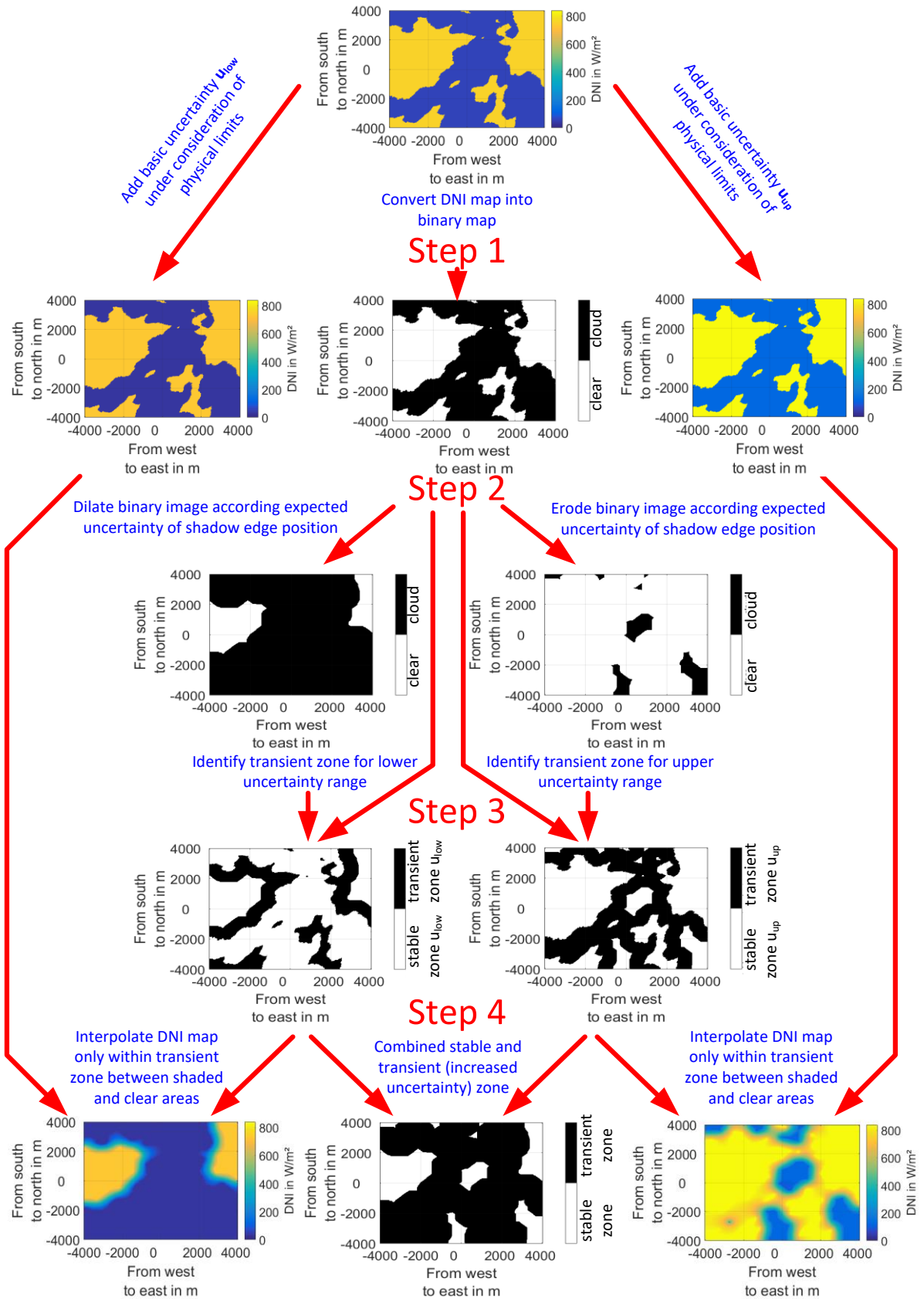


Figure 6.16: Processing steps for determining DNI maps including the spatial uncertainty information.

6.2.5 Final adjustments of uncertainty and validation

The basic uncertainty is defined by a coverage probability of 68.3%. The spatial filter will lead to an increase of the coverage probability due to the partial increase of the uncertainty within the transient zones. The coverage probability after introducing the spatial filters is investigated with the three reference pyrheliometers number 1, 2, and 4 (see Figure 3.2). For this, a new dataset is used, consisting of the entire year 2018. DNI maps with the upper and lower uncertainty range for 16 lead times (0 to 15 in 1-minute steps) are created. Subsequently, it is compared whether the detected deviation between measured and predicted DNI is within the expected uncertainty range for the three corresponding pixels of the DNI maps with uncertainty. Lastly, the resulting coverage probability of the allocated uncertainties within each DNI variability class and lead-time is analyzed over the entire validation data set. The introduction of the spatial filter increased the average coverage probability from 68.3% to roughly 74% (Figure 6.17 (left)) over all DNI variability classes and lead times. Therefore, the basic uncertainty is adjusted (reduced) for each DNI variability class and lead-time, such that the average of all classes per lead-time is roughly 68.3% again (Figure 6.17 (right)).

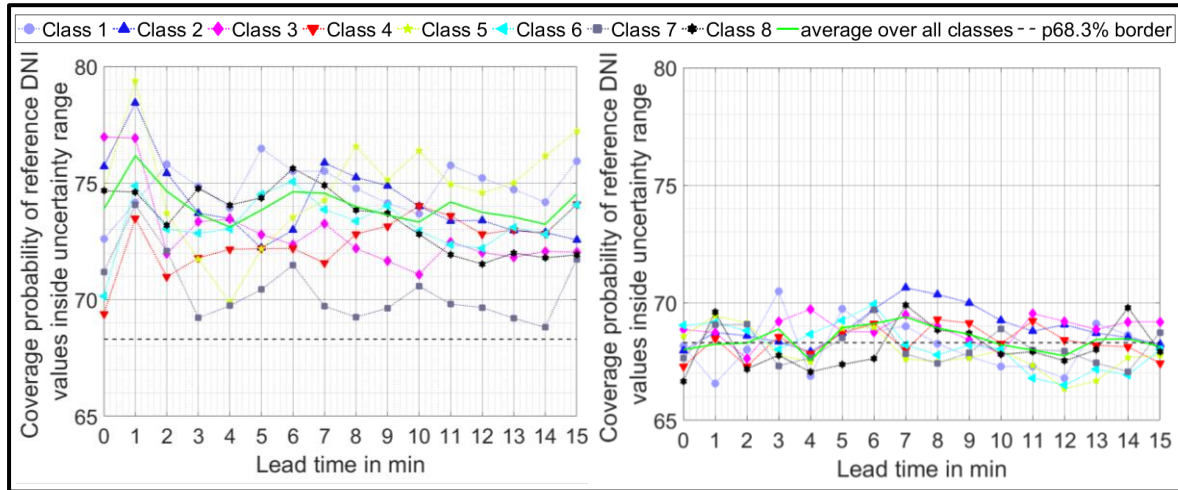


Figure 6.17: (left) Average coverage probability within uncertainty ranges without adjustments of basic uncertainties. (right) Average coverage probability within uncertainty ranges with adjustments of basic uncertainties.

The adjusted (reduced) basic uncertainty is shown in Figure 6.18. The most notable adjustments are needed for the highly variable and heavily clouded class 6. This comes as no surprise since these are the conditions with the largest share of transient zones. As previously mentioned, the transient zones are currently defined by the expected uncertainties due to the cloud height and tracking algorithm. A future real-time quantification of the spatial uncertainty effects of additional uncertainty sources (e.g., segmentation) would allow a more precise description of the transient zones in return of a further reduction of the basic uncertainty.

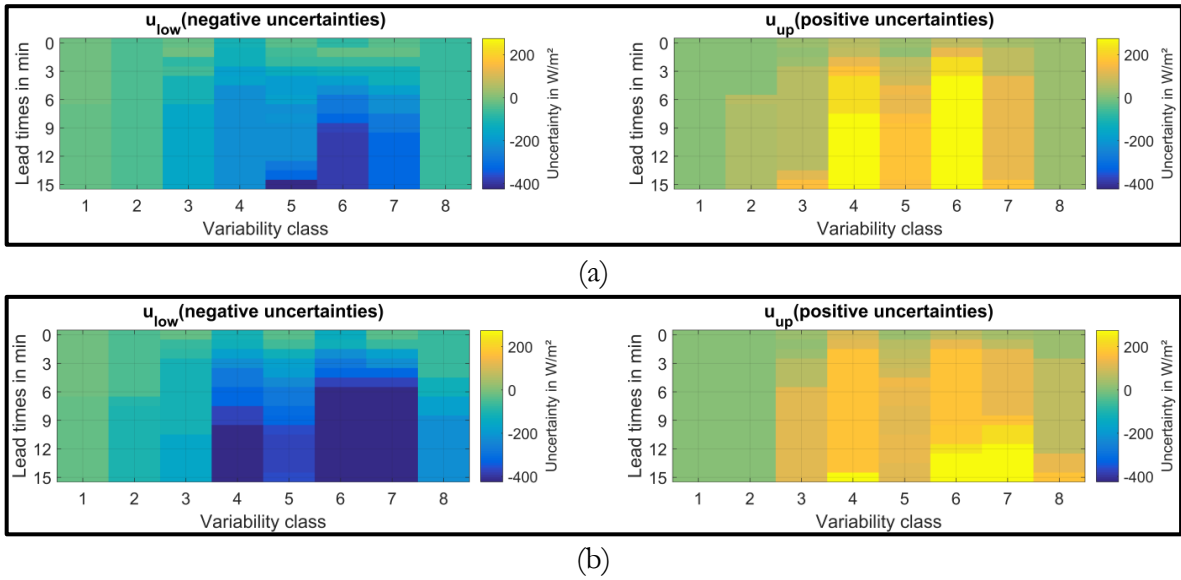


Figure 6.18: Basic uncertainty values adjusted for spatial filter with final coverage probabilities of 68.3% discretized over lead times and variability classes. (a) Sun elevation angles up to 30°. (b) Sun elevation angles above 30°.

Figure 6.19 illustrates the DNI maps with and without final uncertainties for three distinct lead times (0, 4 and 8 min). A highly variable class 4 scenario is shown (average cloud height of 6 km (altostratus clouds), average cloud speed of 16 m/s, Sun elevation angle 40°). These are challenging conditions for the nowcasting system, which is reflected by the large variations between the upper and lower limits. Under such conditions, accurate nowcast for higher lead times are not conceivable with the presented nowcasting system. The uncertainties amount to +79 W/m² and -325 W/m² for the clear areas with a lead-time of 4 min. Figure 6.20 shows a different scenario with DNI variability class 3 and less complex cumulus cloud conditions, with an average cloud height of 1.5 km, an average cloud speed of 8 m/s, and a Sun elevation angle of 55°. The less pronounced effect of the transient zones compared to the more complex class 4 scenario is clearly notable. Furthermore, the absolute uncertainties are considerably lower with +7 W/m² and -52 W/m² for the clear areas with a lead-time of 4 min.

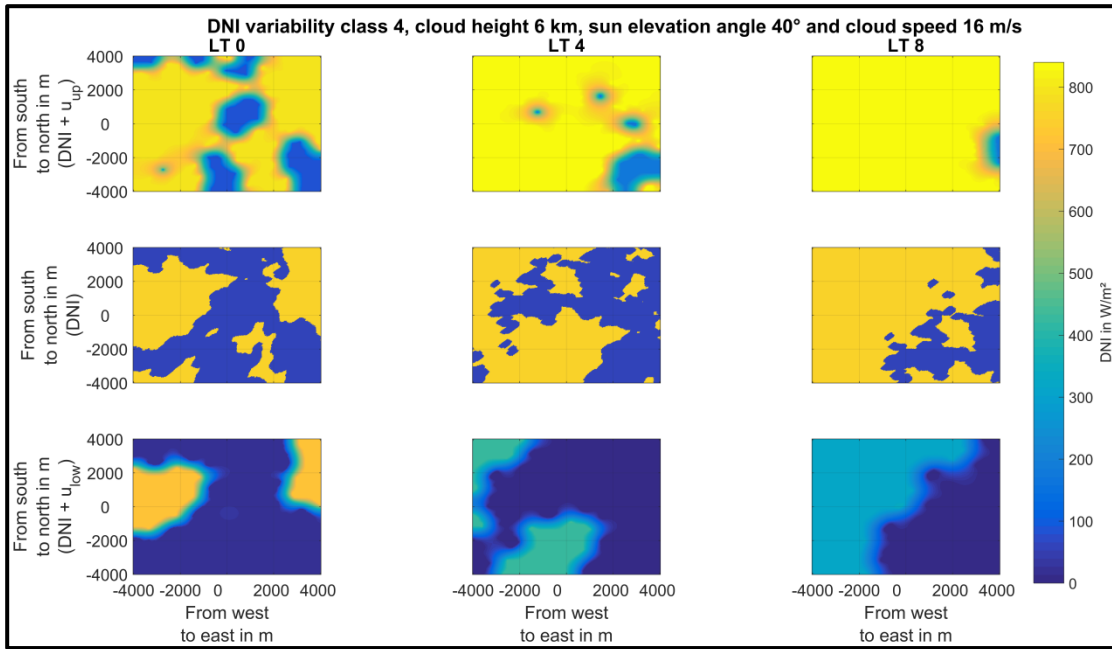


Figure 6.19: DNI and uncertainty maps (class 4: highly variable conditions), first row: DNI map + u_{up} adjusted and eroded, second row: DNI map and third row: DNI map + u_{low} adjusted and dilated, column 1: lead-time of 0 minutes, column 2: lead-time of 4 minutes, and column 3: lead-time of 8 minutes.

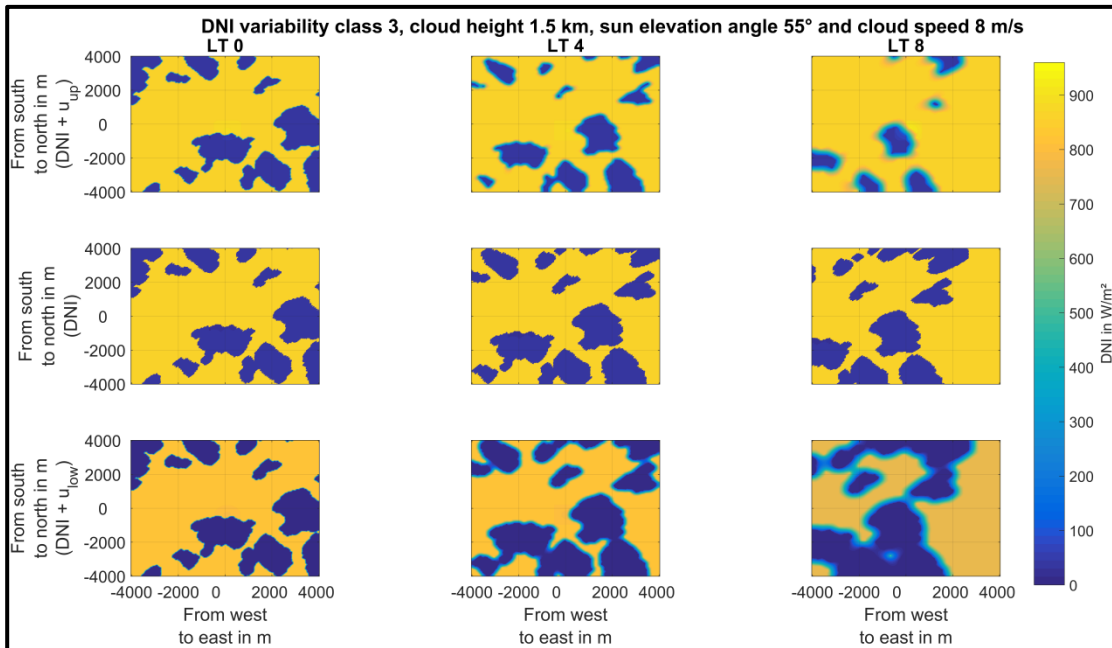
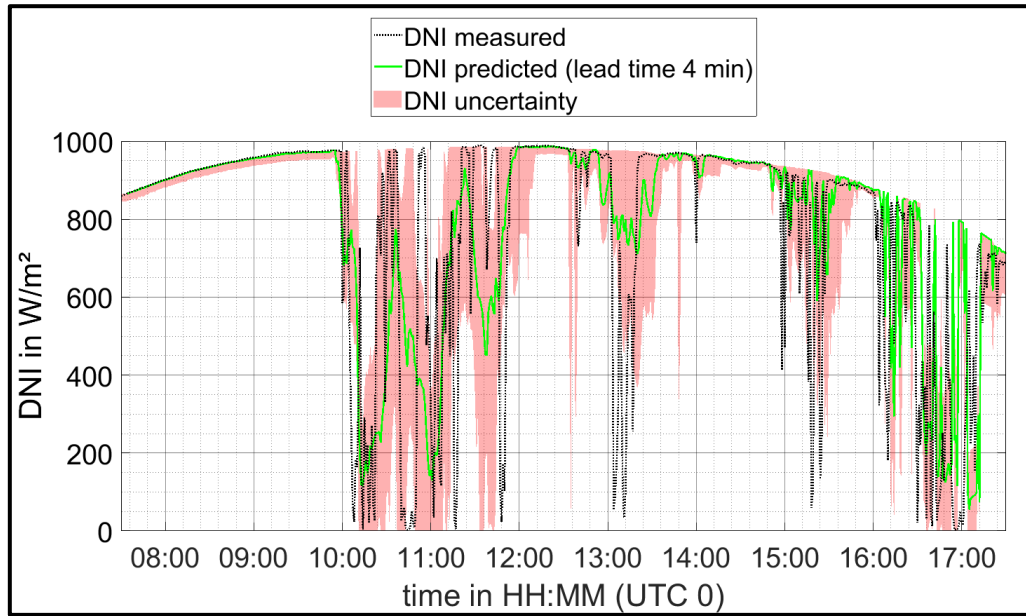
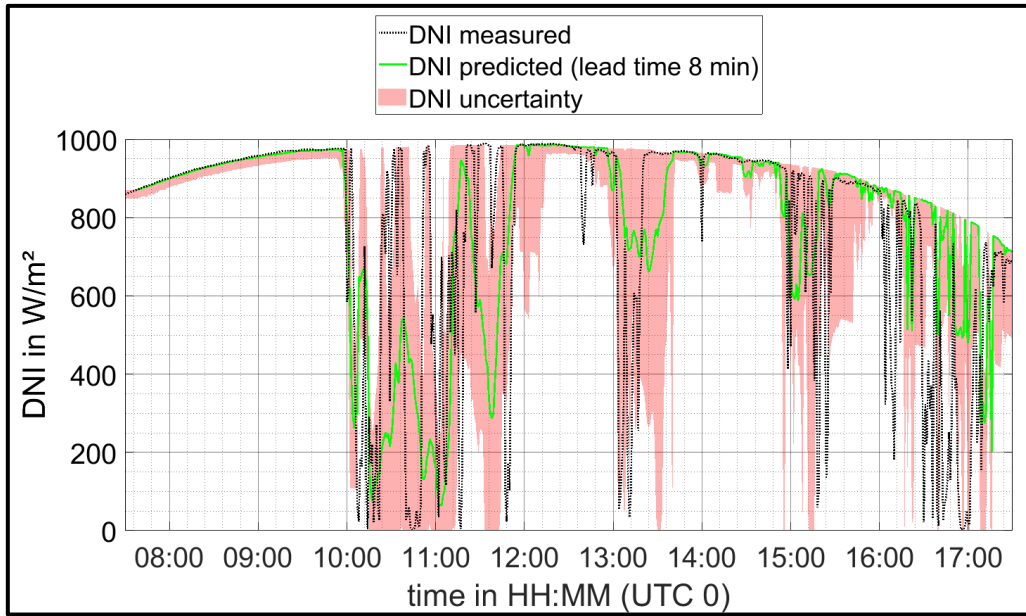


Figure 6.20: DNI and uncertainty maps (class 3). First row: DNI map + u_{up} adjusted and eroded. Second row: DNI map and third row: DNI map + u_{low} adjusted and dilated. Column 1: lead time 0 minutes, column 2: lead time 4 minutes, and column 3: lead time 8 minutes.

The expected uncertainties over a highly variable day, corresponding to a single pixel of the DNI maps, are illustrated in Figure 6.21. The used pixel describes the position of the ASI 2 and reference pyrheliometer 1 (see Figure 3.2). Exemplarily lead-time of 4 and 8 min are shown. The predicted DNI is always within the uncertainties. The DNI measured by the pyrheliometer is partially outside the bandwidth described by the uncertainties. This was to be expected, with a coverage probability of roughly 68.3% for the uncertainty.



(a)



(b)

Figure 6.21: Measured and predicted DNI as well as uncertainty of predicted DNI. Measured and predicted DNI correspond to the position of ASI 2 and reference pyrhelimeter 1. (a) Predicted DNI with a lead time of 4 minutes. (b) Predicted DNI with a lead time of 8 minutes

6.3 Nowcast uncertainties at different geographical locations

For a potential application of the nowcasting system, the expected uncertainty at the site of interest is required. The expected average uncertainty of a nowcasting system depends on the site conditions. Using site specific uncertainties the feasibility of the application can be analyzed. In this section, the expected uncertainties for two sites are determined. Only DNI measurements of the different sites as well as the basic uncertainty introduced in Section 6.2.3 are used. One site is the PSA and the other site is in New Delhi, India. The facility in India

belongs to the National thermal power corporation Energy Technology Research Alliance (NETRA). The exact locations are given in Table 6.4.

Table 6.4: GPS coordinates of both test sites

	Latitude	Longitude	Altitude
PSA	37.0909°N	2.3581°W	500 m
NETRA facility	28.5019°N	77.4650°E	195 m

Pyrheliometric DNI measurements for both sites for the year 2017 are analyzed in one-minute resolution. The variability of the DNI is classified for both sites according to the procedure described in section 6.2.1. The variability class distribution over the entire year 2017 is shown in Figure 6.22. For PSA, more than 60% of the cases are clear sky conditions (class 1 and class 2). Due to the hazy conditions at the NETRA site, class 1 conditions are rare but the more variable class 5 shows the highest occurrence. Overall, the NETRA site has a higher count for the four classes 5, 6, 7, and 8 with a lower average DNI. This is also apparent when looking at the yearly DNI sum. Despite the higher latitude, PSA shows a yearly DNI sum (2017) of 2430 kWh/m² compared to about 1160 kWh/m² at the NETRA site.

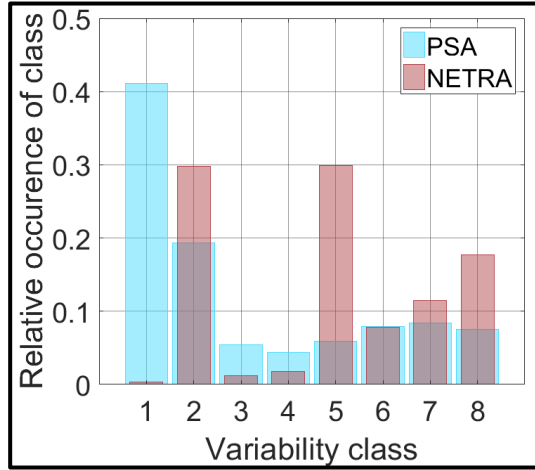


Figure 6.22: Histograms of temporal DNI variability classes at PSA and NETRA for the year 2017.

Each time stamp receives an uncertainty value corresponding to the present DNI variability class, Sun elevation angle, and lead-time from the look-up table illustrated in Figure 6.12. The average uncertainty is calculated over the entire data set and for different lead times. This overall average expected uncertainty is illustrated in Figure 6.23. It can be seen that similar uncertainties are expected for a lead-time of 0 min. As already mentioned, only minor differences are present at a lead-time of 0 min for the uncertainty values between the eight DNI variability classes. However, the expected uncertainties increase more for the NETRA site with an increasing lead time due to the more frequent occurrence of highly variable conditions compared to PSA. Thus, a better overall performance of the nowcasting system is expected for the PSA. Such initial estimates can be made at any site, if sufficient DNI data are available. This site-specific uncertainty estimate can help to evaluate the potential benefit of a nowcasting system for the plant and grid operation.

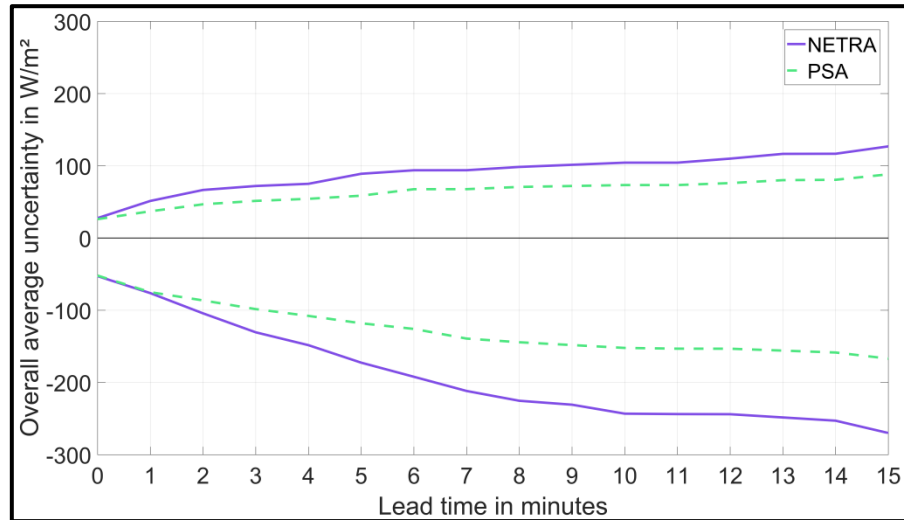


Figure 6.23: Overall average expected nowcasting uncertainty for the NETRA facility and PSA (entire year 2017).

6.4 Conclusion on validation and uncertainty analysis of DNI maps

Three ground based pyrheliometer stations were used to validate the overall DNI nowcast. Over the two years validation period (2016 and 2017) a relative bias, MAD and RMSD of 2%, 4% and 8% respectively were found for a lead time of 0 minutes. The deviation metrics rise up to 5%, 15% and 23% respectively for a lead time of 15 minutes ahead. Cloud tracking and transmittance estimation uncertainties, are the main cause for increased deviation with higher lead times. The increase of the deviations with higher lead times are dominated by a steep rise within the first four minutes, then the deviation metrics curves flatten out. This is due to the fact that in the case of low lead times actual transmittance measurements are frequently available for the relevant clouds. For higher lead times the transmittance values of the relevant clouds are in almost all cases estimated values.

Similar validation procedures are often described in the literature (e.g. **Bernecker et al. 2014**, **Schmidt et al. 2016**, **Xia et al. 2015**, **Fu & Cheng 2013**). All these procedures have in common that the dependency on the weather situation can only be taken into account by choosing a long-term data set for the validation. Within this long term data set strong deviation due to distinct weather conditions are to be expected. For example the influence of complex multi-layer conditions compared to more homogeneous single-layer on the skill score was discussed. We can conclude that the comparison of nowcasting systems on the basis of a single number per metric and different data sets remains a difficult task. Furthermore, they are neither suitable to determine the real time accuracy of a nowcasting system in the actual weather situation, nor suitable to describe any spatially resolved nowcast accuracy.

In this work, a real-time capable method for a weather-dependent uncertainty specification of DNI nowcasts was presented. The DNI was classified in one of eight DNI variability classes, according to (**Schroedter-Homscheidt et al. 2018**). The original classification approach was adapted from 1-hour time intervals to 15-minute intervals.

Initially the two year data set was discretized over the DNI variability classes. A clear dependency between the magnitude of overall MAD and RMSD error metrics and the DNI variability classes was visible, with the highest deviation for the variable classes 4 and 6 as well as class 7. On the other hand, the lowest deviations were observed under class 1 conditions. Yet, the distribution of MAD and RMSD error metrics over individual days indicated that

DNI variability classes by itself do not include all the main influencing factors affecting the system uncertainty. Therefore, a procedure was developed which incorporates also the Sun elevation angle, cloud height and tracking.

First, the DNI variability and the errors of the ASI nowcasts at PSA were studied over the 2-year period. Nowcasts up to 15 minutes ahead were created over the same period. For each data sample, the deviation between three reference pyrheliometers and the corresponding DNI values from the DNI maps was calculated and discretized in a DNI variability class, Sun elevation angle, and lead time. For each combination of the DNI variability class, the Sun elevation angle, and lead-time, the deviation with a coverage probability of 68.3% was identified and saved into a look-up table describing the basic uncertainty due to the atmospheric variability. As expected, the largest deviations were observed for highly variable conditions. Furthermore, the deviations increase with the nowcast horizon.

The nowcasting system creates DNI maps with an edge length of 8 km. Therefore, spatially resolved uncertainty information is of interest. Transient zones from clear to cloudy areas lead to an increased uncertainty, which is not described sufficiently by the basic uncertainty. The uncertainty in the transient zones can be described considering the uncertainty of the position of the cloud shadow edges. The main source for uncertain cloud shadow edge positions are the cloud height detection and cloud tracking. The expected width of the uncertain transient zones was estimated using previously obtained validation results of the cloud height and cloud tracking (see section 4.3 and 4.4). A methodology was presented, which identifies the most accurate and the less accurate zones of the DNI maps, using morphological filters and partial 2-D interpolations. This innovative method allows a spatial accuracy assessment, which goes far beyond the previously used accuracy metrics of RMSD, MAD, bias, and skill scores for spatially resolved DNI nowcast. Such an approach could also be adapted for satellite and weather model based irradiance maps and forecasts.

The uncertainty increase in the transient zones leads to an increase of the average coverage probability of the uncertainties from 68.3% to 74%. The coverage probability was reduced to an average coverage probability of roughly 68.3% by adjusting/reducing the basic uncertainty. For this validation procedure, a new data set (year 2018) was used, which is independent from the dataset used for the uncertainty specification. The final nowcasted DNI maps, as well as upper and lower limits, were presented in two example scenarios. These scenarios represent distinct DNI variability classes, cloud heights, cloud speeds, lead times, and Sun positions. Furthermore, exemplarily measured DNI, predicted DNI, and the allocated uncertainties for a highly variable day were presented, corresponding to a single pixel of the DNI maps. A further improvement of the spatial uncertainty could be achieved, with a real-time quantification of the spatial effects on the uncertainty for additional uncertainty contributors (e.g., segmentation). This would allow a further reduction of the basic uncertainty in return for a simultaneous increase of the uncertainty in corresponding areas of the DNI maps.

The presented nowcasting system is capable of creating such DNI maps in real-time for 16 distinct lead times up to 15 minutes ahead.

Since the DNI variability classes are not site dependent, the expected basic uncertainty of a nowcasting system at any geographical location can be estimated by a sufficiently long time series of DNI measurements of at least one year and the basic uncertainty look-up table. The expected average uncertainties for lead times up to 15 minutes ahead were compared, between the PSA and a NETRA site in Northern India, for the year 2017. Higher uncertainties are expected for the NETRA site, due to more variable conditions.

Further developments could be useful for multi-layer cloud situations. As mentioned in section 6.1, ASI-based nowcasting systems are less accurate during complex multi-layer cloud conditions compared to single-layer cloud conditions. By including an automatic classification between single-layer and multi-layer cloud conditions, as presented by (**Huertas-Tato et al. 2017**), the created look-up tables with p68.3 values could be extended by an additional dimension. This could further improve the allocation of uncertainties, which corresponds- to the prevailing weather conditions.

To the best of my knowledge, the presented procedure is the first to provide real-time uncertainties for ASI-based nowcasting systems.

7 Control optimization of PT solar fields with DNI maps

In this chapter, the actual benefit of spatial DNI information for PT solar field controller is investigated, taking into account the corresponding uncertainties. Spatial DNI informations for the current condition already contain a significant potential for optimizations of PT solar field controller. Therefore, in this work the focus is set in investigating the potential benefit of lead time 0 minutes. Future research will consider also the nowcasts as additional input for solar field control optimizations. Model predictive control strategies could be used for this purpose.

Figure 7.1 illustrates the chosen approach for the investigation of new solar field controller, with access to spatial DNI information. The ASI derived DNI maps are provided to the solar field controller in the form of the DNI field average and the DNI variability classification. The classification considers both the DNI variability in time and space. The uncertainties of the ASI system are considered by including additional spatial DNI information from the fundamentally distinct shadow camera system (see section 2.1.2), which will provide the actual DNI conditions acting on the solar field, whereas the solar field controller will receive the DNI information from the ASI system. Ideally this allows the quantification of the impact achievable by ASI based control schemes, with actual divergent weather conditions unknown by the solar field controller. Of course the shadow camera system is not perfect by itself. However, the spatial DNI information of the ASI system and the shadow camera system are based on completely different approaches and hence represent independent data sets. A benchmarking campaign between the ASI system and the shadow camera system with three reference pyrheliometers over 22 variable days was conducted by **Kuhn et al. 2019b**. For lead time 0 minutes, the shadow camera system reached a rel. RMSD of 10.2%, rel. MAD of 6.7% and a rel. bias of 3.3% compared to a rel. RMSD of 15.1%, rel. MAD of 9.2% and a rel. bias of 6.7% for the ASI system.

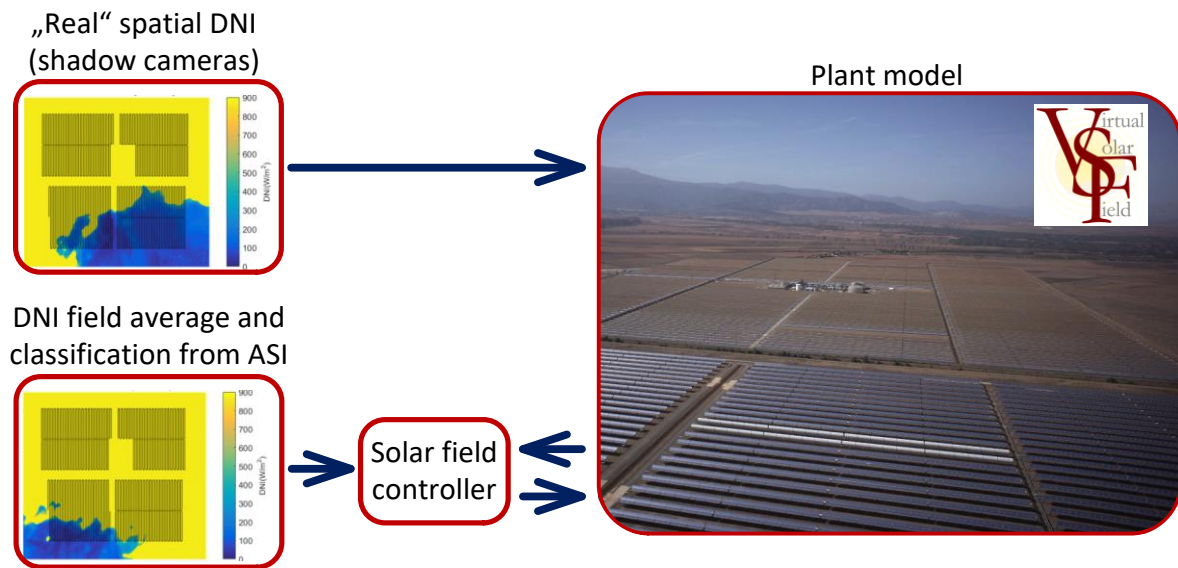


Figure 7.1: Schematic representation of the VSF simulations with spatial DNI information from two distinct nowcasting systems.

Section 7.1 introduces the applied spatial as well as combined spatial and temporal classification methods. Two new solar field control strategies based on the DNI variability classes are presented in section 7.2. These new controllers are tailored to a solar field design according to the Spanish commercial 50 MW power plant La Africana. Section 7.2 includes also results of a comparison of these new control strategies with a state of the art reference controller, again tailored to the La Africana solar field design. In section 7.3, the applicability of the new class dependent control strategies are identified and the performance results of a hybridized control strategy are presented. Due to the availability of the shadow camera system the solar field simulations are limited to 22 days. Therefore, results of a performance estimation of the class dependent control strategies over a 2 year period are presented in section 7.4. Finally, I conclude the findings of this chapter in section 7.5.

The content from this chapter has partially been published in **Nouri et al. 2019d** and **Nouri et al. 2019f**.

7.1 Spatial as well as combined temporal and spatial DNI variability classification

7.1.1 Spatial variability class

A temporal DNI variability classification as presented in section 6.2.1 with eight classes is by itself not sufficient to describe spatial influences that might be decisive for the operation of a PT solar field. This temporal variability classification is a method to describe the temporal variability as observed in a ground observation, but it does not describe the spatial pattern involved in detail. The impact of spatial heterogeneity of DNI on the solar field can be severe even if the temporal variability is low. For example, conditions could occur where only half of the solar field is shaded by clouds with a low transmittance while the other half is fully illuminated. From the viewpoint of temporal variability, the situation is not variable at all if the cloud shadow edge does not change its position. If the temporal variability is derived from

pyrheliometers no variability is detected as long as the cloud shadow edge does not move across the pyrheliometers.

In such a case the two pyrheliometers used for a control may be placed one in the shaded and one in the sunny area. The controller will adjust the flow of the HTF according to the average solar field DNI. This leads to a partial cooling and overheating of the solar field which in turn leads to a flow maldistribution. An even stronger imbalance between shaded and sunny shares of the solar field could increase this issue – if not known to the controller.

Especially problematic are profound overheating issues within sunny parts of the solar field, causing defocusing and energy dumping. The share between shaded and unshaded parts of the solar field is therefore a decisive value for the solar field behavior and requires a specific treatment. Therefore, two new variability indices derived from spatial DNI maps are introduced.

- Shadow area fraction S_A , which describes the relative shaded share of the solar field.
 - $S_A = \frac{A_{SASF}}{A_{SF}} \cdot 100\%$ with A_{SASF} shaded solar field area and A_{SF} complete solar field area.
- Shaded clear sky index S_i , which describes the clear sky index considering only the shaded part of the solar field.
 - $S_i = \frac{DNI_{SASF}}{DNI_{clear}}$ with DNI_{SASF} the average DNI within shaded areas of the solar field and DNI_{clear} as clear sky DNI.

Average values of the spatial DNI variability indices from the last 5 minutes are calculated. The classification in one of 5 spatial DNI variability classes is done according to the thresholds given in Table 7.1. Figure 7.2 illustrates a partially shaded PT solar field and the corresponding instantaneous spatial variability indices.

Table 7.1: Thresholds for spatial variability class

Class	Shadow area fraction S_A [%]	Shaded clear sky index S_i	General description
1	0 – 3	no requirement	Sunny conditions
2	3 – 100	0.9 – 1.0	Low spatial DNI variability: Only shadows from clouds with high transmittance
3	3 – 50	0 – 0.9	High spatial DNI variability
4	50 – 100	0.35 – 0.9	Intermediate spatial variability: Most of the solar field shaded Cases with only thin clouds and only thick clouds excluded
5	60 – 100	0 – 0.35	Low to medium spatial variability: Most of the solar field shaded (overcast) Only shadows from clouds with low transmittance

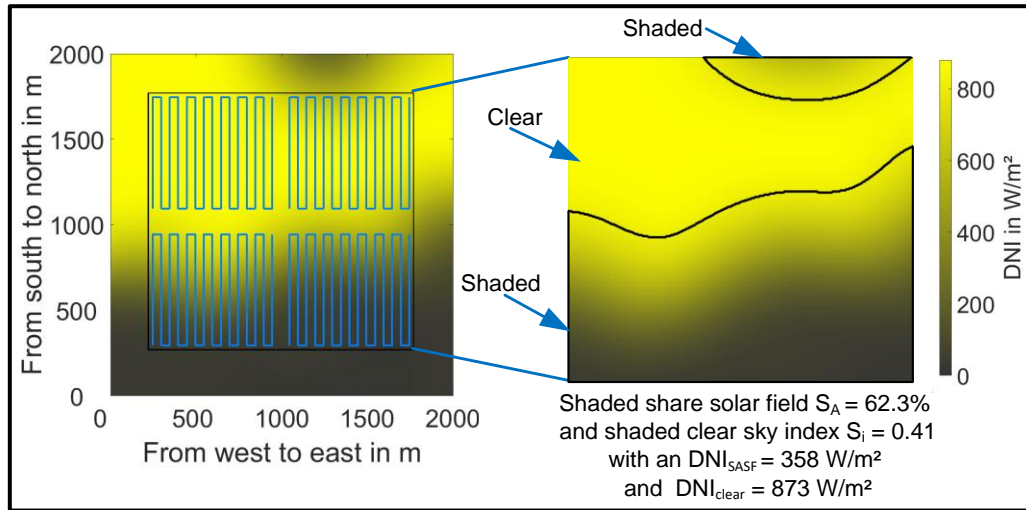


Figure 7.2: Partially shaded solar field with a shaded share of 62.3% and a clear sky index of 0.41 corresponding to spatial DNI variability class 4

Figure 7.3 illustrates both the temporal and the spatial DNI variability class for the 09.09.2015 and PSA. The forenoon of this day is mainly dominated by clear sky conditions. More variable conditions start shortly before 11 o'clock. The afternoon shows high and intermediate variability conditions mainly dominated by class 5 in case of the temporal classification and class 4 in the case of the spatial classification, whereby a stronger diversification is visible for the temporal classification.

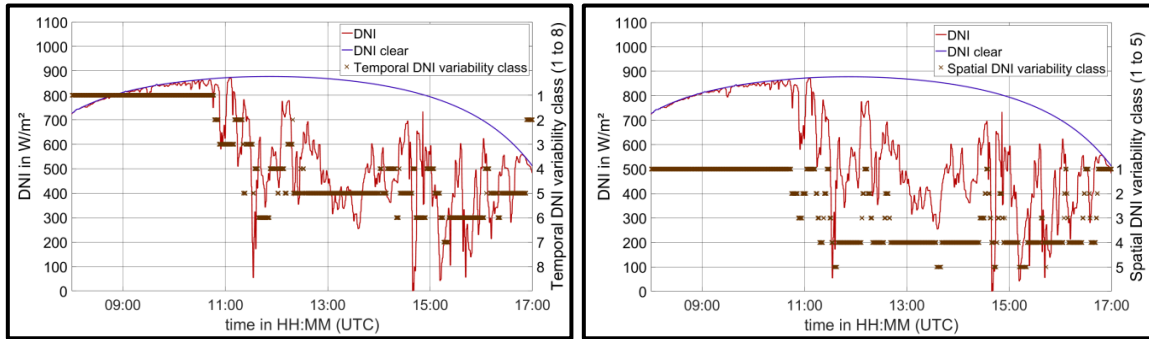


Figure 7.3: DNI variability classification of the 09.09.2015 at the PSA (left) temporal (right) spatial

7.1.2 Combined temporal and spatial variability class

The temporal and spatial DNI variability classes describe two distinct classification approaches of the DNI with different emphases. Forty theoretical combinations of temporal and spatial DNI variability exist, for any arbitrary moment, but in realistic cloud situations not all combinations are likely to occur. The distribution of the occurred combinations of temporal and spatial DNI variability for two complete years at the PSA is depicted in Figure 7.4. The most common conditions for the PSA are described by a spatial DNI variability class 1 and a temporal DNI variability class 1 or 2. These clear sky conditions account for more than 62% of the entire data set. Around 13% of the data set consists of intermediate to highly variable condition, both in time and space (spatial class 3 or 4 and temporal class 3 to 7), which are the most demanding for the PT plant control. From the view of the PT plant control less important overcast conditions make around 14.8% of the data set (spatial class 5 and temporal class 6 to 8). Roughly 4% of the data set is described by a spatial class 2 and temporal class 1 to 7. Such conditions with a low spatial variability but alternating temporal variability occur

mainly due to optical thin cirrus clouds, covering the whole power plant area as a single cloud object, but having an internal spatial heterogeneity in the cloud optical depth. The remaining conditions describe mainly transient conditions with an average occurrence of 0.1% per combination of spatial and temporal class. Two extreme examples are spatial class 5 and temporal class 1 as well as spatial class 1 and temporal class 7, with an occurrence of 0.29% and <0.01% respectively. The conditions at PSA are quite attractive conditions for a parabolic trough power plant and thus relevant for the investigations carried out in this work. For the year 2017 the yearly DNI sum at PSA was 2430 kWh/m².

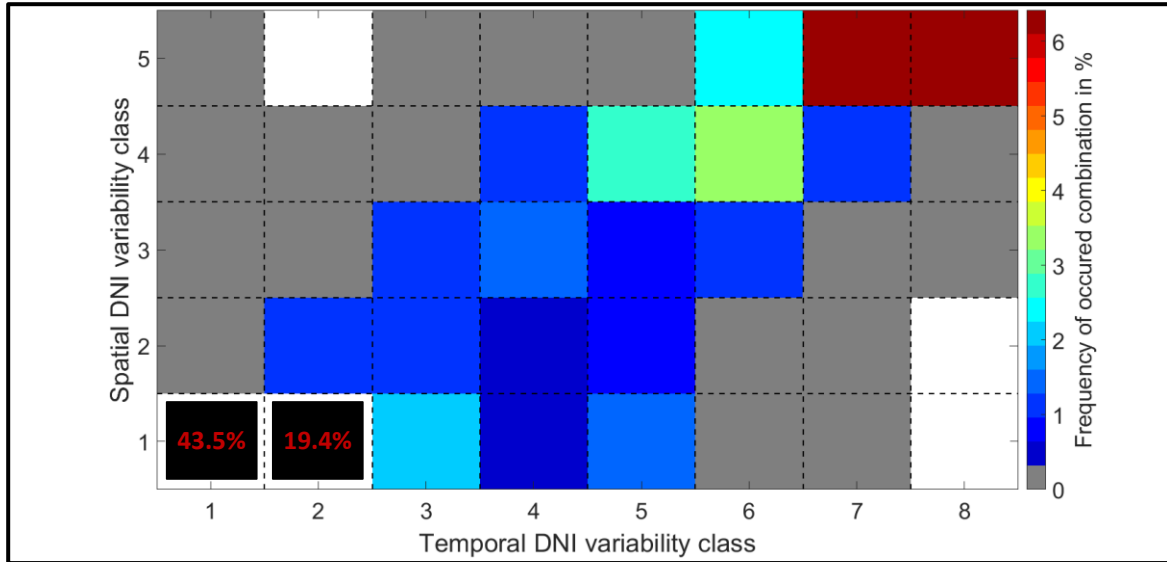


Figure 7.4: Temporal and spatial DNI variability class distribution of possible combinations within the years 2016 and 2017. Combination spatial class 1 & temporal class 1 or 2 account for more than 62% of the data set. Corresponding bins are not described by the colorbar for a better readability of the remaining combinations.

Based on this assessment, the 40 possible combinations of spatial and temporal DNI variability classes are combined to 7 aggregated spatiotemporal classes according to Table 7.2. Due to the power plants' strong sensitivity on the spatial solar share, the main focus is set on the spatial variability, which describes the distribution of the DNI over the spatially extended solar fields. In cases of e.g. spatial class 1, the temporal variability classification is not decisive, as all classes are attributed to the combined variability class 1. However, with the combined classes 6 and 7, conditions with a strong spatial as well as temporal variability are treated separately. In section 7.2.1 two new solar field control strategies with optimized specific control parameters for each of the 7 combined DNI variability classes are presented.

Table 7.2: Combined temporal and spatial variability class

Combined variability class	Spatial variability class	Temporal variability class	General description
1	1	1 - 8	Sunny conditions with no spatial variability; all temporal variability classes possible
2	2	1 - 8	Low spatial DNI variability (almost completely sunny solar field); total spectrum of temporal variability possible
3	3	1 - 3, 5-8	High spatial DNI variability; Almost complete spectrum of temporal variability possible except highly temporal variable class 4 with an intermediate clear sky index
4	4	1 - 3, 5, 7 - 8	Intermediate spatial variability; only low and intermediate temporal variability
5	5	1 - 8	Current overcast conditions with no spatial variability; total spectrum of temporal variability possible
6	3	4	High spatial DNI variability; only highly temporal variable class 4 with an intermediate clear sky index
7	4	4 or 6	Intermediate spatial variability; only highly temporal variable classes 4 and 6

Looking again into our example day the 09.09.2015 (see Figure 7.5), we see a stronger diversification within the variable time window from 10:45 to 16:45 compared to the previous individual variability classifications. Whereas the purely spatial classification within this period is dominated by class 4 with a share of 65% (see Figure 7.3), the combined class is dominated by the classes 4 and 7 with a share of 36% and 29% respectively. Both the combined class 4 and 7 represent an overall intermediate spatial variability, but class 7 stands in addition for a high variability in time.

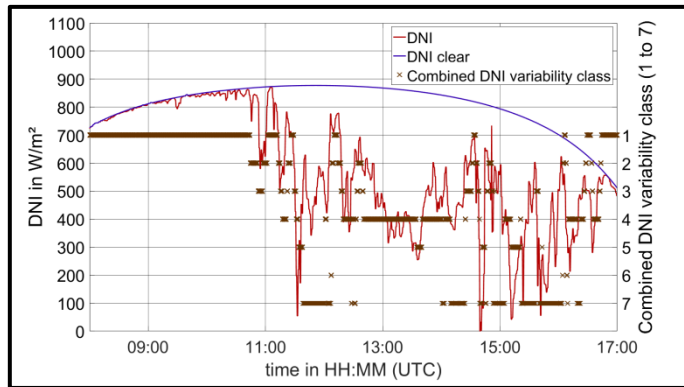


Figure 7.5: Combined DNI variability class of an example day (09.09.2015)

7.2 Introducing and benchmarking novel class dependent solar field controllers

7.2.1 DNI variability class dependent solar field controllers

The control system implemented in VSF is divided to a local collector temperature controller for the SCAs and a field main flow controller. A detailed description of the control system implemented in VSF is published in **Noureldin et al. 2019**. In this work I present a summary. The local collector temperature controller regulates the HTF temperature in the

receiver tubes and ensures that it does not exceed the upper temperature operation limits as defined by the manufactures. This is achieved by manipulating the deviation angle of the SCA from the sun (Φ_d) using a proportional-integral (PI) temperature Feed-Back (FB) controller to ensure that the SCAs are tracking the Sun and defocus them in cases when the temperature limits are exceeded. Each SCA gets an individual temperature set point (T_{SP}) which is derived from the actual field inlet temperature and load. In addition, there is an emergency service function, which defocuses the corresponding SCA completely if the SCA temperature exceeds (T_{SCA}) the temperature limits of the HTF. Figure 7.6 illustrates a PT loop with four SCAs and the corresponding temperature measurements as well as control diagram of a SCA PI temperature FB controller.

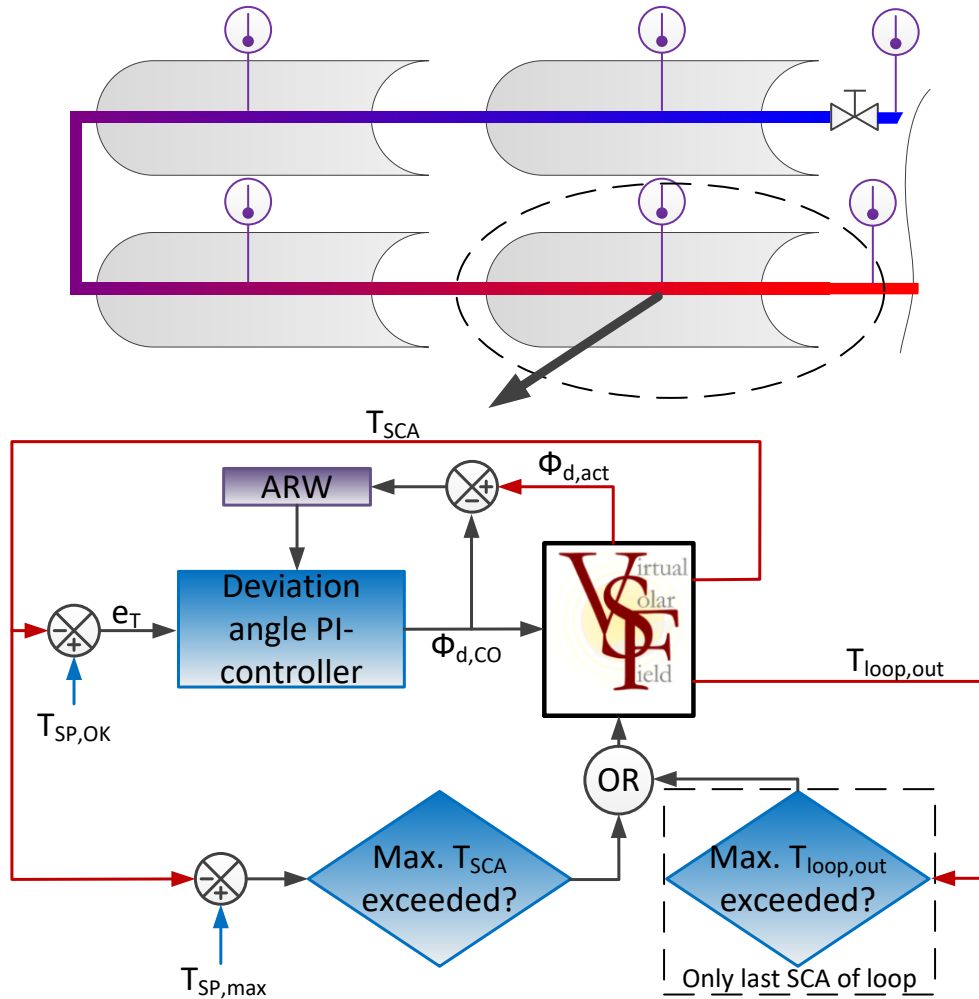


Figure 7.6: Single PT loop with temperature measurements at each of the four SCAs and corresponding control diagram for the local SCA focus controller.

Solar field outlet temperatures can be regulated by the solar field inlet mass flow. This task is handled by the main solar field flow controller (see Figure 7.7). The mass flow can be adjusted by the applied differential pressure (p_δ) through the HTF feed pump. The implemented control concept includes a feed forward (FF) pump controller, a temperature feedback (FB) controller and a focus feedback loop. For the FF part, the required mass flow and, thus, pump pressure is calculated by means of an energy balance over the field fed by the current overall DNI. The DNI value is the average of two pyrheliometer measurements as used in the real power plant (reference controller). Any systematic offsets induced by the FF part are corrected by a temperature FB controller. This controller uses the field outlet

temperature set-point as input and operates with an adaptable time constant adjusted to the throughput time of the solar field. Especially in volatile irradiance situations the large time constant of the solar field makes it challenging to avoid temperature overshoots in associated loops which often trigger defocusing of one or more SCAs in the loops. The focus feedback controller forces the collectors to refocus by increasing the mass flow if overall defocusing states of the field increases. This is done by altering the temperature error (e_T) with a PI controller.

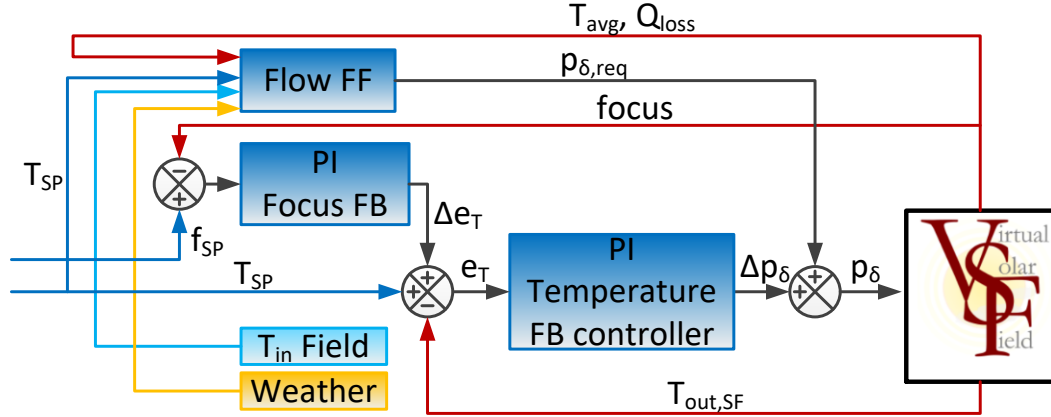


Figure 7.7: Flow controller diagram

The general form for a PI-controller for variable $u(t)$ in response to an error $e(t)$ in the process variable from the set-point is

$$u(t) = K_c e(t) + \frac{K_c}{T_i} \int e(t) dt. \quad \text{Equation 7.1}$$

The behavior of the local collector focus and the field main flow PI controllers can be adjusted according to the first order plus dead-time method. This is achieved by deriving the controller gain, K_c , and integral time, T_i , in **Equation 7.1** from the process gain K_p , time constant T_p , process dead time θ_p , such that

$$K_c = \frac{1}{K_p} \frac{T_p}{(\theta_p + \omega T_p)} \quad \text{Equation 7.2}$$

The controller gain could be further manipulated by introducing the factor ω varying from 0.1 to 10 for aggressive to conservative controller behavior, respectively. The integral time, T_i , is set to the process time constant, T_p . The implemented reference VSF controller uses control parameter as defined in Table 7.3 according to **Noureldin et al. 2019**. The reference controller is designed to emulate state of the art solar field control while eliminating the need for manual intervention from the solar field operators. The controller has proven to work robustly in various weather conditions. The controller parameters presented in Table 7.3 are utilized as the reference case of a field controller not taking into account information on spatial DNI distribution or DNI variability.

Table 7.3: Control parameters of the reference controller according to Noureldin et al. 2019

		Controller	Parameter	Value
local SCA focus controller	main flow controller	temperature FB controller	K_p and T_p	Adaptive
			θ_p	pump pressure dependent
			T_c	aggressive
		focus FB loop	K_p	3 %/°C
			T_p	160 s
			θ_p	Simulation time step (adaptive)
	controller	temperature FB controller (focus controller)	T_c	Aggressive
			K_p	-8 °C/deg
			T_p	5 s
			θ_p	Simulation time step (adaptive)
			T_c	Moderate

In this work, two new control strategies have been developed taking into account information available from the nowcasting system in form of the spatial DNI field average and DNI variability. The concept is to use different values for the controller parameters depending on the irradiance situation. A clear sky situation e.g. can be operated with a more aggressive controller than a strongly fluctuating situation. The adaptation of controller parameters is applied to the main flow controller and to the local focus controllers. For the class dependent controller an optimized set of control parameters is defined for each of the seven combined DNI variability classes (see section 7.1.2). The trimming of the controller parameters has been carried out for a number of test situations and the parameters which best meet the criterion are selected. The first new controller is trimmed to maintain the solar field outlet temperature as constant as possible whereas the second one tries to maximize the solar heat collection by minimizing any defocusing. The controller tuning is based on manual tuning and on the Ziegler-Nichlos method. For the remaining document I will call these controllers OT (objective temperature) and OFR (objective focus rate). The optimized control parameters are listed in Table 7.4 and Table 7.5. These optimized control parameters were identified during a master thesis (**Schlichting 2018**) supervised by the author of this thesis. Whereas the K_p and T_p , values of the controller are pre-defined (for the focus controller) or adaptively calculated for the current field situation (for the temperature FB controller), the trimming is realized by modifying the controller time constant T_c by a factor resulting in a conservative, moderate or aggressive tuning.

Table 7.4: Adjusted control parameters of the class dependent controller OT

class	temperature FB controller			focus FB loop			temperature FB controller (focus controller)		
	K_p	T_p	T_c	K_p	T_p	T_c	K_p	T_p	T_c
1	adaptive	adaptive	moderate	3 %/°C	160 s	Very aggressive	-2 °C/deg	50 s	moderate
2	adaptive	adaptive	aggressive	3 %/°C	160 s	aggressive	-2 °C/deg	50 s	moderate
3	adaptive	adaptive	moderate	deactivated	deactivated	deactivated	-2 °C/deg	50 s	aggressive
4	adaptive	adaptive	moderate	deactivated	deactivated	deactivated	-2 °C/deg	50 s	aggressive
5	adaptive	adaptive	aggressive	deactivated	deactivated	deactivated	-2 °C/deg	50 s	moderate
6	adaptive	adaptive	aggressive	deactivated	deactivated	deactivated	-2 °C/deg	50 s	aggressive
7	adaptive	adaptive	aggressive	deactivated	deactivated	deactivated	-2 °C/deg	50 s	aggressive

Table 7.5: Adjusted control parameters of the class dependent controller OFR

class	temperature FB controller			focus FB loop			temperature FB controller (focus controller)		
	K_p	T_p	T_c	K_p	T_p	T_c	K_p	T_p	T_c
1	adaptive	adaptive	moderate	3 %/°C	160 s	Very aggressive	-6 °C/deg	115 s	moderate
2	adaptive	adaptive	aggressive	3 %/°C	160 s	aggressive	-6 °C/deg	115 s	moderate
3	adaptive	adaptive	conservative	deactivated	deactivated	deactivated	-6 °C/deg	115 s	moderate
4	adaptive	adaptive	moderate	3 %/°C	160 s	moderate	-6 °C/deg	115 s	moderate
5	adaptive	adaptive	conservative	3 %/°C	160 s	moderate	-6 °C/deg	115 s	moderate
6	adaptive	adaptive	aggressive	deactivated	deactivated	deactivated	-6 °C/deg	115 s	moderate
7	adaptive	adaptive	aggressive	deactivated	deactivated	deactivated	-6 °C/deg	115 s	moderate

7.2.2 Selection of assessment days

The benchmark is performed over 22 days distributed over the year 2015 at PSA. The data set is chosen in such a way, that it includes a wide variety of conditions in irradiance, cloud height and type (low layer, middle layer, high layer and multi-layer conditions) as well as DNI variability classes (see Figure 7.8). The cloud height information is shown since the cloud height and the corresponding cloud types are one of the main uncertainty contributors of ASI systems (see chapters 5 and 6). Cloud height measurements are taken by the CHM 15 k Nimbus ceilometer from the G. Lufft Mess- und Regeltechnik GmbH (see section 3.3).

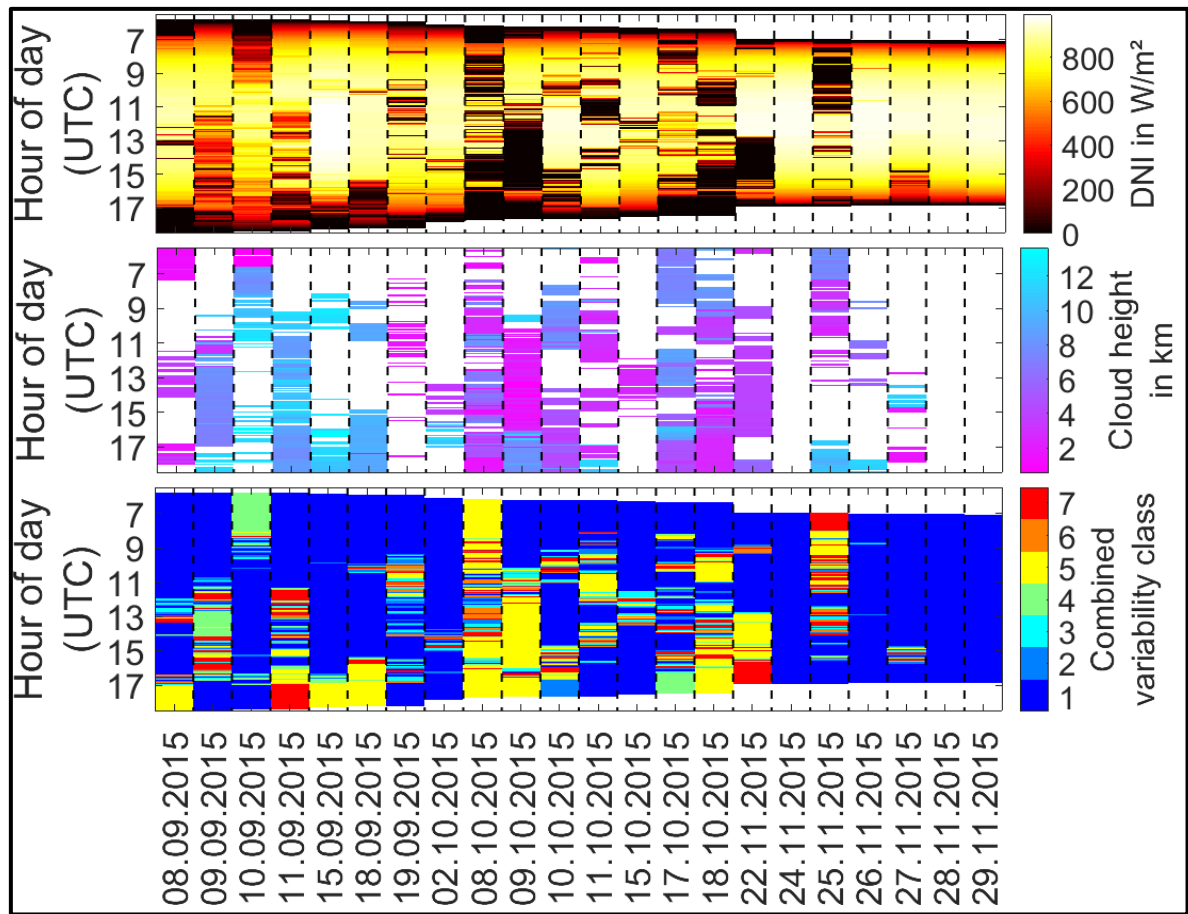


Figure 7.8: DNI, cloud height (as measured by a ceilometer) and combined DNI variability class over the 22 test days

Comparing the distribution in combinations of spatial and temporal DNI variability class (see Figure 7.4 (2 years) and Figure 7.9 (22 days)), we can see that the 22 days include almost all combinations of the 2 year period analyzed in section 7.1.2. Only 6 combinations which exist in the two year period are missing in the 22 days test period. These 6 combinations describe rather rare transient conditions which make less than 0.37% of the entire 2 year data set. Overall the 22 days include with 19.2% a higher share of the intermediate to highly variable conditions (spatial class 3 or 4 and temporal class 3 to 7), compared to 13% in the 2 year data set. In turn less interesting overcast conditions (spatial class 5 and temporal class 6 to 8) have only a share of 7.8% compared to 14.8% within the 2 years. For the remaining combinations the 22 days resemble the two year data set very well.

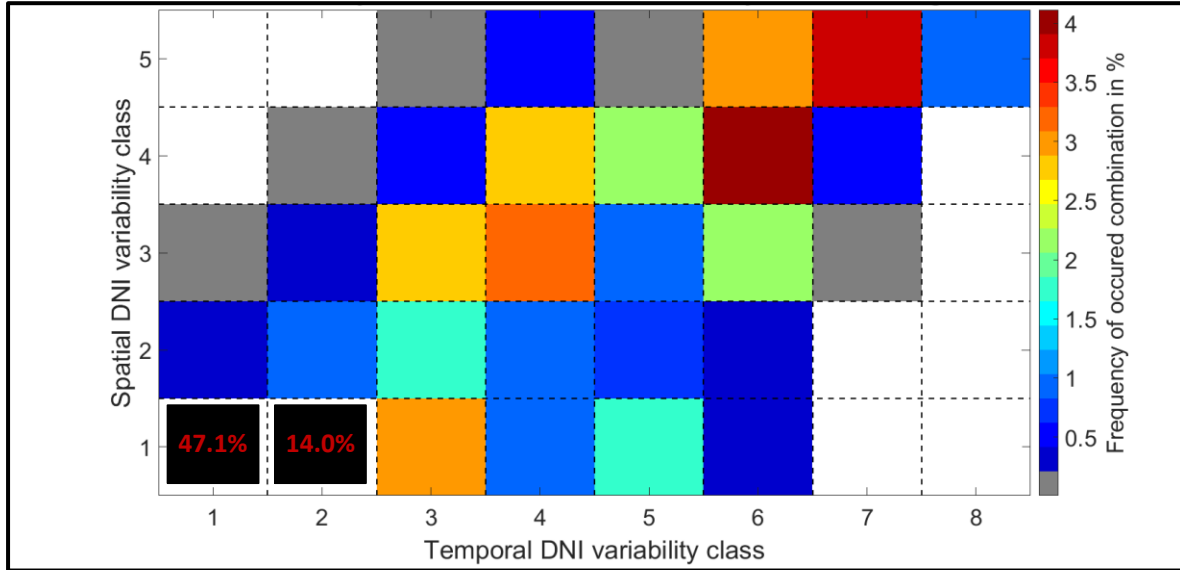


Figure 7.9: Temporal and spatial DNI variability class distribution of possible combinations within 22 test days. Combination spatial class 1 & temporal class 1 or 2 account for more than 61% of the data set. Corresponding bins are not described by the colorbar for a better readability of the remaining combinations.

7.2.3 Comparison with a state of the art reference controller

In this section the two new class dependent solar field controllers are benchmarked against the state of the art reference controller, based on the La Africana power plant design. Five different criteria are used to evaluate the solar field controllers.

- Revenue: Compares the overall expected revenue in € between the new class dependent controller with the reference controller. The revenue is calculated according to the procedure described in section 2.2.2
- The accumulated solar field thermal heat flow $\dot{Q}_{th,SF} = \dot{m} \cdot \bar{c}_p \cdot (T_{out} - T_{in})$ with \dot{m} as the total mass flow rate, T_{in} and T_{out} as the solar field fluid inlet and outlet temperature and \bar{c}_p as the integral average specific heat capacity of the fluid.
- Average solar field focus rate as relative value. It accounts to 100%, if all collectors of the solar field are fully focused.
- RMSD of the solar field outlet temperature with the design set temperature as reference.
- Reduction of emergency defocus incidents: Relative value which compares whether or not the new class dependent controllers are capable in reducing

emergency defocus incidents compared to the reference controller. Emergency defocus incidents occur when the fluid temperature within the PT collectors exceeds a maximum safety threshold.

The revenue is considered as the decisive parameter for the evaluation of the controller performance. The other parameters are compared for a better understanding of the controllers' individual behavior. The spider plot in Figure 7.10 illustrates the overall results for these five criteria. Only relative changes to the reference controller are depicted, where positive values indicate an improvement and negative values a decline in performance in a particular criteria. For example the calculation of change in relative revenue is always calculated according to Equation 7.3

$$C_{rel.rev} = (rev_{classDep}/rev_{ref} - 1) \cdot 100\% \quad \text{Equation 7.3}$$

with rev_{ref} as the revenue of the reference controller and $rev_{classDep}$ as the corresponding revenue of the class dependent controller.

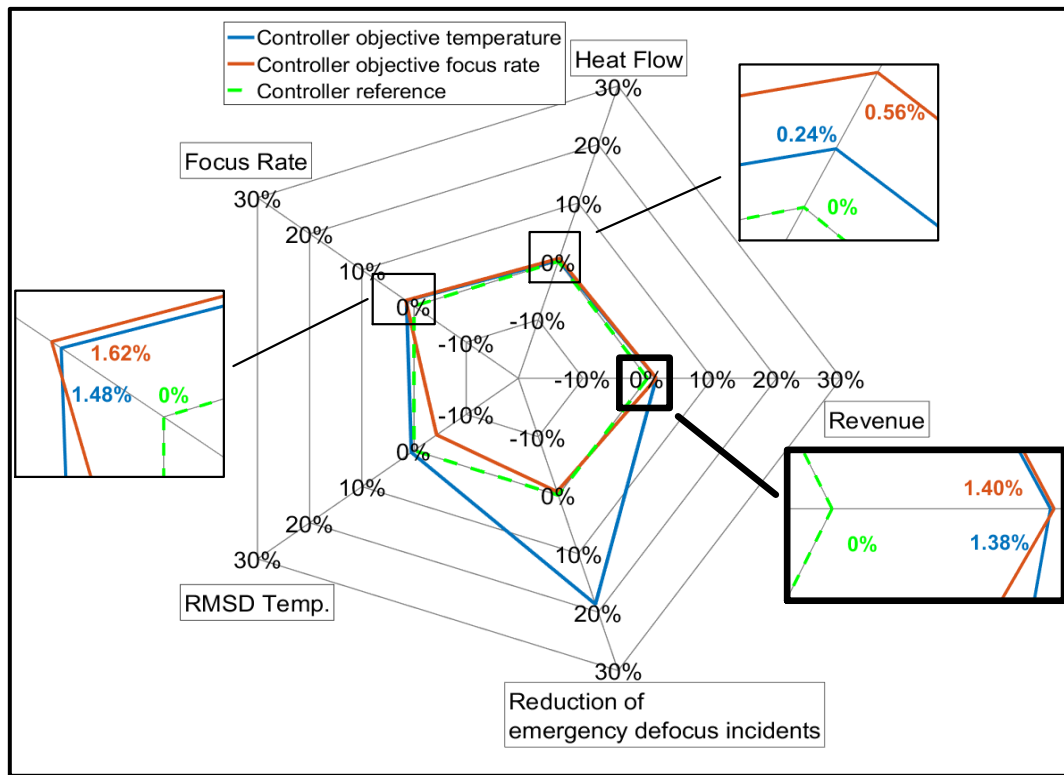


Figure 7.10: Comparison of the three controller setups reference, objective temperature, objective focus rate over five criteria based on 22 test days. Relative changes compared to the reference controller are plotted. Positive values indicate an improvement and negative values a decline in performance in a particular criterion.

The class dependent controller OT outperforms the reference controller in all criteria. In terms of overall revenue the improvement accounts to 1.38%. A particularly significant improvement can be seen for the criteria reduction of emergency defocus incidents with 18.6%. Emergency defocus incidents can lead to strong temperature transients within collectors (temperature gradients above 40°C in 3 minutes are possible), which affect the overall system stability, solar field outlet temperature and focus rate. This reduction of emergency defocus incidents by itself is already an important improvement. Another notable but currently not quantifiable benefit is the potential decrease of material degradation and maintenance costs. As previously mentioned emergency defocus incidents are triggered by

exceeding maximum safety threshold temperatures within the collectors. The emergency defocus means first of all that additional operations of the collector drives and rotation and expansion performing assemblies (REPA) are necessary, which could accelerate degrading effects. Furthermore, frequent temperature transients, especially with temperatures by several degrees above the set point, could affect the lifetime of REPAs, HTFs, receiver tubes and all other components exposed to the transients.

The class dependent controller OFR reaches a revenue increase of 1.40%, nearly identical to the increase for OT. OFR also outperforms the reference in focus rate and heat flow as in the case of OT. However, OFR is outperformed by the reference in terms of RMSD temperature (by 5.4%) and emergency defocus incidents (by 0.6%). Despite the objective of this controller it performs only marginally better than the controller OT in focus rate with an improvement of 1.62% compared to an improvement of 1.48%. This can be partly explained by the significantly higher number of emergency defocus incidents compared to the controller OT. Each emergency defocus incident leads to a short-term total defocusing of a collector and in turn to additional temperature transients which is reflected by the increased RMSD. This leads to a stronger penalization of the controller OFR compared to the controller OT and thus to a similar improvement in revenue, despite the higher overall heat flow for OFR. The higher number of emergency defocus incidents is caused by the OFR controller objective. In order to keep the focus rate as high as possible, the OFR controller uses predominantly the pump pressure as control variable, intending to adapt the mass flow to the prevailing conditions while maintaining a constant high focus rate. This approach usually leads to a higher heat flow, yet, it is more vulnerable under variable quickly changing conditions in which adaptation of the focus rate are inevitable. A partially too late intervention of the local SCA focus controller gives less leeway for countermeasures, which in turn leads to a higher rate of emergency defocus incidents.

For each day, the absolute revenue and the change of relative revenue between the reference controller and the two class dependent controller is compared (see Figure 7.11). Both class dependent controllers outperform the reference controller in 20 out of 22 days. The underperforming days have larger time periods with fast changing variability classes in common (see Figure 7.8). How such underperformance can be avoided is discussed in the next section.

It is observed that the potential gains in revenue are rather different between all days. The lowest revenue is expected on the 25.11.2015 with roughly 7.9 k€ (reference control) and the highest on the 15.09.2015 with roughly 98.8 k€ (reference control). Over all 22 days the absolute benefit of the new class dependent controller amounts to roughly 15 k€ for the controller OT and roughly 15.2 k€ for the controller OFR with an overall absolute revenue of roughly 1,083.3 k€ (reference controller). This is an increase of about 1.4 % in revenue for the new class dependent controller concept.

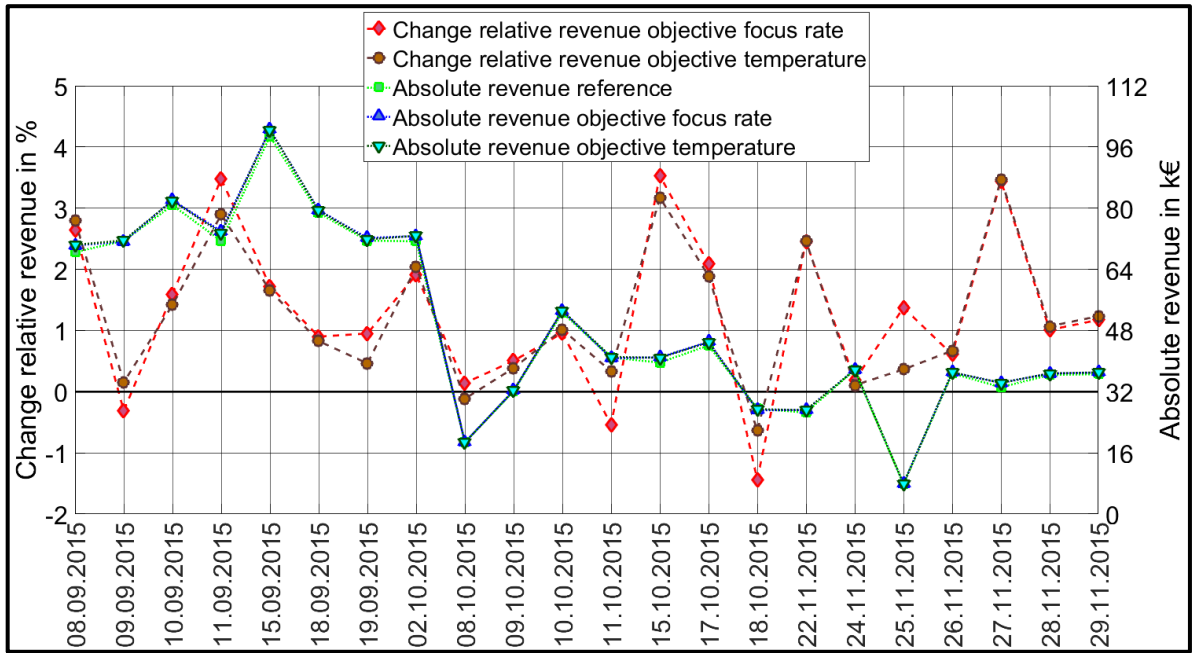


Figure 7.11: Absolute and relative daily revenue for reference controller and the two class dependent controllers.

7.3 Detailed performance assessment and applicability conditions

7.3.1 Identification of applicability conditions

In section 7.2.3 the benefit of the class dependent controllers compared to the reference controller was investigated. These analyses looked at the overall benefit over the entire data set or over complete days. A clear benefit is visible in terms of revenue. Yet, it might be the case that the class dependent controller will be outperformed by the reference controller under certain conditions.

In this section the entire data set is discretized in short data packages and the impact of the combined DNI variability classes as well as the combinations of spatial and temporal DNI variability classes on the expected revenue is analyzed. The goal is to identify a binary decision system, which will decide if a class dependent controller or the reference controller is preferable for the prevailing conditions. This binary decision system is called the identification of applicability of the ASI derived DNI variability class and the enhanced controller.

A new classification of the DNI variability is performed every 30 s which is the ASI system resolution. The spatial DNI variability class uses information of the past 5 minutes and the temporal of the past 15 minutes. For the identification of the applicability conditions, the data set is discretized in sliding data packages with a duration of 10 minutes. The resolution of these sliding data packages corresponds to the temporal resolution of the ASI system of 30 seconds. Each data package time stamp corresponds to the end of the package. The 22 days result in roughly 20000 data packages. These data packages enable a high temporal resolution impact analysis of the actual DNI variability classes on the controllers. No aggregation over the data packages is done. An aggregation would lead to an artificial repetition of the same time stamps within the summed up values.

Having the solar field time constant of approx. 10 min in mind it is obvious that 10 minute data packages might be too short to fully cover some of the processes which unfold more slowly within some parts of the extensive solar field. This leads to the situation that a certain analysis window is not only affected by the DNI situation during this time window but also from the DNI situation and the controller activity in the prevailing time period. Especially when DNI classes rapidly change along the analysis windows, no one to one mapping of classification to controller result exists. Nevertheless, the used 10 minute time windows cover many occurring processes. Larger time windows would corrupt the intention of this analysis, since they would again average out effects which occur within the solar field. In section 7.3.2 the benefit of the applicability conditions will be presented, according to the results presented in section 7.2.3 without the discretization in sliding data packages.

The change in relative revenue of all data packages is discretized and averaged within the combined DNI variability classes (see Figure 7.12). The combined class 1 describes the dominant sunny conditions within the data set with an occurrence of 67%. The controller OT shows an advantage compared to the reference controller for the classes 1, 2, 6 and 7 which account for more than 82% of the data set. The controller has a significant disadvantage during combined class 4 conditions, which describe an intermediate spatial variability with a low to intermediate temporal variability. Under these conditions, more than 50% of the solar field is shaded. The controller OFR shows an even stronger advantage compared to the reference controller for the classes 1, 2, 6 and 7 as well as class 3 which account together for more than 88% of the data set. However, the class 4 and 5 show a very pronounced disadvantage in revenue compared to the reference. The absolute energetic loss for these classes is comparably low, since these classes are rare and as they have a high shaded solar field share and a low cloud transmittance (especially for class 5).

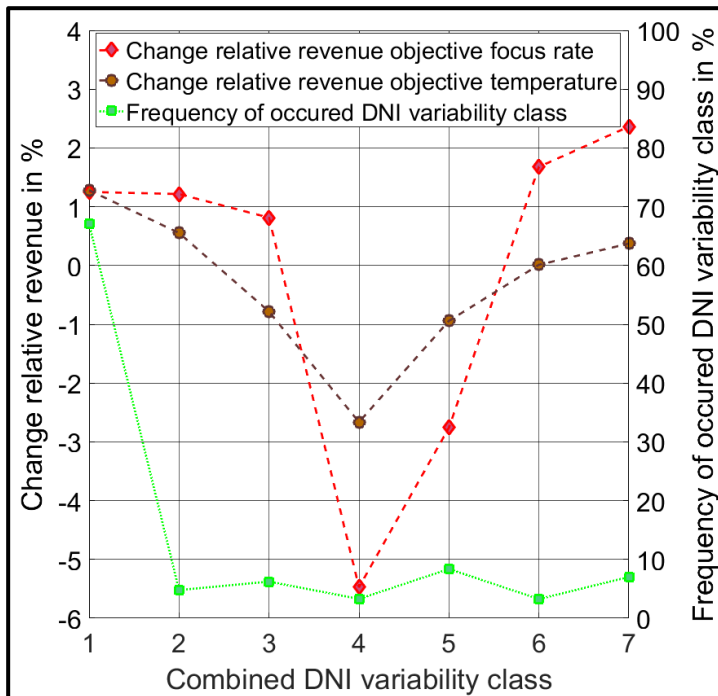


Figure 7.12: Change relative revenue discretized over combined variability classes and occurrence of classes within the complete data set

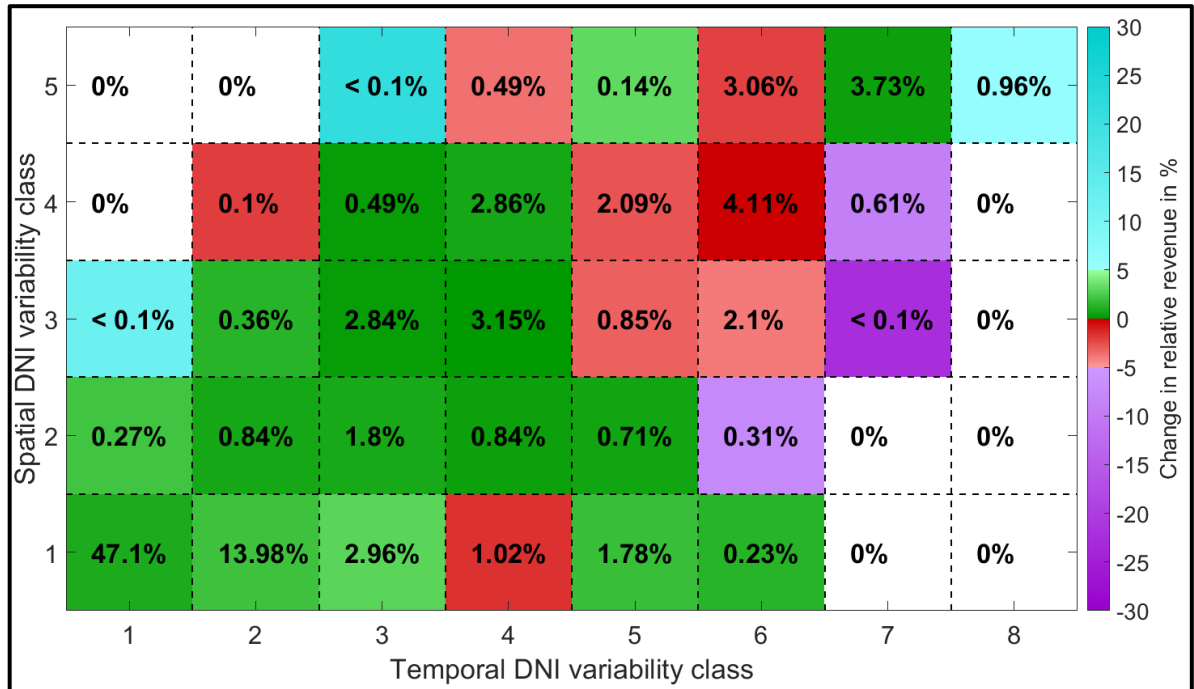
Most of the combined DNI variability classes include more than one combination of spatial and temporal DNI variability class (exception combined class 6). Therefore, the change in relative revenue of all data packages is discretized in the combinations of spatial and

temporal DNI variability classes. The results of this analysis are shown in Figure 7.13, which considers the spatial class on the y axis, the temporal class on the x axis, the change in relative revenue by the color coding and the occurrence of a certain conditions as the stated value within the bins.

The class dependent controller outperform the reference controller in 20 (OT) and 22 (OFR) combinations of spatial and temporal DNI variability conditions respectively (green and cyan bins). They are outperformed in 11 (OT) and 9 (OFR) combinations respectively (red and purple bins), of which 6 are identical for both controllers. The mentioned 20 and 22 combinations of spatial and temporal DNI variability classes account for more than 85% (OT) and 89% (OFR) respectively of the data set. Almost all the conditions with an advantage for the reference controller are found for highly variable conditions, which are connected to a low average DNI and plant yield. For each class dependent controller only one underperforming combination of spatial and temporal DNI variability class is found, which can be connected to a high average DNI and yield. These combinations account for less than 0.3% of the data set.

The combination of spatial class 5 and temporal class 3 shows a change in relative revenue above 20% for both controllers. On the contrary, the combination of spatial class 3 and temporal class 7 shows a change in relative revenue around -20% for both controllers. However, both these combination account for less than 0.1% of the data set and are therefore mostly irrelevant. For the remaining combinations the change in relative revenue is clearly within $\pm 10\%$ (mostly $\pm 5\%$).

The results depicted in Figure 7.13 are utilized for the identification of the applicability of the class-dependent controller. For each combination of spatial and temporal DNI variability class with an expected benefit in revenue it makes sense to use the class dependent controller whereas the reference controller is recommended for the remaining combinations. Thus, this matrix defines the applicability of the class dependent controller.



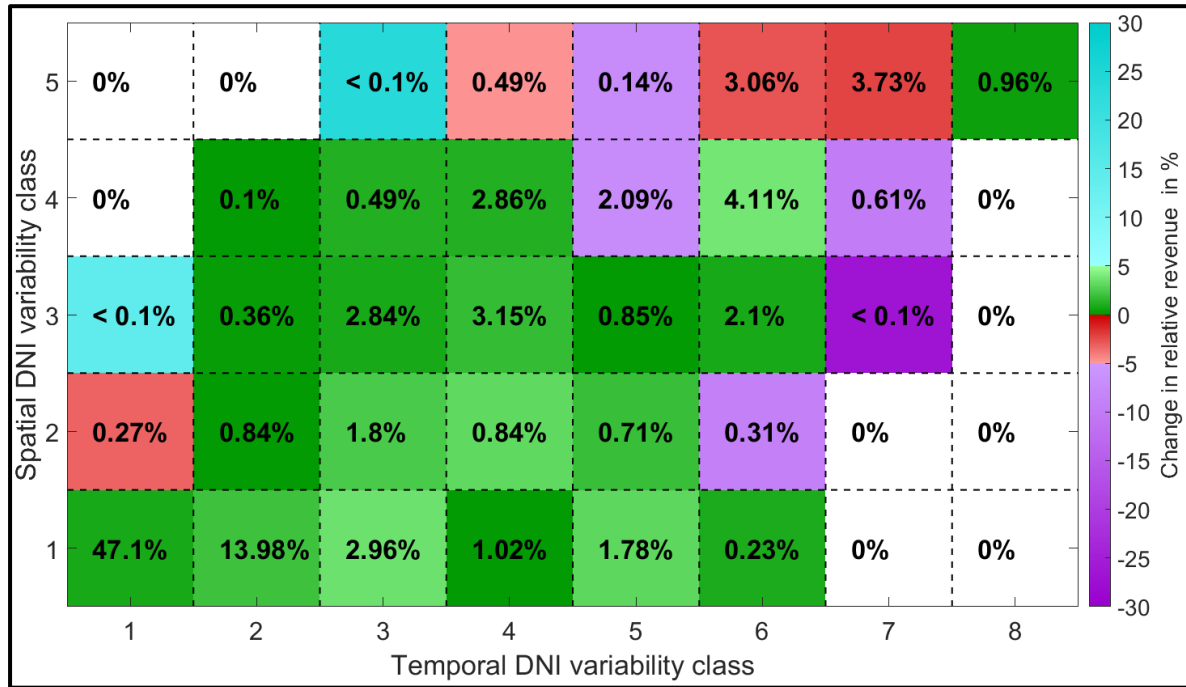


Figure 7.13: Change in relative revenue discretized in combinations of temporal and spatial DNI variability classes. The color coding describes the relative change in revenue within each bin. The occurrence of each bin is indicated by the stated values. (top) controller OT (bottom) controller OFR

7.3.2 Implementation of applicability for the plant control

In this section it is describe how the above findings can be used to create an improved hybridized control strategy. The hybridized control concept consists of two sets of controllers. The first one is the reference controller making use of the irradiance information from the two pyrheliometers. The second one uses the class dependent control parameters and additional information from the ASI system (OT or OFR). As before the ASI information delivers the DNI average over the field as well as the classification into temporal and spatial DNI classes. The applicability matrix defined in the last section is used to decide whether the reference controller or the class dependent controller is used in the current DNI situation represented by the class derived from the ASI information.

All 22 days are evaluated once again with the VSF using this hybridized control strategy for both class dependent controllers. I will continue to call the hybridized controller class dependent controller with the objective temperature OT and focus rate OFR, since for the hybrid operation the class dependent controller account for the predominant share of the data set. Compared to the analysis presented in section 7.3.1, the applied controller is now continuously selected based on the class whereas in the former section the same controller was used throughout the day only adapting its parameters according to the prevailing class. In a first step, the performance based on the 10 min sliding data packages is analyzed according to section 7.3.1. The improvement due to the class dependent controllers with regards to the applicability conditions is evident, when looking into the overall change in relative revenue discretized over the combined temporal and spatial DNI variability classes (see Figure 7.14). The controller OFR shows a significant increase within all classes, notably for class 4 and 5 from previous reductions in revenues of -5.5% and -2.8% to increasing revenues of 5.1% and 3.5%, respectively. The controller OT shows a significant increase especially for the classes 2, 3, 4, 6 and 7. This holds especially for class 4 where the relative revenue changes from a

decrease of -2.7% to an increase of 4.6%. Nonetheless, we see also a slight decrease for class 5. This decrease is possible, due to the possible change of the solar field conditions at any given time (temperature, mass flow, collector focus rate, etc.) compared to the evaluation presented in section 7.3.1. Such deviations in conditions arise from the interaction of the solar field with the hybridized control strategy and may lead to performance reductions despite the hybridized control strategy.

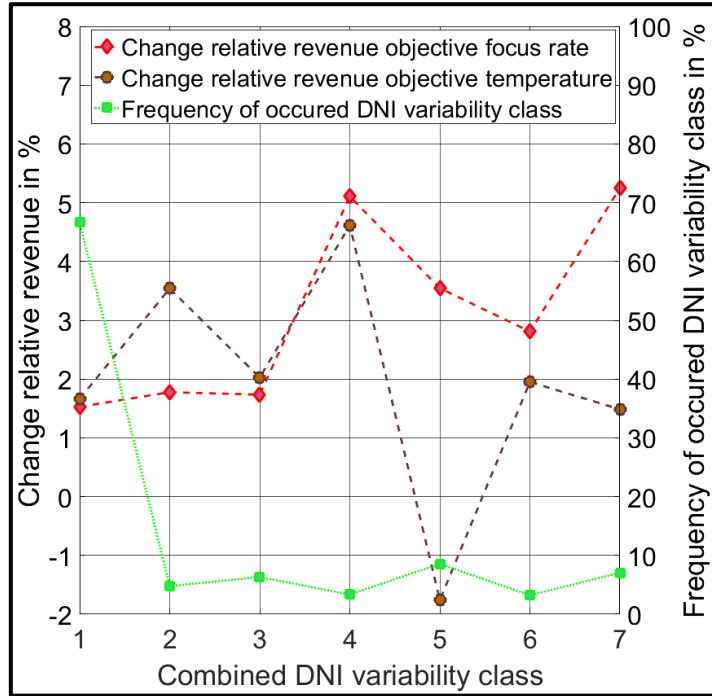


Figure 7.14: Change relative revenue discretized over combined variability classes and occurrence of classes within the complete data set (hybridized controllers with regards to the applicability conditions)

Looking into the change in relative revenue discretized over the combinations of spatial and temporal DNI variability classes, we see that both class dependent controllers outperform the reference controller in 25 combinations. They are outperformed in only 6 combinations, which account for 9% (OT) and 3.2% (OFR) of the data set respectively (see Figure 7.15). Four of these six combinations are identical for both controllers. The considerable higher share in the case of the controller OT is due to the two combinations spatial 5 and temporal 6 or 7. Each of these combinations has a share above 3% of the data set. The absolute energetic effect of these combinations is insignificant as they refer to almost fully shaded conditions. These two combinations also explain the impact of the combined DNI variability class 5 on the controller OT (see Figure 7.14).

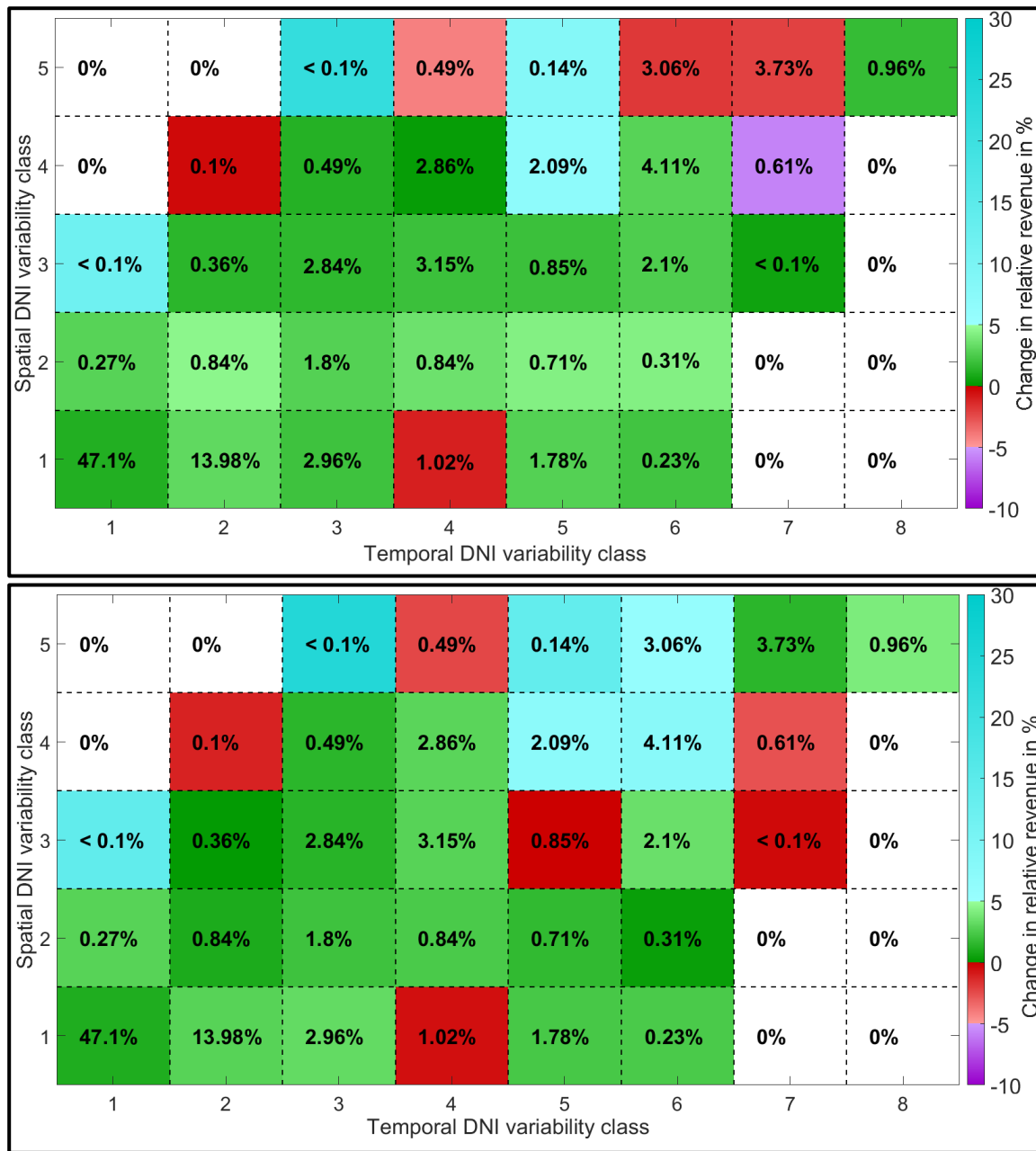


Figure 7.15: Change in relative revenue discretized in combinations of temporal and spatial DNI variability classes for hybridized controllers using the applicability. The color coding describes the relative change in revenue within each bin. The occurrence of each bin is indicated by the stated values. (top) hybridized controller OT using the identified applicability (bottom) hybridized controller OFR using the identified applicability

In a next step the impact of the applicability conditions on the overall results is analyzed according to section 7.2.3, without the discretization of sliding data packages in DNI variability classes. Figure 7.16 shows the change in relative revenue and the absolute revenue discretized over the 22 days. Both class dependent controllers show a significant improvement compared to the results presented in section 7.2.3. The overall absolute revenue compared to the reference controller rises by roughly 20.9 k€ (OT) and roughly 21.2 k€ (OFR) with the hybridized concept. Without the continuous selection between reference and class dependent controller these improvements were considerably lower with roughly 15 k€ (OT) and 15.2 k€ (OFR).

For the hybrid concept the reference controller outperforms the controller OT only on the 08.10.2015 and the controller OFR on the 25.11.2015. These days with roughly 18.7 k€ (08.10.2015 reference controller) and 7.9 k€ (25.11.2015 reference controller) have the lowest overall absolute daily revenue. On 08.10.2015 the combined variability class 5 accounts for 57% of the day (see Figure 7.8). As we see in Figure 7.14 the reference controller outperforms the class dependent controller OT by roughly 1.8% within the combined DNI variability class 5. Therefore, it is not surprising that the reference controller outperforms the controller OT on this day. The 25.11.2015 is a highly complex day with multi-layer cloud conditions (see Figure 7.8). This day for itself is responsible for 27% of all emergency defocus incidents (reference controller) within the 22 days. As it is discussed in section 7.2.3 the controller OFR is much more vulnerable for emergency defocus incidents compared to the controller OT. This explains the strong deviation in revenue change from +8.8% (OT) to -2.1% (OFR). Concerning the high fluctuations of the relative values, it should not be forgotten that this day accounts to an absolute revenue of only 7.9 k€ (reference controller).

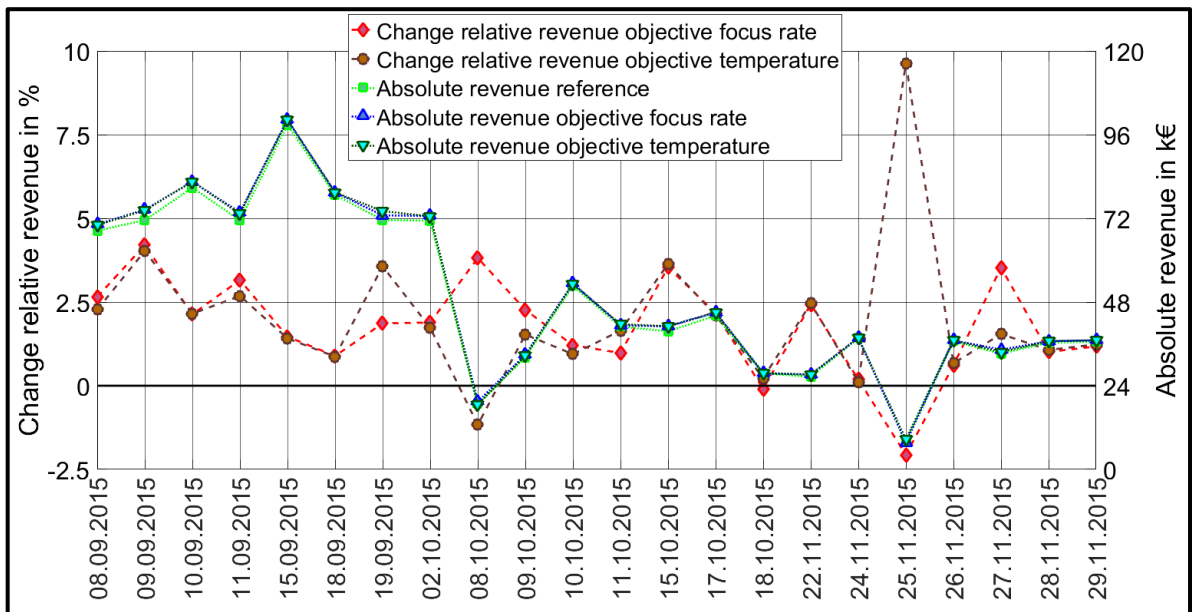


Figure 7.16: Absolute and relative daily revenue for the reference controller and the two hybridized class dependent controllers with regards to the applicability conditions

Figure 7.17 illustrates the overall influence of the controllers with regards to the applicability conditions over the previously introduced five criteria. The class dependent controllers outperform the reference controller in all criteria. The advantages and disadvantages of both class dependent controllers are almost completely balanced in terms of revenue, with a benefit above 1.9% for both class dependent controllers compared to the reference controller. Especially the controller OT shows a significant improvement in the two criteria RMSD temperature and reduction of emergency incidents of 9.5% and 21% respectively. The controller OFR outperforms the controller OT in terms of heat flow, focus rate and revenue.

The observed increase in revenue of nearly 2% is a significant improvement considering the comparably low costs for an ASI system and the still existing and considered uncertainty of the ASI derived DNI maps. It appears that the ASI system is capable in catching the prevailing overall spatial and temporal DNI variability conditions accurately enough for the plant control, despite the existing uncertainties.

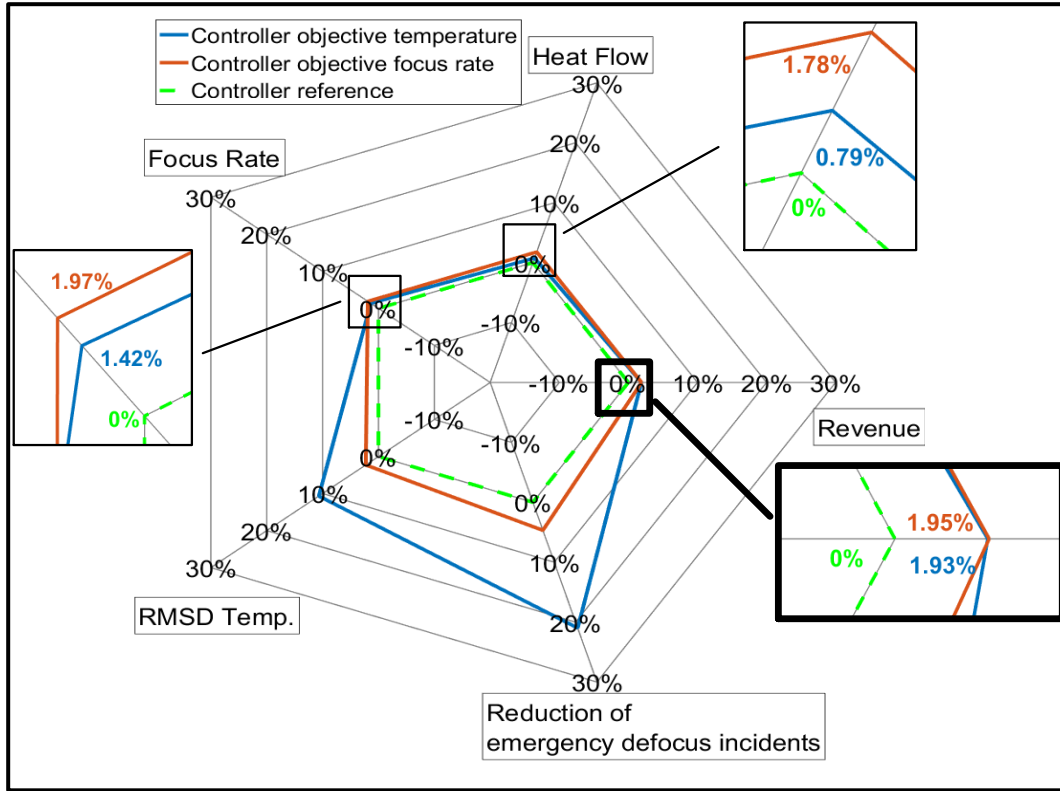


Figure 7.17: Comparison of hybridized class dependent controllers using the applicability concept against the reference controller for five criteria and 22 days. Relative changes compared to the reference controller are plotted. Positive values indicate an improvement and negative values a decline in performance in a particular criterion.

7.4 Performance estimation of class dependent control strategies for whole years

Based on the detailed evaluation over 22 days, the impact of the new control strategies with and without regards to the applicability conditions is estimated over the years 2016 and 2017. For the performance estimation the distribution of the occurred combinations of temporal and spatial DNI variability is analyzed individually for each day of the years 2016 and 2017.

The distribution for a given day is described as $f_{iD,iC}$ for the combinations $iC = 1 \dots 40$. The overall expected relative change in revenue per day ($c_{rel.rev,est,iD}$) is estimated by combining $f_{iD,iC}$ with the expected relative change in revenue for the corresponding class combinations ($c_{rel.rev,exp,iC}$) (see Figure 7.13 and Figure 7.15) according to Equation 7.4.

$$c_{rel.rev,est,iD} = \sum_{iC=1}^{nC=40} f_{iD,iC} \cdot c_{rel.rev,exp,iC} \quad \text{Equation 7.4}$$

The distribution of all occurred combinations over the years 2016 and 2017 at PSA is given in Figure 7.4. Only roughly 0.4% of the two year data set corresponds to DNI variability conditions which did not occur within the 22 day benchmarking campaign. These conditions are not taken into account for the estimation procedure. The energetic effect of these conditions is marginal for PT power plant operation, as they belong to overcast transient conditions.

The resulting distribution of change in relative revenue over all days of the two years without considering the applicability conditions is shown in Figure 7.18. We see a positive benefit in 90.3% (OT) and 78.2% (OFR) of all days. Both controllers show the highest day count for a change in relative revenue of roughly 1%. Min, max and some selected percentile values corresponding to the 2 year data set are shown in Figure 7.19. A clear advantage is visible for the OT controller.

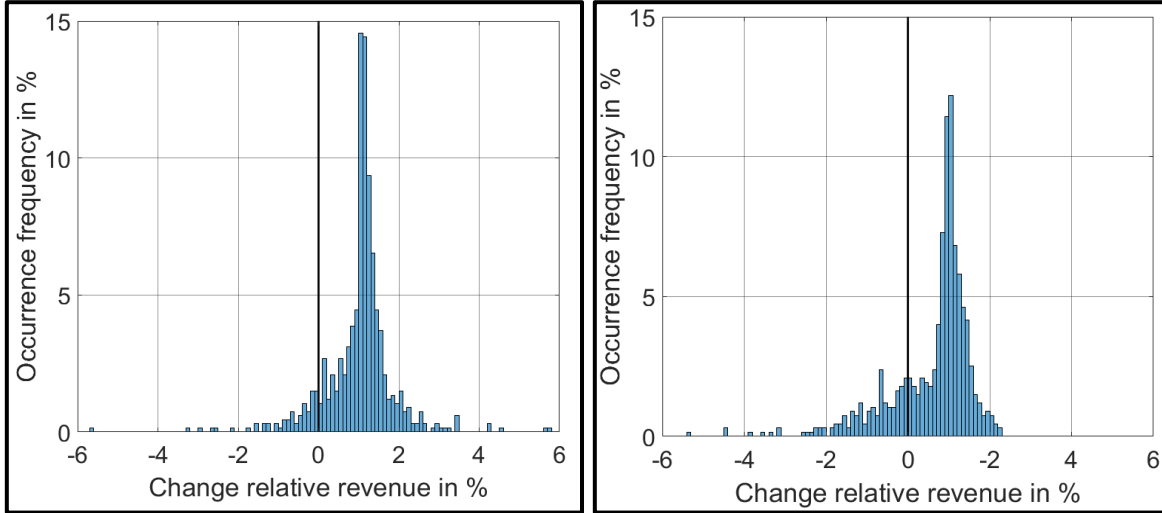


Figure 7.18: Distribution of change in relative revenue per day $c_{rel.rev,est,iD}$ of class dependent controllers compared to the reference controller over the years 2016 and 2017 without regards to the applicability conditions (left) OT (right) OFR

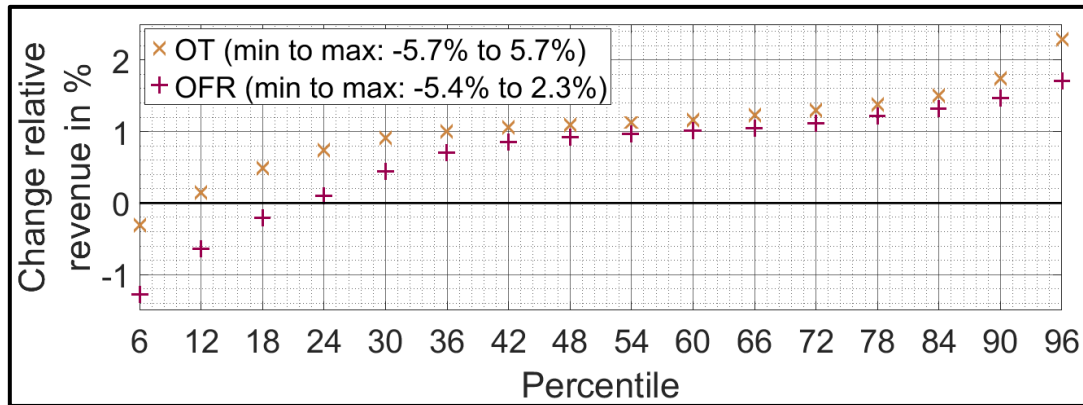


Figure 7.19: Minimum and maximum of change in relative revenue and some selected percentile values of estimated daily change in relative revenue $c_{rel.rev,exp,iD}$ over all days (without regards to the applicability conditions)

This significant revenue deviation between both controllers for the estimated values is not visible in the simulation results presented in section 7.2.3. However, it can be explained by the differences between the 22 days data set and the 2 year data set. As discussed in section 7.2.3 the 22 days data set includes a higher share of interesting highly variable conditions compared to the two year data set and a lower share of less interesting overcast conditions. Exactly these overcast conditions include mainly the days with an estimated negative impact. Looking now into the previously determined expected relative change in revenue for the three overcast combinations, spatial class 5 and temporal class 6 to 8 (see Figure 7.13), we see that the reference controller outperforms OT in spatial class 5 and temporal class 6, whereas OFR is outperformed in spatial class 5 and temporal class 6 as well as 7.

Of course we should always take into account that not all days have the same energetic worth. Figure 7.20 illustrates the estimated change in relative revenue per day over the corresponding daily effective DNI sum. The effective DNI is calculated according to

$$DNI \cdot \cos(\theta)$$

Equation 7.5

with θ as the incidence angle. The incidence angle of a PT collector in north south alignment can be calculated according to

$$\theta = \arccos\left(\sqrt{\cos^2(\theta_z) + \cos^2(\delta) \cdot \sin^2(\omega)}\right)$$

Equation 7.6

(Duffie & Beckman 2006) with θ_z as solar zenith angle, δ as declination and ω as hour angle. It is clearly visible that both class dependent controllers dominate the interesting days with a high daily effective DNI sum. Weighted average values of the change in relative revenue over distinct ranges of Daily effective DNI sum as well as the corresponding data distribution are shown in Figure 7.21. The weighting factor of each day within a range is based on the quotient between daily effective DNI sum and the effective DNI sum over all days within this range. For the OT controller days with a positive benefit are dominant over all ranges, while the OFR controller is in average outperformed by the reference controller for days with an daily DNI sum below 2 kWh/(m²day). Over all days the average change in relative revenue amounts to 1.0% (OT) and 0.9% (OFR) respectively.

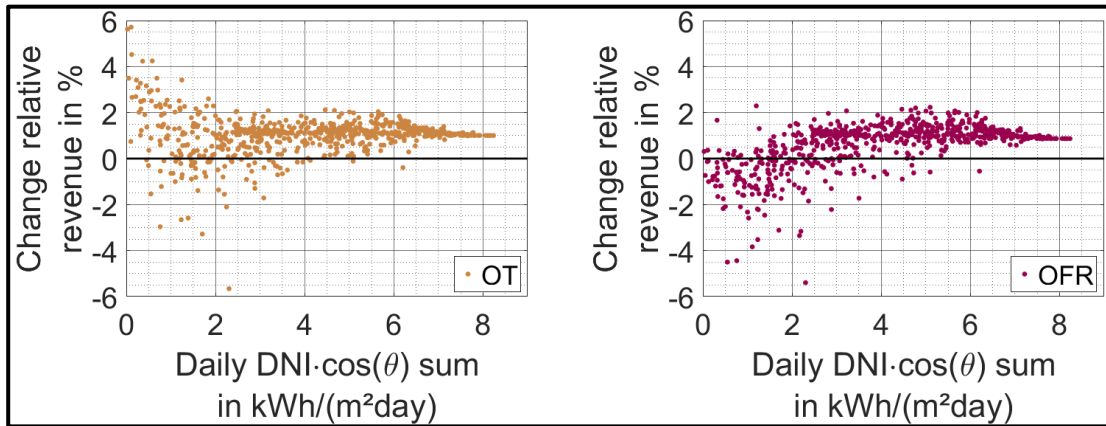


Figure 7.20: Change relative revenue per day over daily DNI sum (without regards to the applicability conditions)

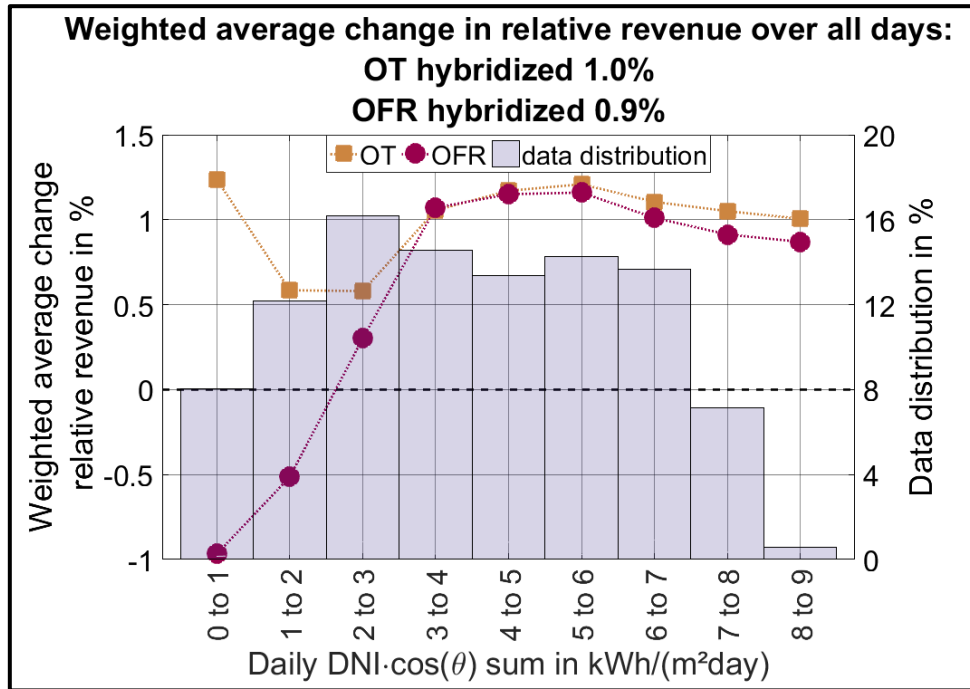


Figure 7.21: Weighted average change relative revenue over all days within distinct ranges of Daily effective DNI sum as well as corresponding data distribution (without regards to the applicability conditions)

The results change clearly when we have a look at the estimation results for the hybrid controllers that also consider the applicability conditions. Now we see a positive benefit in 94.8% for OT controller but 99.9% for OFR controller (see Figure 7.22). In Figure 7.23 we see that the OFR controller outperforms the OT controller over all percentile values.

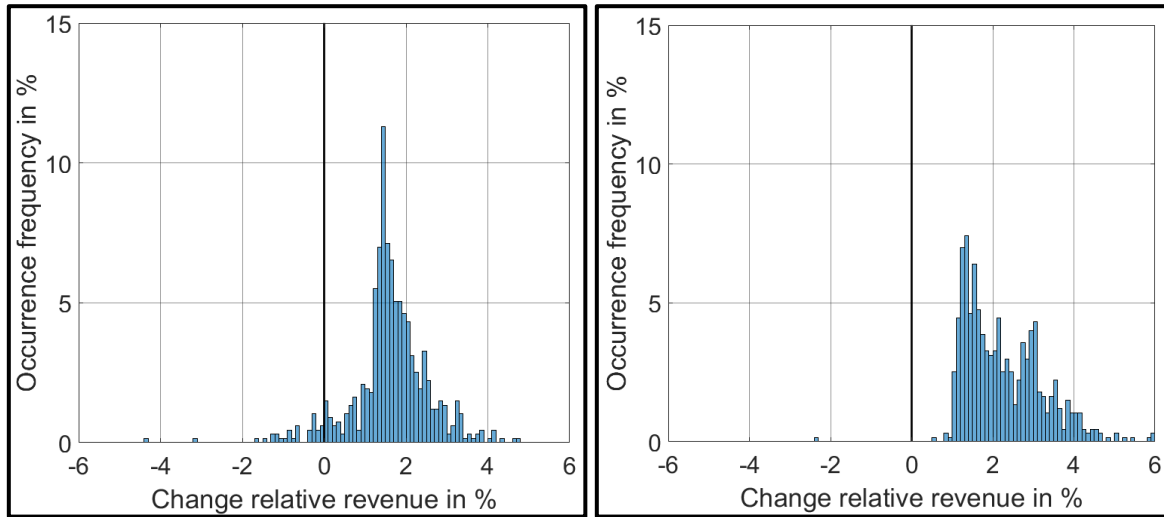


Figure 7.22: Distribution of change in relative revenue per day between hybrid class dependent controllers and reference controller over the years 2016 and 2017 with regards to the applicability conditions (left) OT (right) OFR

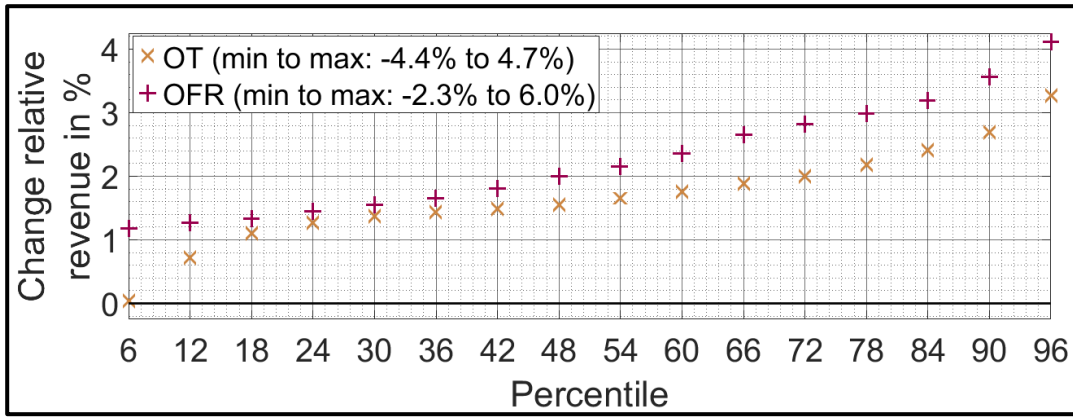


Figure 7.23: Minimum and maximum of change in relative revenue and some selected percentile values of estimated daily change in relative revenue $c_{rel.rev,exp,iD}$ over all days (with regards to the applicability conditions)

The quasi inverted results between both class dependent controllers, compared to the results without regards to the applicability conditions, can be explained again by the used data sets and the previously determined expected relative change in revenue within distinct combinations of spatial and temporal DNI variability classes. As discussed in section 7.3.2 only 6 combinations remain for both controllers, where the reference controller outperforms the corresponding class dependent controller. For the OFR controller the 6 combinations are evenly distributed over distinct variability conditions and none belong to the critical overcast conditions spatial class 5 and temporal class 6 to 8 (see Figure 7.15). This explains why the OFR controller outperforms the reference controller on almost all days. On the contrary, the OT controller is outperformed by two of the critical overcast conditions (spatial class 5 and temporal class 6 to 7). However, as we can see in Figure 7.24 around 91% of all days with a negative benefit for the OT controller belong to energetically rather less interesting days with an daily effective DNI sum below 2 kWh/(m²day). The weighted average changes in relative revenue within distinct ranges of daily effective DNI sum (see Figure 7.25) show a similar benefit for both controllers on days with an daily effective DNI sum above 3 kWh/(m²day). In fact, a small advantage of the OT controller is visible for these ranges. In contrast, a significant advantage of the OFR controller is visible for days with an daily effective DNI sum below 3 kWh/(m²day). Over all days the weighted average change in relative revenue amounts to 1.8% (OT) and 2.0% (OFR) respectively. Again, this is a significant improvement considering the costs for an ASI system and the uncertainty of the ASI derived DNI maps.

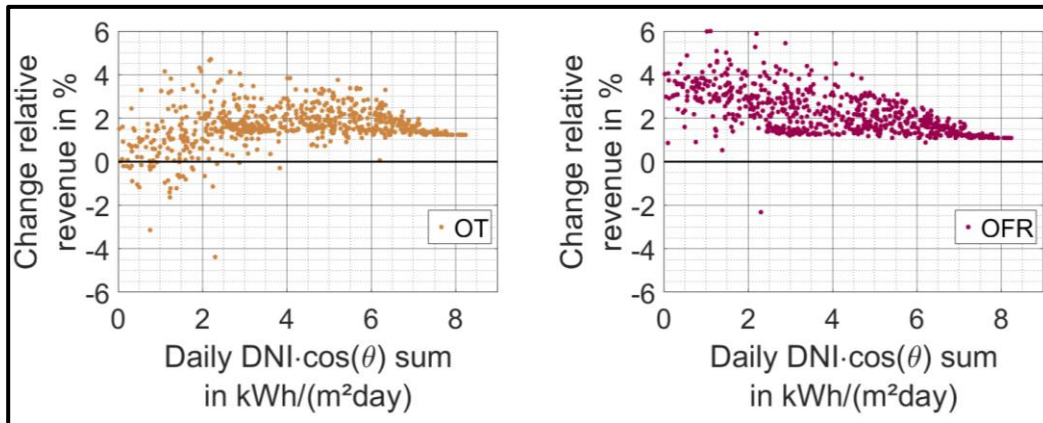


Figure 7.24: Estimated change relative revenue per day over Daily DNI sum (with regards to the applicability conditions)

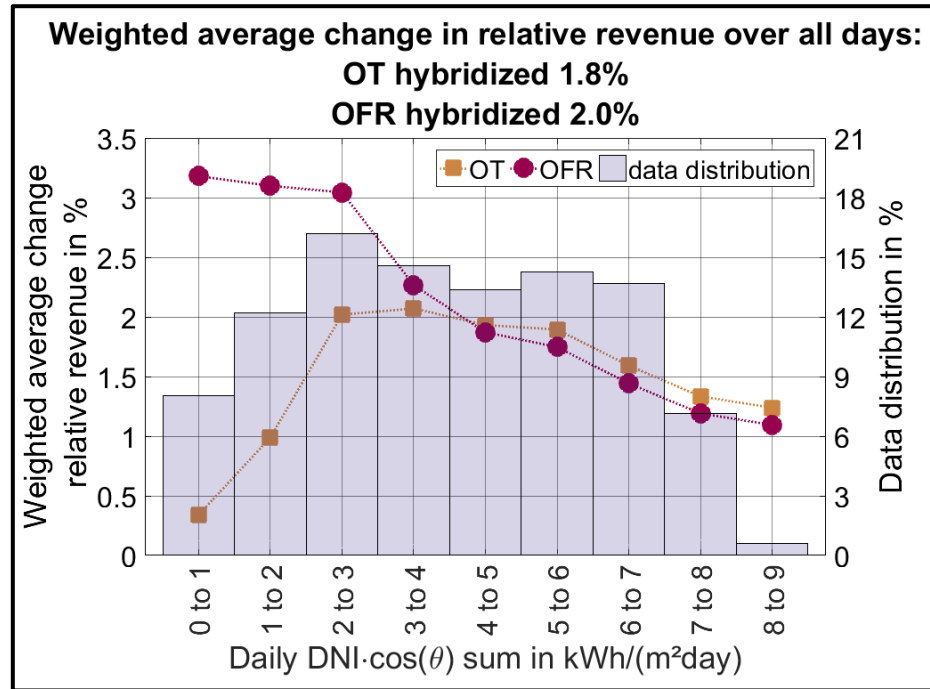


Figure 7.25: Weighted average change relative revenue over all days within distinct ranges of daily effective DNI sum as well as corresponding data distribution (with regards to the applicability conditions)

Lastly, I would like to point out again, that the results in this section are only estimates whose accuracy are not equivalent to the results from the simulations presented in section 7.2 and 7.3. However, the method is a useful tool that allows to estimate the potential benefit from using ASI derived DNI maps for plant control for the long term average and at different sites if DNI maps are available.

7.5 Conclusion on control optimization of PT solar fields with DNI maps

A combined temporal and spatial DNI variability classification consisting of 7 distinct classes was developed, that allows an improved control of PT power plants. This combined classification procedure includes a temporal DNI variability classification with eight distinct classes as well as a spatial DNI variability classification with 5 distinct classes. Spatial DNI information, provided by an ASI system, are used for the spatial DNI variability classification.

Three setups of controller parameters have been defined based on the same underlying control concept. The reference controller is used as the basis for two modified controller setups. The reference controller parameters for these two additional controllers are trimmed in a way to result in more aggressive or conservative behavior of the controller depending on the variability. Individual trimming values are used for each of the combined DNI variability classes. The two trimmed controller configurations differ in their behavior. The first has a trend to strongly improve stability the field outlet temperature (called objective temperature, OT) whereas the second tends to increase the overall focusing rate of the field (called objective focus rate, OFR). These new controllers are tailored for a PT solar field design according to the La Africana 50 MW power plant.

A benchmark over selected 22 days with variable DNI and different cloud conditions has been performed representing a wide variety of irradiance conditions. The chosen 22 days

match the distribution of DNI variability conditions found at PSA over two complete years helping to generate representative results for real situations.

The reference controller considers a state of the art solar field controller with DNI information from two pyrheliometers as typically available ground observations in commercial power plants as e.g. the La Africana power plant in Spain. The DNI information is used in a feedforward loop to calculate the expected mass flow required for the actual irradiance. The two new class dependent controllers do not use the meteo station signals directly, but refer to the average DNI values calculated from the DNI map delivered by the ASI system.

In the performance assessment study, the actual ruling DNI conditions acting on the solar field are provided by a separate measurement system based on shadow cameras, which are looking on the same area from above. These shadow cameras are providing an independent and more accurate estimate of the spatial distribution of DNI. Thanks to the solar towers available at the PSA, this unique assessment opportunity is available, while in commercial PT power plants only the ASI based spatial DNI information is available.

Five different economical and technical performance criteria are compared: the total solar field thermal heat flow, solar field focus rate, RMSD of the solar field outlet temperature (design set temperature as reference), reduction of emergency defocus incidents, and revenue. In terms of revenue as the major economic criterion both class dependent controllers are found to be quite similar, despite the higher heat flow of the OFR controller. OFR outperforms the reference by 1.40% and OT by 1.38% if aggregated over the entire 22 day data set. The controller OT outperforms the reference also in the remaining 4 technical performance criteria. In comparison, the controller OFR outperforms the reference controller in focus rate and heat flow, but is outperformed in RMSD of the solar field outlet temperature and reduction of emergency defocus incidents by the reference controller. This explains the close match in revenue between OFR and OT. The higher RMSD of the solar field outlet temperature translates in a higher volatility of the outlet temperature as well as the associated higher number of emergency defocus incidents, which is considered by the revenue calculation through the penalties.

In a subsequent more detailed evaluation step, it was evaluated under which conditions the new controllers lead to a revenue increase and whether there exit situations causing a revenue decrease. Increasing revenue conditions are considered as applicable, while the aim is to detect the unfavorable conditions with decreased revenue in real time and to avoid using the new controller in such situations. For this evaluation, the revenue changes for the 22 days are discretized in 10 minutes sliding data packages. Furthermore, each of these data packets was discretized to one of 40 theoretically possible combinations of spatial and temporal DNI variability classes. The overall relative change in revenue within each combination was analyzed. Around 85% (OT) and 89% (OFR) of the data set turned out to be applicable for the new controller.

Finally, a hybridized control strategy considering the applicability conditions was investigated. Whenever applicable conditions are present, the variability class dependent controllers with DNI maps are utilized. Otherwise, only the DNI information from two pyrheliometers as input to the reference controller are used. The results of the hybridized control strategy are promising. Both hybridized class dependent controller setups outperform the reference controller in all five criteria. In terms of revenue, the reference controller is outperformed by 1.93% (OT hybridized) and 1.95% (OFR hybridized) respectively, over the entire 22 days data set.

A significant reduction of emergency defocus incidents (21%) is visible for the controller OT (hybridized). This could lead to an additional reduction of maintenance costs, as

emergency defocus incidents are related to strong fluctuation in temperature as well as temperatures above safety thresholds, affecting various components within the solar field but also balance of plant. However, these effects cannot be quantified until now.

The expected additional absolute benefit in revenue increases to roughly 20.9 k€ (OT hybridized) and roughly 21.2 k€ (OFR hybridized) respectively, over the 22 test days compared to the reference controller.

All the presented evaluation strategies, including the ASI system and the VSF simulations, are quasi real time capable with an average processing time of roughly 7 seconds per time stamp (8x3.6GHz Intel Core i9-9900K, 2x16GB DDR4-2666 and PNY Quadro RTX 4000 8GB GDDR6) and could thus provide real-time control recommendations for power plant operators.

In a last study of this thesis an estimation was conducted, to evaluate the potential benefit of the class dependent controller over a larger period of two complete years (2016 and 2017). This estimation does not include any further VSF simulations. Instead, the distribution of occurring spatial and temporal DNI variability combinations were analyzed for each day. Subsequently, these distributions were combined with the expected benefits within the combinations, as determined from the simulation results with 22 days. Without regards of the applicability conditions a benefit of 1.0% (OT) and 0.9% (OFR) respectively is estimated. This increases significantly to 1.8% (OT) and 2.0% (OFR) respectively, when considering the applicability conditions. As discussed in detail, the main reason for the distinct results between the 22 simulated days and two estimated years is the higher share of less interesting overcast conditions within the two years. Of course the results of the two year data set must be viewed with some degree of caution, as they are not achieved by detailed solar field simulations but rather simple estimations.

Finally, I conclude that there are significant possibilities to improve the solar field controller of PT power plants with spatial irradiance information from ASI systems, despite the uncertainties of the DNI maps. The variability classification procedure is a crucial element of the concept and reveals the critical information in a suitable manner as needed by the controller. The classification procedure is a substantial requirement to realize the revenue increase, since situation dependent control parameters can be used. The uncertainties of the spatial DNI information might be considerably high at any given moment and for any discrete spot of the solar field. Yet, the ASI system appears to be capable to catch the prevailing overall spatial and temporal DNI variability conditions accurately enough for the plant control. Overall, it is the classification procedure which uncovers the relevant characteristics of DNI in a proper manner. This became apparent in initial preliminary studies, where the solar field controller had access to the spatial DNI field average from the ASI system, but without the DNI variability classification and the corresponding controller adaptations. Only slight benefit of a few tenth percent in revenue compared to the reference controller were observed in these initial preliminary studies. Theoretically, this slight benefit could be improved, as it is possible to obtain information from the DNI maps with a spatial resolution corresponding to the size of individual SCAs, allowing a more efficient local SCA focus controller. However, the current uncertainty constrains of the nowcasting system do not permit such high resolution control approaches. The used DNI variability classification based control approaches benefit from spatial and temporal aggregation effects, which have a significant influence on the accuracy of the ASI systems.

In this work the controller parameters according to the 7 combined spatial and temporal DNI variability classes are optimized. In future works, it could be interesting to investigate the benefit with individually optimized control parameters for each of the 40 theoretically possible combinations of spatial and temporal DNI variability classes.

Furthermore, the used ASI system provides also predictions up to 15 minutes ahead. However, currently the predictions are not utilized for the power plant controller. A further improvement could be achieved by including model predictive control strategies, which could utilize the predictions.

The presented new control strategies are tailored to the La Africana solar field design. Other power plants may have fundamentally distinct control strategies. Yet, to the best of my knowledge the presented class dependent control strategies are the first which use classified spatial DNI information. Spatial DNI information combined with the DNI classification procedure represent additional input information, which could be beneficiary for any existing and future PT solar field controller, regardless of the used overall control strategy.

8 Final conclusion and outlook

An ASI-based nowcasting system capable of describing complex multi-layer cloud conditions was developed. Moreover, the applicability of the ASI-based nowcasting system DNI maps for an optimized PT power plants operation was investigated. Solar energy is very likely to play a significant role in the future global energy supply. CSP plants with TES, such as PT power plants, could provide a renewable source of dispatchable energy, capable in balancing fluctuations in electrical grids caused by intermittent sources such as solar PV. However, highly variable solar irradiance conditions pose a control challenge for PT power plants. State of the art controllers have only access to DNI information from a single up to a handful of reference stations, considering solar field expansion >1 km in each horizontal dimension. Accordingly, the control system is not adequately informed about the prevailing irradiance conditions, which will cause from time to time inadequate control operations. Eventually this leads to unsuitable mass flows and collector positions within the solar field, which in turn cause partially overheating, defocusing or cooling. Each of these outcomes leads to an overall reduction of the energy yield and therefore to an economic loss.

According to the results spatial DNI information from ASI-based nowcasting systems can greatly improve the solar field control and the plant yield under complex conditions by reducing partially overheating, defocusing or cooling.

In section 8.1 I will conclude the content of the main chapters 4 to 7. More detailed conclusions are given at the end of each main chapter. An outlook for future investigations is given in section 8.2.

8.1 Final conclusion

In a first step distinct 3-D cloud modeling and tracking approaches were developed. Each considered approach treats all detected clouds as individual objects with distinct attributes (geolocation, motion vector, transmittance, etc.), capable of describing complex but frequent multi-layer cloud conditions. A benchmarking campaign over 30 days was performed. A two camera based block correlation method, utilizing difference image, arose as the most appropriate method. Especially advantageous about this method is the complete independence of cloud height and tracking from the cloud segmentation. This 2Cam approach can also be utilized in a nowcasting setup with more than two cameras. For this purpose a four camera system was developed (4CamH), which combines a voxel carving cloud modeling procedure with the cloud height and tracking method from the 2Cam approach. Through aggregation effects of up to 6 two camera pairs, slightly better results are achieved with 4CamH compared to a 2Cam approach. Overall it was observed that the deviation increase for all systems for higher clouds. These effects were studied and discussed in detail. Resolution constraints

present in all camera based cloud height and tracking approaches are the reason for these effects.

The cloud models and motion vectors enable the creation of binary shadow maps for the time of the image acquisition and the immediate future up to 15 minutes ahead. For the conversion of the binary shadow maps into DNI maps the cloud transmittance for each detected and modeled cloud object was determined. For a minority of clouds the transmittance is measured directly by a pyrliometer station. However, the majority of the relevant clouds remain without a transmittance measurement and require a transmittance allocation/estimation procedure. For this purpose, a probabilistic approach was developed and validated within this thesis. Clouds receive an estimated transmittance value based on their height, recent transmittance measurements and the results of a probability analysis over 574 cloudy days. This procedure was validated over the entire years 2016 and 2017 and reached an overall MAD and RMSD of 0.11 and 0.16 respectively. Additionally the probabilistic transmittance estimation approach was benchmarked with two binary, a simple statistical and a persistence approach. The probabilistic approach outperforms clearly all of them. Furthermore, site dependence of the presented approach, as well as the potential of automatic cloud classifications procedures to overcome these shortcomings, were discussed.

The overall accuracy of the nowcasting system in terms of DNI bias, MAD, RMSD and skill score was evaluated with three ground based pyrliometer stations over the entire years 2016 and 2017. This validation procedure corresponds to the state of the art. However, the accuracy of ASI-based nowcasting systems is heavily dependent on the prevailing weather conditions. Therefore, single number error metrics are only suitable to compare distinct nowcasting system when its ensured that both systems were validated under similar weather conditions. Certainly these error metrics are neither suitable to determine the real time accuracy nor to describe any spatially resolved nowcast accuracy. Without the specification of real time uncertainties, an application of the nowcasting system results is not feasible. Therefore, a real time uncertainty analysis method was developed, which takes at all times the prevailing weather conditions into account. A basic uncertainty with a coverage probability of 68.3%, which takes into account the current DNI variability class, Sun elevation angle and lead time, was determined over the years 2016 and 2017 via the observed deviations between the DNI maps and the three reference pyrliometer. The basic uncertainties were applied to all pixels of the DNI maps. Spatial variations of the uncertainties were considered by identifying less accurate transient zones within which the uncertainties are adjusted. This method allows a spatial accuracy assessment, which goes far beyond the previously used accuracy metrics of RMSD, MAD, bias, and skill scores. The final coverage probability of the developed real time uncertainty analysis was validated by the DNI maps with and without uncertainty and the reference pyrliometers over the entire year 2018, which was not used for the determination of the basic uncertainty. It was found that the developed uncertainty analysis achieved the targeted coverage probability of roughly 68.3% over the entire period and for all discretized types of condition.

The average processing time of the presented nowcasting system, including DNI maps with uncertainties for the current conditions as well as 15 distinct nowcast, amounts to roughly 12 seconds per time stamp, using an off-the-shelf computer (8x3.6GHz Intel Core i9-9900K, 2x16GB DDR4-2666 and PNY Quadro RTX 4000 8GB GDDR6). This should be sufficient for most possible real-time applications.

Regarding the application of the ASI system for the control optimization of PT solar fields, the first step was to develop a DNI variability classification procedure which takes into account both spatial and temporal variabilities. The developed classification consists of seven

aggregated combined classes which in turn are based on a temporal classification with eight classes and a spatial classification with five classes. Secondly, two new class dependent solar field controllers, tailored for the La Africana power plant, were developed, with optimized control parameters for each combined DNI variability class. The controllers differ in their objective. One controller intends to optimize the solar field outlet temperature (OT) while the other controller intends to maximize the solar field focus rate (OFR).

A benchmark of the class dependent controllers and the La Africana reference controller has been performed with the VSF over 22 days. For the simulations the class dependent controller received DNI maps from the ASI-based nowcasting system, whereas the actual ruling DNI conditions acting on the solar field are provided by an independent nowcasting system based on shadow cameras. Thereby, the errors of the ASI system are considered, as the expected irradiance conditions represented by the ASI data that are seen by the controller deviate from reality (represented by the shadow camera data). Both class dependent controllers outperform the reference controller significantly in terms of revenue for the 22 example days (OT 1.38% and OFR 1.40%).

Subsequently, applicability conditions were identified, by analyzing the expected change in revenue in comparison to the reference controller within distinct combinations of spatial and temporal DNI variability classes. Applicable conditions are considered present whenever it is expected that the class dependent controller outperforms the reference controller. These applicability conditions are utilized for an improved hybridized control strategy, which substitutes the class dependent controllers by the reference controller whenever the class dependent controllers are not applicable. Under consideration of the applicability the reference controller was outperformed in terms of revenue by 1.93% (OT hybridized) and 1.95% (OFR hybridized). Additionally, the OT hybridized controller showed a significant reduction of emergency defocus incidents (21%). This could lead to further reductions of maintenance costs, as emergency defocus incidents are related to strong fluctuation in temperature as well as temperatures above safety thresholds, affecting various components within the solar field and balance of plant.

Finally, the impact of the class dependent controller as well as the hybridized controller was investigated over a two year period (2016 and 2017). For this purpose, an estimation procedure was introduced, which combines the distribution of occurring spatial and temporal DNI variability combinations with the expected benefits within the combinations from the simulation results over 22 days. The results of the estimation over 2 years resemble the results from the detailed simulations over 22 days, with 1.0% (OT) and 0.9% (OFR) compared to 1.8% (OT hybridized) and 2.0% (OFR hybridized) respectively. The cause for the remaining differences between the simulated and estimated results is discussed in detail, which depends mainly on the different distribution of weather conditions (see 7.4).

It has to be pointed out, that an improvement of about 2% in revenue is significant. This holds in particular, if we take into account that the errors of the ASI system were considered for the study and that no adaptations of the solar field or balance of plant are needed. All involved adjustments consider only the used control parameters. The hardware costs of the ASI-based nowcasting system are marginal, with its 2 to 4 off-the-shelf cameras and one off-the-shelf computer. Experience has shown that the biggest hardware costs are normally those of any scaffolding required for a clear view of the cameras. However, in most cases there will probably be no need for additional scaffolding, since the meteorological stations required in every CSP power plant have the same requirements in terms of a clear view.

8.2 Outlook

Several possible future improvements of the ASI system and its application were identified in the framework of this work. The cloud segmentation can be one of the key processing steps for future improvements. A machine learning approach could be superior, compared to the currently used approach with a clear sky library. Future improvements should also include an automatized cloud classification. As discussed, such a classification could improve the probabilistic cloud transmittance estimation approach. Moreover, even a simple cloud classification, which only distinguishes between different cloud layers, could improve the cloud modeling and tracking approach significantly. Improvements could be achieved especially during complex multi-layer conditions, just by preselecting the parts of the sky used by the cloud modeling and tracking algorithms.

Apart of the objective of this thesis, harbor ASI based nowcasting systems a great potential for energy, meteorology and atmospheric sciences and industry. This is reflected by the interest of the worldwide scientific community on these topics. As **Yang et al. 2018** points out, according to Google scholar, there were alone in 2016 15700 publications related to the topic “solar irradiance forecasting”.

Future improvements of the class dependent control strategies could include a stronger discretization of the control parameters. Moreover, additional model predictive control strategies could exploit the nowcasts provided by the ASI-based nowcasting system.

Of course the here presented control optimizations are tailored to the La Africana solar field design. Yet, as discussed in section 7.5 represent the spatial DNI information combined with the DNI classification procedure additional input information, which could be beneficiary for any existing and future PT solar field controller, regardless of the used overall control strategy.

Furthermore, I would like to point out that the potential benefit of spatial DNI information combined with classification procedures is not limited to PT power plants. Similar benefits might be feasible for other CSP technologies, such as Fresnel and even point focusing tower power plants. Benefits are also expected for solar PV power plants and electrical grids.

The application of ASI systems for the optimization of parabolic trough plant control and further solar energy technologies is highly recommended. A significant revenue increase for parabolic trough plants can already be implemented now. Future research is expected to lead to noticeable further improvements for parabolic trough plants and other solar technologies.

Appendix A. DNI variability classification comparison

For industrial size solar fields, the field average of the irradiance and its variability class is more relevant than the irradiance at a singular point within the solar field. However, for the uncertainty specification, the classification based on a single pyrheliometer measurement is used. To show the potential influence of this decision, it is investigated if the DNI variability class of point-like measurements (pyrheliometer) is well-correlated to the class of the field average. A quadratic area of 2 km² and a data set of 30 days is used. The spatial DNI information (see Figure A1 (left)) is generated by the nowcasting system. All pixels of the DNI map describing the 2 km² area around the pyrheliometer are averaged. Only DNI maps that describe the current situation are used for this study (lead time 0). Over the 30 days, the field average DNI and the corresponding DNI from a pyrheliometer are classified. These DNI variability classes from both sources are compared to each other. The scatter density plot depicted in Figure A1 (right) shows good agreement between the point-like measurement-based classification and the classification based on a spatial solar field average DNI. The relative frequency of the matched classes is described by the color. All bins in one column add up to 100%. A perfect match is achieved for 94.9% of all timestamps. A mismatch by a single class is observed in only 4.5% the cases. A stronger mismatch is observed only in 0.6% of the time stamps. This is expected as the short-term temporal variability is caused by cloud patterns that are typically of larger geographical extension than the solar field size. Therefore, it is considered quantitatively proven, that using a singular point measurement for variability classifications of fields with industrial solar field sizes is justified.

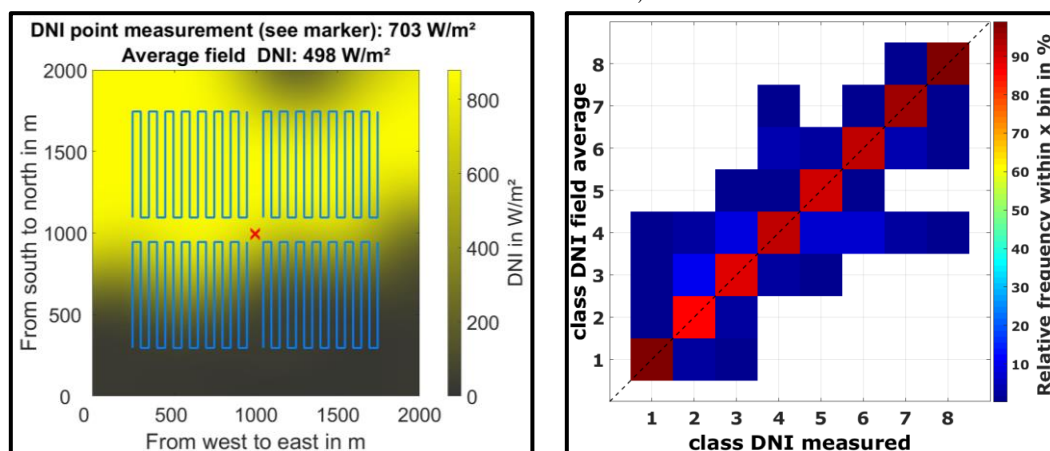


Figure A1: (left) Example DNI map with a marked solar field (2 km²). (right) Scatter density plot comparison of DNI variability classifications of point measurements and spatial field averages. All bins in one column add up to 100%.

Appendix B. Comparison of p68.3 values within distinct Sun elevation angle ranges

The discretization in two Sun elevation ranges above and below 30° is chosen due to notable deviation in p68.3 values in between these ranges. In a first step, the p68.3 values within Sun elevation ranges of 10° are determined, according to section 6.2.3. The nowcasting system does not process Sun elevation angles below 10°, due to the strong distortion of the fisheye lens image at the horizon. Therefore, these Sun elevation angles are not taken into account. The nowcasting system creates only persistence nowcasts for those timestamps with Sun elevation angles below 10°. The last angular range includes all Sun elevation angles above 60°, due to the scarcity of Sun elevation angle above 70° at the PSA. In a subsequent step, the p68.3 values for different lead times and DNI variability classes between the different Sun elevation ranges are compared. For this purpose, the MAD of all p68.3 values of each possible combination of Sun elevation ranges is calculated, treating the upper and lower limit separately. The results of this study are depicted in Figure B1, using two separate plots for the upper and lower p68.3 values. No significant deviations are observed between the two lowest ranges (10° to 20° and 20° to 30°). The same applies for all ranges above 30°. However, notable deviations are apparent between the ranges below and above 30°. This deviation between low and high Sun elevation angles is expected. Clouds that affect the nowcasts during low Sun elevation angles are close to the sky image horizon and, therefore, further away. A relevant cloud at 6 km height seen at a 20° elevation angle is roughly 16.5 km away from the camera. This makes all image processing steps more error prone, especially for the cloud height detection and cloud tracking. In addition, the distortion of the fisheye lens cameras is stronger when closer to the horizon. The cloud height errors have a stronger effect for lower elevation angles. Therefore, it is chosen to discretize the deviation values in the two Sun elevation ranges below and above 30°.

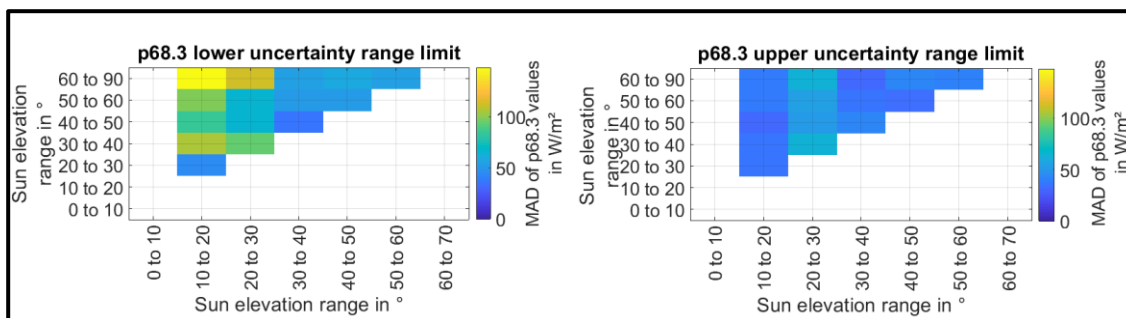


Figure B1: Comparison of p68.3 values for different Sun elevation ranges.

Bibliography

- Abutayeh, M., Alazzam, A., El-Khasawneh, B., 2014. Balancing heat transfer fluid flow in solar fields, *Sol. Energy*, 105, 381-389. doi: 10.1016/j.solener.2014.03.025
- Allmen, M.C., Kegelmeyer Jr., W.P., 1996. The computation of cloud-base height from paired whole-sky imaging cameras. *J. Atmos. Ocean. Technol.* 13 (1), 97–113. [http://journals.ametsoc.org/doi/abs/10.1175/1520-0426\(1996\)013%3C0097:TCOCBH%3E2.0.CO%3B2](http://journals.ametsoc.org/doi/abs/10.1175/1520-0426(1996)013%3C0097:TCOCBH%3E2.0.CO%3B2).
- Bar-Or, R. Z., Koren, I., Altaratz, O., 2010. Estimating cloud field coverage using morphological analysis, *Environ. Res. Lett.*, 5(1), 014022. doi:10.1088/1748-9326/5/1/014022.
- Bauer, K.G., 1976. Comparison of cloud motion winds with coinciding radiosonde winds. *Mon Weather Rev.* 104. 922–931. <https://doi.org/10.1175/1520-0493>
- Beekmans, C., Schneider, J., Läbe, T., Lennefer, M., Stachniss, C., Simmer, C., 2016. Cloud photogrammetry with dense stereo for fisheye cameras. *Atmos. Chem. Phys.* 16 (22), 14231–14248. <http://dx.doi.org/10.5194/acp-16-14231-2016>.
- Bernecker, D., Riess, C., Angelopoulou, E., Hornegger, J., 2014. Continuous short-term irradiance forecasts using sky images. *Sol. Energy*, 110, 303–315. doi: 10.1016/j.solener.2014.09.005.
- Blanc, P., Massip, P., Kazantzidis, A., Tzoumanikas, P., Kuhn, P., Wilbert, S., Schüler, D., Prah, C., 2017. Short-Term Forecasting of High Resolution Local DNI Maps with Multiple Fish-Eye Cameras in Stereoscopic Mode, AIP conference Proceedings 1850. doi: 10.1063/1.4984512
- Bone, V., Pidgeon, J., Kearney, M., Veeraragavan, A., 2018. Intra-hour direct normal irradiance forecasting through adaptive clear-sky modelling and cloud tracking. *Solar Energy* 159, 852–867. <https://doi.org/10.1016/j.solener.2017.10.037>
- Bosch, J.L., Kleissl, J., 2013. Cloud motion vectors from a network of ground sensors in a solar power plant. *Solar Energy* 95, 13-20. <https://doi.org/10.1016/j.solener.2013.05.027>
- Bradshaw, C.J., Brook, B.W., 2014. Human population reduction is not a quick fix for environmental problems. *Proceedings of the National Academy of Sciences*, 111(46), 16610–16615. <https://doi.org/10.1073/pnas.1410465111>
- Braun, M., Stetz, T., Bründlinger, R., Mayr, C., Ogimoto, K., Hatta, H., Kobayashi, H., Kroposki, B., Mather, B., Coddington, M., Lynn, K., 2012. Is the distribution grid ready to accept large-scale photovoltaic deployment? State of the art, progress, and future prospects. *Progress in photovoltaics: Research and applications*, 20(6), 681–697. <https://doi.org/10.1002/pip.1204>
- Breyer, C., Bogdanov, D., Gulagi, A., Aghahosseini, A., Barbosa, L., Koskinen, O., Barasa, M., Caldera, U., Afanasyeva, S., Child, M., Farfan, J., Vainikka, P., 2017. On the role of solar photovoltaics in global energy transition scenarios. *Progr. Photovoltaics* 25, 727–745. doi: 10.1002/pip.2885
- Bright, J. M., Killinger, S., Lingfors, D., & Engerer, N. A., 2018. Improved satellite-derived PV power nowcasting using real-time power data from reference PV systems. *Solar Energy*, 168, 118–139. doi:10.1016/j.solener.2017.10.091
- Bruninx, K., Madzharov, D., Delarue, E., D'haeseleer, W., 2013. Impact of the German nuclear phase-out on Europe's electricity generation—A comprehensive study. *Energy Policy*, 60, 251–261. <https://doi.org/10.1016/j.enpol.2013.05.026>

Bibliography

- Burkholder, F., Kutscher, C., 2009. Heat Loss Testing of Schott's 2008 PTR70 Parabolic Trough Receiver, Technical Report, NREL.
- Chang, F.-L., Li, Z., 2002. Estimating the vertical variation of cloud droplet effective radius using multispectral nearinfrared satellite measurements. *J. Geophys. Res.*, 107, 4257, AAC 7-1-AAC 7-12. doi:10.1029/2001JD000766.
- Chattopadhyay, D., 2014. Modelling renewable energy impact on the electricity market in India. *Renewable and Sustainable Energy Reviews*, 31, 9–22. <https://doi.org/10.1016/j.rser.2013.11.035>
- Chen, J., Rossow, W. B., Zhang, Y., 2000. Radiative effects of cloud-type variations. *J. Climate*, 13, 264–286. doi: 10.1175/1520-0442(2000)013<0264:REOCTV.2.0.CO;2
- Chernykh, I.V., Eskridge, R.E., 1995. Determination of cloud amount and level from radiosonde soundings. *J. Appl. Meteor.*, 35, 1362–1369. <https://doi.org/10.1175/1520-0450>
- Chow, C.W., Urquhart, B., Lave, M., Dominguez, A., Kleissl, J., Shields, J., Washom, B., 2011. Intra-hour forecasting with a total sky imager at the UC San Diego solar energy testbed. *Sol. Energy* 85, 2881–2893. doi: 10.1016/j.solener.2011.08.025.
- Chow, C.W., Belongie, S., Kleissl, J., 2015. Cloud motion and stability estimation for intra-hour solar forecasting. *Solar Energy* 115, 645–655. <http://dx.doi.org/10.1016/j.solener.2015.03.030>.
- Coimbra, C.F.M., Kleissl, J., Marquez, R., 2013. Overview of Solar-Forecasting Methods and a Metric for Accuracy Evaluation. In *Solar Energy Forecasting and Resource Assessment*, Kleissl, J., Eds.; Academic Press: Oxford, UK, 171–194.
- Cook, J., Oreskes, N., Doran, P.T., Anderegg, W.R., Verheggen, B., Maibach, E.W., Carlton, J.S., Lewandowsky, S., Skuce, A.G., Green, S.A., Nuccitelli, D., 2016. Consensus on consensus: a synthesis of consensus estimates on human-caused global warming. *Environmental Research Letters*, 11(4), 048002. doi:10.1088/1748-9326/11/4/048002
- Crăciun, B.I., Kerekes, T., Séra, D., Teodorescu, R., Annakkage, U.D., 2017. Power ramp limitation capabilities of large PV power plants with active power reserves. *IEEE Trans Sustainable Energy*, 8, 573–581. doi: 10.1109/tste.2016.2612121
- Crispel, P., Roberts, G., 2017. All-sky photogrammetry techniques to georeference a cloud field. *Atmos. Meas. Tech.*, 11, 593–609. <https://doi.org/10.5194/amt-11-593-2018>
- Denholm, P., Margolis, R., 2016. Energy Storage Requirements for Achieving 50% Solar Photovoltaic Energy Penetration in California, NREL/TP-6A20-66595, doi: 10.2172/1298934
- Dersch, J., Hennecke, K., Quaschnig, V., 2012. Free Greenius – New Options and Availability. In *Proceedings of the SolarPACES 2012 Conference*, Marrakesch (Marokko)
- Dev, S., Lee, Y.H., Winkler, S., 2017. Color-Based Segmentation of Sky/Cloud Images From GroundBased Cameras. *IEEE Journal of Selected Topics in Applied Earth Observations and Remote Sensing* 10, 231–242. doi:10.1109/JSTARS.2016.2558474.
- Dieckmann, S., 2017. DLR - Institut of Solar Research - greenius - The green energy system analysis tool. URL http://www.dlr.de/sf/desktopdefault.aspx/tabid-11688/20442_read-44865/
- Dlugokencky, E.J., Hall, B.D., Montzka, S.A., Dutton, G., Mühle, J., Elkins, J.W., 2018. Atmospheric composition [in State of the Climate in 2017]. *Bulletin of the American Meteorological Society*, 99(8), 46–49

Bibliography

- Duffie, J., Beckman, W., 2006. Solar Engineering of Thermal Processes, third edition, John Wiley & Sons Hoboken, New Jersey (USA)
- Farneback, G., 2003. Two-frame motion estimation based on polynomial expansion. *Image Anal.*, 10, 363–370. doi: 10.1007/3-540-45103-X_50
- Frederick, J. E., Steele, H. D., 1995. The transmission of sunlight through cloudy skies: An analysis based on standard meteorological information. *J. Appl. Meteor.*, 34, 2755–2761. doi: 10.1175/1520-0450(1995)034<2755:TTOSTC>2.0.CO;2
- Fu Q., 1996. An accurate parameterization of the solar radiative properties of cirrus clouds for climate models. *J. Climate*;9:2058–82. doi: 10.1175/1520-0442(1996)009<2058:AAPOTS>2.0.CO;2
- Fu, C.L., Cheng, H.Y., 2013 Predicting solar irradiance with all-sky image features via regression. *Sol. Energy*, 97, 537–550. doi: 10.1016/j.solener.2013.09.016.
- Fung, V., Bosch, J.L., Roberts, S.W., Kleissl, J., 2013. Cloud shadow speed sensor. *Atmos. Meas. Techn.* 6 (5). <http://dx.doi.org/10.5194/amt-7-1693-2014>.
- García, I., Álvarez, J., Blanco, D., 2011. Performance model for parabolic trough solar thermal power plants with thermal storage: comparison to operating plant data. *Sol. Energy* 95, 2443–2460. doi: 10.1016/j.solener.2011.07.002
- Geuder, N., Wolfertstetter, F., Wilbert, S., Schüler, D., Affolter, R., Kraas, B., Lüpfer, E., Espinar, B., 2015. Screening and Flagging of Solar Irradiation and Ancillary Meteorological Data, *Energy Procedia*, 69, 1989–1998. doi:10.1016/j.egypro.2015.03.205, 2015.
- Gevorgian, V., Booth, S., Review of PREPA technical requirements for interconnecting wind and solar generation, NREL/TP; 5 D 00– 57089, 2013, available online: <http://www.nrel.gov/docs/fy14osti/57089.pdf>
- Gillett, N.P., Arora, V.K., Zickfeld, K., Marshall, S.J., Merryfield, W.J., 2011. Ongoing climate change following a complete cessation of carbon dioxide emissions. *Nature Geoscience*, 4(2), 83–87. doi: 10.1038/NGEO1047
- Giostrì, A., 2012. Transient effects in linear concentrating solar thermal power plant, Ph.D. thesis, Energy Department, Politecnico Di Milano <http://hdl.handle.net/10589/89590>
- Hahn, C. J., Rossow, W. B., Warren, S. G., 2001. ISCCP cloud properties associated with standard cloud types identified in individual surface observations. *J. Climate*, 14, 11–28. doi: 10.1175/1520-0442(2001)014<0011:ICPAWS>2.0.CO;2
- Hanrieder, N., Sengupta, M., Xie, Y., Wilber, S., Pitz-Paal, R., 2016. Modeling beam attenuation in solar tower plants using common DNI measurements. *Solar Energy* 129, 244–255. doi: 10.1016/j.solener.2016.01.051
- Hart, E.K., Jacobson, M.Z., 2011. A Monte Carlo approach to generator portfolio planning and carbon emissions assessments of systems with large penetrations of variable renewables. *Renewable Energy*, 36(8), 2278–2286. <https://doi.org/10.1016/j.renene.2011.01.015>
- Hasenbalg, M., Kuhn, P., Wilbert, S., Kozonek, N., Nouri, B., Ramirez, L., Zarzalejo, L., Schmidt, T., Kazantzidis, A., Blanc, P., Pitz-Paal, R., 2019. Benchmarking of six cloud segmentation algorithms for ground-based all-sky imagers, *Sol. Energy*, (submitted)
- Heard, B.P., Brook, B.W., Wigley, T.M., Bradshaw, C.J., 2017. Burden of proof: A comprehensive review of the feasibility of 100% renewable-electricity systems. *Renewable and Sustainable Energy Reviews*, 76, 1122–1133. <https://doi.org/10.1016/j.rser.2017.03.114>

Bibliography

- Heinle, A., Macke, A., Srivastav, A., 2010. Automatic cloud classification of whole sky images, *Atmos. Meas. Tech.* 3 (2010) 557-567. doi: 10.5194/amt-3-557-2010
- Hess, M., Koepke, P., Schult, I., 1998. Optical properties of aerosols and clouds: The software package OPAC. *Bull. Amer. Meteor. Soc.*, 79, 831–844. doi: 10.1175/1520-0477(1998)079<0831:OPOAAC>2.0.CO;2
- Hirsch, E., Agassi, E., Koren, I., 2011. A novel technique for extracting clouds base height using ground based imaging. *Atmos. Meas. Tech. Discuss.*, 3, 4231–4260. doi:10.5194/amtd-3-4231-2010
- Hirsch, T., Schenk, HE., 2010. Dynamics of oil-based parabolic trough plants—A detailed transient simulation model. In *Proceedings of the SolarPACES 2010 Conference*, Perpignan (France)
- Hirsch, T., Martin, N., Gonzalez. L., Biencinto, M., Wilbert, S., Schroedter-Homscheidt, M., Chenlo, F., Feldhoff, J., 2014. Direct Normal Irradiance Nowcasting methods for optimized operation of concentrating solar technologies, DNICast project, DNICast Deliverable 2.1. <http://www.dnicast-project.net>.
- Hong, Y., Liu, G., Li, J.-L. F., 2016. Assessing the Radiative Effects of Global Ice Clouds Based on CloudSat and CALIPSO Measurements, *J. Climate*, 29, 7651–7674. doi:10.1175/JCLI-D-15-0799.1
- Huang, H., Yoo, S., Yu, D., Huang, D., Qin, H., 2012. Correlation and local feature based cloud motion estimation. In: *Proceedings of the Twelfth International Workshop on Multimedia Data Mining. MDMKDD '12*. ACM, New York, NY, USA, 1–9. <http://doi.acm.org/10.1145/2343862.2343863>.
- Huertas-Tato, J., Rodríguez-Benítez, F.J., Arbizu-Barrena, C., Aler-Mur, R., Galvan-Leon, I., Pozo-Vázquez, D., 2017. Automatic cloud-type classification based on the combined use of a sky camera and a ceilometer. *J. Geophys. Res. Atmos.* 122, 11045–11061. doi: 10.1002/2017JD027131
- IEA, 2019. *Global Energy and CO2 Status Report 2018*, France by IEA – March 2019. <https://www.iea.org/geco/>. Accessed: 2019-06-14
- Ineichen, P., Perez, R., 2002. A new air mass independent formulation for the Linke turbidity coefficient. *Solar Energy* 73, 151–157. doi: 10.1016/S0038-092X(02)00045-2
- Inman, R.H., Pedro, H.T.C., Coimbra, C.F.M., 2013. Solar forecasting methods for renewable energy integration. *Prog. Energy Combust. Sci.* 39, 535–576. doi: 10.1016/j.pecs.2013.06.002.
- IPCC, 2018. *Global warming of 1.5°C. An IPCC Special Report on the impacts of global warming of 1.5°C above pre-industrial levels and related global greenhouse gas emission pathways, in the context of strengthening the global response to the threat of climate change, sustainable development, and efforts to eradicate poverty*. <http://ipcc.ch/report/sr15/> [V. Masson-Delmotte, P. Zhai, H. O. Pörtner, D. Roberts, J. Skea, P.R. Shukla, A. Pirani, W. Moufouma-Okia, C. Péan, R. Pidcock, S. Connors, J. B. R. Matthews, Y. Chen, X. Zhou, M. I. Gomis, E. Lonnoy, T. Maycock, M. Tignor, T. Waterfield (eds.)]. In Press.
- IRENA, 2019. *Renewable capacity statistics 2019*, International Renewable Energy Agency (IRENA), Abu Dhabi. ISBN 978-92-9260-123-2
- International Organization for Standardization, 1990. ISO 9059:1990 Solar energy - Calibration of field pyrheliometers by comparison to a reference pyrheliometer, international standard, Geneva (Switzerland)
- International Organization for Standardization, 1993. ISO 9846:1993 Solar energy - Calibration of a pyranometer using a pyrheliometer, international standard, Geneva

(Switzerland)

- Janotte, N., 2012. Requirements for Representative Acceptance Tests for the Prediction of the Annual Yield of Parabolic Trough Solar Fields, Ph.D. thesis, Fakultät für Maschinenwesen der Rheinisch-Westfälischen Technischen Hochschule Aachen, Aachen Germany
- Jung, S., 2015. Variabilität der solaren Einstrahlung in 1-Minuten aufgelösten Strahlungszeitserien. Master's Thesis, Universität Augsburg, Germany
- Kahn, B.H., Chahine, M.T., Stephens, G.L., Mace, G.G., Marchand, R.T., Wang, Z., Barnet, C.D., Eldering, A., Holz, R.E., Kuehn, R.E., Vane, D.G., 2008. Cloud type comparisons of AIRS, CloudSat, and CALIPSO cloud height and amount, *Atmos. Chem. Phys.*, 8, 1231–1248, <https://doi.org/10.5194/acp-8-1231-2008>.
- Kalman, R.E., 1960. A New Approach to Linear Filtering and Prediction Problems. *J. Basic Eng.* 82. 35-45. doi:10.1115/1.3662552
- Kassianov, E., Long, C.N., Christy, J., 2005. Cloud-base-height estimation from paired ground-based hemispherical observations. *J. Appl. Meteorol.* 44 (8), 1221–1233. <http://dx.doi.org/10.1175/JAM2277.1>.
- Kayetha, V.K., Collins, R.L., 2016. Optically thin midlevel ice clouds derived from Cloud Aerosol Lidar and Infrared Pathfinder Satellite Observations, *J. Appl. Remote Sens.* 10(4), 046007. doi: 10.1117/1.JRS.10.046007.
- Kazantzidis, A., Tzoumanikas, P., Bais, A.F., Fotopoulos, S., Economou, G., 2012. Cloud detection and classification with the use of whole-sky ground-based images, *Atmos. Res.* 113 80-88. doi: 10.1016/j.atmosres.2012.05.005
- Kazantzidis, A., Tzoumanikas, P., Blanc, P., Massip, P., Wilbert, S., Ramirez-Santigosa, L., 2017. Short-term forecasting based on all-sky cameras, In: *Renewable Energy Forecasting*. Woodhead Publishing Series in Energy. Woodhead Publishing, pp. 153–178. doi: 10.1016/B978-0-08-100504-0.00005-6.
- Kennedy, C., Stewart, I.D., Westphal, M.I., Facchini, A., Mele, R., 2018. Keeping global climate change within 1.5 C through net negative electric cities. *Current opinion in environmental sustainability*, 30, 18–25. <https://doi.org/10.1016/j.cosust.2018.02.009>
- Kikuchi, N., Nakajima, T., Kumagai, H., Kuroiwa, H., Kamei, A., Nakamura, R., Nakajima, T. Y., 2006. Cloud optical thickness and effective particle radius derived from transmitted solar radiation measurements: comparison with cloud radar observations, *J. Geophys. Res.* 111, D07205. doi:10.1029/2005JD006363
- King, M. D., 1987. Determination of the scaled optical thickness of clouds from reflected solar radiation measurements. *J. Atmos. Sci.*, 44, 1734–1751. doi: 10.1175/1520-0469(1987)044<1734:DOTSOT>2.0.CO;2
- Knutti, R., Rogelj, J., 2015. The legacy of our CO 2 emissions: a clash of scientific facts, politics and ethics. *Climatic Change*, 133(3), 361–373. doi: 10.1007/s10584-015-1340-3
- Kokhanovsky A. 2004. Optical properties of terrestrial clouds. *Earth Sci Rev* 2004;64:189–241. doi: 10.1016/S0012-8252(03)00042-4
- Koren, I., Remer, L.A., Kaufman, Y.J., Rudich, Y., Martins, J.V., 2007. On the twilight zone between clouds and aerosols *Geophys. Res. Lett.* 34 L08805. doi: 10.1029/2007GL029253
- Kost, C., Shammugam, S., Jülch, V., Nguyen, H., Schlegl, T., 2018. Levelized cost of electricity renewable energy technologies, Fraunhofer ISE, <https://www.ise.fraunhofer.de/en/publications/studies/cost-of-electricity.html>

Bibliography

- Kraas, B., Schroedter-Homscheidt, M., Madlener, R., 2013. Economic merits of a state-of-the-art concentrating solar power forecasting system for participation in the Spanish electricity market. *Sol. Energy*, 93, 244–255. doi: 10.1016/j.solener.2013.04.012.
- Kuhn, P., Nouri, B., Wilbert, S., Prah, C., Kozonek, N., Schmidt, T., Yasser, Z., Ramirez, L., Zarzalejo, L., Meyer, A., Vuilleumier, L., Heinemann, D., Blanc, P., Pitz-Paal, R., 2017a. Validation of an all-sky imager-based nowcasting system for industrial PV plants. *Prog. Photovolt.: Res. Appl.* doi: 10.1002/pip.2968.
- Kuhn, P., Wilbert, S., Prah, C., Schüler, D., Haase, T., Hirsch, T., Wittmann, M., Ramirez, L., Zarzalejo, L., Meyer, A. and Vuilleumier, L., 2017b. Shadow camera system for the generation of solar irradiance maps. *Sol. Energy* 157, 157–170. doi: 10.1016/j.solener.2017.05.074
- Kuhn, P., Wirtz, M., Killius, N., Wilbert, S., Bosch, J.L., Hanrieder, N., Nouri, B., Kleissle, J., Ramirez, L., Schroedter-Homscheidt, M., Heinemann, D., Kazantzidis, A., Blanc, P., Pitz-Paal, R., 2018. Benchmarking three low-cost, low-maintenance cloud height measurement systems and ECMWF cloud heights. *Sol. Energy* 168, 140–152. <https://doi.org/10.1016/j.solener.2018.02.050>
- Kuhn, P., Nouri, B., Wilbert, S., Hanrieder, N., Prah, C., Ramirez, L., Zarzalejo, L., Schmidt, T., Yasser, Z., Heinemann, D., Tzoumanikas, P., 2019a. Determination of the optimal camera distance for cloud height measurements with two all-sky imagers. *Sol. Energy.*, 179, 74–88. doi: 10.1016/j.solener.2018.12.038.
- Kuhn, P., Garsche, D., Wilbert, S., Nouri, B., Hanrieder, N., Prah, C., Zarzalejo, L., Fernández, J., Kazantzidis, A., Schmidt, T., Heinemann, D., Blanc, P., Pitz-Paal, R., 2019b, Shadow-camera based solar nowcasting system for shortest-term forecasts. *Meteorologische Zeitschrift*. Vol. 28 No. 3, 255–270. doi: 10.1127/metz/2019/0954
- Kuhn, P., 2019c. Development and Benchmarking of Solar Nowcasting Systems, Ph.D. thesis, Fakultät für Maschinenwesen der Rheinisch-Westfälischen Technischen Hochschule Aachen, Aachen Germany
- Kutulakos, K.N., Seitz, S.M., 2000. A theory of shape by space carving. *International Journal of Computer Vision* 38, 199–218. <https://doi.org/10.1023/A:100819122>
- Leese, J.A., Novak, C.S., 1971. An automated technique for obtaining cloud motion from geosynchronous satellite data using cross correlation. *J. Appl. Meteor.*, 10, 118–132. <https://doi.org/10.1175/1520-0450>
- Li, C.h., K. Lee, C., 1993. Minimum cross entropy thresholding. *Pattern Recognition* 26, 617–625. [https://doi.org/10.1016/0031-3203\(93\)90115-D](https://doi.org/10.1016/0031-3203(93)90115-D)
- Li, J., Yi, Y., Minnis, P., Huang, J., Yan, H., Ma, Y., Wang, W., Ayers, J.K., 2011. Radiative effect differences between multilayered and single-layer clouds derived from CERES, CALIPSO, and CloudSat data. *J. Quant. Spectrosc. Radiat. Transfer*, 112, 361–375. doi: 10.1016/j.jqsrt.2010.10.006
- Li, Q., Lu, W., Yang, J., 2011. A Hybrid Thresholding Algorithm for Cloud Detection on Ground-Based Color Images. *Journal of Atmospheric and Oceanic Technology* 28, 1286–1296. <https://doi.org/10.1175/JTECH-D-11-00009.1>
- Lilliestam, J., Barradi, T., Caldés, N., Gomez, M., Hanger, S., Kern, J., Komendantova, N., Mehos, M., Hong, W.M., Wang, Z., Patt, A., 2018. Policies to keep and expand the option of concentrating solar power for dispatchable renewable electricity. *Energy policy*, 116, 193–197. doi: 10.1016/j.enpol.2018.02.014

Bibliography

- Lilliestam, J., Pitz-Paal, R., 2018. Concentrating solar power for less than USD 0.07 per kWh: finally the breakthrough?. *Renewable Energy Focus*, 26, 17–21. doi: 10.1016/j.ref.2018.06.002
- Linke, F., 1922. Transmission coefficient and turbidity factor. *J Beitrage Phys Fr Atom*, 10, 91–103
- Lohmann, U., Neubauer, D., 2018. The importance of mixed-phase and ice clouds for climate sensitivity in the global aerosol–climate model ECHAM6-HAM2, *Atmos. Chem. Phys.*, 18, 8807–8828. doi: 10.5194/acp-18-8807-2018
- Lorenz, E., Remund, J., Müller, S., Traunmüller, W., Steinmaurer, G., Pozo, D., Ruiz-Arias, J., Fanego, V., Ramirez, L., Romeo, M., Kurz, C., Pomares, L., Guerrero, C., 2009. Benchmarking of different approaches to forecast solar irradiance. 24th European Photovoltaic Solar Energy Conference, Hamburg, Germany, 21–25.
- Luhmann, T., 2003. *Nahbereichsphotogrammetrie: Grundlagen, Methoden und Anwendungen*. 2. Auflage, Herbert Wichmann Verlag, Heidelberg
- MacDougall, A.H., Zickfeld, K., Knutti, R., Matthews, H.D., 2015. Sensitivity of carbon budgets to permafrost carbon feedbacks and non-CO₂ forcings. *Environmental Research Letters*, 10(12), 125003. doi: 10.1088/1748-9326/10/12/125003
- Madhavan, B. L., Kalisch, J., Macke, A., 2016. Shortwave surface radiation network for observing small-scale cloud inhomogeneity fields, *Atmos. Meas. Tech.*, 9, 1153–1166. doi:10.5194/amt-9-1153-2016
- Manabe, J., 1969. Climate and the ocean circulation I. The atmospheric circulation and the hydrology of the earth surface. *Mon. Wea. Rev.*, 97, 739–774. doi: 10.1175/1520-0493(1969)097<0775:CATOC>2.3.CO;2
- Marquez, R., Coimbra, C. F., 2013. Proposed metric for evaluation of solar forecasting models., *Journal of solar energy engineering*, 135(1). doi: 10.1115/1.4007496
- Martinez, D.M., Ebenhack, B.W., 2008. Understanding the role of energy consumption in human development through the use of saturation phenomena. *Energy Policy*, 36(4), 1430–1435. <https://doi.org/10.1016/j.enpol.2007.12.016>
- Martone, M., Bräutigam, B., Rizzoli, P., Gonzalez, C., Bachmann, M., Krieger, G., 2012. Coherence evaluation of TanDEM-X interferometric data. *ISPRS Journal of Photogrammetry and Remote Sensing*, 73, 21–29. <https://doi.org/10.1016/j.isprsjprs.2012.06.006>
- Martucci, G., Milroy, C., O’Dowd, C.D., 2010. Detection of cloud-base height using Jenoptik CHM15K and Vaisala CL31 ceilometers. *J. Atmos. Ocean. Technol.* 27 (2), 305–318. <http://dx.doi.org/10.1175/2009JTECHA1326.1>.
- Matthews, H.D., Caldeira, K., 2008. Stabilizing climate requires near-zero emissions. *Geophysical research letters*, 35(4). <https://doi.org/10.1029/2007GL032388>
- Matthews, H.D., Gillett, N.P., Stott, P.A., Zickfeld, K., 2009. The proportionality of global warming to cumulative carbon emissions. *Nature*, 459(7248), 829–832. doi: 10.1038/nature08047
- Mehos, M., Turchi, C., Jorgenson, J., Denholm, P., Ho, C., Armijo, K., 2016. On the Path to SunShot: Advancing Concentrating Solar Power Technology, Performance, and Dispatchability. Golden, CO: National Renewable Energy Laboratory. NREL/TP-5500-65688. <http://www.nrel.gov/docs/fy16osti/65688.pdf>.

Bibliography

- Meinshausen, M., Meinshausen, N., Hare, W., Raper, S.C., Frieler, K., Knutti, R., Frame, D.J., Allen, M.R., 2009. Greenhouse-gas emission targets for limiting global warming to 2 C. *Nature*, 458(7242), 1158–1162. doi: 10.1038/nature08017
- Mejia, F. A., Kurtz, B., Murray, K., Hinkelman, L. M., Sengupta, M., Xie, Y., Kleissl, J., 2016. Coupling sky images with radiative transfer models: A new method to estimate cloud optical depth, *Atmos. Meas. Tech.*, 9, 4151–4165. doi:10.5194/amt-9-4151-2016.
- Menzel, W.P., Smith, W.L., Stewart, T. R., 1983. Improved cloudmotion wind vector and altitude assignment using VAS, *J. Climate Appl.Meteorol.*, 22, 377–384. <https://doi.org/10.1175/1520-0450>
- Moran, K.P., Martner, B.E., Post, M.J., Kropfli, R.A., Welsh, D.C., Widener, K.B., 1998. An unattended cloud-profiling radar for use in climate research. *Bull. Amer. Meteor. Soc.*, 79, 443– 455. <https://doi.org/10.1175/1520-0477>
- Nguyen, D.A., Kleissl, J., 2014. Stereographic methods for cloud base height determination using two sky imagers. *Solar Energy* 107, 495–509. <http://dx.doi.org/10.1016/j.solener.2014.05.005>.
- Nieman, S.J., Schmetz, J., Menzel, W.P., 1993. A comparison of several techniques to assign heights to cloud tracers. *Appl. Meteor.*, 32, 1559-1568. <https://doi.org/10.1175/1520-0450>
- Noh, Y., Forsythe, J., Miller, S., Seaman, C., 2017. Cloud-base height estimation from VIIRS. Part II: A statistical algorithm based on A-Train satellite data. *J. Atmos. Oceanic.*, 34, 585–598, doi:10.1175/JTECH-D-16-0110.1.
- Noureldin, K., González-Escalada, L.M., Hirsch, T., Nouri, B., Pitz-Paal, R., 2016. Modelling and optimization of transient processes in line focusing power plants with single-phase heat transfer medium, *AIP Conference Proceedings*. Vol. 1734. doi: 10.1063/1.4949169
- Noureldin, K., Hirsch, T., Pitz-Paal, R., 2017. Virtual Solar Field-Validation of a detailed transient simulation tool for line focus STE fields with single phase heat transfer fluid. *Sol. Energy*146, 131–140. doi: 10.1016/j.solener.2017.02.028
- Noureldin, K., Hirsch, T., Kuhn, P., Nouri, B., Yasser, Z., Pitz-Paal, R., 2018. Modelling an automatic controller for parabolic trough solar fields under realistic weather conditions. *AIP Conference Proceedings*. Vol. 2033. doi: 10.1063/1.5067211
- Noureldin, K., 2019. Modelling and Control of Transients in Parabolic Trough Power Plants with Single-Phase Heat Transfer Fluids, Ph.D. thesis, Fakultät für Maschinenwesen der Rheinisch-Westfälischen Technischen Hochschule Aachen, Aachen Germany
- Nouri, B., Wilbert, S., García, G., Ramírez, L., Zarzalejo, L., Valenzuela, R., Ferrera, F., Guillot, E., 2016. Report on calibration campaigns for pyrheliometer and pyranometer, Sfera 2 project, Deliverable 11.3
- Nouri, B., Röger, M., Janotte, N., Hilgert, C., 2018a Characterization and corrections for clamp-on fluid temperature measurements in turbulent flows. *Journal of Thermal Science and Engineering Applications*. Vol. 10, 031011.
- Nouri, B., Kuhn, P., Wilbert, S., Prah, C., Pitz-Paal, R., Blanc, P., Schmidt, T., Yasser, Z., Ramirez Santigosa, L., Heineman, D., 2018b. Nowcasting of DNI Maps for the Solar Field Based on Voxel Carving and Individual 3D Cloud Objects from All Sky Images, *AIP Conference Proceedings*. Vol. 2033. doi:10.1063/1.5067196
- Nouri, B., Kuhn, P., Wilbert, S., Hanrieder, N., Prah, C., Zarzalejo, L., Kazantzidis, A., Blanc, P., Pitz-Paal, R., 2019a, Cloud height and tracking accuracy of three all sky imager systems for individual clouds. *Sol. Energy* 177, 213–228. doi: 10.1016/j.solener.2018.10.079

Bibliography

- Nouri, B., Wilbert, S., Segura, L., Kuhn, P., Hanrieder, N., Kazantzidis, A., Schmidt, T., Zarzalejo, L., Blanc, P., Pitz-Paal, R., 2019b, Determination of cloud transmittance for all sky imager based solar nowcasting. *Sol. Energy*, 181, 251–263. doi: 10.1016/j.solener.2019.02.004.
- Nouri, B., Wilbert, S., Kuhn, P., Hanrieder, N., Schroedter-Homscheidt, M., Kazantzidis, A., Zarzalejo, L., Blanc, P., Kumar, S., Goswami, N., Shankar, R., Affolter, R., Pitz-Paal, R., 2019c. Real-Time Uncertainty Specification of all Sky Imager Derived Irradiance Nowcasts. *Remote Sens.* 11(9), 1059. doi: 10.3390/rs11091059
- Nouri, B., Noureldin, K., Schlichting, T., Wilbert, S., Hirsch, T., Schroedter-Homscheidt, M., Kuhn, P., Kazantzidis, A., Zarzalejo, L.F., Blanc, P., Fernández, J., Pitz-Paal, R., 2019d. Optimization of parabolic trough power plant operation using irradiance maps from all sky imagers. *Sol. Energy* 198, 434–453. doi: 10.1016/j.solener.2020.01.045
- Nouri, B., Wilbert, S., Blum, N., Kuhn, P., Schmidt, T., Yasser, Z., Schmidt, T., Zarzalejo, L., Lopes, F., Silva, H., Schroedter-Homscheidt, M., Kazantzidis, A., Raeder, C., Blanc, P., Pitz-Paal, R., 2019e. Evaluation of an All Sky Imager Based Nowcasting System for Distinct Conditions and Five Sites. 25th SolarPACES Conference
- Nouri, B., Noureldin, K., Schlichting, T., Wilbert, S., Hirsch, T., Schroedter-Homscheidt, M., Kuhn, P., Kazantzidis, A., Zarzalejo, L., Blanc, P., Yasser, Z., Fernández, J., Pitz-Paal, R., 2019f. A way to increase parabolic trough plant yield by roughly 2% using all sky imager derived DNI maps. 25th SolarPACES Conference
- Oberländer, D., Prah, C., Wilbert, S., Müller, S., Stanicki, B., Hanrieder, N., 2015. Cloud shadow maps from whole sky imagers and voxel carving. *ICEM, Boulder*.
- Ohring, G., Adler, S., 1978. Some experiments with a zonally-averaged climate model, *Journal of Atmospheric Science*. 35, 186–205. doi: 10.1175/1520-0469(1978)035<0186:SEWAZA>2.0.CO;2
- Peng, Z., Yu, D., Huang, D., Heiser, J., Yoo, S., Kalb, P., 2015. 3D cloud detection and tracking system for solar forecast using multiple sky imagers *Sol. Energy* 118, 496–519. <https://doi.org/10.1016/j.solener.2015.05.037>.
- Perez, R., Kivalov, S., Schlemmer, J., Hemker Jr, K., Hoff, T., 2011. Parameterization of site-specific short-term irradiance variability. *Sol. Energy*, 85, 1343–1353. doi: 10.1016/j.solener.2011.03.016.
- Perez, R., David, M., Hoff, T.E., Jamaly, M., Kivalov, S., Kleissl, J., Lauret, P., Perez, M., 2016. Spatial and temporal variability of solar energy. *Found. Trends Renew. Energy* 1 (1), 1–44. doi: 10.1561/27000000006.
- Pitz-Paal, R., 2017. Concentrating solar power: still small but learning fast. *Nature Energy*. 2(7):17095. doi: 10.1038/nenergy.2017.95
- Platzer, WJ., 2016. Combined solar thermal and photovoltaic power plants—An approach to 24h solar electricity?. *AIP Conference Proceedings*. Vol. 1734. doi: 10.1063/1.4949173
- Pruppacher, R. H., Klett, J. D., 1997. *Microphysics of Clouds and Precipitation*. 2nd ed. Atmospheric and Oceanographic Sciences Library, Vol. 18, Kluwer Academic Publishers, ISBN 978-0-306-48100-0
- Quaschnig, V., 2015. *Regenerative Energiesysteme: Technologie-Berechnung-Simulation*. Carl Hanser Verlag GmbH Co KG. ISBN 978-3-446-44267-2
- Quesada-Ruiz, S., Chu, Y., Tovar-Pescador, J., Pedro, H., Coimbra, C., 2014. Cloud tracking methodology for intra-hour DNI forecasting. *Sol. Energy* 102, 267–275. doi: 10.1016/j.solener.2014.01.030.

Bibliography

- Raschke, R.A., Cox, S.K., 1983. Instrumentation and technique for deducing cloud optical thickness. *J. Clim. Appl. Meteorol.* 22 (11), 1887 – 1893. doi: 10.1175/1520-0450(1983)022<1887:IATFDC>2.0.CO;2
- REN21, 2018. Renewables 2018 Global Status Report, Paris: REN21 Secretariat. ISBN 978-3-9818911-3-3
- Richardson, W., Krishnaswami, H., Vega, R., Cervantes, M., 2017. A Low Cost, Edge Computing, All-Sky Imager for Cloud Tracking and Intra-Hour Irradiance Forecasting. *Sustainability* 2017. 9(4). 482. <https://doi.org/10.3390/su9040482>
- Rogelj, J., Schaeffer, M., Friedlingstein, P., Gillett, N.P., Van Vuuren, D.P., Riahi, K., Allen, M., Knutti, R., 2016. Differences between carbon budget estimates unravelled. *Nature Climate Change*, 6(3), 245–252. doi: 10.1038/NCLIMATE2868
- Rossow, W. B., Schiffer, R. A., 1999. Advances in understanding clouds from ISCCP. *Bull. Amer. Meteor. Soc.*, 80, 2261-2287. doi: 10.1175/1520-0477(1999)080<2261:AIUCFI>2.0.CO;2
- Sassen, K., 1991. The polarization lidar technique for cloud research: A review and current assessment. *Bull. Amer. Meteor. Soc.*, 72, 1848–1866. <https://doi.org/10.1175/1520-0477>
- Sassen, K., Wang, Z., 2012. The clouds of the middle troposphere: Composition, radiative impact, and global distribution, *Surv.Geophys.*, 33(3–4), 677–691. doi:10.1007/s10712-011-9163-x.
- Scaramuzza, D., Martinelli, A., Siegwart, R., 2006. A toolbox for easily calibrating omnidirectional cameras. In: 2006 IEEE/RSJ International Conference on Intelligent Robots and Systems. IEEE, 5695–5701.. <<http://ieeexplore.ieee.org/abstract/document/4059340/>>
- Schellnhuber, H.J., Rahmstorf, S., Winkelmann, R., 2016. Why the right climate target was agreed in Paris. *Nature Climate Change*, 6(7), 649–653.
- Schlichting, T., 2018. Bewertung der Verwendbarkeit von Strahlungskarten für den Einsatz in der Regelung eines Parabolrinnensystems, Master thesis, Fakultät für Ingenieurwissenschaften, Universität Duisburg-Essen, Germany
- Schmidt, T., Kalisch, J., Lorenz, E., Heinemann, D., 2016. Evaluating the spatio-temporal performance of sky-imager-based solar irradiance analysis and forecasts. *Atmos. Chem. Phys.* 16, 3399–3412. <http://dx.doi.org/10.5194/acp-16-3399-2016>.
- Schmidt, T., 2017. High resolution solar irradiance forecasts based on sky images, Ph.D. thesis, Fakultät für Mathematik und Naturwissenschaften der Carl von Ossietzky Universität Oldenburg, Oldenburg Germany
- Schroedter-Homscheidt, M., Gesell, G., 2016. Verification of sectoral cloud motion based direct normal irradiance nowcasting from satellite imagery, *AIP Conf. Proc.* 1734, 150007. doi: 10.1063/1.4949239
- Schroedter-Homscheidt, M., Kosmale, M., Jung, Sandra., Kleissl, Jan., 2018. Classifying ground-measured 1 minute temporal variability within hourly intervals for direct normal irradiances, *Meteorol. Z.*, doi: 10.1127/metz/2018/0875
- Schwarzbözl, P., Gross, V., Quasnig, V., Ahlbrink, N., 2011. a low-cost dynamic shadow detection system for site evaluation. In proceeding of the 17th SolarPACES, Granada, Spain, 20–23 September
- Seiz, G., Shields, J., Feister, U., Baltsavias, E., Gruen, A., 2007. Cloud mapping with ground-based photogrammetric cameras. *Int. J. Remote Sens.* 28 (9), 2001–2032. <http://dx.doi.org/10.1080/01431160600641822>.

Bibliography

- Sun, Z., Shine, K. P., 1994. Studies of the radiative properties of ice and mixed-phase clouds. *Quart. J. Roy. Meteor. Soc.*, 120, 111–137. doi: 10.1002/qj.49712051508
- Stein, J.S., Hansen, C.W., Reno, M.J., 2012. The variability index: A new and novel metric for quantifying irradiance and PV output variability. In *Proceedings of the World Renewable Energy Forum, Denver, USA, 13–17 May*
- Stubenrauch, C. J., Chedin, A., Rädcl, G., Scott, N.A. Serrar, S., 2006. Cloud properties and their seasonal and diurnal variability from TOVS Path-B. *J. Climate*, 19, 5531–5553. doi: 10.1175/JCLI3929.1
- Taravat, A., Frate, F. D., Cornaro, C., Vergari, S., 2015. Neural Networks and Support Vector Machine Algorithms for Automatic Cloud Classification of Whole-Sky Ground-Based Images, *IEEE Geoscience and Remote Sensing Letters* 12(3), 666–670. doi: 10.1109/LGRS.2014.2356616
- Titov, G. A., 1998. Radiative horizontal transport and absorption in stratocumulus clouds. *Journal of the Atmospheric Sciences*, 55, 2549–2560. doi: 10.1175/1520-0469(1998)055<2549:RHTAAI>2.0.CO;2
- Tzoumanikas, P., Nikitidou, E., Bais, A.F., Kazantzidis, A., 2016. The effect of clouds on surface solar irradiance, based on data from an all-sky imaging system, *Renew. Energy* 95, 314–322. doi: 10.1016/j.renene.2016.04.026.
- UN, 1992. United Nations Framework Convention on Climate Change. <https://unfccc.int/resource/docs/convkp/conveng.pdf>
- UNFCCC, 2015. Adoption of the Paris Agreement FCC/CP/2015/L.9/Rev.1. <https://unfccc.int/resource/docs/2015/cop21/eng/l09r01.pdf>
- Van Den Boomgaard, R., Van Balen, R., 1992. Methods for fast morphological image transforms using bitmapped binary images. *CVGIP: Gr. Models Image Process*, 54, 252–258. doi:10.1016/1049-9652(92)90055-3.
- Venema, V., Russchenberg, H., Apituley, A., Lammeren, A., Ligthart, L., 2000. Cloud boundary height measurements using lidar and radar. *Phys. Chem. Earth*, 25B, 129–134, doi:10.1016/S1464-1909(99)00139-2.
- Wacker, S., Grobner, J., Zysset, C., Diener, L., Tzoumanikas, P., Kazantzidis, A., Vuilleumier, L., Stockli, R., Nyeki, S., Kämpfer, N., 2015. Cloud observations in Switzerland using hemispherical sky cameras, *J. Geophys. Res. Atmos.* 120. doi: 10.1002/2014JD022643.
- Wagner, PH., Wittmann, M., 2014. Influence of different operation strategies on transient solar thermal power plant simulation models with molten salt as heat transfer fluid. *Energy Procedia*, 49, 1652-1663. doi: 10.1016/j.egypro.2014.03.174
- Wang, G., Kurtz, B., Kleissl, J., 2016. Cloud base height from sky imager and cloud speed sensor. *Sol. Energy* 131, 208–221. <http://dx.doi.org/10.1016/j.solener.2016.02.027>.
- Wang J., T. Uttal, and M. Rozendaal, 1999: Variability of cloud vertical structure during ASTEX from a combination of rawinsonde, radar, ceilometer and satellite data. *Mon. Wea. Rev.*, 127, 2484-2502. <https://doi.org/10.1175/1520-0493>
- Wang, J., Rossow, W., Zhang, Y., 2000. Cloud Vertical Structure and Its Variations from a 20-Yr Global Rawinsonde Dataset. *J. Clim.* 13, 3041 – 3056, [https://doi.org/10.1175/1520-0442\(2000\)013<3041:CVSAIV>2.0.CO;2](https://doi.org/10.1175/1520-0442(2000)013<3041:CVSAIV>2.0.CO;2)
- Wang, Z., K. Sassen, 2001. Cloud type and macrophysical property retrieval using multiple remote sensors. *Appl. Meteor.*, 40, 1665-1682. <https://doi.org/10.1175/1520-0450>.

Bibliography

- West, S.R., Rowe, D., Sayeef, S., Berry, A., 2014. Short-term irradiance forecasting using skycams: motivation and development. *Sol. Energy*, 110, 188-207. <http://dx.doi.org/10.1016/j.solener.2014.08.038>.
- Wilbert, S., Janotte, N., Pitz-Paal, R., van Wely, L., Geuder, N., 2010, September. Reduced uncertainties of field pyrheliometers through improved sensor calibration. In *Proc. SolarPACES Conf., Perpignan, France*.
- Wilbert, S., Nouri, B., Prah, C., Garcia, G., Ramirez, L., Zarzalejo, L., Valenzuela, L., Ferrera, F., Kozonek, N., Liria, J., 2016a. Application of Whole Sky Imagers for Data Selection for Radiometer Calibration. In: *EU PVSEC 2016 Proceedings*, 1493–1498. doi: 10.4229/EUPVSEC20162016-5AO.8.6
- Wilbert, S., Kleindiek, S., Nouri, B., Geuder, N., Habte, A., Schwandt, M., Vignola, F., 2016b. Uncertainty of rotating shadowband irradiometers and Si-pyranometers including the spectral irradiance error. *AIP Conference Proceedings* 1734. doi: 10.1063/1.4949241
- Woyte, A., Van Thong, V., Belmans, R., Nijs, J., 2006. Voltage fluctuations on distribution level introduced by photovoltaic systems. *IEEE Transactions on energy conversion*, 21, 202–209. doi: 10.1109/TEC.2005.845454
- Xia, M., Lu, W., Yang, J., Ma, Y., Yao, W., Zheng, Z., 2015. A hybrid method based on extreme learning machine and k-nearest neighbor for cloud classification of ground-based visible cloud image. *Neurocomputing* 160, 238–249. <https://doi.org/10.1016/j.neucom.2015.02.022>
- Yang, D., Kleissl, J., Gueymard, C.A., Pedro, H.T., Coimbra, C.F., 2018. History and trends in solar irradiance and PV power forecasting: A preliminary assessment and review using text mining. *Sol. Energy*, 168, 60–101. doi: 10.1016/j.solener.2017.11.023
- Ye, L., Cao, Z., Xiao, Y., 2017. DeepCloud: Ground-Based Cloud Image Categorization Using Deep Convolutional Features, *IEEE Transactions on Geoscience and Remote Sensing* 55(10), 5729–5740. doi: 10.1109/TGRS.2017.2712809
- Young, A.T., 1994. Air mass and refraction. *Applied optics*, 33(6), pp.1108-1110.
- Zaher, A., Thil, S., Nou, J., 2017. Comparative study of algorithms for cloud motion estimation using sky-imaging data. *IFAC-PapersOnLine* ,50,6108–6113. <http://dx.doi.org/10.1016/j.ifacol.2017.08.1488>.
- Zangvil, A., Lamb P.J., 1997. Characterization of sky conditions by the use of solar radiation data *Solar Energy*,61, pp. 17-22. doi: 10.1016/S0038-092X(97)00035-2
- Zaversky, F., Medina, R., García-Barberena, J., Sánchez, M., Astrain, D., 2013. Object-oriented modeling for the transient performance simulation of parabolic trough collectors using molten salt as heat transfer fluid. *Sol. Energy*, 95, 192–215. doi: 10.1016/j.solener.2013.05.015